

# Deciphering Variants of (Uncertain) Significance



**A context-based approach  
to unravel  
Variants of (Uncertain)  
Significance**

Irena Muffels

ISBN:	978-94-6506-367-6
Cover Design:	Irena Muffels
Layout and design:	Irena Muffels
Printing:	Ridder Print
© Copyright 2024:	Irena Muffels

Financial support for the research presented in this thesis was generously provided by United for Metabolic Diseases.

# **A context-based approach to unravel Variants of (Uncertain) Significance**

## **Een contextuele benadering om varianten van (onbekende) betekenis te ontrafelen**

(met een samenvatting in het Nederlands)

### **Proefschrift**

ter verkrijging van de graad van doctor aan de Universiteit  
Utrecht op gezag van de rector magnificus,  
prof. dr. Kummeling, ingevolge het besluit van het college voor  
promoties in het openbaar te verdedigen op

woensdag, 25 september, des middags te vier uur.

door

**Irena Josephina Johanna Muffels**

geboren op 21 juni 1994  
te Breda

**Promotor:**

Prof. dr. E.E.S. Nieuwenhuis

Copromotoren:

P.M. van Hasselt

S.A. Fuchs

**Beoordelingscommissie:**

Prof. dr. K.P.J. Braun (voorzitter)

Prof. dr. V.V.A.M. Knoers

Prof. dr. D. Lefeber

Prof. dr. E. Morava-Kozicz

Prof. dr. H.R. Waterham



## Table of contents

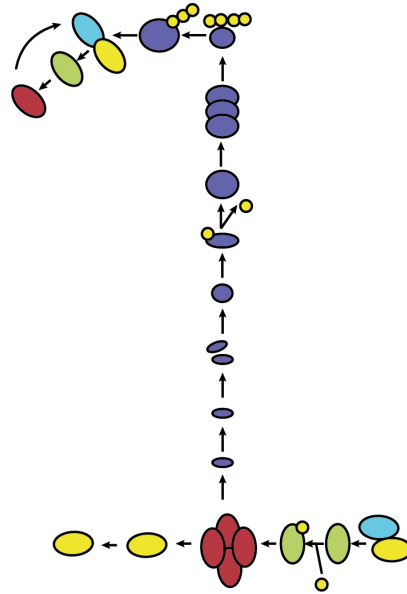
	Page
Chapter 1. General Introduction	10
Chapter 2. <i>NAA80</i> bi-allelic missense variants result in high-frequency hearing loss, muscle weakness and developmental delay.	22
Chapter 3. Bi-allelic variants in <i>NAE1</i> cause intellectual disability, ischiopubic hypoplasia, stress-mediated lymphopenia and neurodegeneration.	58
Chapter 4. <i>LIMK1</i> gain- and loss-of-function heterozygous missense variants cause divergent clinical phenotypes, due to altered actin cytoskeletal and exocytosis dynamics.	112
Chapter 5. Imaging Flow Cytometry-based cellular screening elucidates pathophysiology in individuals with Variants of Uncertain Significance.	146
Chapter 6. Imaging Flow Cytometry identifies divergent responses to mitochondrial pathology in patients with mitochondrial disease.	200
Chapter 7. Tailored amino acid treatment for mitochondrial Aminoacyl-tRNA synthetase deficiencies.	240
Chapter 8. QARS1 Deficiencies: unveiling mitochondrial dysfunction, impaired tRNA <sup>Gln</sup> import and therapeutic insights of glutamine supplementation.	284
Chapter 9. General Discussion and summary	308

Appendices		Page
	Nederlandse Samenvatting	326
	List of Publications	335
	About the Author	338
	Dankwoord/Acknowledgements	339





# Chapter



General Introduction:

## **Challenges in the modern era of genomics**

‘The great book of nature’, Galileo wrote in 1623, ‘can be read only by those who know the language in which it was written.’ This quote takes on tangible significance in human genetics, as the deciphering of the entire human DNA sequence in 2003 through the Human Genome Project furnished humanity with the ‘book of life’ comprising nearly 262.000 pages.<sup>1</sup> The results produced by the world’s largest collaborative project have been hailed as ‘The end of the beginning.’ Indeed, since 2003, genomic biology has taken flight, fueled by the increased accessibility of genomic sequencing as part of the diagnostic practice. Increased computational power and sophisticated data analysis tools have done the rest. Having the entire human genome at our fingertips, which complex genetic questions could not be solved?

While the ‘genome-first era’ has greatly enhanced our knowledge about inherited diseases, simultaneously it has revealed the astonishing complexity of genetics, bringing on many novel challenges. It is evident that humans are not merely a sum of their DNA base pairs inherited at birth; rather, genetics exists within a complex context affected by many factors such as epigenetics, the environment and genetic interactions. Large-scale sequencing projects, such as Genome-Wide Association Studies alongside data-driven tools capable of quantifying all biomolecules within a cell (transcriptomics, proteomics and metabolomics) have further enriched our understanding of genetic complexity. Yet, the immense volume of data generated with these techniques often transcends human comprehension. Without clear context, researchers and clinicians are at risk of ‘drowning in data lakes’.

### *Genetic Variation in health and disease*

With the unraveling of the entire human DNA sequence came the possibility to sequence the entire genome to search for genetic variation contributing to disease. Subsequently, technical advancements have led to a significant reduction of sequencing time and costs, leading to more and more patients having their DNA searched for genetic pathologies.

If family members are known to carry a genetic disease, the genome can be search in a targeted fashion. If no clear etiology is suspected, part(s) of the

genome or the entire genome can be searched (Gene Panels, Whole Exome (WES) or Whole Genome sequencing (WGS)). While WES or WGS represent effective methods to identify genetic pathology, they pose a risk of identifying potentially undesirable, accidental findings. Additionally, WGS or WES can reveal genetic variants of uncertain significance, which are highly challenging to interpret. In the next few paragraphs, we will elaborate as to why genetic variants of uncertain significance are generally considered challenging.

### *The Challenges of Variants of Uncertain Significance*

Variants of Uncertain Significance (VUS) are genetic variants identified through genome sequencing with uncertain clinical significance. In other words, a VUS might represent harmless genetic variation, or at the opposite end of the spectrum, lead to severe genetic disease. While numbers vary greatly, in approximately 25-73% of patients having Whole Exome or Whole Genome sequencing performed, Variants of Uncertain Significance are found.<sup>2,3</sup> VUSes inflict a considerable burden on patients, particularly in the case of pediatric patients, exhibiting severe symptoms without definitive diagnosis or treatment options. The prospect of a cause for their symptoms but lingering uncertainty is highly distressing for patients and their parents. Moreover, it is highly complex to subscribe the right therapy when diagnosis is not known. Until now, many patients with VUS are still left without a diagnosis, prognosis or therapeutic options.

When genetic variants are identified through genetic sequencing, they are compared to large population screening results, sometimes referred to as the healthy reference genome.<sup>4-6</sup> Genetic variants leading to monogenetic disease are subject to evolutionary constraint, making them absent or rarely seen in population databases, especially when it concerns heterozygous pathogenic variants. Therefore, most variation that is observed with high frequency in population databases is omitted from further analysis. All variants that remain, are analyzed using several tools and guidelines to aid their interpretation. First of all, so-called in-silico prediction tools exist, that use freely available data to predict the impact of the genetic variant. Depending

on the tool that is used, evolutionary conservation of the (neighboring) residue(s) among species, impact on RNA splice sites, and previously identified variants in the same gene are assessed. In the end, formal guidelines and expert opinion aid the judgment regarding pathogenicity, taking these in-silico predictions into account, but also other factors.<sup>7</sup> One of these factors is the gene's evolutionary constraint. Certain genes are essential for life or reproduction, and as a result, are much less tolerant for genetic variation leading to loss-of-function compared to other genes. This information can be used to predict the impact of genetic variants, especially when it concerns heterozygous variants. If the effect of the variant remains uncertain after employing these guidelines, it is considered a Variant of Uncertain Significance. In order to resolve a VUS, follow-up studies are usually needed, including experimental and/or functional studies to establish pathogenicity.

Many different types of functional studies to establish pathogenicity currently exist. For well-known disease genes, previously established functional assays can be re-used when a novel variant is found in the same gene. If functional studies are not available, they have to be developed. These assays can be developed at different levels, for example on RNA-, protein- or cellular pathway levels. Based on in-silico predictions, protein structure and available literature, one can decide which of these levels should take precedence. For example, when the variant is thought to result in a truncated protein, protein and/or RNA levels can be assessed. However, while RNA- and protein studies are useful to assess the direct impact of the genetic variant, they usually do not provide information about the impact on cellular functionality and/or the clinical phenotype. Most genes operate in a complex cascade of proteins, so-called cellular pathways, and understanding the impact on these pathways is essential to fully appreciate disease pathophysiology.

While the ACMG guidelines consider functional studies as a criterion for pathogenicity (“PS3: Well-established functional studies show a deleterious effect”) they do not provide detailed guidance on how all functional evidence should be graded.<sup>7</sup> The magnitude of genes housing VUSes has led to a plethora of assays being developed, that usually cannot be performed in

one single hospital, let alone one single country, impeding diagnostic follow-up. Moreover, not all functional assays are diagnostically verified nor protocolized, making their interpretation challenging at times. Most genes have pleiotropic functions, making it unclear which functionalities should be studied and how this relates to the clinical phenotype. In another subset of cases, the Variant of Uncertain Significance is located in a gene with unknown function (Gene of Uncertain Significance, GUS), making it almost impossible to discern functionality at all. How can we structure and prioritize the assessment of functional consequences of a VUS in a field with so many unknowns?

### *The need for Context*

In the coming era, the quantity and complexity of genetic information will only increase. In its slipstream, the number of VUS cases will increase as well, leading to the unavoidable necessity of their interpretation. Currently, existing guidelines fail to provide clarity in the majority of VUS cases. While functional studies are essential to unravel the impact of a genetic variant, there is no consensus on how to structure these. Additionally, as mentioned earlier, structuring functional follow-up studies can be incredibly complex for a number of reasons. Thus, the unresolved paradox of the increasing availability of genetic data simultaneously generating significant uncertainty, requires a new outlook on this part of genetics. Part of the solution might lie in providing a context or framework that simplifies and structures the interpretation of genetic findings.

Over the years, several of these frameworks have been developed to aid the interpretation of VUSes, including statistical methodologies, integration of OMICS data, and the adoption of phenotype first strategies.<sup>8-15</sup> Especially when it comes to appreciating milder phenotypes or phenotypes associated with pleiotropic genes. Additionally, the deluge of data produced with OMICS-based frameworks is difficult to interpret without prior knowledge of the gene that houses the VUS and the pathways it operates in. Finally, most of these frameworks do not offer clear guidance on how to structure follow-up experiments.

An effective framework or context has the ability to answer fundamental genetic questions. In other words, it helps pinpoint ‘where to look.’ In this regard, we feel as this requires to view the gene within its broader context, being aware of not applying excessive detail that obscures judgment.

One approach could be by appreciating the functional interaction of the affected gene or protein with other biomolecules, or appreciating the gene within its cellular functional context. For example, most genetic lysosomal storage disorders are characterized by excessive lysosomal accumulation within cells, that can be visualized and/or quantified. This functional phenotype reveals one of the key characteristics and pathophysiological mechanisms of lysosomal storage disorders. These simple yet recognizable functional characteristics could potentially help predict pathogenicity of a VUS, and discern pathophysiological mechanisms caused by a VUS. We advocate that appreciation of a VUS or genetic disease within its functional context could provide a useful framework for VUS elucidation.

Another approach of how to apply context could be through viewing a genetic finding in the broader tapestry of medicine or other relevant scientific domains. For example, several phenotype-first approaches have been developed, that help interpret VUSes in the light of similar phenotypes compared to well-known diseases. Another example could be of appreciating the variant in its dynamic context, through appreciation of its expected protein interactions and kinetic properties.

### *Outline of this thesis*

In this thesis, we explored the potential of a framework for individuals with VUS using several approaches. In the first three chapters, we elucidated VUS cases, thereby illustrating the inherent complexity that comes with solving these cases. Additionally, we tried to answer specific genetic questions that were raised, by viewing them in the broader tapestry of medical and scientific domains. In the second part of this thesis, we used a functional cellular screening to allow straightforward assessment of pathogenicity and

pathophysiology for individuals with VUS. In the final part of this thesis, we applied our straightforward functional screening tool in known genetic diseases to uncover novel insights into disease mechanisms.

### *Elucidation of three VUS cases*

In **Chapter 2**, we describe our seemingly most straightforward VUS case: two brothers with genetic variants in the *NAA80* gene. Since we knew the function of NAA80 and the cellular implications if the gene was dysfunctional, the set-up of our experiments was more or less decided. What puzzled us, was the fact that we were only able to identify *NAA80* variants in one single family in the entire world, even though these variants are not subject to significant mutational constraint. In order to solve this mystery, we compared the clinical phenotype of individuals with *NAA80* variants to the phenotype of patients with other actin-related diseases. Viewing these findings in the light of NAA80 enzyme kinetics, we found that there was a very small range where actins would have been affected to a degree severe enough to induce a phenotype, without compromising over 50% of the cytoplasmic actin population, which would be lethal. The chance of a genetic variant inducing an effect that falls exactly within this range is extremely small, hence explaining the limited number of patients observed. Thus, for this chapter, context was provided by using enzyme kinetics and phenotypic similarities, which helped us to solve the intricate question of how this disease became so rare.

In **Chapter 3**, we describe four individuals with genetic missense variants in the *NAE1* gene. While our initial experiments suggested *NAE1* variants were indeed pathogenic, the large number of clinical symptoms and cellular pathways affected made it challenging to discern pathophysiological mechanisms. We believed there was only a handful of mechanisms primarily affected in patients with *NAE1* variants, and decided to structure the phenotypic features based on their uniqueness. We felt that the most unique phenotypic features would most clearly provide insight in the role of NAE1. Indeed, focusing on the most rare phenotypic features helped to structure our experimental findings and put the RNA sequencing results into perspective. For



this chapter, context was provided by combining phenotypic uniqueness with our biochemical data, allowing us to design and structure our functional experiments and shed light on NAE1's most important functions.

In **Chapter 4**, we describe a complex VUS case related to missense variants in the *LIMK1* gene in two children. They showed divergent clinical phenotypes, suggesting that they might not harbor the same disease. However, when we assessed LIMK1 in the context of its complex interactions, this led us to believe that pathogenic variants could affect the pathway in potentially opposite ways. Indeed, we found that *LIMK1* variants were predicted to have opposite effects, leading to either increased or decreased LIMK1 activity. Functional studies performed in fibroblasts supported these opposite effects on LIMK1 activity. Assessing insulin exocytosis in insulin-secreting cell lines expressing these two variants revealed opposite effects on exocytosis dynamics, which might explain the frequent hypoglycemic events observed in one of the patients. Thus, we were able to make sense as of why these divergent phenotypes were observed in the individuals harboring variants in the same gene, by exploring these variants in relation to their effects on the complex LIMK1 dynamics.

### *Functional screening for individuals with VUS*

In the next part of this thesis, we focused on optimizing the process of VUS elucidation. As said in the first part of this introduction, we aimed to do so by providing context using a functional cellular screening.

In **Chapter 5**, we explored the potential of a functional framework to interpret VUSes. To this aim, we screened patient fibroblasts derived from individuals with VUS using Imaging Flow Cytometry (IFC). We designed six assays that quantified essential components of cellular health frequently involved in disease: mitochondrial, Golgi, autophagic and lysosomal health, together with NF- $\kappa$ B translocation and ER-stress. We included molecular compounds and positive control patients that were known to induce aberrancies on their designated assays. Additionally, we verified whether these positive control patients would show aberrancies beyond the assay for which

they were primarily selected, to see whether the combination of six assays would be beneficial.

Next, we included fibroblasts of 20 individuals with VUS. For individuals with VUS in well-known disease genes, we included patients harboring pathogenic variants in the same gene as comparison. Well-established diagnostic functional assays were used to verify the accuracy of IFC predictions. We found IFC was able to provide relevant functional aberrancies for all individuals with VUS included in this study. In addition, for 12/20 individuals, IFC-based screening revealed detailed and potentially relevant clues about underlying pathophysiology which can be used to aid VUS elucidation.

In **Chapter 6**, we explored the potential of the IFC-based assays focused on mitochondrial function to assess its potential to discriminate between several subtypes of mitochondrial disease and their underlying pathophysiological mechanisms. While we expected to see mostly disease subtype-specific aberrancies on mitochondrial assays, we identified two large clusters of patients showing similar responses to mitochondrial injury that transcended disease subtypes, and can be characterized as either a hypo- (cluster 1 or a hypermetabolic (cluster 2 response. When assessing the location of the genetic variants and their predicted impact, we found that the first cluster correlated with a specific disruption of complex I assembly, while the second cluster was was expected to have severely disrupted proton pumping activity.

In **Chapter 7**, we used our IFC-based screening to assess mitochondrial function in fibroblasts of patients with pathogenic *ARS2* variants during amino acid supplementation. This chapter builds on earlier work in patients with pathogenic *ARS1* variants, where we found that amino acid treatment relieved clinical symptoms. We aimed to translate this approach to *ARS2*-deficient patients, however, as cellular growth was not affected in these patients, we sought for alternative read-outs. Using the IFC-based mitochondrial assay complemented with Oxygen Consumption measurements using seahorse, we found that amino acid depletion had detrimental effects on mitochondrial function. To prevent depletion, we treated *ARS2* deficient

patients with amino acids, and found improvements of clinical symptoms for all patients.

For Chapter 6, we assessed mitochondrial function in a large number of different ARS1-, ARS2- and combined ARS deficiencies. To our surprise, we found that there was one cytosolic ARS deficiency (QARS1 deficiency where we observed mitochondrial dysfunction, which was not observed in all other cytosolic ARS1 deficiencies. In **Chapter 8**, we explored the pathophysiology behind the mitochondrial dysfunction in QARS1 patient-derived fibroblasts, and how this was related to the unique mechanism of tRNA charging with glutamine in mitochondria and the potential import of cytosolically charged tRNA<sup>Gln</sup>. Additionally, we explored the safety and efficacy of glutamine supplementation at a clinical level. Thus, functional studies, including IFC-based functional screening, helped to delineate the disease mechanism behind QARS1 deficiency.

### References

1. Craig Venter J, Adams MD, Myers EW, Li PW, Mural RJ, Sutton GG, et al. The sequence of the human genome. *Science* (80- ). 2001;291(5507):1304–51.
2. Dixon-Salazar TJ, Silhavy JL, Udpa N, Schroth J, Bielas S, Schaffer AE, et al. Exome Sequencing Can Improve Diagnosis and Alter Patient Management. *Sci Transl Med*. 2012;4(138).
3. Trujillano D, Bertoli-Avella AM, Kumar Kandaswamy K, Weiss ME, Köster J, Marais A, et al. Clinical exome sequencing: Results from 2819 samples reflecting 1000 families. *Eur J Hum Genet*. 2017;25(2):176–82.
4. Chen S, Francioli LC, Goodrich JK, Collins RL, Wang Q, Alföldi J, et al. A genome-wide mutational constraint map quantified from variation in 76,156 human genomes. *bioRxiv*. 2022;
5. Karczewski KJ, Francioli LC, MacArthur DG. The mutational constraint spectrum quantified from variation in 141,456 humans. *Yearb Paediatr Endocrinol*. 2020;
6. Karczewski KJ, Weisburd B, Thomas B, Solomonson M, Ruderfer DM, Kavanagh D, et al. The ExAC browser: Displaying reference data information from over 60 000 exomes. *Nucleic Acids Res*. 2017;45(D1):D840–5.
7. Richards S, Aziz N, Bale S, Bick D, Das S, Gastier-Foster J, et al. Stan-

dards and guidelines for the interpretation of sequence variants: A joint consensus recommendation of the American College of Medical Genetics and Genomics and the Association for Molecular Pathology. *Genet Med.* 2015;17(5):405–24.

8. Bains S, Dotzler SM, Krijger C, Giudicessi JR, Ye D, Bikker H, et al. A phenotype-enhanced variant classification framework to decrease the burden of missense variants of uncertain significance in type 1 long QT syndrome. *Hear Rhythm.* 2022;19(3):435–42.

9. Dekker J, Schot R, Bongaerts M, de Valk WG, van Veghel-Plandsoen MM, Monfils K, et al. Web-accessible application for identifying pathogenic transcripts with RNA-seq: Increased sensitivity in diagnosis of neurodevelopmental disorders. *Am J Hum Genet.* 2023;110(2):251–72.

10. Gijavanekar C, Elsea SH. Clinical Untargeted Metabolomics as a Functional Screen to Improve Variant Classification. *Curr Protoc.* 2023;3(4).

11. Liang KX, Kristiansen CK, Mostafavi S, Vatne GH, Zantingh GA, Kianian A, et al. Disease-specific phenotypes in iPSC-derived neural stem cells with POLG mutations. *EMBO Mol Med.* 2020;12:e12146.

12. Lyra PCM, Nepomuceno TC, de Souza MLM, Machado GF, Veloso MF, Henriques TB, et al. Integration of functional assay data results provides strong evidence for classification of hundreds of BRCA1 variants of uncertain significance. *Genet Med.* 2021;23(2):306–15.

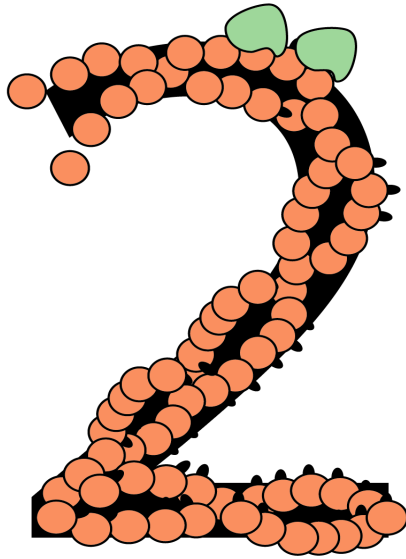
13. Oulas A, Minadakis G, Zachariou M, Spyrou GM. Selecting variants of unknown significance through network-based gene-association significantly improves risk prediction for disease-control cohorts. *Sci Rep.* 2019;9(1).

14. Qian D, Li S, Tian Y, Clifford JW, Sarver BAJ, Pesaran T, et al. A Bayesian framework for efficient and accurate variant prediction. *PLoS One.* 2018;13(9).

15. Weile J, Sun S, Cote AG, Knapp J, Verby M, Mellor JC, et al. A framework for exhaustively mapping functional missense variants. *Mol Syst Biol.* 2017;13(12).



# Chapter



***NAA80* bi-allelic missense variants result in high-frequency hearing loss, muscle weakness and developmental delay.**

***NAA80* bi-allelic missense variants result in high-frequency hearing loss, muscle weakness and developmental delay.**

Irena J. J. Muffels,<sup>1</sup> Elsa Wiame,<sup>2</sup> Sabine A. Fuchs,<sup>1</sup> Maarten P. G. Massink,<sup>3</sup> Holger Rehmann,<sup>4</sup> Jiska L. I. Musch,<sup>1</sup> Gijs Van Haften,<sup>5</sup> Didier Vertommen,<sup>6</sup> Emile van Schaftingen,<sup>7</sup> and Peter M. van Hasselt<sup>1</sup>

<sup>1</sup> Department of Metabolic Diseases, Division of Pediatrics, Wilhelmina Children's Hospital University Medical Centre, Utrecht.

<sup>2</sup> Laboratoire de biologie moléculaire, UCLouvain-Cliniques Universitaires Saint-Luc, Brussels.

<sup>3</sup> Department of Genetics, Section of Genome Diagnostics, Division Laboratories, Pharmacy and Biomedical Genetics, Utrecht.

<sup>4</sup> Department of Energy and Biotechnology, Flensburg University of Applied Sciences, Flensburg.

<sup>5</sup> Department of Genetics, Division Laboratories, Pharmacy and Biomedical Genetics, Utrecht.

<sup>6</sup> Mass Spectrometry Platform, de Duve Institute, UCLouvain, Brussels.

## Abstract

**Background:** The recent identification of NAA80/NAT6 as the enzyme that acetylates actins generated new insight into the process of posttranslational actin modifications; however, the role of NAA80 in human physiology and pathology has not been clarified yet.

**Results:** We report two individuals from a single family harbouring a homozygous c.389T>C, p.(Leu130Pro) *NAA80* genetic variant. Both individuals show progressive high-frequency sensorineural hearing loss, craniofacial dysmorphisms, developmental delay and mild proximal and axial muscle weakness.

Based on the molecular structure, we predicted and confirmed the *NAA80* c.389T>C, p.(Leu130Pro) variant to result in protein destabilization, causing severely decreased NAA80 protein availability. Concurrently, individuals exhibited a 50% decrease of actin acetylation. Patient-derived fibroblasts and peripheral blood mononuclear cells showed increased migration, increased filopodia counts and increased levels of polymerized actin, in agreement with previous observations in *NAA80* knock-out cells. Furthermore, the significant clinical overlap between individuals with *NAA80* variants and individuals with pathogenic variants in several actin subtypes reflects the general importance of controlled actin dynamics for the inner ear, brain and muscle.

**Conclusion:** Taken together, we describe a new syndrome, caused by *NAA80* genetic variants leading to decreased actin acetylation and disrupted associated molecular functions. Our work suggests a crucial role for NAA80-mediated actin dynamics in neuronal health, muscle health and hearing.



## Introduction

Actins are among the most conserved and ubiquitously expressed proteins in vertebrates. In humans, six actin genes exist; four actins are primarily involved in muscle contraction, whereas b-actin (*ACTB*) and c-1-actin (*ACTG1*) are cytosolic and facilitate cellular movement, exocytosis, organelle trafficking and regulation of genetic transcription.<sup>1-3</sup> In muscle cells, actins and myosins form tightly organized myofibrils that facilitate muscle contraction,<sup>4</sup> whereas in non-muscle cells, the actin network is highly dynamic, resulting in dynamic modelling of actin filaments that fit the cells' particular needs.<sup>5,6</sup>

Actins differ mostly at their N-terminus, which consists of three or four acidic residues (glutamate or aspartate), the first of which is acetylated on its amino group to suppress the positive charge of the amine. The acetyltransferase involved in this modification is NAA80, that belongs to a family of N-acetyltransferases, modifying the N-terminus of a wide range of proteins.<sup>7-11</sup> NAA80 is specific for actin as a result of the untypically highly acidic N-terminus of actins. In fact, no other N-acetyltransferase can compensate for loss of NAA80.<sup>7,8,10</sup> The specificity of NAA80 for actin is not only due to the acidic character of the N-terminus of actins, but also due to other specific interactions that NAA80 can establish with actins. These include formation of a ternary complex with Profilin-2 (PFN2), a protein known to bind to monomeric actin.<sup>7,12</sup> In most cell types, 99% of the N termini of all actin subtypes are acetylated.<sup>8</sup>

At a cellular level, the increased negative charge density induced by actin acetylation is thought to result in altered actin dynamics, including actin stability and elongation, that influence cell size, filopodia formation and cellular migration.<sup>9,13</sup> For example, *NAA80* knockout cell lines showed increased filopodia counts, increased cell size and increased cellular migration.<sup>9</sup> However, consequences of absent actin acetylation have only been studied in immortalized cell lines, which may be more tolerant to actin cytoskeletal dysfunction than well-differentiated tissues. As a result, the importance of

actin acetylation in organisms has yet to be determined.

Here, we describe two brothers, homozygous for a c.389T>C, p.(Leu130Pro) variant in *NAA80*, with high-frequency sensorineural hearing loss and craniofacial dysmorphisms. We found that the *NAA80* variants impacted protein stability, resulting in decreased NAA80 protein levels and decreased actin N-terminal acetylation. At a cellular level, changes in filopodia formation, actin polymerization and motility were observed. The brothers with *NAA80* genetic variants have significant phenotypic overlap with patients harbouring c-actin and b-actin mutations, suggesting that disrupted cytoskeletal actin dynamics might be causing the observed phenotype. Together, these results implicate an important role for actin acetylation in human physiology and pathology.

## Materials and Methods

### *Ethics*

Informed consent was obtained from the parents of probands 1.2 and 1.4 to collect residual material collected for diagnostic purposes to include in the Wilhelmina Children's Hospital metabolic biobank (TCBio 19-489/B, <https://tcbio.umcutrecht.nl>). From proband 1.2, we included both fibroblasts and PBMCs. From proband 1.4 we were only able to include PBMCs. In the same biobank, we included residual material of four different paediatric healthy fibroblast lines. Healthy adult donor PBMCs (N = 6) were obtained by using the Minidonor Service, an ethics review board approved blood donation facility at the UMC Utrecht (protocol number 18-774). Since healthy donor material availability was limited, we were not able to match individuals exactly by age and gender with healthy donors. Additionally, informed consent was obtained for publication of facial images and medical images of both individuals. All procedures performed in studies involving human participants were in accordance with the ethical standards of the institutional and/or national research committee(s) and with the Helsinki Declaration (as revised in 2013).

### *Whole-exome sequencing and genetic analyses*

Exomes were enriched using Agilent SureSelect XT Human All Exon kit V5 and sequenced on a HiSeq sequencing system (Illumina). Reads were aligned to hg19 using Burrows–Wheeler Aligner. Variants were called using Genome Analysis Toolkit Variant Caller and annotated, filtered and prioritized using the Bench NGS Lab platform (Agilent-Cartagenia, Leuven, Belgium) and/or an in-house designed ‘variant interface’ and manual curation. The minimal coverage of the full target was 15 94.2%. All common polymorphisms with a minor allele frequency >0.25 were filtered out using several public databases including 1000 genomes database,<sup>14</sup> Ensembl GRCh37 genome browser,<sup>15</sup> exome aggregation consortium database,<sup>16</sup> genome aggregation database (gnomAD)<sup>17</sup> and database of single-nucleotide polymorphisms. All variants with one of the following effects were included: Splice-site, STARTLOSS, STOP, Frameshift, STOPLOSS, NONSYNONYMOUS. Variant calling was performed using the complete human reference genome (hg19, NCBI release GRCh37). Sanger sequencing was performed to identify if the same genetic variants were present in other probands, using the following primers: for *NAA80*: 5'-GATGCTTGTGCTGACCTCA-3' and 3'-GGGCTGGTTCAGCACC-5', for *PLXNB1*: 5'-CCCCTGGCTCC CAGGTCGC-3' and 3'-GCTCACACT-CGACCCGGGCC-5', for *HDAC6*: 5'-AACTATGACCTCAACCGGCCA-3' and 3'-CTGTGAACCAACATCAGCTCT-5', for *PRR14L*: 5'-TCTAG-CCTGGCATGGTGG-3' and 3'-GCTGGAGATTCACATCAATCATTT-50. Individuals were evaluated according to the Wilhelmina Children's hospital clinical practice, and all laboratory analyses were performed in ISO 9001/ISO15189 accredited diagnostic laboratories.

### *Structural assessment of variants*

A sequence-based search of the pdb database (12 December 2020) identified the entries 6NAS, 6NBE, 6NBW and 5WJD as informative. To assess putative structural consequences of the variants, the identified structural data were inspected and individual structures superimposed in Bragi.<sup>18</sup> Graphical representations were generated based on pdb entry 6NBE using MolScript19 and Raster3D.<sup>20</sup> NAA80 expression in *Escherichia coli* and in HAP1 cells

Recombinant NAA80 expression and purification from *Escherichia coli* were performed as previously described.<sup>8</sup> Phosphorylated primers 5'-CTG-CCAAGCCCCACCCACACTTG-3' and 5'-CATCAGGCAGAGGGG-GAAGGCATCTG-3' were used to introduce the c.389T>C, p.(Leu130Pro) variant in *NAA80* sequence cloned in pET-22b and the construct was validated by sequencing. To generate lentiviral constructs for the expression of wild-type and mutant NAA80 in *NAA80* knockout HAP1 cells, the *NAA80* open reading frame (with and without the c.389T>C, p.(Leu130Pro) variant) was inserted in the XbaI and BsrGI sites of the vectors pUB81, pUB82 and pUB83. These vectors are derivatives of the pLVX-PURO (Clontech, Mountain View, USA) driving expression of the gene of interest under the control of EF-1 alpha, SV40 and CMV promoter.<sup>21</sup> Human Embryonic Kidney 293T cells were transiently co-transfected with these lentiviral vectors and second generation packaging plasmids psPAX2 and pMD2 with Jet-Pei reagent. Forty-eight hours after transfection, *NAA80* knockout HAP1 cells were infected as described previously and selected with 2 mg/ml puromycin.

#### *Wild-type NAA80 cDNA transduction in fibroblasts*

Patient cells and healthy control fibroblasts were transduced by combining 8 mg/ml Polybrene (#TR-1003-G, Bio-connect, Huissen, The Netherlands) with 100 ml of lentiviral vectors with second generation packaging plasmids. Selection was performed using 2 mg/ml puromycin.

#### *Western blot*

Procedures for western blot in HAP1 knockout cells were described previously.<sup>8</sup> For the fibroblast western blots, cells were harvested with 0.05% trypsin/EDTA, washed once with Phosphate Buffered Saline (PBS) without calcium and magnesium and lysed in Laemmli buffer (SDS, Glycerol, Tris) supplemented with a protease inhibitor cocktail (#P8340, Sigma Aldrich, Darmstadt, Germany). Protein concentration was determined using the Bicinchoninic acid assay kit, using bovine serum albumin as standard (#23225, Thermo Fisher Scientific, Waltham, USA). Blotting was performed using wet transfer (1.5 hours, 100 Volt) in blotting buffer (20% methanol, Sodium Dodecyl Sulfate (SDS)/glycine). The following antibodies were

used: anti-NAA80 (#15476-1; Proteintech, Rosemont, USA) and B-tubulin (CST2128S, Cell Signaling Technology, Danvers, USA).

### *Mass spectrometry analysis of actin N-termini*

A mass spectrometry approach was used to quantify actin N-terminal acetylation precisely. As acetylation of a peptide changes the intensity of the signal obtained by mass spectrometry, we converted in vitro non-acetylated actin to fully acetylated actin by incubation with labelled  $^{13}\text{C}_2$ ,  $\text{D}_3$ -acetyl-CoA and recombinant NAA80. Trypsin digestion and mass spectrometry allowed the quantification of the non-labelled N-terminal peptide (i.e. the endogenously acetylated) and the labelled N-terminal peptide (i.e. unacetylated in intact cells).

In practice,  $^{13}\text{C}_2$ ,  $\text{D}_3$ -acetyl-CoA was synthesized from acetic anhydride- $^{13}\text{C}_4$ ,  $\text{D}_6$  (Sigma-Aldrich) and coenzyme A (sodium salt; from Sigma-Aldrich) as previously described.<sup>22</sup> Fibroblasts (from one confluent 10-cm plate), PBMC (from 9 ml of fresh blood) or buffy coat cells (from 9 ml fresh blood) were resuspended in a buffer containing 25 mM HEPES, pH 7.4, 0.5 mM phenylmethylsulfonyl fluoride, 5 mg/l leupeptin and 5 mg/l antipain, submitted to two cycles of freezing in liquid nitrogen and thawing, and lysed by vortex-mixing. Cell extracts were centrifuged for 15 min at 15,000g and 4°C. Protein concentration was determined with the Bradford assay using  $\gamma$ -globulin as a standard. Fifty micrograms of cell extract supernatants were incubated at 37°C, in a mixture (100  $\mu\text{l}$ ) containing 50 mM Tris, pH 7.5, 25 mM Kalium Chloride, 1 mM  $\text{MgCl}_2$  and 0.15 mM  $^{13}\text{C}_2$ ,  $\text{D}_3$ -acetyl-CoA. The reaction was initiated by the addition of 150 ng recombinant NAA808 and stopped after 5 min with 400  $\mu\text{l}$  cold methanol and 100  $\mu\text{l}$  chloroform.

For mass spectrometry analysis, samples were treated essentially as described.<sup>8</sup> Separation was performed with a linear gradient of 4–50% solvent B (0.1% fluoroacetic acid in 98% acetonitrile) for 100 min, 50–75% solvent B for 10 min and holding at 95% for the last 5 minutes at a constant flow rate of 300 nl/min. Intact peptides were detected in the Orbitrap at a resolution of 120 000. Peptides were selected for tandem mass spectrometry (MS/

MS) using high energy collision dissociation setting at 35; ion fragments were detected in the Orbitrap at a resolution of 50 000. A targeted mass list was included for the six theoretical peptide sequences (see **Supplementary Table 1**), considering oxidation of Met, acetylation of the N-terminus, incorporation of 2  $^{13}\text{C}$  and 3 deuterium and charge states +2. The electrospray voltage applied was 2.1 kV. MS1 spectra were obtained with an automatic gain control target of  $4 \times 10^5$  ions and a maximum injection time of 50 ms, and targeted-MS2 spectra were acquired with an automatic gain control target of  $2 \times 10^5$  ions and a variable injection time. For MS scans, the m/z scan range was 350–1800. The resulting MS/MS data were processed and quantified using Skyline (version 19.1.0.193).<sup>23</sup>

Trypsin was specified as cleavage enzyme allowing up to two missed cleavages, four modifications per peptide and two charges. Mass error was set to 10 ppm for precursor ions and 0.05 Da for fragment ions. An example of analysis is illustrated in **Supplementary Fig. 1**.

#### *Filopodia count*

Fibroblasts of proband 1.2 were cultured in Ham F12 medium (#11765054, Thermo Fisher) supplemented with 10% fetal bovine serum (#F7524, Sigma Aldrich), 100 UI/ml penicillin and 100  $\mu\text{g/ml}$  streptomycin, in a humidified incubator at 37°C and 5% CO<sub>2</sub>. Cells were split at 80% confluency. For the assay, cells were plated in a 96-well plate (500 cells/well). After 24 hours, cells were fixed with 4% formaldehyde and permeabilized with 0.1% Triton X-100. Cells were incubated with phalloidin-tetramethylrhodamine B isothiocyanate (TRITC) (#P1951, Sigma-Aldrich, 1:100) and mounted with Hoechst (#B2261, Sigma 1:2000). Cells were visualized with the Leica TCS SP8 (Wetzlar, Germany) using 63X enlargement. Pictures were analysed with FiJi ImageJ software, using the FiloQuant package.<sup>24</sup> For analysis, GraphPad Prism was used (Version 8.0.0 for Windows, GraphPad Software, San Diego, USA).

#### *Flow cytometry analysis*

Actin polymerization was determined by staining PBMCs and fibroblasts

with Phalloidin-TRITC and subsequent analysis by flow cytometry. For fibroblasts, cells were plated in a 6-well plate ( $5 \times 10^4$  cells/well) and grown until 80% confluency. Cells were harvested using TrypLE (#12604013, ThermoFisher), washed and immediately fixed and permeabilized. Afterwards, cells were incubated Phalloidin-TRITC (1:1000) and DRAQ5 (1:8000). For PBMCs, after fixation and permeabilization, they were stained with 1:100 phalloidin-TRITC and 1:8000 DRAQ5 (#424101, Biolegend, San Diego, USA). Cells were analysed with BD LSR Fortessa (BD Biosciences, San Jose, USA). Analysis of flow cytometry data was performed with FlowJo (version 10.6.2., Becton, Dickinson and Company; 2019).

#### *Boyden chamber analysis*

Fibroblasts were plated in a 24-well Transwell insert (Corning, Glendale, USA) at a density of  $1 \times 10^4$  in normal culture medium without fetal bovine serum. The bottom chamber was coated with collagen-I (#354236, Corning) and filled with either serum free medium or 600  $\mu$ l HAM-F12 culture medium containing 10% fetal bovine serum. After 24 hours, the top chamber was scraped with a cotton swab and 400  $\mu$ l of 0.5% trypsin was added to the bottom chamber. Afterwards, 400  $\mu$ l culture medium containing 1000 $\times$  diluted Hoechst 3342 (#B2261, Sigma Aldrich) was added to the bottom chambers with the cells and immediately visualized with the EVOS™ XL Imaging System (ThermoFisher).

PBMCs were isolated from whole blood using Ficoll (#17-1440-02, GE Healthcare Hoevelaken, The Netherlands). Briefly, Ficoll was layered under whole blood mixed with one volume PBS and the whole was centrifuged for 20 min at 2400 rpm. PBMCs were collected, washed and frozen in 10% Dimethyl sulfoxide (DMSO) in fetal bovine serum. On the day of the assay, PBMCs were thawed and plated at a density of 50 000 cells in the upper part of 96-well transwell insert (# 3388, Corning). PBMCs were allowed to migrate for 4 hours. Cells in both bottom and upper part of the transwell were fixed, permeabilized and stained with 1:100 phalloidin-TRITC and 1:8000 DRAQ5. Cells were counted using BD Fortessa LRS. The percentage of migrated cells was calculated by dividing cell count in the bottom chamber

by the total number of cells (top and bottom chamber).

### *Phenotypic overlap*

To calculate the overlap between the phenotype of individuals with *NAA80* variants to patients with other genetic diseases, we used PHRANK.<sup>25</sup> As input we used the top-23 features with the highest occurrence ratio in our patients and the human phenotype ontology to disease list extracted from <https://hpo.jax.org/app/download/annotation> in July 2021.<sup>26</sup> To extract phenotypic features of individuals with actin genetic variants, a literature search was performed in May 2020. Individual features in case reports were scored using human phenotype ontology scores and binary code (1= present, 0= not present) by two independent researchers. Occurrence ratios were calculated by dividing the percentage of individuals with a phenotypic feature by the number of genes associated with the phenotypic feature in human phenotype ontology. To avoid doubles ('abnormality of the metopic ridge' and 'prominent metopic ridge'), we used the human phenotype ontology code that was furthest up the tree.

### *Statistical analysis*

Differences in actin acetylation percentages were analysed using Student's t-test (separate analysis for fibroblasts and PBMCs). The data are presented as mean  $\pm$  SD.

Differences in Phalloidin median fluorescence intensity were analysed using Student's t-test in case of two groups or ANOVA in case of three groups. The data are presented as mean  $\pm$  SD. For the migration assays, ANOVA was used to compare groups. The data are presented as mean  $\pm$  SD. Statistical analysis was carried out with Prism (GraphPad).

### *Data availability*

The authors declare that all data supporting the findings of this study are available within the paper and its supplementary information. Occurrence ratios for individuals with variants in *NAA80* or actin genes are added as **Supplementary Table 4**. The new variant described in this study was ente-



red in ClinVar, accession number: VCV001301869.1

## Results

### *Phenotypic description*

Proband 1.2 was born to Portuguese parents. After an unremarkable gestation and birth, he was diagnosed with bilateral high-frequency sensorineural hearing loss of 40 dB at the age of five weeks (**Figure 1A**). Upon clinical examination, several dysmorphic features were noted, including hypertelorism, low posterior hair line, highly arched eyebrows, low-set protruding ears, small mouth, diastema, peg-shaped lateral incisors, disorganized implant of the toes and tapered fingers (**Figure 1B–D**). In the following years, proband 1.2 exhibited periodic hypotonia, feeding difficulties, fatigue, swelling of his extremities and vomiting, which worsened during infections. He had behavioural disturbances, including rage and auto-mutilation, triggered by either loud noises or visual images. Additional phenotypic features included sleeping difficulties, loud snoring, gait ataxia and mild constipation requiring laxatives. Brain MRI revealed an enlarged right lateral ventricle system, a decreased amount of white matter volume and asymmetrical subcortical white matter lesions (**Figure 1E**). Overall development was mildly delayed, with an estimated intelligence quotient of 79 at the age of three. Extensive etiological workup at our Hospital Center for Evaluation of Developmental Delay, including clinical chemistry and metabolic screening in urine and plasma, did not reveal a cause for his clinical symptoms. Cardiac evaluation revealed mild systolic dysfunction, but no other abnormalities. SNP array revealed several small (<5 MB) and one large (8.8 MB) homozygous identity by descent regions (**Supplementary Table 2**). The large identity by descent region (8.8 MB) that was found in the patient exceeds the size of identity by descent regions found in outbred populations and suggests parents are distantly related.<sup>27,28</sup> Parents originate from the same region in Portugal. Subsequent trio-exome sequencing allowed the identification of four genetic variants of unknown significance (**Supplementary Table S3**), from which the variant in the *NAA80* gene was considered most likely

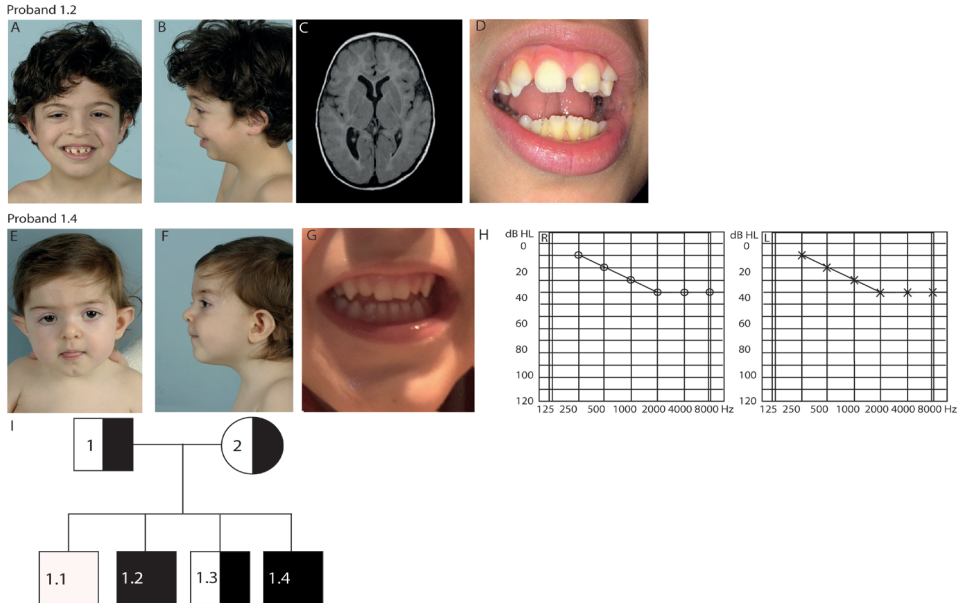


**Figure 1: NAA80 individuals present with craniofacial dysmorphisms, abnormal brain MRI and high-frequency hearing loss.** (A) Pure Tone Audiometry showing intensity measured in decibels (dB) represented on the x-axis and the frequency measured in Hertz (Hz) on the y-axis of the left ear (L) and right ear (R) of proband 1.2 showing high frequency hearing loss in the 2000–8000kHz region. (B) Front view of proband 1.2 at the age of 7 years showing small upper lip, hypertelorism, abnormally shaped ears, ptosis and epicanthus fold. (C) Lateral view of proband 1.2 showing retrognathia. (D) Brain MRI image of proband 1.2 showing asymmetrical posterior horns. (E) Close-up of proband 1.2 showing diastema and peg-shaped lateral incisors. (F) Front view of proband 1.4 at the age of 1 year showing small upper lip, long philtrum, bulbous tip of the nose, ptosis, epicanthus fold, ocular hypertelorism, abnormally shaped ears. (G) Lateral view of proband 1.4. (H) Close-up of proband 1.4 showing peg-shaped lateral incisors. (I) Family pedigree of the NAA80 family. Black squares indicate affected male [homozygous for NAA80 c.389T>C, p.(Leu130Pro) variant]. Semi-black squares indicate that the individual is a carrier of a heterozygous NAA80 variant.

to be pathogenic: NC\_000003.11: g.50334572A>G, c.389T>C, p.(L130P) (OMIM: 607073). Both parents were heterozygous for this variant.

Proband 1.4 was born 6 years later after an unremarkable pregnancy. His birth was complicated by respiratory distress due to meconium aspiration syndrome, necessitating mechanical ventilation for 24 hours. He had similar

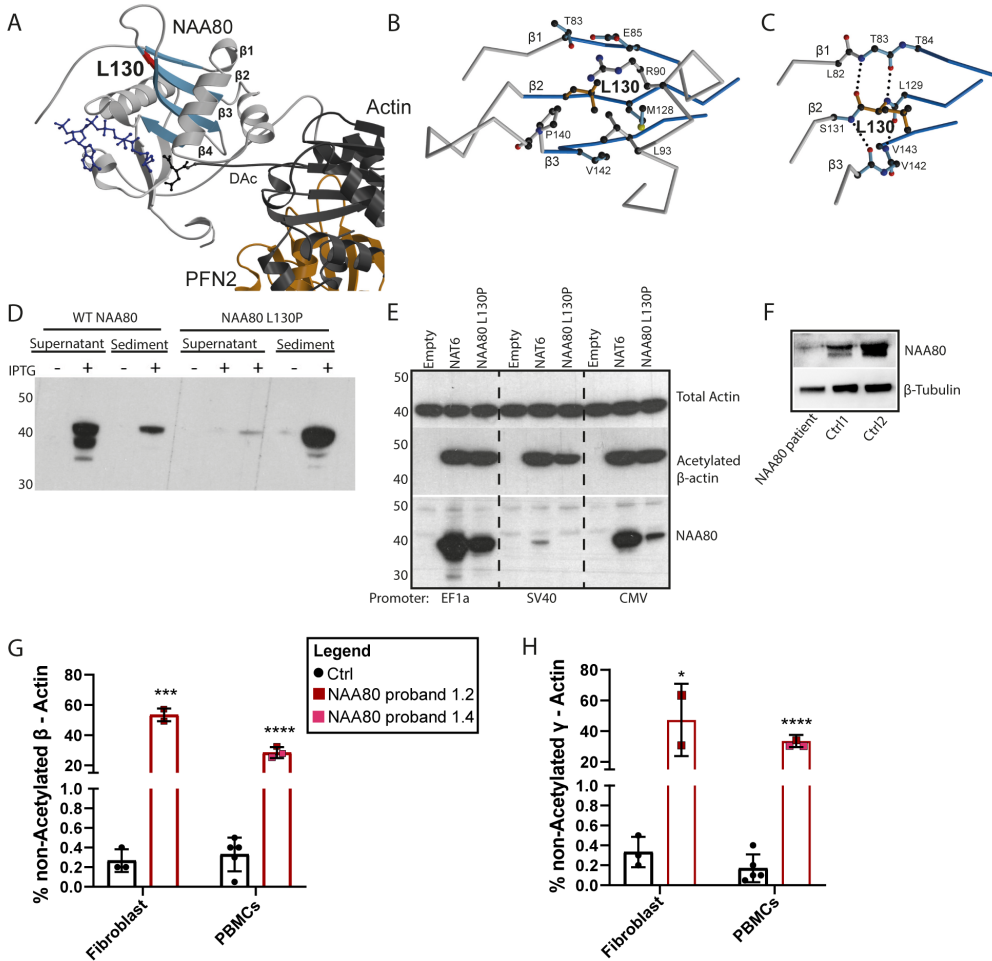
dysmorphic features as proband 1.2, including hypertelorism, low posterior hair line, highly arched eyebrows, low-set protruding ears, peg-shaped lateral incisors, small mouth and thin lips (**Figure 1E–G**). In addition, a bilateral sensorineural hearing loss of 70 dB, most prominent in the high frequency 3 kHz area, was detected. He also experienced periodic hypotonia, feeding difficulties, mild constipation, sleeping difficulties and snoring. Additionally, he has multiple obstructive and central apnoeas per night (not resulting in hypoxia). Sanger sequencing confirmed homozygosity for the same variant in *NAA80*: c.389T>C, p.(L130P) in proband 1.4, which was not present healthy probands 1.1 and 1.3 (**Figure 1I**). Additionally, Sanger sequencing confirmed homozygosity for the same variant in *PLXNB1* in proband 1.2 and 1.4: NC\_000003.11: g.48460754T>C, c.2731A>G, p.(S911G). The *PLXNB1* variant was not identified in the healthy siblings.

With Sanger sequencing, we found the other genetic variants identified in proband 1.2 did not segregate within the family (**Supplementary Table 3**).

*Structural analysis of the NAA80 c.389T>C, p.(Leu130Pro) genetic variant* *NAA80* includes an N-terminal extension, followed by a catalytic domain (residues 78-220), a proline-rich loop and a stretch of residues also belonging to the catalytic domain.<sup>7</sup> Leu130 is localized at the end of  $\beta$ -strand  $\beta$ 1, which is part of a central  $\beta$ -sheet of the catalytic domain (**Figure 2A**). The side chain of Leu130 points into a hydrophobic environment (**Figure 2B**). The backbone of Leu130 is involved in the formation of the hydrogen bond network of the central  $\beta$ -sheet, with direct hydrogen bonds to Thr83 in  $\beta$ 1 (**Figure 2C**). Replacement by a proline is expected to disturb the hydrogen bond network, in particular of the nitrogen atom in the peptide bond. Furthermore, adaptations would be required due to the sterical demands of the proline ring. These effects are expected to weaken and disturb the local fold of the protein.

*The NAA80 c.389T>C, p.(Leu130Pro) variant causes defective protein folding, resulting in limited protein availability*

The wild-type and the mutant *NAA80* protein with a C-terminal poly-His tag



**The NAA80 c.389T>C, p.(Leu130Pro) variant decreases NAA80 stability and decreases actin acetylation.** (A) Crystal structure of NAA80 bound to the actin–profilin complex. NAA80 is shown in grey with  $\beta$ -strands 1–4 highlighted in blue and Leu130 in red. Actin is shown in dark grey and profilin in orange. Coenzyme A (CoA) in blue and the acetylated N-terminal aspartate (DAc) in dark grey are in ball-and-stick representation. The colour-coding is used throughout the figure. (B) Detailed view of the local environment of the side chain of Leu130. The peptide chain is shown as  $C\alpha$ -trace with selected side chains in ball-and-stick representation. (C) Hydrogen network of the backbone surrounding Leu130.

With the exception of Leu130, residues are shown without sidechains as glycine. Dotted lines represent hydrogen bonds. (D) Western blot analysis of the expression of wild-type (WT) and mutant NAA80 in *Escherichia coli*. Induction of the expression with IPTG leads to the appearance of a protein that is mainly present in the supernatant (SN) of bacterial extracts in the case of the wild-type protein and in the sediment in the case of the mutant. (E) Western blot of HAP1 NAA80 knockout cells infected with lentiviral vectors driving the expression of WT NAA80, Leu130Pro NAA80 and no protein (empty). Mutant NAA80 generates decreased levels of NAA80 protein, and with the weakest promoter, detectably decreased acetylated  $\beta$ -actin levels. One representative experiment out of two is shown. (F) Western blot showing severely decreased NAA80 protein expression in fibroblasts of proband 1.2 compared to two healthy donors,  $\beta$ -tubulin was used as a housekeeper. One representative experiment out of two is shown. (G) Bar graph representing the proportions of 'endogenously' unacetylated  $\beta$ -actin (expressed as percentage of acetylated + unacetylated  $\beta$ -actin) of healthy controls (black) and probands 1.2 and 1.4 (red). Two independent experiments were performed of both the fibroblasts (proband 1.2) and the PBMCs (both probands), and each cell type was compared to three different healthy control samples (combined data from two experiments). Coloured squares represent mean values of all technical replicates, bars represent mean values of healthy controls (Ctrl) or individuals  $\pm$  SD. \* $P < 0.05$ , \*\*\* $P < 0.001$  (Student's t-test). Acetylation of the N-terminus of actins was determined by /MS/MS analysis of tryptic peptides as described in the 'Materials and Methods' section. (H) Bar graph represents the percentage of unacetylated  $\gamma$ -actin in three healthy controls (black) and proband 1.2 and 1.4 (red). Two independent experiments were performed of both the fibroblasts (proband 1.2 only) and the PBMCs (both patients), and each cell type was compared to three different healthy control samples (two experiments). Coloured squares represent technical replicates, bars represent mean per donor  $\pm$  SD. \* $P < 0.05$ , \*\*\* $P < 0.001$  (Student's t-test).

were expressed in *E. coli*, and bacterial extracts were centrifuged and analysed by sodium dodecyl sulphate polyacrylamide gel electrophoresis and western blot. Mutant protein was predominantly insoluble, contrasting with wild-type protein, which was essentially soluble, with only a very small proportion in the sediment (**Figure 2D**).

These findings align with the prediction that the *NAA80* variant induces defective protein folding.

To measure the impact of the *NAA80* genetic variant on protein levels in mammalian cells, we infected *NAA80*-knockout HAP1 cells with constructs expressing mutant or wild-type *NAA80* cDNA with promoters of different strengths, EF1A being the strongest and SV40 being the weakest promoter. Lower protein levels of mutant *NAA80* compared with healthy donors were observed with all promoters (**Figure 2E**). Similarly, in fibroblasts of individuals with *NAA80* variants, *NAA80* protein levels were lower compared to healthy controls (**Figure 2F**). Use of the weakest promoter resulted in partial restoration of actin acetylation, as determined by western blotting with antibodies specific for the acetylated form of beta actin, while stronger promoters led to maximal or near maximal acetylation, indicating that the mutated protein still shows residual activity (**Figure 2E**). In addition, we found that expression of low levels of wild-type *NAA80* in HAP1 knockout cells was already sufficient to reach maximal or near-maximal acetylation (**Figure 2E**). It should be noted that the western blot approach used in this experiment does not allow precise quantification of the level of acetylation.

*The NAA80 c.389T>C, p.(Leu130Pro) genetic variant results in decreased, but not absent, actin acetylation*

To accurately determine the levels of acetylated actin, the level of N-terminal acetylation of  $\beta$ - and  $\gamma$ -actin in fibroblasts and PBMCs from individuals with *NAA80* variants was analysed by mass spectrometry (**Figure 2G and H**). In healthy donors, approximately 0.5% of beta and gamma-actins were not acetylated. However, for the *NAA80* individuals, 25–65% of beta and gamma-actins were not acetylated, depending on the cell type and the type of cytoplasmic actin that was measured (**Figure 2G and H**).

*Fibroblasts of individuals with NAA80 variants show increased rates of polymerized actin, increased filopodia counts and increased cellular migration*  
The depolymerization rate for acetylated actin is approximately 2-fold higher than for non-acetylated actin.<sup>9</sup> Therefore, we hypothesized that the higher proportion of non-acetylated actin in individuals with *NAA80* variants would decrease the overall depolymerization rate, resulting in increased levels of polymerized actin. Indeed, PBMCs and fibroblasts displayed increased phalloidin staining, corresponding with increased levels of polymerized actin (**Figure 3A and B**). Expressing wild-type *NAA80* with the SV40 promoter in fibroblasts of individuals with *NAA80* variants normalized phalloidin staining intensity (**Supplementary Figure 2 and Figure 3C**).

Since HAP1-*NAA80* knockout cells showed increased filopodia formation and cellular migration<sup>9</sup>, filopodia counts and migration dynamics were quantified. In fibroblasts of individuals with *NAA80* variants, increased filopodia counts were observed (**Figure 3D**). The introduction of wild-type *NAA80* protein with the SV40 promoter lowered filopodia counts to the level observed in healthy controls (**Figure 3D**). Cellular migration in response to chemotactic stimuli was tested using the Boyden chamber assay. Both fibroblasts and PBMCs of *NAA80* individuals showed increased movement in response to chemotactic stimuli (**Figure 3E and F**). In fibroblasts, expression of *NAA80* wild-type with the SV40 promoter protein lowered migration levels to the level observed in healthy controls (**Figure 3G**).

Together, these results indicate that the *NAA80* genetic variants result in decreased *NAA80* protein levels and acetylation activity causing a distinct cellular phenotype, similar to that observed in *NAA80* HAP1 knockout cell lines.

*Individuals with the NAA80 c.389T>C, p.(Leu130Pro) variant show significant phenotypic overlap with individuals with pathogenic variants in ACTB and ACTG1*

To relate our molecular findings to the clinical phenotype, individuals in

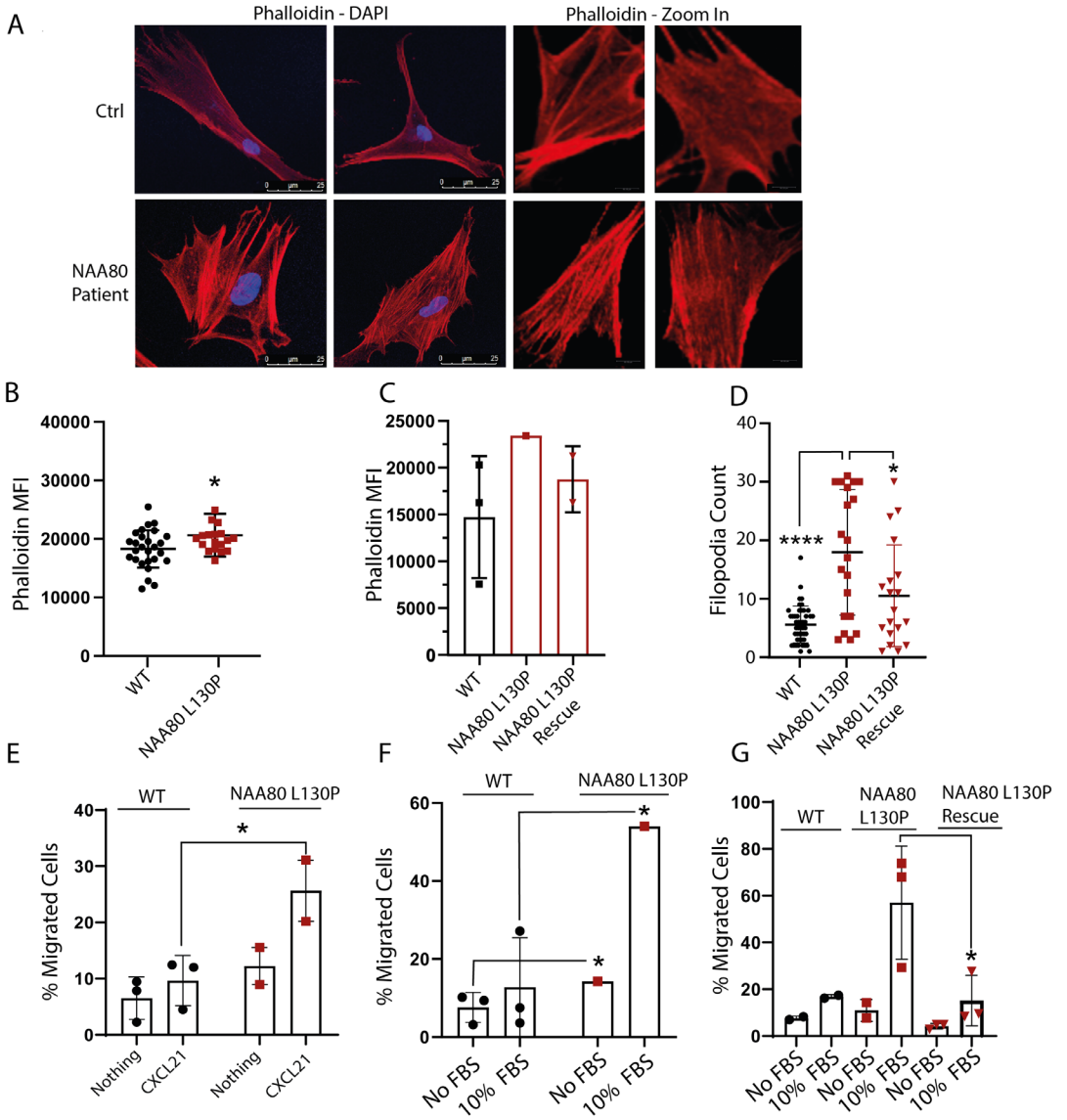


**Figure 3. *NAA80* variants lead to increased actin polymerization, filopodia count and cellular migration.** (A) Microscopy images of healthy Ctrl fibroblasts (upper panel) and *NAA80* individual fibroblasts (lower panel). *NAA80* individual fibroblasts show increased filopodia counts and altered morphology of the polymerized actin network. (B) Phalloidin mean fluorescence intensity of healthy controls (N = 3, nine technical replicates) and



## Chapter 2

---

NAA80 patient PBMCs (N = 2, nine technical replicates). Dots represent the mean phalloidin staining (median fluorescence intensity) of each replicate, the line represents the mean of all replicates  $\pm$ SD. \*\*\*\*P < 0.001 (Student's t-test). (C) Phalloidin median fluorescence intensity of healthy controls (N = 3, one technical replicate each) and NAA80 individual fibroblasts (N = 1, one technical replicate) and fibroblasts of proband 1.2 expressing WT NAA80 with CMV or SV40 promoter (N = 2, both one replicate). Bar represents mean fluorescence intensity of the phalloidin staining  $\pm$ SD. (D) Filopodia count of healthy control (N = 3) and individual fibroblasts (N = 1) transfected with an empty vector and SV40 promoter, and individual fibroblasts with NAA80 WT expressing plasmid with SV40 promoter (N = 1). Dots represent filopodia count per cell, lines represent mean filopodia count of all cells  $\pm$ SD. \*P < 0.05, \*\*\*\*P < 0.001 (ANOVA). (E) Cellular migration measured with the Boyden chamber assay of PBMCs with normal culture medium (nothing) or CXCL21 enriched culture medium (CXCL21) in the bottom chamber. Dots and squares represent mean migration of three technical replicates, bars represent mean migration of healthy controls combined (N = 3) or NAA80 individuals (N = 2)  $\pm$ SD. \*P < 0.05 (Student's t-test). (F) Cellular migration of control and NAA80 individual fibroblasts, measured with the Boyden chamber assay, with normal culture medium without (No FBS) or with (10% FBS) enriched culture medium in the bottom chamber. Dots or squares represent mean migration of three technical replicates, bars represent mean migration percentage of three donors  $\pm$ SD. \*P < 0.05 (Student's t-test). (G) Cellular migration of healthy control (N = 2) and NAA80 individual fibroblasts transduced with an empty vector (N = 1, three technical replicates) and NAA80 individual fibroblasts transduced with a NAA80 wild-type expressing vector (N = 1, three technical replicates). Bars represent mean migration per condition  $\pm$ SD. \*P < 0.05.

this study were compared with individuals harbouring genetic variants in other actin genes. For comparison, we used occurrence ratios that grant more weight to specific features (e.g. high-frequency hearing loss) than to non-specific features (developmental delay) by dividing the percentage of individuals presenting with a phenotypic feature by the total number of genes associated with that phenotypic feature.<sup>29</sup> With this approach, one can define overlap for rarely seen phenotypic features, which may point in the direction of shared pathophysiology.

To calculate the similarity between phenotypes, we employed the PHRANK<sup>25</sup> tool, using the top-23 phenotypic features with the highest occurrence ratio (depicted in **Figure 4**), comparing it to the phenotype of each actin gene. We found that Baraitser-Winter (OMIM #243310, resulting from pathogenic *ACTB* and *ACTG1* variants) was in the top three of diseases that most resembled the phenotype observed in individuals with *NAA80* variants, together with Rubinstein–Taybi syndrome (OMIM #180849) and Wolf–Hirschhorn syndrome (OMIM #194190).

Strikingly, comparing individuals with *NAA80* variants to patients with pathogenic *ACTB* variants gave a similarity score of 60.29, and 30.37 when compared to patients with pathogenic *ACTG1* variants (**Figure 4**). The overlap with patients with *ACTA1* variants was only modest: individuals with *NAA80* variants exhibited moderate axial hypotonia and proximal muscle weakness, while individuals with pathogenic *ACTA1* variants have overt nemaline myopathy (similarity score of 20). The similarity scores of *NAA80* and *ACTG2*, *ACTC1* and *ACTA2* were negligible (1.00, 0.00 and 0.00, respectively). While individuals with *ACTG2* variants show intestinal pseudo-obstruction, mild constipation is seen in individuals with *NAA80* variants. Similarly, the ventricular dysfunction seen in individuals with *NAA80* variants could reflect a minor *ACTC1* dysfunction. Together, these results show that the individuals in this study resemble the phenotype seen in individuals with pathogenic *ACTG1*, *ACTB* and *ACTA1* variants, but not in individuals with pathogenic *ACTG2*, *ACTC1* and *ACTA2* variants.

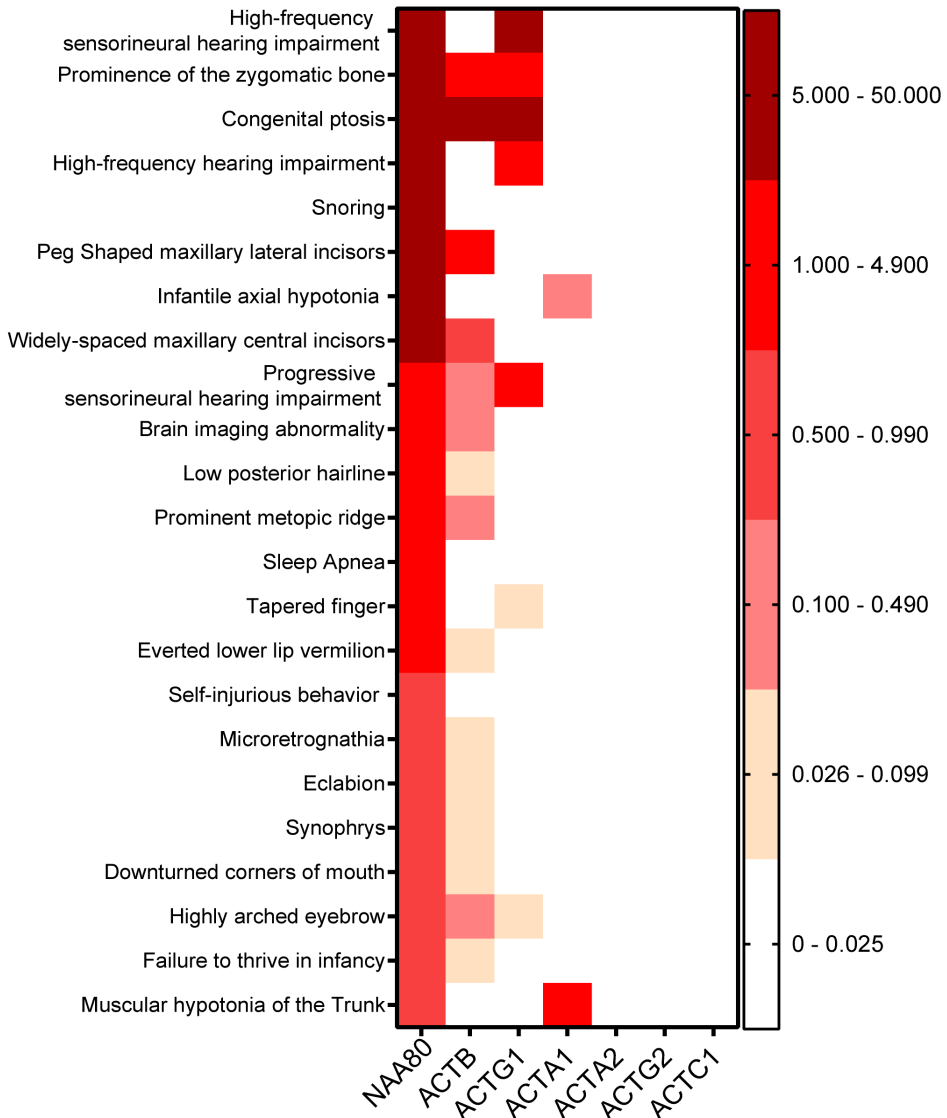


**Figure 4. The most specific phenotypic features of NAA80 individuals overlap with those of individuals with ACTB, ACTG1 and ACTA variants.** Colour coded occurrence ratios of the most specific phenotypic features of individuals with *NAA80* variants with corresponding occurrence ratios of individuals with other actin genetic variants. ACTG1 = actin- $\gamma$ ; ACTB = actin- $\beta$ ; ACTA1 = muscle  $\alpha$ -actin; ACTA2 = smooth muscle actin- $\alpha$ ; ACTG2 = gamma-enteric smooth muscle actin; ACTC1 = cardiac, muscle alpha actin.

## Discussion

Until now, the consequences of N-terminal actin acetylation have remained largely unexplored *in vivo*. Here, we describe a new syndrome characterized by high-frequency hearing loss, developmental delay and muscle weakness, caused by homozygous *NAA80* c.389T>C, p.(Leu130Pro) variants. We provide evidence that the c.389T>C, p.(Leu130Pro) variant destabilizes NAA80, resulting in decreased, but not absent, enzymatic activity and consequently decreased actin acetylation. This resulted in increased filopodia formation, increased cellular movement and increased levels of polymerized actin. Together, our results underscore the importance of NAA80-mediated actin acetylation *in vivo*.

The shared clinical features of individuals with *NAA80* variants and individuals with pathogenic *ACTB/ACTG1* variants, for example hearing loss, suggest a similar underlying pathophysiological mechanism. Most individuals with *ACTB/ACTG1* variants that exhibit hearing loss have normal actin abundance, but show altered actin dynamics *in vitro*, suggesting that altered actin dynamics rather than absolute actin concentrations contribute to hearing loss.<sup>30–33</sup> Auditory hair cells consist of a particularly stable actin core with new actin incorporation only at the distal tips, hence requiring controlled actin dynamics.<sup>34</sup> To facilitate a stable actin core and controlled incorporation of F-actin, actin stabilizing proteins such as PLS1, FSCN2 and XIRP2 are highly expressed in the inner ear.<sup>35–38</sup> For example, loss of plastin-1 (PLS1) function, which limits actin depolymerization to prevent thinning of the actin bundle, results in hearing loss.<sup>35,38,39</sup> As NAA80-mediated actin acetylation results in altered actin dynamics,<sup>9</sup> it is likely that normal cytoskeletal architecture is disrupted in individuals with *NAA80* variants, causing hearing loss.

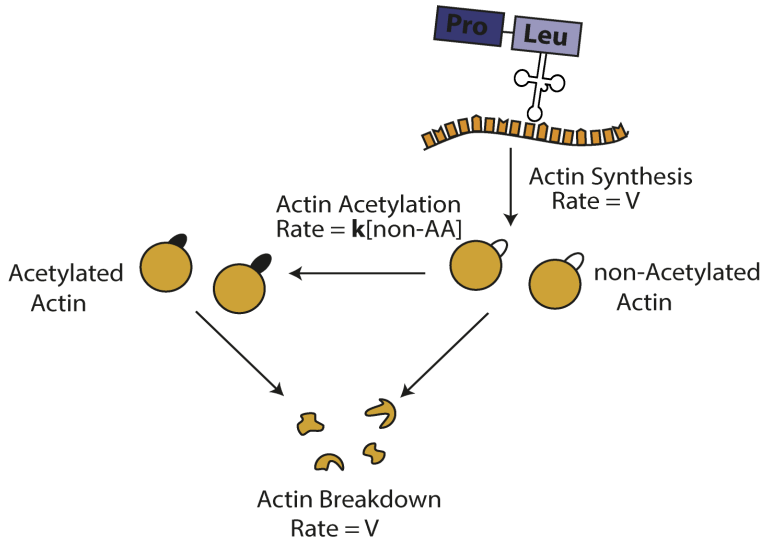
We found increased filopodia counts in fibroblasts of individuals with *NAA80* variants. In the brain, filopodia are precursors for dendritic spines, that eventually form excitatory synapses.<sup>40–43</sup> Disturbances in filopodia formation can lead to severe neuronal migration disorders, illustrated by

the observation that genetic variants in actin remodelling genes, including *PAFAH1B1*, show decreased filopodia formation and decreased neuronal migration, resulting in autism spectrum disorder, developmental delay and epileptic seizures.<sup>44-46</sup> Likewise, individuals with *ACTB* and *ACTG1* variants and Baraitser-Winter syndrome frequently present with neuronal migration disorders like lissencephaly and pachygyria resulting in mild intellectual disability and seizures.<sup>47</sup> However, the consequences of increased filopodia formation, which occurs in our patients, have not yet been established. Speculatively, excessive filopodia numbers could lead to uncontrolled formation of excitatory synapses that might relate to the individuals' hyperarousal, behavioural disturbances and mild intellectual disability. Additionally, the asymmetry seen in the lateral ventricles of proband 1.2 could reflect a minor neuronal migration disorder.

Even though NAA80 is predicted to have similar affinity for all six actin isoforms, there was no overt clinical overlap between individuals with *NAA80* variants and individuals with *ACTA2*, *ACTG2* and *ACTC1* genetic variants. Some of these features might not have yet developed in individuals with *NAA80* variants, as *ACTA2*- and *ACTC1*-related features often do not manifest until the second or third decade of life.<sup>48-53</sup> However, individuals with *ACTG2* genetic variants are usually identified early in life, with severe chronic intestinal pseudo obstruction.<sup>54,55</sup> Alternatively, one could speculate that the constipation and mild ventricular dysfunction seen in individuals with *NAA80* variants reflects mild *ACTG2* and *ACTC1* dysfunction, in a similar way as the myopathy of individuals with *NAA80* variants could reflect a minor form of the severe, lethal myopathy seen in individuals with *ACTA1* variants. The latter would imply that NAA80-mediated acetylation might have a more modest role in the function of muscle actin isoforms, which might relate to the more stable nature of actin isoforms within muscle, making them less vulnerable to flawed actin dynamics.

Surprisingly, the severely reduced NAA80 availability only resulted in a modest ( $\approx 50\%$ ) decrease of actin acetylation. The relationship between NAA80 activity and substrate availability (unacetylated actins) can be

A



B

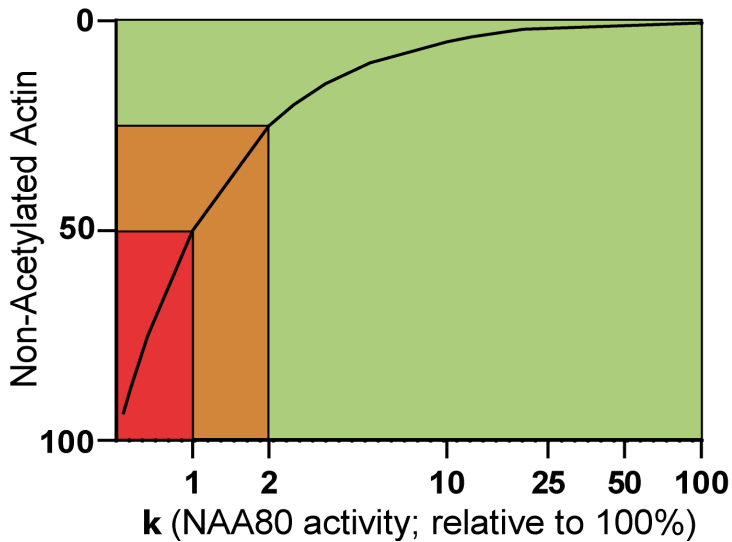


**Figure 5.** Graphical model showing the NAA80 activity (x-axis) versus the amount of substrate (non-acetylated actin, y-axis). (A) Under steady-state conditions, actin is synthesized, acetylated and degraded. For the sake of simplicity, we assume that the degradation of acetylated and non-acetylated actins proceed with the same rate constant.

If we assume that the rate of acetylation is proportional to the non-acetylated actin (non-AA) concentration,  $V=k[\text{non-AA}]$ , where  $k$  is the constant rate of the reaction catalysed by NAA80. The concentration of non-AA is therefore equal to  $V/k$ . (B) An increase in the proportion of non-acetylated actin from 0.5% (normal value) to 25% or 50% may be due to a reduction in the NAA80 activity of 50- and 100-fold, respectively (i.e. from a value of 100% to 2 or 1% approximately). Therefore, the reduced NAA80 activity caused by *NAA80* variants in our individuals falls within a critical range (orange area) that is disease-causing but not lethal. Less than 1% NAA80 activity is thought to be lethal (red area). Over 2% of NAA80 residual activity probably does not result in overt clinical symptoms (green area). Note that all percentages mentioned are based on estimates. Note that the x-axis has a logarithmic scale.

studied with a simplified model, in which we assume that NAA80 activity ( $k$ ) is proportional to the concentration of non-acetylated actin (non-AA), i.e. that it is equal to  $k \cdot [\text{non-AA}]$  (**Figure 5**). If we consider that the rate of non-acetylated actin formation and degradation ( $V$ ) is the same in control cells and in cells with the *NAA80* variant, a 50-fold or 100-fold increase in the concentration of non-acetylated actin (i.e. 25% or 50% in individual cells versus 0.5% in controls) can be accounted for by a 50-fold or 100-fold decrease in the value of  $k$ . Thus, 50% actin acetylation agrees with extremely low, but not absent, residual NAA80 activity, estimated in the range of 1–2% of normal activity.

If NAA80 activity were to drop below the level observed in the individuals with *NAA80* variants, over 50% of actins would be affected. This level is probably lethal, since bi-allelic actin variants—affecting over 50% of actins—do not exist. In contrast, if *NAA80* variants resulted in more residual activity than is seen in the individuals included in this study, actin acetylation still reaches approximately 85%, a level that will probably not cause an overt clinical phenotype. Thus, it is likely that only a narrow range of residual NAA80 catalytic activity is tolerated and disease causing. There is a slim chance that *NAA80* variants cause actin acetylation levels that fall exactly within this critical range, which explains why we could not identify additional individuals with *NAA80* variants, despite extensive searches in GeneMatcher and population databases.

In conclusion, we here demonstrate that patients with *NAA80* variants are pathogenic and result in actin acetylation defects. Since NAA80 activity is directly linked to substrate availability, only a specific range of NAA80 catalytic activity is tolerated and disease causing, explaining why bi-allelic *NAA80* variants are extremely rare. The significant clinical overlap between individuals with *NAA80* and *ACTB/ACTG1* variants suggests a more prominent role for NAA80 for cytoplasmic actin isoforms. These insights underscore the importance of fine-tuned actin dynamics by actin acetylation for human health.

**Acknowledgements**

The authors thank Gaëtan Herinckx for his help with the sample preparation for mass spectrometry analysis.

**Funding**

Funding for this project was granted by the Wilhelmina Children's hospital (WKZ) Stimuleringsubsidie 2019-2020 and United for Metabolic Diseases (UMD).

**Competing interests**

The authors report no competing interests.



## References

1. Pollard TD, Cooper JA.. Actin, a central player in cell shape and movement. *Science*. 2009;326(5957):1208–1212.
2. Bunnell TM, Burbach BJ, Shimizu Y, Ervasti JM..  $\beta$ -Actin specifically controls cell growth, migration, and the G-actin pool. *Mol Biol Cell*. 2011;22(21):4047–4058.
3. Belyantseva IA, Perrin BJ, Sonnemann KJ, et al.  $\gamma$ -Actin is required for cytoskeletal maintenance but not development. *Proc Natl Acad Sci USA*. 2009;106(24):9703–9708.
4. Vandekerckhove J, Bugaisky G, Buckingham M.. Simultaneous expression of skeletal muscle and heart actin proteins in various striated muscle tissues and cells. *J Biol Chem*. 1986;261(4):1838–1843.
5. Hooek TC, Newcomb PM, Herman IM..  $\beta$  Actin and its mRNA are localized at the plasma membrane and the regions of moving cytoplasm during the cellular response to injury. *J Cell Biol*. 1991;112(4):653–664.
6. Micheva KD, Vallée A, Beaulieu C, Herman IM, Leclerc N.. B-Actin is confined to structures having high capacity of remodelling in developing and adult rat cerebellum. *Eur J Neurosci*. 1998;10(12):3785–3798.
7. Rebowski G, Boczkowska M, Drazic A.. Mechanism of actin N-terminal acetylation. *Sci Adv*. 2020;6(15):eaay8793.
8. Wiame E, Tahay G, Tyteca D, et al. NAT6 acetylates the N-terminus of different forms of actin. *FEBS J*. 2018;285(17):3299–3316.
9. Drazic A, Aksnes H, Marie M, et al. NAA80 is actin’s N-terminal acetyltransferase and regulates cytoskeleton assembly and cell motility. *Proc Natl Acad Sci USA*. 2018;115(17):4399–4404.
10. Goris M, Magin RS, Foynt H, et al. Structural determinants and cellular environment define processed actin as the sole substrate of the N-terminal acetyltransferase NAA80. *Proc Natl Acad Sci USA*. 2018;115(17):4405–4410.
11. Aksnes H, Drazic A, Marie M, Arnesen T.. First things first: vital protein marks by N-terminal acetyltransferases. *Trends Biochem Sci*. 2016;41(9):746–760.
12. Ree R, Kind L, Kaziales A, et al. PFN2 and NAA80 cooperate to efficiently acetylate the N-terminus of actin. *J Biol Chem*. 2020;295(49):16713–16731.
13. Varland S, Vandekerckhove J, Drazic A.. Actin post-translational modifications: the cinderella of cytoskeletal control. *Trends Biochem Sci*. 2019;44(6):502–516.
14. Donnelly P, Green ED, Knoppers BM, et al. The 1000 Genomes Project Consortium. A global reference for human genetic variation. *Nature*. 2015;526(7571):68–74.
15. Zerbino DR, Achuthan P, Akanni W, et al. Ensembl 2018. *Nucleic Acids Res*. 2018;46(D1):D754–D761.
16. Lek M, Karczewski K, Minikel E, et al. Analysis of protein-coding genetic variation in 60,706 humans. *Nature*. 2016;536:285–291
17. Karczewski KJ, Francioli LC, Tiao G, et al. The mutational constraint spectrum quantified from variation in 141,456 humans [Published online 2019:531210]. *bioRxiv*.
18. Schomburg D, Reichelt J.. BRAGI: a comprehensive protein modeling program

- system. *J Mol Graph.* 1988;6(3):161–165.
19. Kraulis PJ. MOLSCRIPT. A program to produce both detailed and schematic plots of protein structures. *J Appl Crystallogr.* 1991;24(5):946–950.
  20. Merritt EA, Murphy ME, Raster3D version-2.0 - A program for photorealistic molecular graphics. *Acta Crystallogr D Biol Crystallogr.* 1994;50(Pt 6):869–873.
  21. Ury B, Potelle S, Caligiore F, et al. The promiscuous binding pocket of SLC35A1 ensures redundant transport of CDP-ribitol to the Golgi. *J Biol Chem.* 2021;296:100789.
  22. Dewulf JP, Wiame E, Dorboz I, et al. SLC13A3 variants cause acute reversible leukoencephalopathy and  $\alpha$ -ketoglutarate accumulation. *Ann Neurol.* 2019;85(3):385–395.
  23. Pino LK, Searle BC, Bollinger JG, Nunn B, MacLean B, MacCoss MJ.. The Skyline ecosystem: informatics for quantitative mass spectrometry proteomics. *Mass Spectrom Rev.* 2020;39(3):229–244.
  24. Jacquemet G, Paatero I, Carisey AF, et al. FiloQuant reveals increased filopodia density during breast cancer progression. *J Cell Biol.* 2017;216(10):3387–3403.
  25. Jagadeesh K, Birgmeier J, Guturu H, et al. Phrank measures phenotype sets similarity to greatly improve Mendelian diagnostic disease prioritization. *Genet Med.* 2019;21:464–470.
  26. Köhler S, Gargano M, Matentzoglou N, et al. The human phenotype ontology. *Nucleic Acids Res.* 2021;49(D1):D1207–D1217.
  27. Palamara PF, Lencz T, Darvasi A, Pe'er I.. Length distributions of identity by descent reveal fine-scale demographic history. *Am J Hum Genet.* 2012;91(5):809–822.
  28. Shetty A, O'Connell J, Mitchell B, O'Connor T. Rare variant enriched identity-by-descent enables the detection of distant relatedness and older divergence between populations [Published online May 7, 2020]. *bioRxiv.* doi:10.1101/2020.05.05.079541.
  29. Haijes HA, Jaeken J, van Hasselt PM.. Hypothesis: determining phenotypic specificity facilitates understanding of pathophysiology in rare genetic disorders. *J Inher Metab Dis.* 2020;43(4):701–711.
  30. Bryan KE, Wen KK, Zhu M, et al. Effects of human deafness  $\gamma$ -actin mutations (DFNA20/26) on actin function. *J Biol Chem.* 2006;281(29):20129–20139.
  31. Zhu M, Yang T, Wei S, et al. Mutations in the  $\gamma$ -actin gene (ACTG1) are associated with dominant progressive deafness (DFNA20/26). *Am J Hum Genet.* 2003;73(5):1082–1091.
  32. Vedula P, Kashina A.. The makings of the 'actin code': regulation of actin's biological function at the amino acid and nucleotide level. *J Cell Sci.* 2018;131(9):jcs215509.
  33. Rivière JB, Van Bon BWM, Hoischen A, et al. De novo mutations in the actin genes ACTB and ACTG1 cause Baraitser-Winter syndrome. *Nat Genet.* 2012;44(4):440–444.
  34. Drummond MC, Barzik M, Bird JE, et al. Live-cell imaging of actin dynamics reveals mechanisms of stereocilia length regulation in the inner ear. *Nat Commun.* 2015;6:doi:10.1038/ncomms7873
  35. Roy P, Perrin BJ.. The stable actin core of mechanosensory stereocilia features conti-

- nuous turnover of actin cross-linkers. *Mol Biol Cell*. 2018;29(15):1856–1865.
36. Perrin BJ, Strandjord DM, Narayanan P, et al. Beta-actin and fascin-2 cooperate to maintain stereocilia length. *J Neurosci*. 2013;33(19):8114–8121.
  37. Scheffer DI, Zhang D-S, Shen J, et al. XIRP2, an actin-binding protein essential for inner ear hair-cell stereocilia. *Cell Rep*. 2015;10(11):1811–1818.
  38. Taylor R, Bullen A, Johnson SL, et al. Absence of plastin 1 causes abnormal maintenance of hair cell stereocilia and a moderate form of hearing loss in mice. *Hum Mol Genet*. 2015;24(1):37–49.
  39. Morgan A, Koboldt DC, Barrie ES, et al. Mutations in PLS1, encoding fimbrin, cause autosomal dominant nonsyndromic hearing loss. *Hum Mutat*. 2019;40(12):2286–2295.
  40. Marrs GS, Green SH, Dailey ME.. Rapid formation and remodeling of postsynaptic densities in developing dendrites. *Nat Neurosci*. 2001;4(10):1006–1013.
  41. Ziv NE, Smith SJ.. Evidence for a role of dendritic filopodia in synaptogenesis and spine formation. *Neuron*. 1996;17(1):91–102.
  42. Vaughn JE. Fine structure of synaptogenesis in the vertebrate central nervous system. *Synapse*. 1989;3(3):255–285.
  43. Niell CM, Meyer MP, Smith SJ.. In vivo imaging of synapse formation on a growing dendritic arbor. *Nat Neurosci*. 2004;7(3):254–260.
  44. Cardoso C, Leventer RJ, Dowling JJ, et al. Clinical and molecular basis of classical lissencephaly: mutations in the LIS1 gene (PAFAH1B1). *Hum Mutat*. 2002;19(1):4–15.
  45. Kholmanskikh SS, Koeller HB, Wynshaw-Boris A. et al. Calcium-dependent interaction of Lis1 with IQGAP1 and Cdc42 promotes neuronal motility. *Nat Neurosci*. 2006;9(1):50–57.
  46. Kholmanskikh SS, Dobrin JS, Wynshaw-Boris A, Letourneau PC, Ross ME.. Disregulated RhoGTPases and actin cytoskeleton contribute to the migration defect in Lis1-deficient neurons. *J Neurosci*. 2003;23(25):8673–8681.
  47. Verloes A, Di Donato N, Masliah-Planchon J, et al. Baraitser-Winter cerebrofrontofacial syndrome: delineation of the spectrum in 42 cases. *Eur J Hum Genet*. 2015;23(3):292–301. [PMC free article] [PubMed] [Google Scholar]
  48. Guo DC, Papke CL, Tran-Fadulu V, et al. Mutations in smooth muscle alpha-actin (ACTA2) cause coronary artery disease, stroke, and Moyamoya disease, along with thoracic aortic disease. *Am J Hum Genet*. 2009;84(5):617–627.
  49. Guo DC, Pannu H, Tran-Fadulu V, et al. Mutations in smooth muscle alpha-actin (ACTA2) lead to thoracic aortic aneurysms and dissections. *Nat Genet*. 2007;39(12):1488–1493.
  50. Yuan SM.  $\alpha$ -Smooth muscle actin and ACTA2 gene expressions in vasculopathies. *Brazilian J Cardiovasc Surg*. 2015;30(6):644–649.
  51. Monserrat L, Hermida-Prieto M, Fernandez X, et al. Mutation in the alpha-cardiac actin gene associated with apical hypertrophic cardiomyopathy, left ventricular non-compaction, and septal defects. *Eur Heart J*. 2007;28(16):1953–1961. [Google Scholar]
  52. Olson TM, Doan TP, Kishimoto NY, Whitby FG, Ackerman MJ, Fananapazir L.. In-

- herited and de novo mutations in the cardiac actin gene cause hypertrophic cardiomyopathy. *J Mol Cell Cardiol.* 2000;32(9):1687–1694.
53. Mogensen J, Klausen IC, Pedersen AK, et al. Alpha-cardiac actin is a novel disease gene in familial hypertrophic cardiomyopathy. *J Clin Invest.* 1999;103(10):R39–R43.
  54. Lehtonen HJ, Sipponen T, Tojkander S, et al. Segregation of a missense variant in enteric smooth muscle actin  $\gamma$ -2 with autosomal dominant familial visceral myopathy. *Gastroenterology.* 2012;143(6):1482–1491.e3.
  55. Wangler MF, Gonzaga-Jauregui C, Gambin T, et al. Baylor-Hopkins Center for Mendelian Genomics. Heterozygous de novo and inherited mutations in the smooth muscle actin (ACTG2) gene underlie megacystis-microcolon-intestinal hypoperistalsis syndrome. *PLoS Genet.* 2014;10(3):e1004258.

# Supplementary Files and Figures

**Supplementary Table S1**

Actin type	Acetylation	Sequence	m/z	targeted [M+2H] <sup>2+</sup>
beta	no	DD <b>D</b> DIAALVVDNGSGM <b>C</b> CK	1795.783	898.395
beta	<sup>12</sup> C/ <sup>1</sup> H acetate	DD <b>D</b> DIAALVVDNGSGM <b>C</b> CK	1837.793	919.400
beta	<sup>13</sup> C/ <sup>2</sup> H acetate	DD <b>D</b> DIAALVVDNGSGM <b>C</b> CK	1742.819	921.913
gamma	no	EEEIAALVIDNGSGM <b>C</b> CK	1851.845	926.426
gamma	<sup>12</sup> C/ <sup>1</sup> H acetate	EEEIAALVIDNGSGM <b>C</b> CK	1893.855	947.431
gamma	<sup>13</sup> C/ <sup>2</sup> H acetate	EEEIAALVIDNGSGM <b>C</b> CK	1898.881	949.944

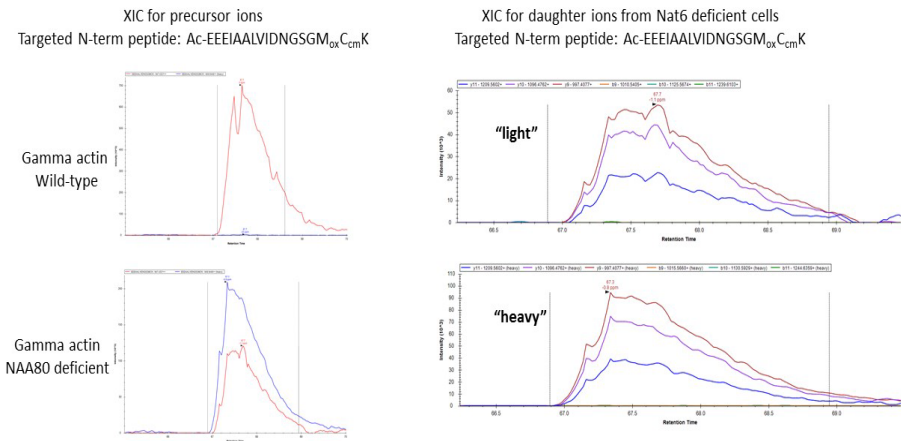
**Supplementary Table S1:** List of the 6 theoretical peptide sequences that were targeted by mass spectrometry. Meaning of bold amino acids: oxidation of **M** (+15.994 Da), carbamidomethyl of **C** (+57.021 Da), N-term acetylation for **E** or **D** (+42.010 Da for <sup>12</sup>C<sub>2</sub>/<sup>1</sup>H<sub>3</sub> and +47.037 Da for <sup>13</sup>C<sub>2</sub>/<sup>2</sup>H<sub>3</sub>).

**Supplementary Table S2**

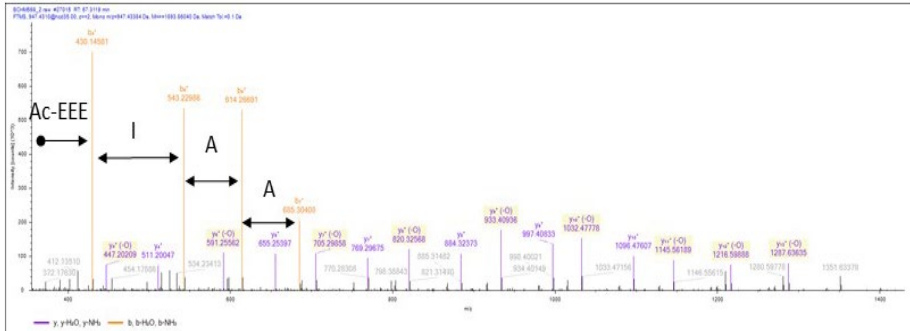
Label	Chromosome	Start	Stop	Size
ROH	3	45.476.694	54.264.197	8.788 MB
ROH	9	65.629.772	69.824.256	4.194 MB
ROH	5	129.486.905	132.169.532	2.683 MB
ROH	15	42.922.656	45.394.057	2.471 MB
ROH	1	142.541.502	144.931.626	2.39 MB
ROH	12	85.356.224	87.722.701	2.366 MB
ROH	5	44.442.578	46.404.402	1.962 MB

**Supplementary Table S2:** Identity by descent (IBD) regions found in proband 1.2 with SNP Array. Runs of Homozygosity (ROH) are contiguous regions of the genome where the individual is homozygous across all sites.

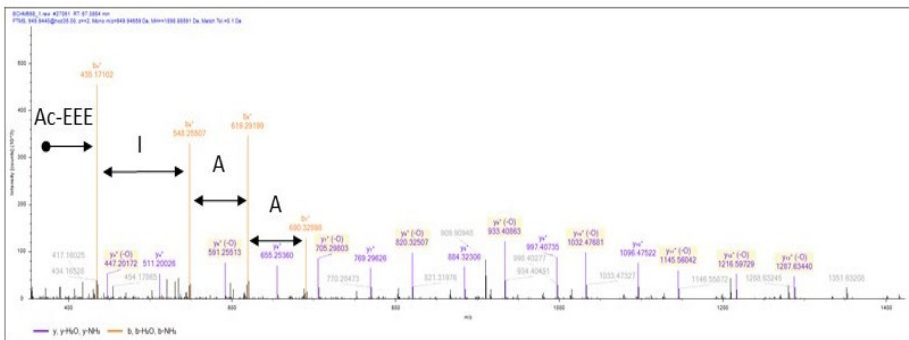
**Supplementary Figure 1:**



MS/MS spectra for  $^{12}\text{C}_2/^1\text{H}_3$  "light" peptide

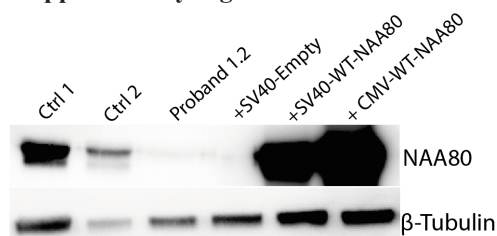


MS/MS spectra for  $^{13}\text{C}_2/^2\text{H}_3$  "heavy" peptide



**Supplementary Figure 1:** Identification and quantification of the N-terminal acetylated peptide from gamma actin by targeted mass spectrometry. A PRM MS/MS method was designed to measure the two acetylated forms (light or heavy) of the processed N-term peptide taking oxidation of Met (Mox) and carbamidomethylation of Cys (Cm) as fixed modifications. *Left upper panel:* XIC of the two precursors ions (light in red  $m/z=947.432$ , heavy in blue  $m/z=949.948$ ) for a control and the NAA80 deficient individual. *Right upper panel:* example from a NAA80 deficient individual of the XIC of all daughter ions taken into account for quantification by their area under the curve (AUC). *Lower panel:* MS/MS spectra of the light and heavy +2 precursors ions, the b-ions series shows the incorporation of a heavy acetylated group at the N-term side of the peptide with a mass difference of 5.027 Da from their light counterpart. (-O) denotes neutral loss of H4COS from the side chain of Cys.

**Supplementary Figure 2:**



**Supplementary Figure 2:** Western blot showing NAA80 expression in healthy controls (Ctrl 1, Ctrl 2) and proband 1.2 with and without (SV40-Empty) vectors expressing NAA80 WT cDNA using either a CMV or SV40 promoter.

**Supplementary Table S3:**

Gene	Considerations regarding pathogenicity	Chromosome	Start	Stop	Genotype	cDNA	Protein	PhyloP and PhastCons
PRR14L	The PRR14L variant is not present in affected proband 1.4. Phenylalanine and Tyrosine have similar properties and this change is thus not expected to impact the protein structure significantly.	22	32084196	3.2E+07	A/T	c.6125T>A	p.F2042Y	PhyloP: 3.958, PhastCons: 1
PLXNB1	Segregates with affected individuals (proband 1.2 and 1.4). Affected residue is not conserved. Serine and glycine have similar properties and this change is thus not expected to impact the protein structure significantly. The variant is located in a region of low conservation in the protein. Serine to glycine has been observed in other species.	3	48460754	4.8E+07	C/C	c.2731A>G	p.S911G	PhyloP: -0.153, PhastCons: 0
NAA80	Segregates with affected individuals (proband 1.2 and 1.4). Very conserved residue, amino-acid change predicted to result in altered protein confirmation (loss of proline).	3	50334572	5E+07	G/G	c.323T>C	p.L108P	PhyloP: 4.572, PhastCons: 1
HDAC6	The HDAC6 variant is also present in one of the healthy male siblings (proband 1.1).	X	48663916	4.9E+07	C/	c.383G>C	p.C128S	PhyloP: 1.82, PhastCons: 0.998

**Supplementary Table S3:** Genetic variants in proband 1.2 found with Whole Exome Sequencing that remain after filtering.

**Supplementary Table S4**

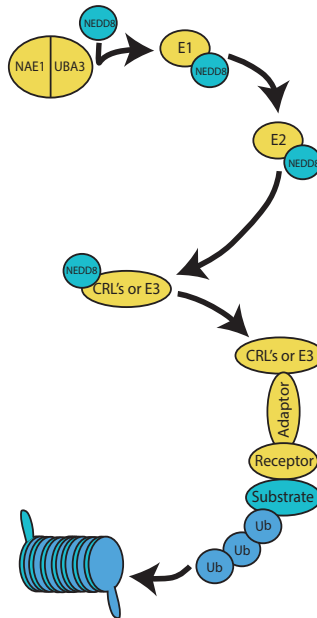
Phenotypic Feature	NAA80	ACTB	ACTG1	ACTA1	ACTA2	ACTG2	ACTC1
High-frequency sensorineural hearing impairment	50	0	35	0	0	0	0
Prominence of the zygomatic bone	25	1.515152	1.282051	0	0	0	0
Congenital ptosis	25	5.30303	8.333333	0	0	0	0
High-frequency hearing impairment	14.28571	0	1.848539	0	0	0	0
Snoring	14.28571	0	0	0	0	0	0
Peg Shaped maxillary lateral incisors	11.11111	1.31	0	0	0	0	0
Infantile axial hypotonia	7.69	0	0	0.3042156	0	0	0
Widely-spaced maxillary central incisors	7.14	0.67	0	0	0	0	0
Progressive sensorineural hearing impairment	2.325581	0.422833	1.471985	0	0	0	0
Brain imaging abnormality	1.5625	0.260417	0	0	0	0	0
Low posterior hairline	1.470588	0.039872	0	0	0	0	0
Prominent metopic ridge	1.25	0.113636	0	0	0	0	0
Sleep Apnea	1.162791	0	0	0	0	0	0
Tapered finger	1.07526	0.017618	0.053419	0	0	0	0
Everted lower lip vermillion	1.02	0.030921	0	0	0	0	0
Self-injurious behavior	0.99	0	0	0	0	0	0
Microretrognathia	0.980392	0.089127	0	0	0	0	0
Eclabion	0.9259259	0.028058	0	0	0	0	0
Synophrys	0.892857	0.040584	0	0	0	0	0
Downturned corners of mouth	0.862069	0.026123	0	0	0	0	0
Highly arched eyebrow	0.7462687	0.135685	0.0333	0	0	0	0
Failure to thrive in infancy	0.6493506	0.059032	0	0	0	0	0
Muscular hypotonia of the Trunk	0.5813953	0	0	1.0290698	0	0	0

**Supplementary Table S4:** Phenotypic features with their corresponding occurrence ratio in individuals with NAA80 genetic variants or actin mutations (ACTB, ACTG1, ACTA1, ACTA2, ACTG2, ACTC1).





# Chapter



**Bi-allelic variants in *NAE1* cause intellectual disability, ischiopubic hypoplasia, stress-mediated lymphopenia and neurodegeneration**

## **Bi-allelic variants in *NAE1* cause intellectual disability, ischiopubic hypoplasia, stress-mediated lymphopenia and neurodegeneration.**

Irena J J Muffels<sup>1</sup>, Imre F Schene<sup>2</sup>, Holger Rehmann<sup>3</sup>, Maarten P G Massink<sup>4</sup>, Maria M van der Wal<sup>5</sup>, Corinna Bauder<sup>6</sup>, Martha Labeur<sup>7</sup>, Natalia G Armando<sup>8</sup>, Maarten H Lequin<sup>9</sup>, Michiel L Houben<sup>10</sup>, Jaques C Giltay<sup>4</sup>, Saskia Haitjema<sup>11</sup>, Albert Huisman<sup>11</sup>, Fleur Vansenne<sup>12</sup>, Judith Bluvstein<sup>13</sup>, John Pappas<sup>14</sup>, Lala V Shailee<sup>15</sup>, Yuri A Zarate<sup>16</sup>, Michal Mokry<sup>17</sup>, Gijs W van Haaften<sup>18</sup>, Edward E S Nieuwenhuis<sup>19</sup>, Damian Refojo<sup>20</sup>, Femke van Wijk<sup>4</sup>, Sabine A Fuchs<sup>2</sup>, Peter M van Hasselt<sup>21</sup>

<sup>1</sup> Department of Metabolic Diseases, Division Pediatrics, Wilhelmina Children's Hospital University Medical Center Utrecht, Utrecht University, 3584 EA Utrecht, the Netherlands; Center for Translational Immunology (CTI), Division Pediatrics, Wilhelmina Children's Hospital University Medical Center Utrecht, Utrecht University, Utrecht, the Netherlands.

<sup>2</sup> Department of Metabolic Diseases, Division Pediatrics, Wilhelmina Children's Hospital University Medical Center Utrecht, Utrecht University, 3584 EA Utrecht, the Netherlands.

<sup>3</sup> Department of Energy and Biotechnology, Flensburg University of Applied Sciences, Flensburg, Germany.

<sup>4</sup> Department of Genetics, Division Pediatrics, Wilhelmina Children's Hospital University Medical Center Utrecht, Utrecht University, Utrecht, the Netherlands.

<sup>5</sup> Center for Translational Immunology (CTI), Division Pediatrics, Wilhelmina Children's Hospital University Medical Center Utrecht, Utrecht University, Utrecht, the Netherlands.

<sup>6</sup> Department of Neuroendocrinology, Max Planck Institute of Psychiatry, Munich, Germany; Institute of Developmental Genetics, Helmholtz Zentrum München, Munich, Germany.

<sup>7</sup> Department of Neuroendocrinology, Max Planck Institute of Psychiatry, Munich, Germany.

<sup>8</sup> Instituto de Investigación en Biomedicina de Buenos Aires (IBioBA) - CONICET - Partner Institute of the Max Planck Society, Buenos Aires, Argentina.

<sup>9</sup> Division Imaging and Oncology University Medical Center Utrecht, Utrecht University, Utrecht, the Netherlands.

<sup>10</sup> Department of General Pediatrics, Wilhelmina Children's Hospital, University Medical Center Utrecht, Utrecht University, Utrecht, the Netherlands.

<sup>11</sup> Central Diagnostics Laboratory, University Medical Center Utrecht, Utrecht, the Netherlands.

<sup>12</sup> Department of Medical Genetics, University Medical Center Groningen, Groningen, the Netherlands.

**American Journal of Human Genetics 223;11(1):146-16**

<sup>13</sup> Dravet Center and Comprehensive Epilepsy Center, NYU School of Medicine, New York, NY, USA.

<sup>14</sup> NYU Clinical Genetic Services, NYU Grossman School of Medicine, New York, NY, USA.

<sup>15</sup> Department of Radiology, NYU Grossman School of Medicine, New York, NY, USA.

<sup>16</sup> Section of Genetics and Metabolism, University of Arkansas for Medical Sciences, Little Rock, AR, USA.

<sup>17</sup> Laboratory of Experimental Cardiology, Department of Cardiology, University Medical Center Utrecht, University of Utrecht, Utrecht, the Netherlands.

<sup>18</sup> Department of Genetics, Division Laboratories, Pharmacy and Biomedical Genetics, University Medical Center Utrecht, Utrecht, the Netherlands.

<sup>19</sup> Department of Biomedical and Life Sciences, University College Roosevelt, Middelburg, the Netherlands.

<sup>20</sup> Instituto de Investigación en Biomedicina de Buenos Aires (IBioBA) - CONICET - Partner Institute of the Max Planck Society, Buenos Aires, Argentina; Molecular Neurobiology, Max Planck Institute of Psychiatry, Munich, Germany.

<sup>21</sup> Department of Metabolic Diseases, Division Pediatrics, Wilhelmina Children's Hospital University Medical Center Utrecht, Utrecht University, 3584 EA Utrecht, the Netherlands.

Electronic address: [p.vanhasselt@umcutrecht.nl](mailto:p.vanhasselt@umcutrecht.nl).

## Abstract

Neddylation has been implicated in various cellular pathways and in the pathophysiology of numerous diseases. We identified four individuals with bi-allelic variants in *NAE1*, which encodes the neddylation E1 enzyme. Pathogenicity was supported by decreased NAE1 abundance and overlapping clinical and cellular phenotypes. To delineate how cellular consequences of NAE1 deficiency would lead to the clinical phenotype, we focused primarily on the rarest phenotypic features, based on the assumption that these would best reflect the pathophysiology at stake. Two of the rarest features, neuronal loss and lymphopenia worsening during infections, suggest that NAE1 is required during cellular stress caused by infections to protect against cell death. In support, we found that stressing the proteasome system with MG132-requiring upregulation of neddylation to restore proteasomal function and proteasomal stress led to increased cell death in fibroblasts of individuals with *NAE1* variants. Additionally, we found decreased lymphocyte counts after CD3/CD28 stimulation and decreased NF- $\kappa$ B translocation in individuals with *NAE1* variants. The rarest phenotypic feature-delayed closure of the ischiopubic rami-correlated with significant downregulation of RUN2X and SOX9 expression in transcriptomic data of fibroblasts. Both genes are involved in the pathophysiology of ischiopubic hypoplasia. Thus, we show that NAE1 plays a major role in (skeletal) development and cellular homeostasis during stress. Our approach suggests that a focus on rare phenotypic features is able to provide significant pathophysiological insights in diseases caused by mutations in genes with pleiotropic effects.

## Introduction

Covalent attachment of ubiquitin, NEDD8, and SUMO proteins to target proteins (called ubiquitination, neddylation, and sumoylation, respectively) is an important mechanism for eukaryotic protein regulation.<sup>1</sup> Neddylation involves the attachment of NEDD8 to a protein target through a sequential, three-step process, that is facilitated by so-called E1, E2, and E3 enzymes.<sup>2,3,4</sup> The E1 complex consists of APPBP1—encoded by *NAE1* (MIM: 603385)—and UBA<sup>3,5,6,7</sup> While UBA3 acts as the activating enzyme, APPBP1 accelerates the kinetics of this first step.<sup>6</sup> The E2 enzyme aids a consecutive transthioylation reaction of NEDD8. E3 enzymes catalyze the transfer of NEDD8 from the E2 enzyme onto the neddylation target. The best-known targets of neddylation are cullins, that form cullin-RING ligase complexes upon neddylation (CRLs),<sup>8,9</sup> which can tag proteins for degradation via the 26S proteasome. Additionally, non-cullin neddylation targets have been described.<sup>2,10</sup>

Neddylation is thought to be involved in the pathophysiology of many diseases, including Alzheimer disease,<sup>11,12</sup> Parkinson disease,<sup>13</sup> certain auto-immune diseases,<sup>14</sup> malignancies,<sup>15,16,17</sup> and hepatic fibrosis.<sup>18</sup> This is not surprising, given that neddylation is a key regulator of a wide array of essential intracellular pathways, including NF- $\kappa$ B,<sup>14,19</sup> HIF-1 $\alpha$ ,<sup>20</sup>  $\beta$ -catenin,<sup>21</sup> and XPC.<sup>22,23</sup> Despite neddylation's broad involvement in disease, the exact pathophysiological role of neddylation in these diseases remains elusive, partly due to the large variety of cellular pathways affected by neddylation.

Through GeneMatcher,<sup>24</sup> we identified four individuals harboring *NAE1* genetic variants, that led to decreased *NAE1* abundance and altered neddylation dynamics. Next, we aimed to study the cellular impact, but the large variety of cellular pathways that could be affected by faulty neddylation called for prioritization. Based on the rationale of information theory, which states that the information content of rare events is highest,<sup>25</sup> we studied the underlying cellular mechanisms of phenotypic features that were present in all individuals but rarely present in individuals with other genetic diseases.<sup>26</sup>

The three rarest phenotypic features consisted of ischiopubic synchondrosis hypoplasia, infection-triggered lymphopenia, and infection-triggered neurodegeneration. In vitro biochemical analysis of these features helped to delineate the most important functions of NAE1 for human health: facilitating (skeletal) development and maintaining homeostasis during cellular stress, through a subset of regulatory pathways.

## Materials and Methods

### *Ethics*

Individuals 1 and 2 were recruited in the Wilhelmina Children's Hospital Utrecht. Informed consent was obtained to use residual material collected for diagnostic purposes, to include in the Wilhelmina Children's Hospital metabolic biobank (TCBio 19-489/B, <https://tcbio.umcutrecht.nl>). By using the same biobank, we included residual material of pediatric healthy fibroblast lines. Healthy adult donor peripheral blood mononuclear cells (PBMCs) were obtained through the Minidonor Service, an ethics review board-approved blood donation facility at the UMC Utrecht (protocol number 18-774). To compare the clinical phenotype of individuals with NAE1 variants to a pediatric reference population, clinical data from the Utrecht Patient-Oriented Database (UPOD) was used. UPOD is an infrastructure of relational databases comprising data on affected individuals that visited the University Medical Center Utrecht (UMC Utrecht) since 2004. UPOD data acquisition and management are in accordance with Dutch regulations concerning privacy and ethics. The structure and content of UPOD have been described in more detail elsewhere.<sup>27</sup> Pelvic X-rays were analyzed using the picture archiving and communication system (PACS IDS7 22.1.5). The storage and handling of medical data was recorded in a data management plan which can be consulted via <https://dmponline.dcc.ac.uk/plans/66973>. Individual 3 was recruited via the Dravet Center and Comprehensive Epilepsy Center in New York, and individual 4 was recruited via the University of Arkansas for Medical Sciences. They were recruited through the PhenomeCentral repository. Funding for PhenomeCentral was provided by Genome Canada and Canadian Institute of Health Research (CIHR).<sup>28</sup> From all four

individuals, informed consent was obtained for publication of facial images and medical information. All procedures performed in studies involving human participants are in accordance with national and local institutional review boards (IRBs) of the participating centers.

#### *Whole-exome sequencing*

Exomes were enriched using Agilent SureSelect XT Human All Exon kit V5 and sequenced on a HiSeq sequencing system (Illumina). Reads were aligned to hg19 using a Burrows-Wheeler Aligner. Variants were called using Genome Analysis Toolkit Variant Caller and annotated, filtered, and prioritized using the Bench NGS Lab platform (Agilent-Cartagenia) and/or an in-house designed “variant interface” and manual curation. The minimal coverage of the full target was  $>15 \times 95\%$ . All common polymorphisms with a minor allele frequency (MAF) higher than 0.25 were filtered out using several public databases including 1,000 genomes database,<sup>29</sup> Ensembl GRCh37 genome browser,<sup>30</sup> exome aggregation consortium database (ExAC),<sup>31</sup> genome aggregation database (gnomAD),<sup>32</sup> and database of single nucleotide polymorphisms (dbSNP). Variant calling was performed using the complete human reference genome (hg19, NCBI release GRCh37).<sup>33</sup>

#### *RNA sequencing*

RNA sequencing was performed as previously described.<sup>34</sup> Briefly, total RNA was isolated from fibroblast cultures using Trizol LS reagent (Invitrogen). mRNA was isolated using Poly(A) Beads (NEXTflex). Sequencing libraries were prepared using the Rapid Directional RNA-Seq Kit (NEXTflex) and sequenced on a NextSeq500 (Illumina) to produce 75 base long reads (Utrecht DNA Sequencing Facility). Sequencing reads were mapped against the reference genome (hg19 assembly, NCBI37) using BWA35 package (mem -t 7 -c 100 -M -R). RPKM values were calculated using the `mseq_countgeneread` function from Cisgenome v.233 and log2 transformed for further analysis. To perform statistical enrichment in a ranked gene list, the differential gene expression score was calculated: (overall mean RPKM)  $\times$   $\text{abs}(\log_2 \text{FC}) \times -\log_{10}(\text{adjusted p value})$ . Subsequent analysis was performed using the Gene Set Enrichment Analysis (GSEA) tool from Broad



Institute with the following settings: GSEA pre-ranked, 1000 permutations, GO v.7.1 (updated on: 30-Mar-2021) and KEGG cellular processes.<sup>36</sup>

Statistical overrepresentation in Gene Ontology (GO) terms among differentially expressed downregulated genes (Log2Fold  $< -2$  and adjusted p value  $< 0.05$ ) were analyzed using R (v.4.0.3) and R Studio (v.1.3.1093) using the ClusterProfiler package.<sup>37</sup> A list of all expressed genes within control subjects and the affected individuals with a base mean  $> 2$  was used as background.

*Plasmid cloning of NAE1 shRNA and NAE1 rescue construct*

Restriction enzymes (AgeI, EoRi-Hf, NheI, MluI) were purchased from New England Biosciences. NAE1 shRNA was cloned into Tet-pLKO-puro (Addgene). Targeting sequences were obtained using the TRC sequencing database<sup>38</sup> and can be found in **Table S4**. To generate shRNA-expressing plasmids, the stuffer DNA was removed from pLKO-Tet-On by an AgeI/EcoRI digest and replaced with double-stranded oligonucleotides encoding the desired shRNA and AgeI/EcoRI sites. This product was transformed to Stellar competent bacteria (Takara Bio). The bacteria were midi prepped according to the manufacturer's protocol (Invitrogen) to obtain plasmid DNA. The sequence was verified by sequencing the entire insert. Lentiviruses were generated by co-transfecting HEK293 cells with 6  $\mu\text{g}$  of the NAE1 shRNA-encoding plasmid and lentiviral packaging plasmids pMD2.G (Addgene) and psPAX (Addgene). After three days, lentiviruses were obtained by spinning down the filtered HEK293 medium at  $50,000 \times g$  for 120 min. The pellet contained the lentiviruses. Fibroblasts were transduced by incubation of 8  $\mu\text{g}/\text{mL}$  polybrene with lentivirus containing medium for 24 h. The transduced fibroblasts with build-in construct were selected with Puromycin (Santa Cruz Biotechnology). shRNA expression was induced by addition of 1  $\mu\text{g}/\text{mL}$  doxycycline (Sigma) for 7 days.<sup>39,40</sup>

The WT NAE1 cDNA of isoform a (GenBank: NM\_003905.4) was cloned from human cDNA using flanking primers that contained complimentary 3' and 3' coding sequences and either MluI or NheI restriction sites, respecti-

vely. The pLenti CMV Puro vector (Addgene) was digested with Nhe1 and Mlu1 and then ligated with the insert. Plasmid DNA and lentiviruses were generated similar to the generation of NAE1 shRNA-containing plasmids.

#### *Fibroblast viability assays*

Fibroblasts were obtained from individual 1, individual 2, both parents of individual 1, and healthy control subjects. Cells were cultured in fibroblast culture medium (HAM F12 with 10% fetal bovine serum, penicillin [100 UI/mL] and streptomycin [100 µg/mL]), in a humidified incubator at 37°C and 5% CO<sub>2</sub>. Medium was changed every 3–4 days. Cells were split at 80% confluency.

For the viability assays, cells were seeded (2,000 cells/well) in a 96-well plate. The following day, normal culture medium was removed, and medium with different stressors—MG132 (Cayman Chemicals) or MLN4924 (Focus Biomolecules)—was added at the indicated concentrations. After 24 h, culture medium was removed and replaced with 1:2,000 HOECHST 33342 (Sigma) and 1:20 propidium iodide (ThermoFisher). Fluorescent images were obtained with the EVOS XL Imaging System (ThermoFisher). The percentage of dead cells was calculated by dividing the number of PI-positive cells by the number of HOECHST-positive cells.

#### *Western blotting*

Western blots of cullin 1, cullin 3, and NAE1 were performed in the Max Planck Institute. Cell lysates were prepared by adding RIPA lysis buffer (50 mM TrisHCl [pH 8.0], 150 mM NaCl, 1% NP-40, 0.5% sodium deoxycholate, 0.1% SDS) supplemented with protease inhibitors (Sigma), Phosphostop (Roche), 20 µM N-ethylmaleimide (NEM) (Sigma-Aldrich), and 1,10-orthophenanthroline (OPT) (Sigma-Aldrich) to the cells, scraping into a 1.5 mL tube, sonicating, and centrifuging. Protein concentrations were determined by Bradford protein assay (Biorad). Equal amounts of protein (6 µg) were loaded into each lane of an 8%–15% SDS-PAGE gel, subjected to electrophoresis, and transferred onto a PVDF membrane (Millipore). Binding of secondary horseradish peroxidase-conjugated antibodies was visualized by

chemiluminescent substrate (Millipore). Western blotting membranes were probed with NAE1 (dilution 1:1,000, Novus Biologicals), cullin 1 (dilution 1:1,000, Thermofisher Scientific), cullin 3 (dilution 1:1,000, Cell Signaling Technology),  $\beta$ -actin (dilution 1:1,000, Cell Signaling Technology). The intensity values were normalized against total protein using stain-free detection gels (Bio Rad). Western blots of NAE1 in fibroblasts transduced with NAE1 shRNA or cDNA were performed in the UMC Utrecht, as described previously.<sup>41</sup>  $\beta$ -actin (dilution 1:1,000, Cell Signaling Technology) or HSP90 (dilution 1:1,000, Cell Signaling Technology) were used as housekeeper.

#### *Flow cytometry*

PBMC's were isolated from the whole blood fraction using Ficoll (GE Healthcare). CD3<sup>+</sup> cells were separated from the PBMC fraction using Pan T cell isolation kit (Miltenyi). Cells were stimulated with soluble anti-CD3<sup>+</sup> (Life Technologies, clone OKT3) and anti-CD28<sup>+</sup> (Thermofisher) at 1  $\mu$ g/mL for 1 day. Cells were stained with CD3 (dilution 1:50, Biolegend), CD4 (dilution 1:200, eBioscience), CD8 (dilution 1:25, BD), CD45RA (dilution 1:500, Biolegend), CD45RO (dilution 1:12.5, Beckman Coulter) for 20 min at 4°C, followed by incubation with Annexin-V and 7-AAD (dilution 1:20, BD Biosciences) for 15 min at room temperature.

For the analysis of double-negative (CD3<sup>+</sup>, CD4<sup>-</sup>, CD8<sup>-</sup>) T cell counts, number of naive T cells, and the MLN4924 assay, PBMCs were cultured in RPMI with 10% heat-inactivated FCS, 1% penicillin/streptomycin, and 1% L-glutamine for 1 day with or without MLN4924, on a plate coated with 0.1  $\mu$ g/mL anti-CD3. Afterwards, cells were stained with CD3, CD4, CD8, CD45RA, CD45RO, Fixable Viability Dye eFluor 506, fixed with formaldehyde, and permeabilized with methanol. Cells were immediately analyzed using BD LSRFortessa. Flow cytometry analysis was performed using FlowJo (v.10.6.2, Becton, Dickinson and Company; 2019). Gating strategy is shown in **Figure S2**.

#### *Imagestream NF- $\kappa$ B translocation*

CD3<sup>+</sup> T cells were stimulated with anti-CD3<sup>+</sup>/CD28<sup>+</sup> at 2  $\mu$ g/mL for the

indicated time points (0, 15, and 35 min). After stimulation, cells were fixed immediately using 4% paraformaldehyde. Fixed cells were permeabilized with 0.1% Triton X-100 for 10 min and stained with p65 (dilution 1:16,000, Cell Signaling Technology) and DRAQ5 (dilution 1:8,000, Biolegend) antibodies for 20 min at 4°C, followed by incubation with FITC-anti Rabbit (Jackson) for 20 min at 4°C. Data were collected with Amnis Imagestream MkII Imaging Flow Cytometer (Luminex) and data analysis was performed with IDEAS v.6.0 software. Nuclear area was determined using the morphology mask. Cells with a similarity score >0 were considered translocated. Gating strategy can be found in **Figure S3**.

#### *Data analysis*

Statistical analysis was performed using GraphPad Prism v.6 for Windows (GraphPad Software). Final counts are presented as the mean percentages  $\pm$  SEM; one- or two-way ANOVA were performed for multiple comparisons. As post hoc, uncorrected Fisher's least discriminant analysis was used. To assess normality, Shapiro-Wilk test was used. Unpaired two-tailed Student's t tests or Mann-Whitney U were used for dual comparisons.  $p < 0.05$  was considered significant: \* $p < 0.05$ , \*\* $p < 0.01$ , \*\*\* $p < 0.001$ , \*\*\*\* $p < 0.0001$ .

#### *Occurrence ratio*

The occurrence ratio was calculated by dividing the percentage of individuals showing a rare trait by the number of associated genes, extracted from the Human Phenotype Ontology database (HPO) at 20-02-2021.<sup>42</sup>

## Results

### *Clinical features of individuals with NAE1 variants*

The index proband (individual 1) was born as the second child to healthy non-consanguineous parents. She presented with a ventricular septal defect, coarctation of the aorta, and failure to thrive. At one year of age, she was admitted to the ICU with a severe viral respiratory tract infection that led to subsequent loss of developmental milestones and profound therapy-resistant epilepsy. Brain MRI before ICU admission was normal, but after the ICU admission it showed brain atrophy, as evidenced by enlarged ventricles and diminished white matter volume. A subsequent viral respiratory infection a year later resulted in a similar loss of milestones. During these and other infections, she exhibited lymphopenia, which normalized upon recovery. Pelvic X-ray taken at age four showed absence of the os pubis ramus inferior and hip dysplasia. Extensive etiological workup did not lead to a diagnosis. Whole-exome sequencing revealed several genetic variants of uncertain significance (**Table S1**). Of these variants, the *NAE1* variant was considered the most promising candidate, based on conservation, constraint metrics, and predictions: NM\_003905.4: c.[147G>C]; [254G>A], p.[Leu49Phe]; [Arg85Gln].

Through GeneMatcher,<sup>24</sup> three additional individuals with similar phenotypic features, harboring homozygous variants in *NAE1*, were identified (**Table 1**). Additionally, individual 4 has a pathogenic genetic variant in *SCN1A* (MIM: 182389) and displays phenotypic features associated with Dravet syndrome<sup>43</sup> (MIM: 607208) as well as *NAE1* deficiency (**Table S2**).

All individuals showed similar facial features (**Figure 1**): broad forehead (individuals 1, 2, 4), downslant palpebral fissures (individuals 1, 2, 3), epicanthus/telecanthus (individuals 1, 3), round face (individuals 1, 3), prominent cheeks (individuals 1, 3, 4), broad nasal tip (individuals 1, 3, 4), pointed chin (individuals 1, 2, 4), and full lower lip (individuals 2, 4).

All individuals developed epilepsy and experienced exacerbation of epilepsy and/or developmental decline during infectious periods. All individuals

**Table 1. Overview of symptoms of individuals with NAE1 variants**

<b>NAE1 variant</b>	<b>Individual 1 c.[147G&gt;C]; [254G&gt;A]p. [Leu49Phe]; [Arg85Gln]</b>	<b>Individual 2c, [254G&gt;A]; [254G&gt;A]p. [Arg85Gln]; [Arg85Gln]</b>	<b>Individual 3 c, [1289 G&gt;A]; [1289G&gt;A] p.[Arg430Gln]; [Arg430Gln]</b>	<b>Individual 4 c, [882C&gt;G]; [882C&gt;G]p. [Cys294Trp]; [Cys294Trp]</b>
Other variants identified with WES	full list in <a href="#">Table S1</a>	no	no	SCN1A:c.[1624C>T]; [=], p.[Arg542*]; [=],
Current age (years)	12	19	4	9
Gender	F	M	M	F
Pregnancy term (weeks)	40	36	37	40
Birth weight (g)	2,615 (-1.8 SDS)	2,767 (0.05 SDS)	2,140 (-1.6 SDS)	2,300 (-2.48 SDS)
Head circumference (cm)	51 (-0.47 SDS) (8 y)	54 (-0.59 SDS) (13 y)	47.3 (-1.5 SDS) (2 y 5 m)	48.7 (-1.73 SDS) (6 y 6 m)
Height (cm)	116 (-2.53 SDS) (8 y)	150 (-1.5 SDS) (13 y)	91 (-1 SDS) (2 y 5 m)	97 (-5.9 SDS) (7 y)
Cleft palate	-	+	-	-
Asymmetrical palate	+	+	-	N/A
Heart defects	+ ventricular septal defect and coarctation of the aorta	-	-	-
Developmental delay	severe	moderate	moderate	severe
Seizures	+	-	+	+
Hypotonia during infancy	+	-	+	+
Underdeveloped corpus callosum	+	+	+	+
Decreased myelination	+	+	+	+
Enlarged ventricles	+	-	+	+
Loss of milestones after infections	+	+	+	+
Neurodegeneration	+	+	+	+
Decreased bone density (DEXA scan)	+	+	+	+
Joint dislocation	+	+	-	-
Joint hyperextensibility	+	+	-	+
Joint stiffness	-	-	-	+
Resistant to sunburns	+	+	+	-
Recurrent infections	+ respiratory, urinary tract, skin	+ respiratory, skin	+ respiratory	+ respiratory, urinary tract
Hepatomegaly at infancy	+	-	+	-
Splenomegaly at infancy	+	+	+	-
Decreased amount of immunoglobulins	+ IgG	+ IgG, IgM	-	-
Leukopenia	+	+	-	+
Periodic lymphopenia	+	+	-	+
AST/ALT increase	+ during infections	-	-	-
Delayed closure of ischiopubic rami	+	+	N/A	N/A
Increased size of ischiopubic rami	+	+	+	+

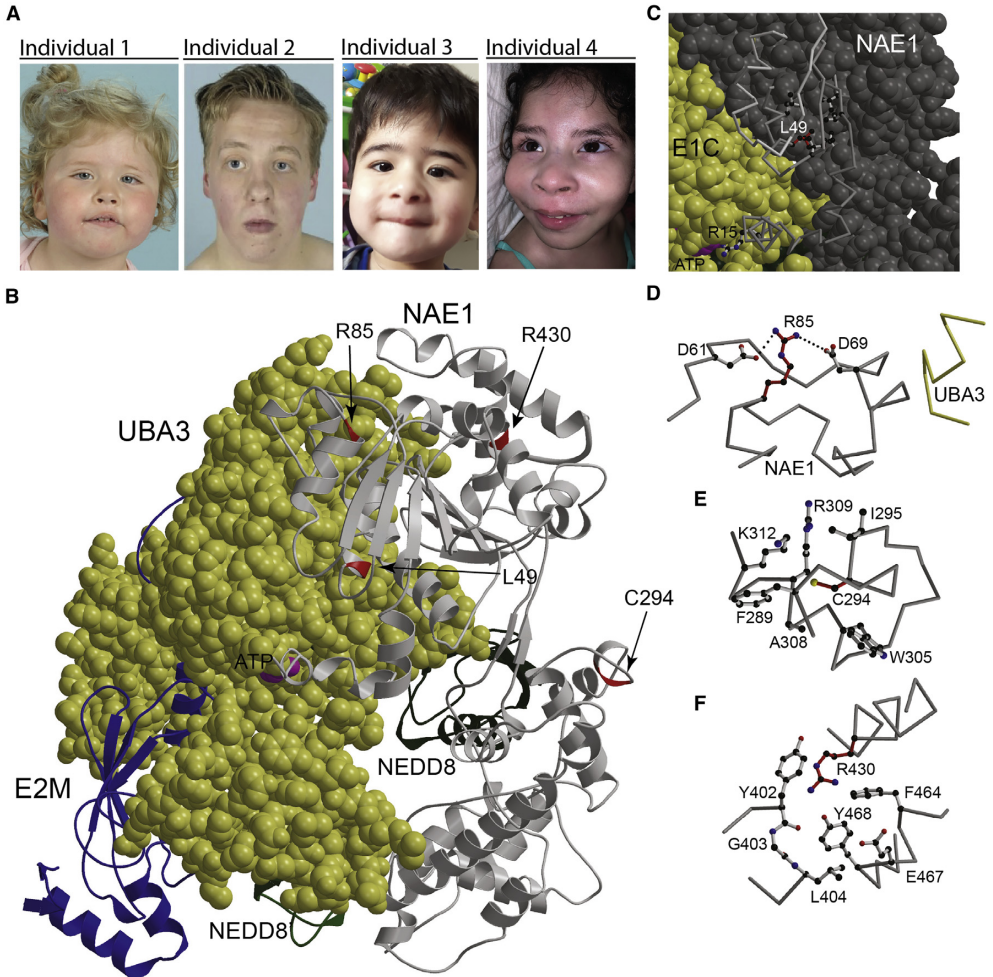


**Figure 1: Facial features of the cohort and structural analysis of NAE1 variants**

(A) Representative photographs illustrating facial features of individuals with *NAE1* variants.

(B) Graphical representation of UBA3 (space filling, yellow) in complex with NAE1 (light gray), the E2 of neddylation (EM2, blue), and two molecules of NEDD8 (light and dark green). The positions of Leu49, Arg85, Arg430, and Cys294 are marked in red. ATP is space filling in magenta. The color coding is used throughout the entire figure.

(C) The local environment of Leu49. NAE1 is represented in part as space filling and in part as backbone trace.

(D–F). Local environments of Arg85, Arg430, and Cys294. Dotted lines indicate hydrogen bonds. Figures were generated by use of programs Molscript and Raster3D.<sup>44,45</sup>

showed moderate to severe developmental delay. All individuals showed under-developed corpus callosum and enlarged lateral ventricles in MRI. During infancy, three out of four individuals showed splenomegaly. All individuals had frequent infections, which were mostly respiratory tract infections, but urinary tract infections (2/4) and skin infections (2/4) were also observed. Three out of four individuals had documented lymphopenia during infections, that normalized during recovery. All individuals showed hypoplastic ischiopubic rami and decreased bone mineral density (assessed using dual energy X-ray absorptiometry [DEXA] scans). Fibroblasts and PBMCs were obtained from two individuals (individuals 1 and 2) for biochemical analyses. A summary of clinical features can be found in **Table 1** and the **Supplemental note**.

*NAE1 abundance and the ratio of neddylated to non-neddylated cullin are altered in individuals with NAE1 variants*

The amino acid positions where the *NAE1* missense variants are located are highly conserved in other species (**Figure S5**). All variants cluster together in the three-dimensional structure of the protein, even though they are located at the N- and C-terminal portions of the protein (**Figure 1B**). Leu49 (individual 1) is part of the hydrophobic core of *NAE1* (**Figure 1C**). A phenylalanine at this position is sterically not tolerated and is expected to result in (local) perturbation of the fold. This may reduce the ability of *NAE1* to interact with *UBA3* and impacts the positioning of Arg15. Arg15 is in close proximity to the *UBA3*-bound ATP and is required for efficient catalysis. Arg85 is partially surface exposed but the guanidine group is engaged in hydrogen bonds with Asp61 and Asp69. Substitution of Arg85 by glutamine (individual 1 and 2) disturbs this network of hydrogen bonds, which would destabilize the local fold, which may extend to the interaction surface with *UBA3* in proximity to Asp69 (**Figure 1D**). Cys294 (individual 4) points into the hydrophobic core (**Figure 1E**). A substitution by a sterically very demanding tryptophan is incompatible with the local fold and would result in destabilization of the entire protein.

The side chain of Arg430 (individual 3) points inwards, and a substitution by a glutamine might thus destabilize the local fold (**Figure 1F**).



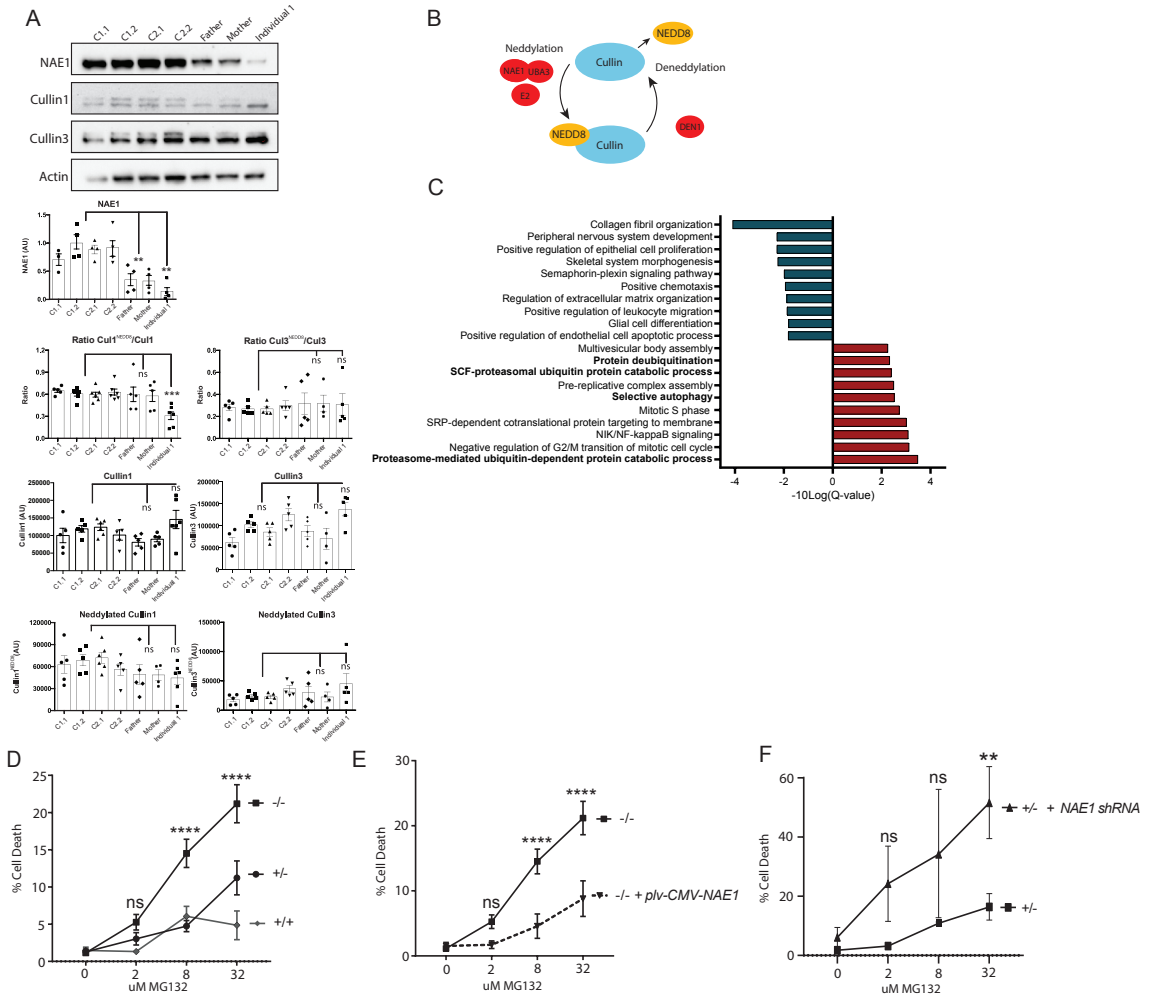


**Figure 2: NAE1 abundance and neddylation to non-neddylation ratio are reduced in individuals with NAE1 variants**

(A) Western blots showing NAE1, neddylated, and non-neddylated cullin 1/cullin 3 abundance in dermal fibroblasts of healthy control subjects (2 healthy controls [C1 and C2]; 2 biological replicates per healthy control [C1.1, C1.2, C2.1, C2.2]; 6 technical replicates each), heterozygous carriers (father and mother of individual 1; 5 technical replicates each), and the fibroblasts of individual 1 with bi-allelic *NAE1* genetic variants (6 technical replicates). Bar graphs represent the average band intensity of all technical replicates per donor  $\pm$  SEM. All band intensities were normalized to total protein content. Quantification was performed using ImageJ. One way ANOVA, Post-hoc: Dunnett's multiple comparisons test (\*\*p < 0.01, \*\*\*p < 0.001).

(B) Graphic showing the neddylation and deneylation cycles of cullins.

(C) Gene set enrichment analysis of the pre-ranked (based on differential expression score) transcriptomic dataset of individual 1- and 2-derived fibroblasts compared to 3 healthy control fibroblast lines. For this analysis, all genes were taken into account. The top 10 most significantly enriched (based on FDR (Q-value); blue, downregulated; red, upregulated) pathways are shown. Pathways in bold are associated with protein degradation and proteasome function. Pathways were aligned to the GO Ontology database.

(D) Cell death in fibroblasts derived from individuals 1 and 2, parents of individual 1, and healthy control subjects, after treatment with MG132 for 24 h at the indicated concentrations (in  $\mu\text{M}$ ). Cell death was assessed by dividing the amount of PI-positive cells by the total amount of cells. Error bars represent SEM of 3 technical replicates of 2 donors for

Western blot analysis of fibroblasts from individuals 1 and 2 with *NAE1* genetic variants showed a reduction of NAE1 by almost 80% compared to healthy control subjects (**Figures 2A, S4E, and S4F**), whereas heterozygous carriers of *NAE1* variants (parents of individual 1) exhibited a reduction of approximately 50% of NAE1 abundance (**Figure 2A**).

Next, we quantified both neddylated (cullin<sup>NEDD8</sup>) and non-neddylated cullin 1 and cullin 3 (**Figure 2B**). Even though the amount of neddylated cullins was normal, the ratio of neddylated to non-neddylated cullin 1 was significantly decreased in individual 1 and showed a trend toward a decreased ratio in individual 2 (**Figures 2A, S4E, and S4F**). The ratio of cullin 3 similarly showed a trend toward a decreased ratio in both individuals (**Figures 2A, S4E, and S4F**). *CUL1* and *CUL3* mRNA levels were unchanged, indicating that the altered ratio does not result from transcriptional upregulation (**Figures S4C and S4D**). These results indicate that NAE1 deficiency appears to alter the neddylated to non-neddylated cullin ratio.

To determine the effects of the altered neddylated to non-neddylated cullin ratio on proteasome function, we studied the transcriptomic profile of dermal fibroblast lines of individuals with *NAE1* variants and healthy pediatric dermal fibroblast lines (**Figure S1, Table S5**). Four out of ten most significantly upregulated enriched pathways (highest false discovery rate) found with gene set enrichment analysis included pathways involved in protein degradation. This is probably the result of proteasome dysfunction, causing compensatory upregulation of alternative cellular protein degradation

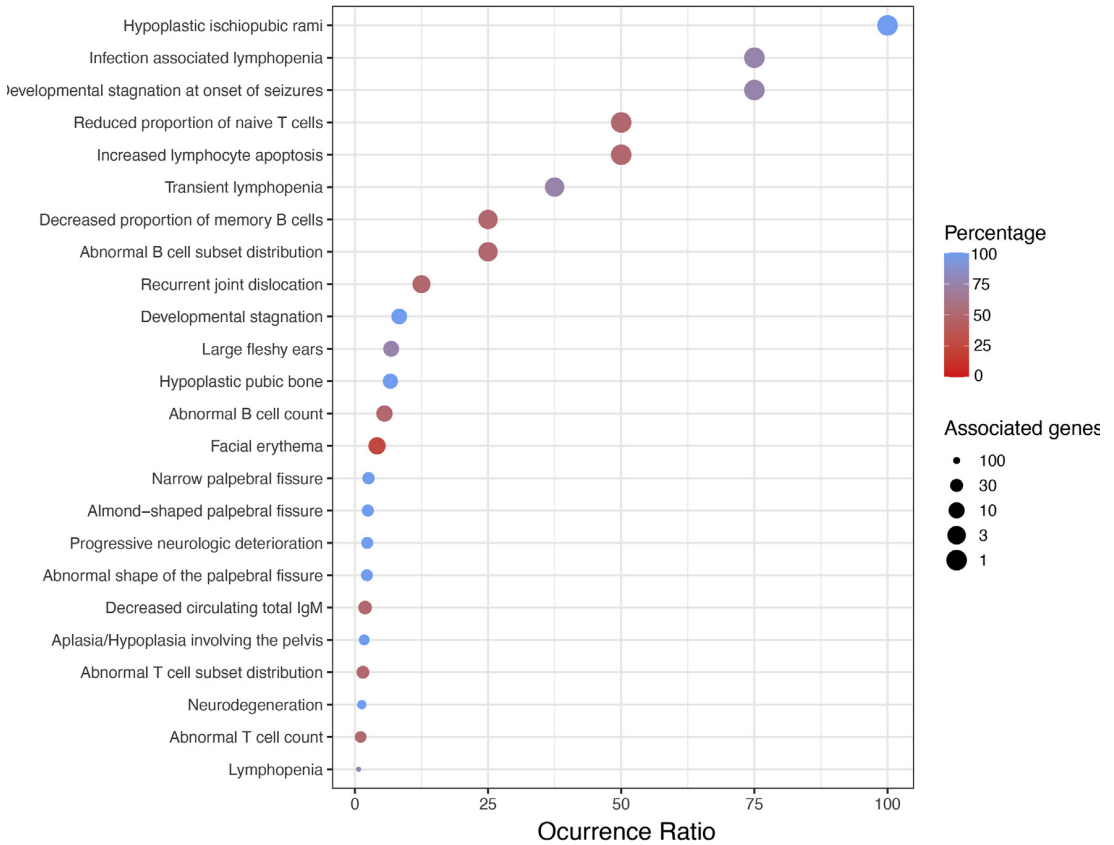


**Figure 3: Rarest clinical features in individuals with NAE1 variants**

Dot plot showing features with occurrence ratio >0.5 in individuals with NAE1 variants. Color coding refers to the percentage of individuals in our cohort experiencing a specific symptom. Dot size refers to the number of associated genes in HPO, transformed with  $-10\log$  to give features with the lowest amount of associated genes the largest dot size. The occurrence ratio was calculated by dividing the percentage of individuals experiencing a specific symptom by the number of associated genes.

ways (Figure 2C). Functionally, this was evidenced by increased sensitivity to proteasome inhibitor MG132 (Figures 2D and S7). Addition of a wild-type NAE1 cDNA expressing plasmid to cells from individuals with NAE1 variants decreased MG132 sensitivity (Figures 2E and S4B), while addition of NAE1-shRNA to cells from heterozygous carriers mimicked the

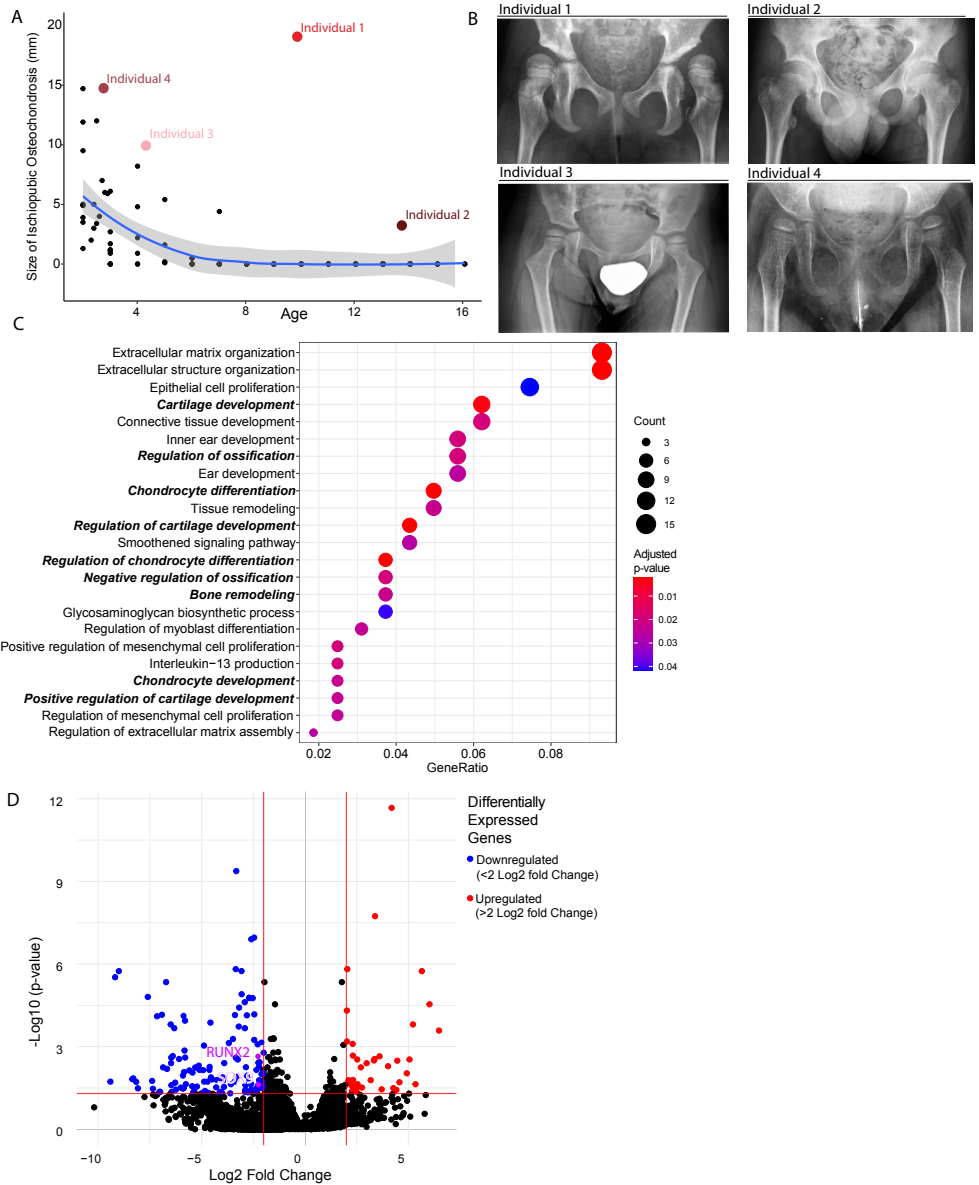


**Figure 4: Individuals with *NAE1* variants show hypoplasia of the ischiopubic synchondrosis**  
 (A) Size of the ischiopubic synchondrosis was measured in n = 200 pediatric individuals that had pelvic X-rays taken (black dots). The blue line represents the mean size of the ischiopubic synchondrosis in this population with a 95% confidence interval depicted in gray. Red/pink colored dots are the values of the individuals with *NAE1* variants.  
 (B) Pelvic X-rays of individuals with *NAE1* variants showing increased size of the ischiopubic

synchondrosis.

(C) Graph showing the 23 most overrepresented pathways in fibroblasts of individuals with *NAE1* variants using significantly downregulated genes (adjusted p value < 0.05, log<sub>2</sub>fold-change >2 and <2, **Table S5**) as input. Five out of nine pathways (bold) that are significantly enriched are involved in endochondral bone development and might explain delayed closure of ischiopubic synchondrosis in individuals with *NAE1* variants. The X axis shows the GeneRatio, defined as the number of genes associated with the pathway divided by the total number of selected genes.

(D) Volcano plot showing differentially expressed genes in individual 1 and 2 fibroblasts versus three healthy age-matched control subjects. *RUNX2* and *SOX9* (in purple) are involved in bone development and are linked to disease presenting with os pubis ramus inferior hypoplasia and are both downregulated in individuals with *NAE1* variants.

phenotype of individuals with *NAE1* variants (**Figures 2F and S4A**). These results suggest that proteasome function might be affected as a result of decreased *NAE1* abundance.

#### *Characterization of rare phenotypic features in individuals with *NAE1* variants*

After determining the pathogenicity of *NAE1* variants, we studied the cellular and clinical consequences of *NAE1* deficiency. To specify our search, we delineated the rarest phenotypic features by calculating the occurrence ratio of all phenotypic traits. The occurrence ratio takes both the prevalence within the cohort and the rareness of a feature within the population into account.<sup>26</sup> This approach identified the three rarest phenotypic features, shared by at least 75% of the cohort: hypoplastic ischiopubic rami, infection-associated lymphopenia, and neurodevelopmental setback during infections (**Figure 3, Table S3**).

#### *Individuals with *NAE1* variants show hypoplasia of the os pubis ramus inferior*

In individual 1, we observed increased size of the ischiopubic synchondrosis (**Figure 4A**), which prompted us to study the pelvic X-rays of the rest of the cohort. For comparison, we determined the size of the ischiopubic synchondrosis at different ages using pelvic X-rays of a pediatric reference population (**Figures 4A and 4B**). All individuals with *NAE1* variants showed increased size of the ischiopubic synchondrosis compared to the

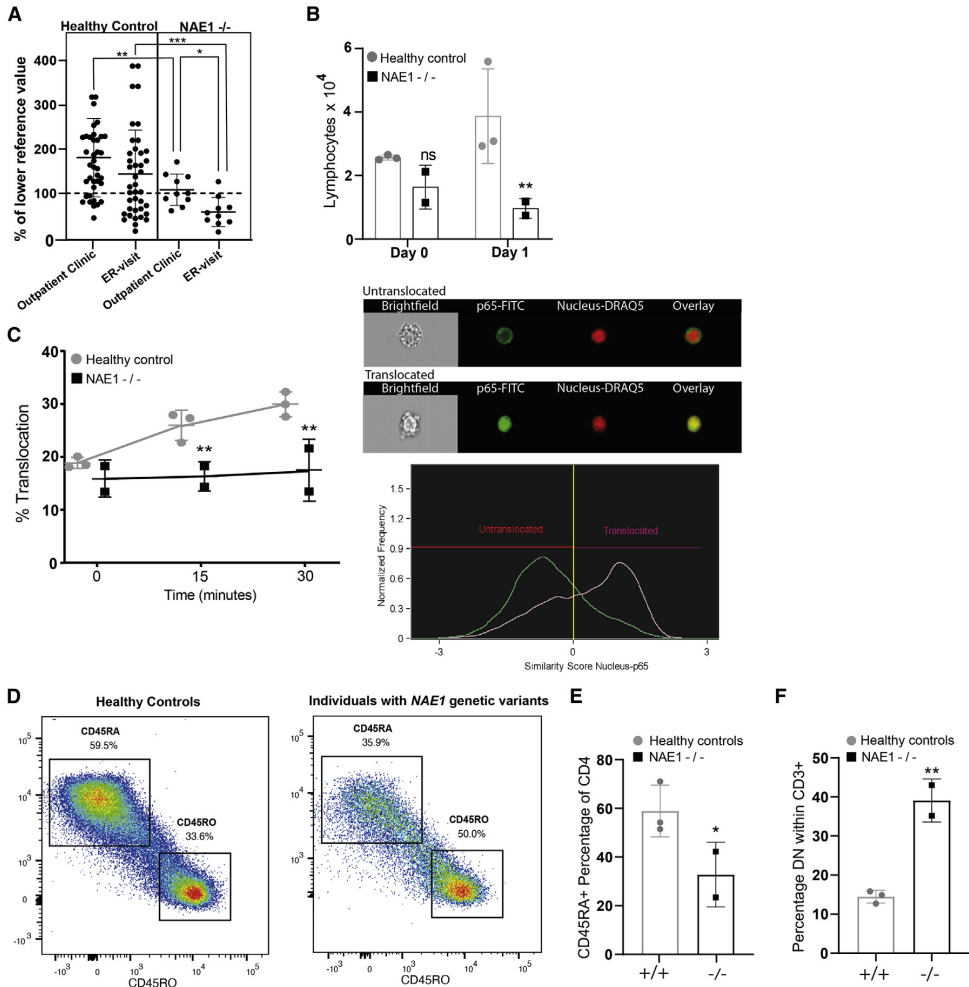


**Figure 5: Individuals with NAE1 variants experience lymphopenia during inflammation.** (A) Lymphocyte counts (combined B cell and T cell counts) during outpatient clinic visits and during infections for which individuals visited the emergency room (ER visits). All counts were normalized to the lower reference value of the corresponding age and depicted as a percentage. Individual data points of individuals (dots) are shown, line and error bars reflect the mean  $\pm$  SD, two-way ANOVA. Post Hoc: uncorrected Fisher's LSD (\* $p < 0.05$ , \*\* $p < 0.01$ , \*\*\* $p < 0.001$ ).

(B) Flow cytometry analysis of absolute CD3+ counts after treatment for 1 day with 1  $\mu$ g/ml anti-CD3/CD28 of individuals with NAE1 variants (-/-) (2 donors, 1 technical replicate) versus healthy controls (3 donors, 1 technical replicate). Bars represent mean value  $\pm$  SD two-way ANOVA, Fisher's LSD (\*\* $p < 0.01$ ).

(C) Percentage of NF- $\kappa$ B (p65) nuclear translocation in individuals with *NAE1* variants (2 donors, 1 technical replicate) and healthy controls (3 donors, 1 technical replicate) CD3+ cells after stimulation with 2  $\mu$ g/ml anti-CD3/CD28 for different timepoints (minutes) measured with Imaging Flow Cytometry Lines represent mean  $\pm$  SD two-way ANOVA repeated measurement, without correction. Post-Hoc: Fisher's LSD (\*\* $p < 0.01$ ). The images on the right show an example of cytoplasmic (untranslocated) and nuclear (translocated) location of p65 in the cell. The graph shows how translocation was quantified, by using the similarity score (pixel similarity p65/nucleus). All cells with similarity scores higher than zero were considered as 'translocated' cells.

(D) Graph showing the intensity of CD45RA (Y axis) and CD45RO (X axis) of all cells within the CD4+ population in healthy controls (3 donors, 1 technical replicate) and individuals with *NAE1* variants (2 donors, 1 technical replicate) without anti-CD3/CD28 stimulation.

(E) Bar graph showing the percentages of CD45RA positive cells within the CD4 population in the healthy control (3 donors, 1 technical replicate) and individuals with *NAE1* variants (2 donors, 1 technical replicate), bar graph represents the mean value  $\pm$ SD Students' T-test (\* $p < 0.05$ ).

(F) Bar graphs showing percentage of CD3 positive but CD4 and CD8 negative T cells in individuals with *NAE1* variants (2 donors, 1 technical replicate) and healthy controls (4 donors, 1 technical replicate each) without anti-CD3/CD28 stimulation, bars represent mean  $\pm$  SD; Student's t test (\*\* $p < 0.01$ ).

reference population. In transcriptomic data, Gene Ontologies (Biological Function) aligned to significantly downregulated genes ( $>2$ -fold, adjusted  $p$  value  $< 0.05$ ) in fibroblasts of individuals with *NAE1* variants compared to healthy control fibroblasts and were enriched for cartilage development, ossification, and chondrocyte differentiation (**Figure 4C**). Two of the main drivers for these pathways included SOX9 (MIM: 608160) (log2fold change  $-2$ , adjusted  $p$  value = 0.03) and RUNX2 (MIM: 600211) (log2fold change  $-2.3$ , adjusted  $p$  value = 0.002) (**Figure 4D**). Both SOX9 and RUNX2 are associated with congenital skeletal disorders (campomelic and cleidocranial dysplasia [MIM: 114290 and MIM:119600]) that result in hypoplastic ischiopubic rami.<sup>46,47,48</sup> Thus, *NAE1* might influence expression of these genes, resulting in altered endochondral bone development.

*Individuals with NAE1 variants experience lymphopenia and decreased NF- $\kappa$ B translocation during infections*

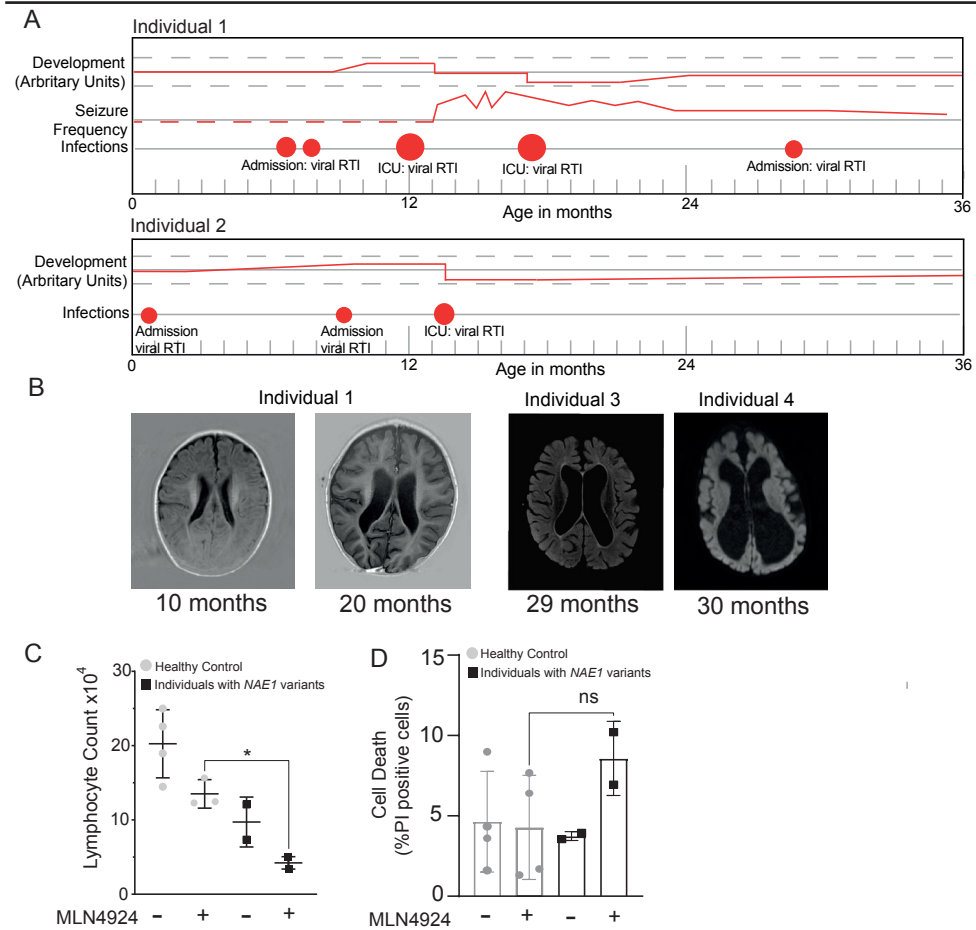


**Figure 6: Individuals with NAE1 variants experience neurodegeneration and seizure frequency during infections**

(A) Timeline showing the development and seizure frequency (red line) in individual 1 and 2. Development and seizure frequency were quantified by parents of individuals 1 and 2 (arbitrary units). If the red line drops below the 0-point (the black line), this indicates that development decelerated. Circles indicate infections, massive red circles indicate infections requiring admissions. The bigger the circle, the longer the time of admission.

(B) MRI images of individual 1, individual 3, and individual 4 are shown. For individual 1, MRI was taken at 10 months of age and at 20 months of age (after ICU admission). Note the brain loss occurring between this time. The MRI of individual 3 was taken at approximately 29 months of age, 6–7 months after his seizures began which were treated with ACTH. For individual 4, brain MRI was obtained at the age of 2.5 years, showing severe brain loss, resulting from



multiple severe infections.

(C) Bar graph showing the lymphocyte count after 1 day of anti-CD3 (0.1  $\mu\text{g/mL}$ ) stimulation with and without the addition of MLN4924 (200 nM) in healthy controls (3 donors, 1 technical replicate each) and lymphocytes of individuals with *NAE1* variants (2 donors, 1 technical replicate each). Bars represent mean value  $\pm$  SD, two-way ANOVA, post hoc: Fisher's LSD (\* $p < 0.05$ ).

(D) Bar graph showing the percentage of death cells (PI positive) over the total amount of cells (counted using Hoechst) in fibroblasts, with or without MLN4924 treatment (500 nM) in healthy controls (3 donors, 1 technical replicate each, gray bars) and individuals with *NAE1* variants (2 donors, 1 technical replicate each, black bars). Bars represent mean value  $\pm$  SD, two-way ANOVA, post hoc: Fisher's LSD. (not significant,  $p > 0.05$ ).

The second rarest phenotypic feature was the lymphopenia, which worsened during infections (**Figure 5A**). This clinical observation could be mimicked in vitro, where we found that individuals with *NAE1* variants showed a trend toward decreased CD3<sup>+</sup> T cell counts without stimulation, which became significant during stimulation with CD3/CD28 for 24 h (**Figure 5B**). We found the lymphopenia was not the result of a proliferation defect, as the proliferation rates of T cells in healthy control subjects and affected individuals were similar (**Figure S6**).

Neddylation is an important regulator of NF- $\kappa$ B,<sup>19,49</sup> a signaling molecule known to promote lymphocyte survival.<sup>50</sup> Therefore, we studied NF- $\kappa$ B activation by measuring p65 nuclear translocation in CD3<sup>+</sup> T cells upon stimulation with anti-CD3/CD28. Indeed, p65 nuclear translocation in response to CD3/CD28 stimulation was reduced in individuals with *NAE1* variants (**Figure 5C**).

Another rare feature involved the significantly decreased percentages of naive (CD45RA-positive) CD4<sup>+</sup> cells in steady-state conditions (**Figures 5D and 5E**). Additionally, when performing the gating of CD4 and CD8 subpopulations within CD3, we noticed increased percentages (40%) of double-negative (CD4<sup>-</sup>CD8<sup>-</sup>) CD3<sup>+</sup> cells (**Figure 5F**). Double-negative T cells are immature thymic T cells which are normally found in low (<10%) percentages in peripheral blood, and their physiological role remains poorly understood.<sup>51</sup> Gene set enrichment analysis using the KEGG database

showed several pathways that could potentially link neddylation dysfunction to the observed immunologic phenotype, including downregulated WNT/ $\beta$ -catenin and MAP-kinase signaling (**Figure S1**).

Together, these findings indicate that lymphocytes of individuals with *NAE1* variants have different immunological characteristics at baseline, indicated by their decreased naive T cell percentages and increased double-negative cell counts. Additionally, their defective neddylation leads to perturbed NF- $\kappa$ B signaling during infections, which might limit NF- $\kappa$ B-mediated lymphocyte survival, causing lymphopenia.

*Individuals with NAE1 variants experience neurodegeneration and increased seizure frequency during infections*

All individuals with *NAE1* variants showed brain loss and setbacks in development, mostly related to major hospital admissions due to severe viral respiratory tract infections (**Figures 6A and 6B**). Similarly, seizure frequency worsened after these severe infections. Neddylation is upregulated during several types of cellular stress, including DNA damage,<sup>52,53</sup> hypoxia,<sup>54</sup> and proteotoxic stress.<sup>55</sup> Therefore, we hypothesized that neddylation is sufficient in homeostatic conditions in individuals with *NAE1* variants, but insufficient in conditions that require upregulated neddylation such as physical stress caused by infections, and attempted to test this hypothesis in fibroblasts. It proved difficult to mimic infectious conditions in fibroblasts, and therefore we tried to downregulate the neddylation system instead, to a level where it would already be impaired in homeostatic conditions. We did so by using the neddylation inhibitor MLN4924. We found that *NAE1* deficiency leads to increased sensitivity to MLN4924-mediated cell death in fibroblasts. In PBMCs, we found that while MLN4924 caused decreased cell counts in all donors, this resulted in significantly lower cell count only in individuals with *NAE1* genetic variants (**Figures 6C and 6D**). The increased MLN4924 sensitivity suggests that individuals with *NAE1* variants cannot adequately upregulate their neddylation.

## Discussion

In this work we describe four unrelated individuals with intellectual disability harboring bi-allelic variants in *NAE1*. Reduced NAE1 abundance and decreased ratios of neddylated to non-neddylated cullins in fibroblasts supported pathogenicity. Subsequent phenotypic specificity analysis revealed ischiopubic synchondrosis hypoplasia, infection-triggered lymphopenia, and infection-triggered neurodegeneration as the rarest phenotypic features. We found several pathways involved in endochondral bone remodeling that showed altered expression and downregulated RUNX2 and SOX9 expression. Moreover, we found enhanced cell death in fibroblasts after stressing the system with MG132 and MLN4924. In contrast to healthy controls subject, CD3/CD28 signaling led to decreased lymphocyte counts in individuals with NAE1 variants, which was accompanied by decreased NF- $\kappa$ B translocation. These results provide in-depth support for the pathogenicity of the genetic variants and suggest that NAE1 deficiency impairs homeostasis during cellular stress and leads to disturbances in (skeletal) development.

The pathogenicity of the *NAE1* variants was supported by the significant reduction of NAE1 abundance, resulting in a lower cullin 1<sup>NEDD8</sup>/cullin 1 ratio. The unaltered CUL1 mRNA levels argue against transcriptional regulation, and thus provide indirect support for increased stability of non-neddylated cullins, which are exposed to fewer neddylation cycles.<sup>56</sup> Since cullin function is controlled by cycles of cullin neddylation and deneddylation, maintaining a proper cullin 1<sup>NEDD8</sup>/cullin 1 ratio is crucial to ensure cullin-mediated functions.<sup>57</sup> As fibroblasts of individuals with *NAE1* genetic variants were more sensitive to MG132 treatment, we speculate that the altered cullin 1<sup>NEDD8</sup>/cullin 1 ratio results in proteasome dysfunction. However, it should be noted that non-cullin neddylation targets, which we did not study in this research, might also be involved in the pathophysiology.

Both the neurological and immunological phenotype of individuals with *NAE1* variants reflect impairments in development and stress response. During routine outpatient clinic visits, we found low to normal lymphocyte

counts, but during infections, lymphopenia became more obvious. Lymphocyte survival in resting and activated conditions is partially regulated by NF- $\kappa$ B activation, which in turn is regulated by neddylation.<sup>50</sup> In lymphocytes of individuals with *NAE1* variants, NF- $\kappa$ B activation was severely decreased, which might explain the decreased lymphocyte counts both in resting and activated conditions. Anti-CD3/CD28 signaling requires upregulation of neddylation, which in turn influences activity of many other pathways in T cells.<sup>58</sup> One example is WNT/ $\beta$ -catenin signaling, important for thymic function.<sup>21,59,60</sup> Defective WNT signaling can explain the decreased numbers of naive T cells, as WNT signaling can keep T cells in a naive state, corresponding with low expression of AXIN2 in memory T cells.<sup>61</sup> Moreover, defective WNT signaling and subsequent thymic dysfunction can explain the increased percentages of double-negative (CD4–CD8–) T cells, which might represent immature T cells leaving the thymus prior to complete maturation. Thus, similar to the neurodegeneration, the lymphocyte phenotype might be the result of developmental and stress-mediated defects.

While the stress-mediated neurodegeneration was the most severe phenotypic feature in our cohort, additional neurodevelopmental abnormalities were seen, not related to neurodegeneration. This is not surprising, given the fact that recent evidence indicates that *NAE1* is essential for development, maintenance, and outgrowth of neuronal spines.<sup>10,59,62,63</sup> Regarding the infection-mediated neurodegeneration, several mechanisms might be involved. First, during cellular stress caused by infections, unfolded proteins accumulate, requiring neddylation-mediated Parkin and PINK1 activation<sup>13,64</sup> to break down these unfolded proteins and prevent neuronal apoptosis and brain damage. Dysfunction of these pathways has been implicated in the pathophysiology of Alzheimer and Parkinson disease.<sup>11,12,64</sup> Other pathways are also involved in neuronal integrity, like the neddylation-controlled WNT/ $\beta$ -catenin pathway.<sup>59</sup> Dysfunction of this pathway can result in loss of cell-cell adhesion and neuronal apoptosis.<sup>65</sup> Not only the integrity but also the excitability of neurons during stress is under the control of neddylation.<sup>63</sup> Mice with defective neddylation display decreased Nav1.1 stability during

fever, leading to increased neuronal excitability and epilepsy.<sup>66</sup> Finally, in mice, double-negative T cells can significantly enhance neuroinflammation during brain injury.<sup>67</sup> Therefore, the high numbers of double-negative T cells found in individuals with *NAE1* variants might have enhanced neuroinflammation. Additional experiments using different stressors—preferably in neurons—will be an important step to reliably establish the link between neddylation, stress, and cell death, and how this links to stress-mediated neurodegeneration.

Currently, there is no gold standard how to elucidate pathophysiologic cellular mechanisms leading to a specific phenotype caused by variants of uncertain significance (VUSs). As a result, researchers tend to focus on the most severe clinical phenotypes. Instead, we propose that focusing on information-dense phenotypes could provide more insight in the underlying pathophysiology. In our case, focusing on the most severe phenotypic features would have led us to focus on the neurodegeneration and epilepsy, which probably would have given insight in the mechanism of disease in the brain, but would have overlooked the influence of faulty neddylation on the immune system and (bone) development. Our overarching view led to a clear pattern in lymphocyte values, that dropped significantly during infections, which resembled the neurodegeneration, that similarly worsened during infections. This framework allowed us to delineate the most important pathophysiological mechanism: during stress, neddylation needs to be upregulated, protecting cells from stress. We suspect individuals with *NAE1* variants are unable to adequately upregulate their neddylation for this purpose, resulting in stress-mediated cell death.

Naturally, the complexity and resources needed to discover the pathophysiology of VUSs limits the number of genetic diagnoses that can be made. When considering variants in pleiotropic genes, the wealth of pathways and phenotypic features that can be studied threatens to complicate this process even more. Therefore, smart prioritization is of the essence. This work exemplifies the power of a focus on the most informative features. If validated on a larger scale, this approach could be beneficial for complex VUSs in

genes encoding pleiotropically acting proteins.

In conclusion, this study shows that NAE1 deficiency leads to developmental delay, epilepsy, ischiopubic synchondrosis hypoplasia, and infection-triggered lymphopenia and neurodegeneration. It thereby unveils the importance of proper NAE1 function in facilitating development and suggests a crucial role for neddylation in maintaining cellular homeostasis during cellular stress.

### **Acknowledgements**

This work was supported by the Max Planck Society (D.R.), the VolkswagenStiftung (D.R.), the Agencia Nacional de Promoción Científica y Tecnológica, Argentina (D.R.) and the Fondo para la convergencia estructural del mercosur-FOCEM (COF 03/11) (D.R.). We would like to thank the parents of individual 1 for drafting Figure 6A.

### **Author Contributions**

Concept: P.M.v.H. and I.J.J.M. Designing experiments: I.J.J.M., I.F.S., M.M.v.d.W., C.B., M.L., D.R., F.v.W., S.A.F., E.E.S.N., and P.M.v.H. Conducting experiments: I.J.J.M., I.F.S., M.M.v.d.W., C.B., M.L., N.G.A. Acquiring (medical) data of study participants and cells: I.J.J.M., Y.A.Z., L.V.S., J.B., J.P., M.L.H., J.C.G., S.H., A.H., F.V., M.P.G.M., M.L., P.M.v.H. Analyzing data: I.J.J.M., I.F.S., M.P.G.M., M.M.v.d.W. Genetic testing and interpretation of variants: M.P.G.M., G.v.H. Molecular predictions: M.P.G.M., H.R. Writing the manuscript: I.J.J.M. and P.M.v.H. Supervision of experiments and writing process: P.M.v.H., S.A.F., F.v.W., E.E.S.N., D.R.

S.A.F., D.R., and F.v.W. spent equal time and effort on supervision of the manuscript.

### **References**

1. Kerscher O., Felberbaum R., Hochstrasser M. Modification of proteins by ubiquitin and ubiquitin-like proteins. *Annu. Rev. Cell Dev. Biol.* 2006;22:159–180.
2. Enchev R.I., Schulman B.A., Peter M. Protein neddylation: Beyond cullin-RING ligases. *Nat. Rev. Mol. Cell Biol.* 2015;16:30–44.
3. Whitby F.G., Xia G., Pickart C.M., Hill C.P. Crystal structure of the human ubiquitin-like protein NEDD8 and interactions with ubiquitin pathway enzymes. *J. Biol. Chem.* 1998;273:34983–

- 34991.
- Schulman B.A., Harper J.W. Ubiquitin-like protein activation by E1 enzymes: The apex for downstream signalling pathways. *Nat. Rev. Mol. Cell Biol.* 2009;10:319–331.
  - Walden H., Podgorski M.S., Huang D.T., Miller D.W., Howard R.J., Minor D.L., Holton J.M., Schulman B.A. The structure of the APPBP1-UBA3-NEDD8-ATP complex reveals the basis for selective ubiquitin-like protein activation by an E1. *Mol. Cell.* 2003;12:1427–1437.
  - Malik-Chaudhry H.K., Gaieb Z., Saavedra A., Reyes M., Kung R., Le F., Morikis D., Liao J. Dissecting distinct roles of NEDDylation E1 ligase heterodimer APPBP1 and UBA3 reveals potential evolution process for activation of ubiquitin-related pathways. *Sci. Rep.* 2018;8:10108.
  - Bohnsack R.N., Haas A.L. Conservation in the mechanism of Nedd8 activation by the human AppBp1-Uba3 heterodimer. *J. Biol. Chem.* 2003;278:26823–26830.
  - Wada H., Kito K., Caskey L.S., Yeh E.T., Kamitani T. Cleavage of the C-terminus of NEDD8 by UCH-L3. *Biochem. Biophys. Res. Commun.* 1998;251:688–692.
  - Mendoza H.M., Shen L.N., Botting C., Lewis A., Chen J., Ink B., Hay R.T. NEDP1, a highly conserved cysteine protease that deNEDDylates cullins. *J. Biol. Chem.* 2003;278:25637–25643.
  - Vogl A.M., Phu L., Becerra R., Giusti S.A., Verschueren E., Hinkle T.B., Bordenave M.D., Adrian M., Heidersbach A., Yankilevich P., et al. Global site-specific neddylation profiling reveals that NEDDylated cofilin regulates actin dynamics. *Nat. Struct. Mol. Biol.* 2020;27:210–220.
  - Dil Kuazi A., Kito K., Abe Y., Shin R.W., Kamitani T., Ueda N. NEDD8 protein is involved in ubiquitinated inclusion bodies. *J. Pathol.* 2003;199:259–266.
  - Chen Y., Neve R.L., Liu H. Neddylation dysfunction in Alzheimer’s disease. *J. Cell Mol. Med.* 2012;16:2583–2591.
  - Choo Y.S., Vogler G., Wang D., Kalvakuri S., Iliuk A., Tao W.A., Bodmer R., Zhang Z. Regulation of parkin and PINK1 by neddylation. *Hum. Mol. Genet.* 2012;21:2514–2523.
  - Liu K., Chen K., Zhang Q., Zhang L., Yan Y., Guo C., Qi J., Yang K., Wang F., Huang P., et al. TRAF6 neddylation drives inflammatory arthritis by increasing NF- $\kappa$ B activation. *Lab. Invest.* 2019;99:528–538.
  - Schoppmann S.F., Vinatzer U., Popitsch N., Mittlböck M., Liebmann-Reindl S., Jomrich G., Streubel B., Birner P. Novel clinically relevant genes in gastrointestinal stromal tumors identified by exome sequencing. *Clin. Cancer Res.* 2013;19:5329–5339.
  - Soucy T.A., Dick L.R., Smith P.G., Milhollen M.A., Brownell J.E. The NEDD8 conjugation pathway and its relevance in cancer biology and therapy. *Genes Cancer.* 2010;1:708–716.
  - Delgado T.C., Barbier-Torres L., Zubiete-Franco I., Lopitz-Otsoa F., Varela-Rey M., Fernández-Ramos D., Martínez-Chantar M.L. Neddylation, a novel paradigm in liver cancer. *Transl. Gastroenterol. Hepatol.* 2018;3:37.
  - Zubiete-Franco I., Fernández-Tussy P., Barbier-Torres L., Simon J., Fernández-Ramos D., Lopitz-Otsoa F., Gutiérrez-de Juan V., de Davalillo S.L., Duce A.M., Iruzubieta P., et al. Deregulated neddylation in liver fibrosis. *Hepatology.* 2017;65:694–709.
  - Read M.A., Brownell J.E., Gladysheva T.B., Hottelot M., Parent L.A., Coggins M.B., Pierce J.W., Podust V.N., Luo R.S., Chau V., Palombella V.J. Nedd8 modification of cul-1 activates

- SCF(beta-TrCP))-dependent ubiquitination of IkappaBalpha. *Mol. Cell Biol.* 2000;20:2326–2333.
20. Liakopoulos D., Büsgen T., Brychzy A., Jentsch S., Pause A. Conjugation of the ubiquitin-like protein NEDD8 to cullin-2 is linked to von Hippel-Lindau tumor suppressor function. *Proc. Natl. Acad. Sci. USA.* 1999;96:5510–5515.
  21. Tripathi R., Kota S.K., Srinivas U.K. Cullin4B/E3-ubiquitin ligase negatively regulates  $\beta$ -catenin. *J. Biosci.* 2007;32:1133–1138.
  22. Sugasawa K., Okuda Y., Saijo M., Nishi R., Matsuda N., Chu G., Mori T., Iwai S., Tanaka K., Tanaka K., Hanaoka F. UV-induced ubiquitylation of XPC protein mediated by UV-DDB-ubiquitin ligase complex. *Cell.* 2005;121:387–400.
  23. Liu L., Lee S., Zhang J., Peters S.B., Hannah J., Zhang Y., Yin Y., Koff A., Ma L., Zhou P. CUL4A abrogation augments DNA damage response and protection against skin carcinogenesis. *Mol. Cell.* 2009;34:451–460.
  24. Sobreira N., Schiettecatte F., Valle D., Hamosh A. GeneMatcher: a matching tool for connecting investigators with an interest in the same gene. *Hum. Mutat.* 2015;36:928–930.
  25. Shannon C.E. A mathematical theory of communication. *Bell Syst. Tech. J.* 1948;27:623–656.
  26. Haijes H.A., Jaeken J., van Hasselt P.M. Hypothesis: determining phenotypic specificity facilitates understanding of pathophysiology in rare genetic disorders. *J. Inherit. Metab. Dis.* 2020;43:701–711.
  27. Ten Berg M.J., Huisman A., Van Den Bemt P.M.L.A., Schobben A.F.A.M., Egberts A.C.G., Van Solinge W.W. Linking laboratory and medication data: new opportunities for pharmacoepidemiological research. *Clin. Chem. Lab. Med.* 2007;45:13–19.
  28. Buske O.J., Girdea M., Dumitriu S., Gallinger B., Hartley T., Trang H., Misyura A., Friedman T., Beaulieu C., Bone W.P., et al. PhenomeCentral: a portal for phenotypic and genotypic matchmaking of patients with rare genetic diseases. *Hum. Mutat.* 2015;36:931–940.
  29. The 1000 Genomes Project Consortium. Auton A., Abecasis G.R., Altshuler D.M., Durbin R.M., Abecasis G.R., Bentley D.R., Chakravarti A., Clark A.G., Donnelly P., et al. A global reference for human genetic variation. *Nature.* 2015;526:68–74.
  30. Zerbino D.R., Achuthan P., Akanni W., Amode M.R., Barrell D., Bhai J., Billis K., Cummins C., Gall A., Girón C.G., et al. Ensembl 2018. *Nucleic Acids Res.* 2018;46:D754–D761.
  31. Lek M., Karczewski K., Minikel E., Samocha K., Banks E., Fennell T., et al. Analysis of protein-coding genetic variation in 60,706 humans. *Nature.* 2016;536:285–291.
  32. Karczewski K.J., Francioli L.C., Tiao G., Cummings B.B., Alfoldi J., Wang Q., et al. The mutational constraint spectrum quantified from variation in 141,456 humans. *Nature.* 2020;581:434–443.
  33. Jiang H., Wang F., Dyer N.P., Wong W.H. CisGenome browser: A flexible tool for genomic data visualization. *Bioinformatics.* 2010;26:1781–1782.
  34. Mijnheer G., Lutter L., Mokry M., van der Wal M., Scholman R., Fleskens V., Pandit A., Tao W., Wekking M., Vervoort S., et al. Conserved human effector Treg cell transcriptomic and epigenetic signature in arthritic joint inflammation. *Nat. Commun.* 2021;12:2710.
  35. Li H., Durbin R. Fast and accurate short read alignment with Burrows – Wheeler transform.



- Bioinformatics. 2009;25:1754–1760.
36. Subramanian A., Tamayo P., Mootha V.K., Mukherjee S., Ebert B.L., Gillette M.A., Paulovich A., Pomeroy S.L., Golub T.R., Lander E.S., Mesirov J.P. Gene set enrichment analysis: A knowledge-based approach for interpreting genome-wide expression profiles. *Proc. Natl. Acad. Sci. USA.* 2005;102:15545–15550.
  37. Yu G., Wang L.G., Han Y., He Q.Y. ClusterProfiler: An R package for comparing biological themes among gene clusters. *OMICS A J. Integr. Biol.* 2012;16:284–287.
  38. Yang X., Boehm J.S., Yang X., Salehi-Ashtiani K., Hao T., Shen Y., Lubonja R., Thomas S.R., Alkan O., Bhimdi T., et al. A public genome-scale lentiviral expression library of human ORFs. *Nat Methods.* 2011;8:659–61.
  39. Wiederschain D., Wee S., Chen L., Loo A., Yang G., Huang A., Chen Y., Caponigro G., Yao Y.M., Lengauer C., et al. Single-vector inducible lentiviral RNAi system for oncology target validation. *Cell Cycle.* 2009;8:498–504.
  40. Wee S., Wiederschain D., Maira S.M., Loo A., Miller C., deBeaumont R., Stegmeier F., Yao Y.M., Lengauer C. PTEN-deficient cancers depend on PIK3CB. *Proc. Natl. Acad. Sci. USA.* 2008;105:13057–13062.
  41. Muffels I.J.J., Wiame E., Fuchs S.A., Massink M.P.G., Rehmann H., Musch J.L.I., Van Haften G., Vertommen D., van Schaftingen E., van Hasselt P.M. NAA80 bi-allelic missense variants result in high-frequency hearing loss, muscle weakness and developmental delay. *Brain Commun.* 2021;3:1–32.
  42. Köhler S., Gargano M., Matentzoglou N., Carmody L.C., Lewis-Smith D., Vasilevsky N.A., Danis D., Balagura G., Baynam G., Brower A.M., et al. The human phenotype ontology in 2021. *Nucleic Acids Res.* 2021;49:D1207–D1217.
  43. Ishii A., Watkins J.C., Chen D., Hirose S., Hammer M.F. Clinical implications of SCN1A missense and truncation variants in a large Japanese cohort with Dravet syndrome. *Epilepsia.* 2017;58:282–290.
  44. Kraulis P.J. MOLSCRIPT. A program to produce both detailed and schematic plots of protein structures. *J. Appl. Cryst.* 1991;24(pt 5):946–950. [Google Scholar]
  45. Merritt E.A., Murphy M.E. Raster3D version 2.0 A program for photorealistic molecular graphics. *Acta Crystallogr. D Biol. Crystallogr.* 1994;50:869–873.
  46. Gao X., Li K., Fan Y., Sun Y., Luo X., Wang L., Liu H., Gong Z., Wang J., Wang Y., et al. Identification of RUNX2 variants associated with cleidocranial dysplasia. *Hereditas.* 2019;156:31.
  47. Matsushita M., Kitoh H., Kaneko H., Mishima K., Kadono I., Ishiguro N., Nishimura G. A novel SOX9 H169Q mutation in a family with overlapping phenotype of mild campomelic dysplasia and small patella syndrome. *Am. J. Med. Genet.* 2013;161A:2528–2534.
  48. Wagner T., Wirth J., Meyer J., Zabel B., Held M., Zimmer J., Pasantes J., Bricarelli F.D., Keutel J., Hustert E., et al. Autosomal sex reversal and campomelic dysplasia are caused by mutations in and around the SRY-related gene SOX9. *Cell.* 1994;79:1111–1120.
  49. Ehrentraut S.F., Curtis V.F., Wang R.X., Saeedi B.J., Ehrentraut H., Onyiah J.C., Kelly C.J., Campbell E.L., Glover L.E., Kominsky D.J., Colgan S.P. Perturbation of neddylation-dependent NF- $\kappa$ B responses in the intestinal epithelium drives apoptosis and inhibits resolution of mucosal inflammation. *Mol. Biol. Cell.* 2016;27:3687–3694.

50. Gerondakis S., Siebenlist U. Roles of the NF-kappaB pathway in lymphocyte development and function. *Cold Spring Harb. Perspect. Biol.* 2010;2:a000182.
51. Liapis K., Tsagarakis N.J., Panitsas F., Taparkou A., Liapis I., Roubakis C., Tsokanas D., Vasileiou P., Grigoriou E., Kakiopoulos G., et al. Causes of double-negative T-cell lymphocytosis in children and adults. *J. Clin. Pathol.* 2020;73:431–438.
52. Cui D., Xiong X., Sun Y., Zhao Y. FBXW7 confers radiation survival by targeting p53 for degradation. *SSRN Electron. J.* 2019
53. Nishitani H., Shiomi Y., Iida H., Michishita M., Takami T., Tsurimoto T. CDK inhibitor p21 is degraded by a proliferating cell nuclear antigen-coupled Cul4-DDB1Cdt2 pathway during s phase and after UV irradiation. *J. Biol. Chem.* 2008;283:29045–29052.
54. Ryu J.H., Li S.H., Park H.S., Park J.W., Lee B., Chun Y.S. Hypoxia-inducible factor  $\alpha$  subunit stabilization by NEDD8 conjugation is reactive oxygen species-dependent. *J. Biol. Chem.* 2011;286:6963–6970.
55. Maghames C.M., Lobato-Gil S., Perrin A., Trauchessec H., Rodriguez M.S., Urbach S., Marin P., Xirodimas D.P. NEDDylation promotes nuclear protein aggregation and protects the ubiquitin proteasome system upon proteotoxic stress. *Nat. Commun.* 2018;9:4376.
56. Wu J.T., Lin H.C., Hu Y.C., Chien C.T. Neddylation and deneddylation regulate Cull1 and Cul3 protein accumulation. *Nat. Cell Biol.* 2005;7:1014–1020.
57. Liu Q., Zhou Y., Tang R., Wang X., Hu Q., Wang Y., He Q. Increasing the Unneddylated Cullin1 Portion Rescues the csn Phenotypes by Stabilizing Adaptor Modules To Drive SCF Assembly. *Mol. Cell Biol.* 2018;38:e00109-17.
58. Cheng Q., Liu J., Pei Y., Zhang Y., Zhou D., Pan W., Zhang J. Neddylation contributes to CD4+ T cell-mediated protective immunity against blood-stage Plasmodium infection. *PLoS Pathog.* 2018;14:e1007440.
59. Zhang L., Jing H., Li H., Chen W., Luo B., Zhang H., Dong Z., Li L., Su H., Xiong W.C., Mei L. Neddylation is critical to cortical development by regulating Wnt/ $\beta$ -catenin signaling. *Proc. Natl. Acad. Sci. USA.* 2020;117:26448–26459.
60. Weerkamp F., Baert M.R.M., Naber B.A.E., Koster E.E.L., De Haas E.F.E., Atkuri K.R., van Dongen J.J.M., Herzenberg L.A., Staal F.J.T. Wnt signaling in the thymus is regulated by differential expression of intracellular signaling molecules. *Proc. Natl. Acad. Sci. USA.* 2006;103:3322–3326.
61. Tiemessen M.M., Baert M.R.M., Kok L., van Eggermond M.C.J.A., van den Elsen P.J., Arens R., Staal F.J.T. T cell factor 1 represses CD8 + effector T cell formation and function. *J. Immunol.* 2014;193:5480–5487.
62. Vogl A.M., Brockmann M.M., Giusti S.A., MacCarrone G., Vercelli C.A., Bauder C.A., Richter J.S., Roselli F., Hafner A.S., Dedic N., et al. Neddylation inhibition impairs spine development, destabilizes synapses and deteriorates cognition. *Nat. Neurosci.* 2015;18:239–251.
63. Brockmann M.M., Döngi M., Einsfelder U., Körber N., Refojo D., Stein V. Neddylation regulates excitatory synaptic transmission and plasticity. *Sci. Rep.* 2019;9:17935.

64. Xiong H., Wang D., Chen L., Choo Y.S., Ma H., Tang C., Xia K., Jiang W., Ronai Z., Zhuang X., Zhang Z. Parkin, PINK1, and DJ-1 form a ubiquitin E3 ligase complex promoting unfolded protein degradation. *J. Clin. Invest.* 2009;119:650–660.
65. Chen Y.Z. APP induces neuronal apoptosis through APP-BP1-mediated downregulation of  $\beta$ -catenin. *Apoptosis.* 2004;9(4):415–422.
66. Chen W., Luo B., Gao N., Li H., Wang H., Li L., Cui W., Zhang L., Sun D., Liu F., et al. Neddylation stabilizes Nav1.1 to maintain interneuron excitability and prevent seizures in murine epilepsy models. *J. Clin. Invest.* 2021;131:e136956.
67. Meng H., Zhao H., Cao X., Hao J., Zhang H., Liu Y., Zhu M.S., Fan L., Weng L., Qian L., et al. Double-negative T cells remarkably promote neuroinflammation after ischemic stroke. *Proc. Natl. Acad. Sci. USA.* 2019;116:5558–5563.

### **Supplemental Note: Detailed case reports of individuals with *NAE1* genetic variants.**

#### **Individual 1:**

The first individual is the second child of healthy, Dutch, non-consanguineous parents. During pregnancy, the girl was diagnosed with an aortic coarctation and a ventricular septal defect. After birth, several craniofacial dysmorphias were noted. She has underdeveloped denture and a strikingly asymmetrical palate. During infancy, failure to thrive, generalized hypotonia, mild developmental delay and feeding difficulties were noted. At the age of one she was admitted to the ICU due to a lower respiratory tract infection, which was treated with antibiotics and dexamethasone. This admission was followed by a loss of milestones and a debut of profound therapy resistant epilepsy. Brain MRI, which had been normal, now revealed brain atrophy as evidenced by enlarged ventricles, diminished white matter volume and a thin corpus callosum. Laboratory tests revealed lymphopenia, leukopenia, hyperglycemia, AST, ALT and AF increase, anemia and decreased immunoglobulin levels. Other laboratory values were within normal range. Currently, her development is still severely delayed. She cannot sit without support; she can produce a few sounds but no words.

#### **Individual 2:**

Individual 2, is the first child of healthy, Dutch parents. His parents come from a region with known inbred population and cannot rule out distant

relatedness. During pregnancy, he received multiple blood transfusions due to hemolysis as a result of rhesus incompatibility. At birth, craniofacial dysmorphias were noted: widely spaced eyes, a long small face, cheiloschisis, and an asymmetrical palate. His development was normal until the age of 14-months (rolling over at 7 months, sitting at 10 months). At 14 months, he was admitted to the ICU with severe pneumonia, and he was treated with antibiotics and dexamethasone. After ICU admission his development declined, he could not sit without support anymore. After initial regression, he slowly started to regain some of his developmental progress. Eventually, at two and a half years of age he was able to walk. Brain MRI showed diminished white matter volume, and thin corpus callosum. Laboratory tests revealed mild leukopenia and low immunoglobulin levels (G1, G2, G3 and M). He did not develop normal antibody titers after vaccination. During infections, lymphocytopenia and leukopenia were observed. He has recurrent episodes of Impetigo and HSV-1 infection, which can be severe. Currently, he can sit, walk and communicate verbally (produce complete sentences).

**Individual 3:**

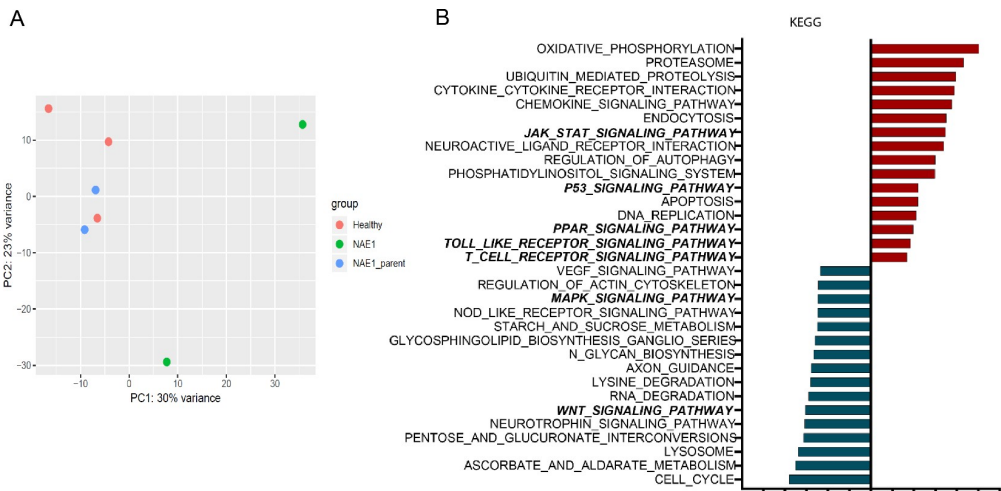
Individual 3 was born as the first child to healthy, consanguineous (first-degree cousins) parents. Pregnancy and birth were unremarkable. As an infant, plagiocephaly, sleep difficulties, hyporeflexia, low muscle tone and spasms were noted. For the spasms, he was first treated with Levetiracetam, but this was ineffective. He was then given ACTH with resolution of the infantile spasms. He had lost developmental milestones with the spasms but regained some of them after 6-weeks of ACTH treatment. His EEG showed interictal tracing with generalized background slowing and multifocal epileptiform discharges. Brain MRI showed severe, diffuse white matter volume loss. At 14 months of age, his development was still delayed. He could roll, but could not sit unassisted, he could say about 3 words with meaning. At 2.5 years of age, he can roll, sit with support, vocalize, and knows parents from strangers. With vigabatrin (113 mg/kg/day), his epilepsy is treated effectively. On physical examination, three small hyperpigmented lesions (right abdomen and left leg) were noted.

**Individual 4:**

Individual 4 was born after normal pregnancy to healthy, non-consanguineous

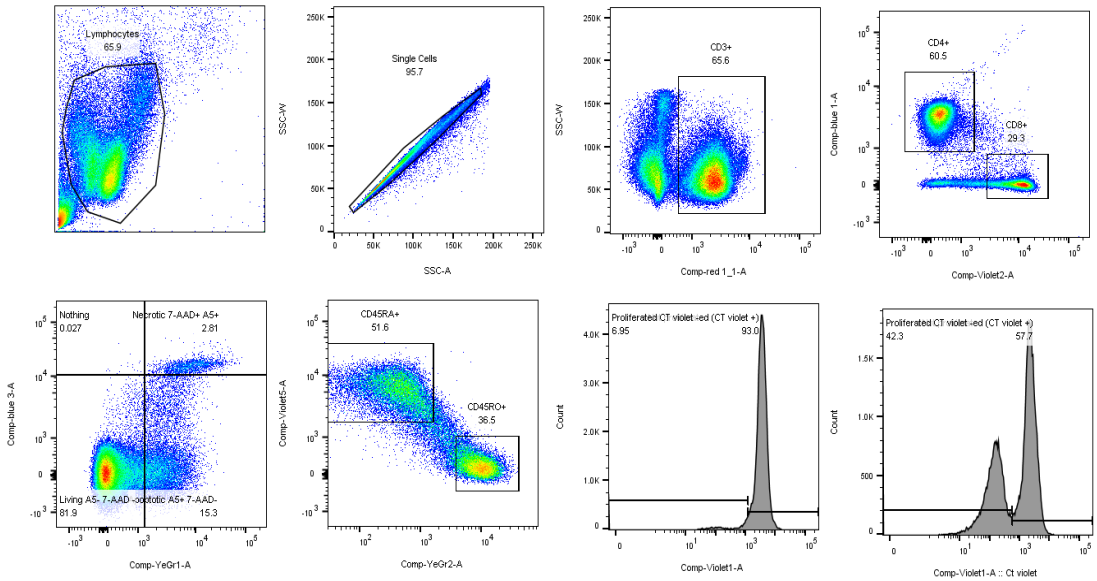
parents. After birth, anteverted nares, large appearing ears, epicanthal folds, narrow palpebral fissures were noted, together with limited range of motion at the elbows, knees and feet. As an infant, she developed epilepsy, and it became clear that her development was severely delayed. Seizures and development worsened significantly during and after infections accompanied by fever. She had multiple respiratory infections, urinary tract infections and bacteremia's, for which she was admitted to the hospital repeatedly. Brain MRI performed at the age of 4.5 years showed progressive global volume loss (compared to earlier brain MRI taken at age 2.5), with marked ventriculomegaly, thinning of the white matter and the corpus callosum, and decreased cerebral cortex volume.

**Figure S1: Analysis of bulk RNA sequencing data.**



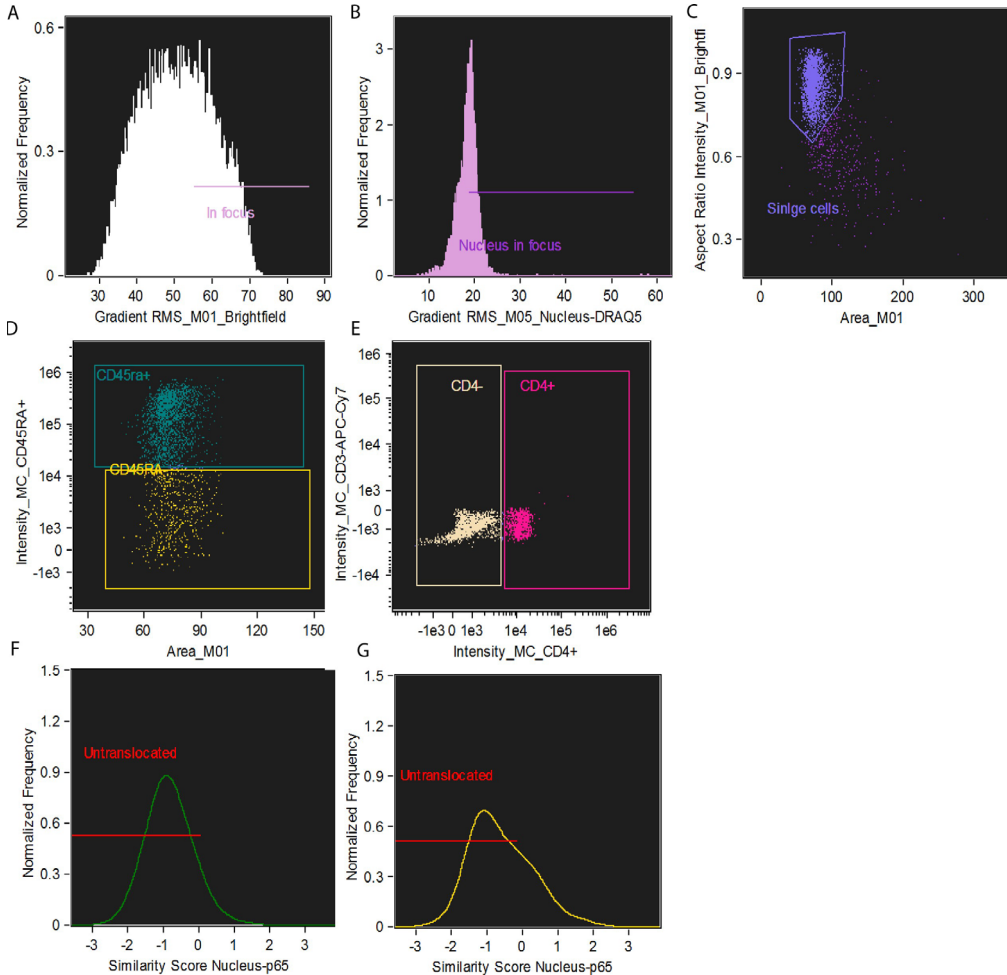
**Figure S1: Analysis of bulk RNA sequencing data of individual 1 and individual 2 dermal fibroblasts, parents of individual 1 (heterozygous carriers), and three healthy controls. (A) PCA plot based on the top 2000 differentially expressed genes. (B) Pre-ranked Gene Set Enrichment analysis showing the top 32 significantly enriched (FDR<0.05) pathways (KEGG). Y-axis shows Normalized Enrichment Score (NES).**

**Figure S2: Gating strategy of flow cytometry experiments.**



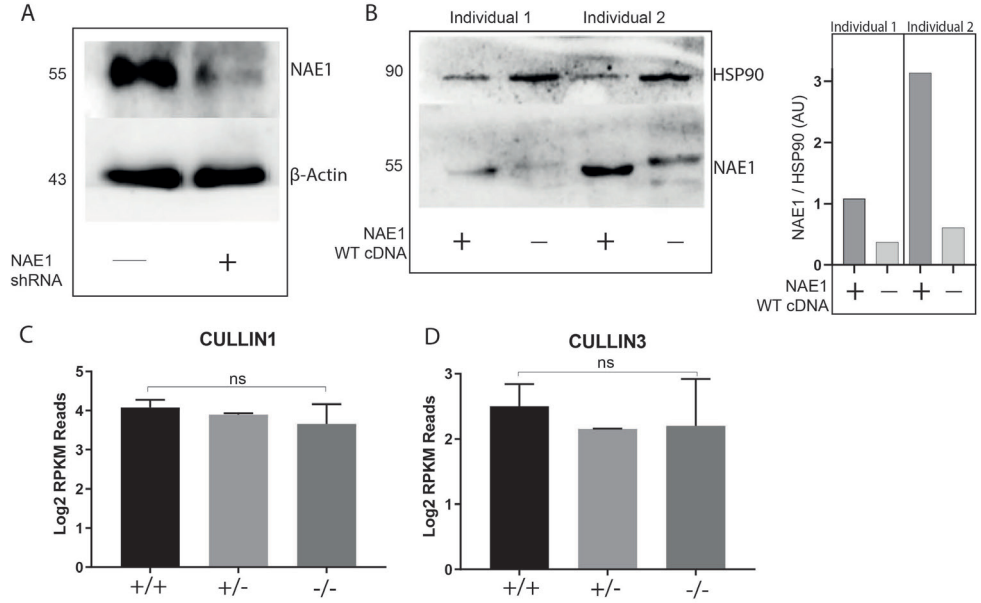
**Figure S2: Flow Cytometry Gating Strategy.** Lymphocytes were gated using FSC-A and SSC-A. Single cells were gated using SSC-A and SSC-W. Next, CD3, CD4, CD8, CD45RA, CD45RO cells were gated. Living cells were gated using Annexin V and 7-AAD staining.

**Figure S3: Imagestream Gating Strategy**



**Figure S3: Imagestream Gating Strategy.** (A) Using the Brightfield channel, cells out of focus were discarded (Gradient\_RMS\_M01). (B) Next, cells in focus in the nuclear channel were gated (Gradient\_RMS\_M05, nuclear channel). (C) Single cells were gated using brightfield Area\_M01 and Aspect\_Ratio\_M01. (D) Next, cells were gated on CD45RA and CD4 expression. (E) The bottom two images show unstimulated CD3 cells (left side, green line). Every similarity score with a value below 0 is gated as untranslocated (red line). (F) The bottom right image shows an example of stimulated CD3+ cells (yellow line).

**Figure S4: Western blots and RNA sequencing data of individuals with *NAE1* genetic variants.**





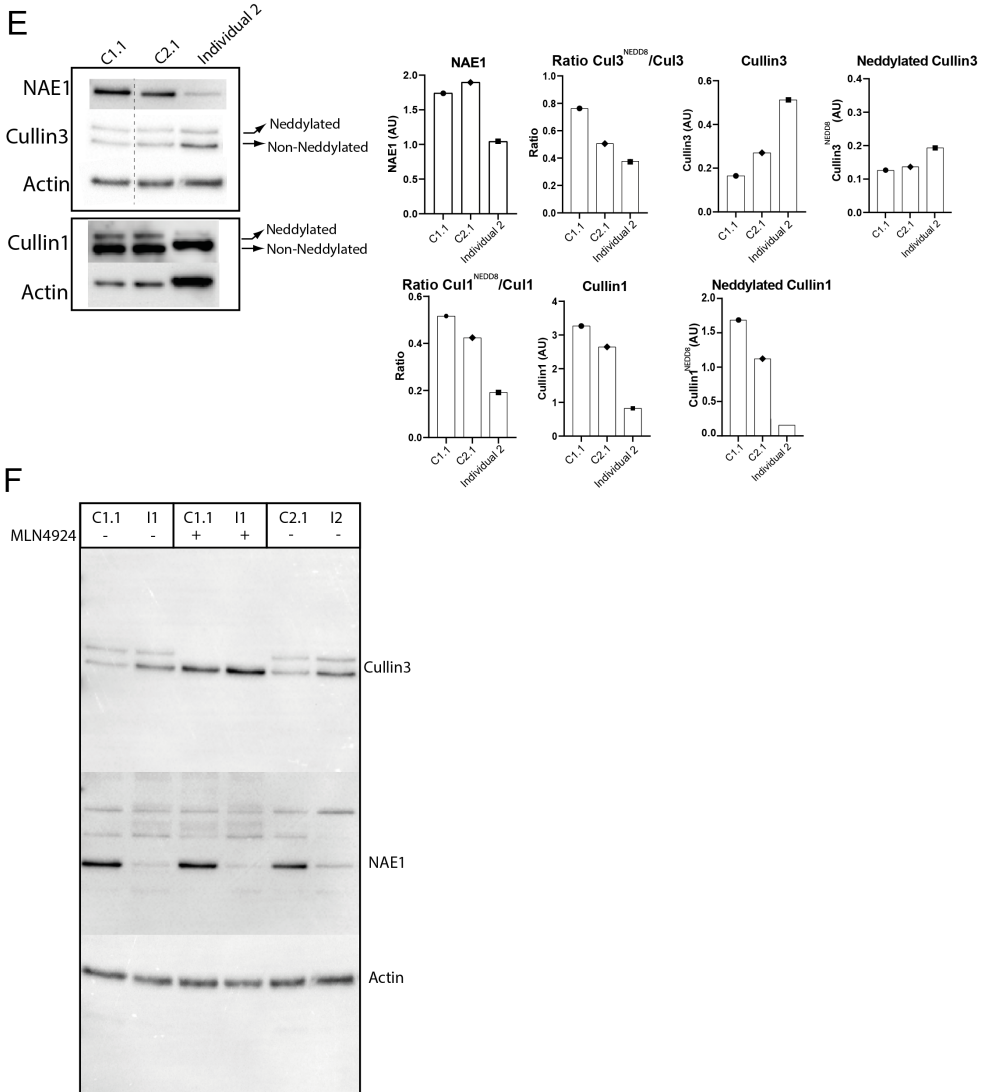


**Figure S4:** (A) Western blot showing NAE1 abundance in heterozygous carriers of *NAE1* genetic variants (parents of individual 1) with and without addition of NAE1 shRNA.  $\beta$ -actin was used as a housekeeper. (B) Western blot showing NAE1 protein levels in individual 1 and individual 2 with and without vector expressing NAE1 wildtype cDNA ('rescue'). HSP90 was used as a housekeeper. The quantification of the blots is shown in bar graphs. Quantification was performed using ImageLab (Biorad). (C, D) CULLIN1 and CULLIN3 log<sub>2</sub> RPKM reads derived from fi-

broblast RNA sequencing data. Bar shows mean log<sub>2</sub> RPKM reads of all donors (+/+ N=3, +/- N=2, -/- N=2). Error bars show SD of the log<sub>2</sub> RPKM reads. (E) Western blot showing cullin1, cullin3 and NAE1 abundance in two controls (C1.1 and C2.1) and individual 2. The bar graphs show the quantification of the blots, all normalized to actin. Quantification was performed using ImageLab. The dotted line indicates where the blots were cut. Quantification was performed using ImageLab. (F) Uncropped blots used for **Figure S4F** (NAE1, actin and cullin3).

**Figure S5: Conservation of the residues altered in individuals with NAE1 genetic variants.**

Q13564 Homo Sapiens	1	MAQLG-KLLKEQKYDRQLRLWGDHGQEALES	AHVCLINATATGTEILKNI	VLP	PGIGSFTI	59	
Q9Z1A5 Rattus Norvegicus	1	MAQQG-KILKEQKYDRQLRLWGDHGQEALES	AHVCLINATATGTEILKNI	VLP	PGIGSFTI	59	
Q8VBW6 Mus Musculus	1	MAQPG-KILKEQKYDRQLRLWGDHGQEALES	AHVCLINATATGTEILKNI	VLP	PGIGSFTI	59	
Q5ZIE6 Gallus Gallus	1	MAQPGRASLKEQRYDRQLRLWGDHGQEALES	AHVCLINATATGTEILKNI	VLP	PGIGSFTI	60	
Q75XP2 Danio Rerio	1	--MTDPKTSKEQKYDRQLRLWGDHGQEALENA	HVCLINATASGTEILKNI	VLP	PGI	58	
Q13564 Homo Sapiens	60	IDGNQVSGEDAGN	NFFLQKSSIGK	RAEAAMEFLQELNS	SDVSGSFVEES	PENLLDNDPSF 119	
Q9Z1A5 Rattus Norvegicus	60	IDGNQVSGEDVGN	NFFLQKCSIGK	RAQAAMEFLQELNS	SDVSGSFVEES	PENLLDNDPSF 119	
Q8VBW6 Mus Musculus	60	IDGNLVSGEDAGN	NFFLQKSSIGK	RAQAAMEFLQELNS	SDVSGSFVEES	PENLLDNDPSF 119	
Q5ZIE6 Gallus Gallus	61	VDGNRVSGEDVGN	NFFLQKSHIGS	RAQSAATELLQELNS	SDVSGNFVEES	PETLLDNDPSF 120	
Q75XP2 Danio Rerio	59	VDGHKVSGEDVGN	NFFLSSAIGK	RAQAATELLQELNS	SDVSGNFVEES	PKLLDNDCEF 118	
Q13564 Homo Sapiens	240	KEDFRDLIRQGIL	KNENGAP	EEENFEEA	AIKNVNTALNTTQIPSSIEDIFNDDRC	INITK 299	
Q9Z1A5 Rattus Norvegicus	240	KEDFRELI	RQGI	KNENGAP	EEENFEEA	AIKNVNTALNTTQIPSSIEDIFNDDRC	INITK 299
Q8VBW6 Mus Musculus	240	KEDFRDLIRQGIL	KNENGAP	EEENFEEA	AIKNVNTALNTTQIPSSIEDIFNDDRC	INITK 299	
Q5ZIE6 Gallus Gallus	241	KEAFRQLIRQGI	LKNENG	TPEEENFEEA	AIKNVNTALNTTKIPRCIEEIFNDDC	VNITK 300	
Q75XP2 Danio Rerio	239	KEAFRQLLREGI	LKNENG	GLEEENFEEA	AIKNVNTALNPTKISSGTDIFNAEQ	ENITS 298	
Q13564 Homo Sapiens	420	DNEIVLYLMLRA	VDRFHKQGRYPGV	SNYQVEEDIGK	LKSCLTGFLQEYGLSVMVKDDYV	479	
Q9Z1A5 Rattus Norvegicus	420	DNEIVLYLMLRA	VDRFHKQHGRYPGV	SNYQVEEDIGK	LKSCLTGFLQEYGLSVMVKDDYV	479	
Q8VBW6 Mus Musculus	420	DNEIVLYLMLRA	VDRFHKQHGRYPGV	SNYQVEEDIGK	LKSCLTGFLQEYGLSVMVKDDYV	479	
Q5ZIE6 Gallus Gallus	421	DSEVVLVYLM	RAVDRFYKHGRYPGV	YNYQVEDDIGK	LKSCLTSFLQEHGLSVLVKDDYV	480	
Q75XP2 Danio Rerio	419	DSEMVLVYLM	RSVDRFYQHSRYPGV	YNYQVEEDINK	LKLCVNSLLQEYSLNVVVKDDYI	478	

**Figure S5:** Showing conservation of the residues altered in individuals with NAE1 variants: Leu49, (top row), Arg85 (second row), Cys294 (third row) and Arg430 (bottom row). All residues are conserved in other species (rat, mouse, chick, zebrafish) that express NAE1 (ULA1).

**Figure S6: Proliferation levels are similar between individuals and healthy controls.**

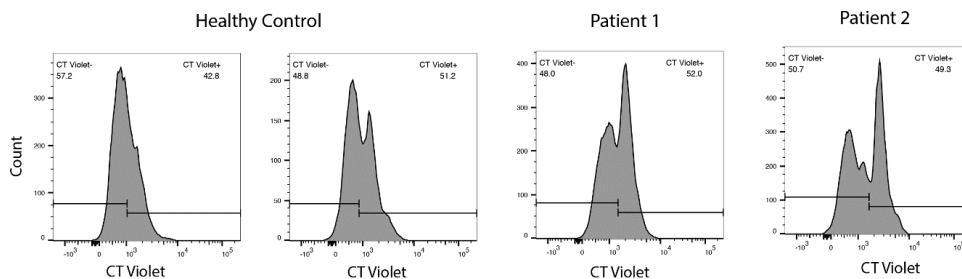


**Figure S6:** CD3+ lymphocytes were stained with 2uM CellTrace Violet (Thermofisher) and stimulated with soluble anti-CD3+ (Life technologies, clone OKT3) and anti-CD28+ (Thermofisher) at 1 ug/ml for 3 days. With every cell division, the intensity of CellTrace Violet diminishes. Gating was performed based on the CT violet staining intensity at day zero. Proliferation was similar in healthy controls and individuals with *NAE1* genetic variants (p=0.5).

**Figure S7: Representative example of microscopic images taken after MG132 treatment in a healthy control and individual 1.**

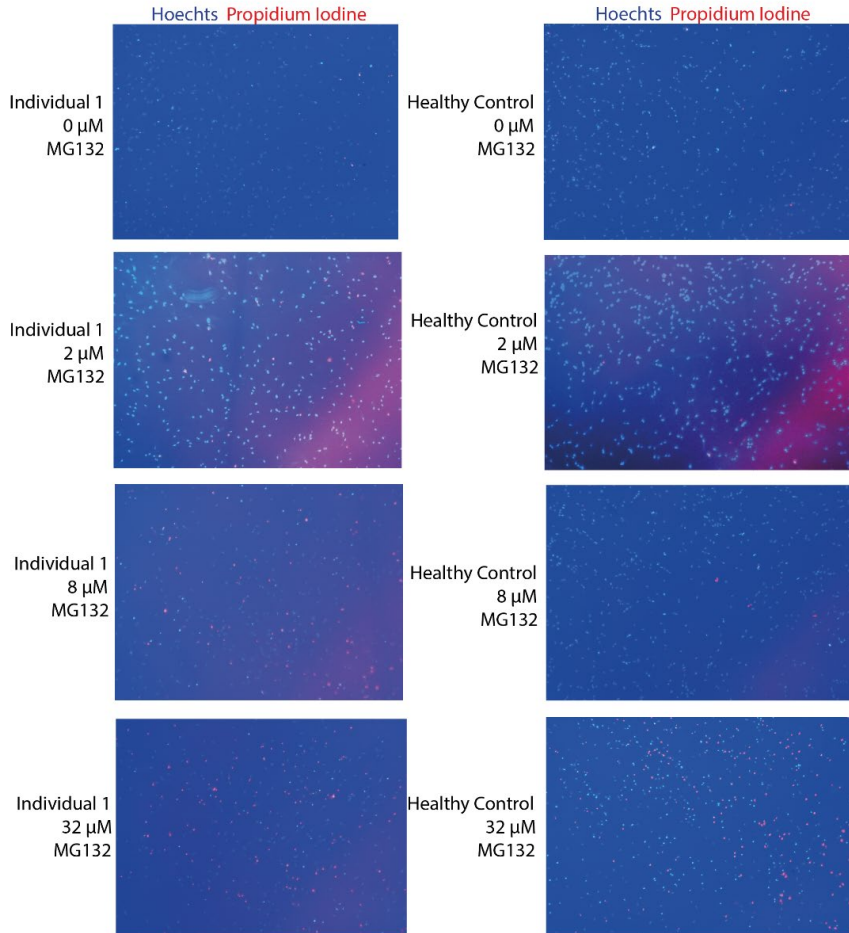


**Figure S7:** Representative example of microscopic images taken after MG132 treatment in a healthy control and individual 1. Staining was performed by incubating fibroblasts with Hoechts (1:2000) and PI (1:20) for 5 minutes. Cell death was calculated by dividing the number of PI positive cells by the total number of cells.

**Table S1: Overview of genetic variants identified with WES (after filtering) in individual 1.**

Gene	Mode of inheritance	Variant	GnomAD	CADD Score	PolyPhen-2	Mutation Taster	Prediction
<i>NAE1</i>	Compound heterozygous	NM_003905.4: c.147G>C p.Leu49Phe Nonsynonymous	pLI=0, 1x reported in GnomAD.	31.	Probably damaging (0.99).	Disease Causing Might Introduce splice site changes.	Variant of Unknown Significance
<i>NAE1</i>	Compound heterozygous	NM_003905.4: c.254G>A, p.Arg85Gln Nonsynonymous	pLI=0, 4x reported in GnomAD.	24	Probably Damaging (0.99).	Disease Causing	Variant of Unknown Significance
<i>TASOR</i>	Compound heterozygous	NM_001112736.2 c.1840T>A, p.Leu614Ile Nonsynonymous	pLI=1 Reported 318x in GnomAD. MAF $\geq$ 0.001	23.1	Possibly Damaging (0.615).	Disease Causing	Benign (BS1, BS2)
<i>TASOR</i>	Compound heterozygous	NM_001112736.2 c.3094A>G p.Ile1032Val Nonsynonymous	pLI = 1. Reported 36x in GnomAD. MAF <0.001.	16	Benign (0.003).	Polymorphism.	Benign (BS1, BS2)
<i>PIWIL2</i>	De Novo	NM_00113572.1 c.1899C>T, p.Gly633=, Synonymous	pLI=0.	10.5	NA	Disease Causing, introduces a cryptic splice site	Likely benign (BP1, BP5).
<i>DPY19L4</i>	De novo	NM_181787.3 c.1338T>C p.Gly446= Synonymous	GnomAD: pLI=0 3x reported: other missense variant at the same AA position	3.5	NA	Disease Causing, Introduces Splice site changes.	Likely benign (BP1, BP5)

**Table S1:** Overview of genetic variants identified after filtering in individual 1 with Whole Exome Sequencing (WES). Filtering methods can be found in the methods section. The genetic variants are sorted based on Combined Annotation Dependent Depletion (CADD) score (high-low). The ‘Prediction’ Column represents the likelihood of pathogenicity based on the “Standards and Guidelines for the Interpretation of Sequence Variants” drafted by the American College of Medical Genetics and Genomics (ACMG).<sup>1</sup> Additionally, MutationTaster<sup>2</sup>, PolyPhen-2<sup>3</sup>, CADD<sup>4</sup> score and GnomAD constraint metrics<sup>5</sup> (Probability of loss of function intolerance, pLI) were used. To indicate the likelihood of pathogenicity, we employed a color scheme. For CADD scores, values 0-10 were colored green, 10-20 were colored yellow and values >20 were colored red. For Polyphen-2, probably damaging was colored red, possible damaging was colored yellow and benign was colored green. For MutationTaster, ‘Disease Causing variants’ were colored red and ‘polymorphisms’ were colored green. In the column showing the predictions using the ACMG guidelines, a Variant of Unknown Significance was colored red and likely benign was colored green. Based on these predictions and functional studies, the *NAE1* genetic variants were considered likely pathogenic.

**Table S2: Comparison of the phenotype of individuals with Dravet syndrome (MIM: 607208) caused by SCN1A mutations to the phenotype of individual 4 from the NAE1 cohort.**

Phenotypic Feature	Dravet Syndrome	Individual 4	Cohort of individuals with NAE1 genetic variants
Short stature	-0.5 SDS	-5.0 SDS	-1, -1.5, -2.3 SDS
Microcephaly	+	-	-
<b>Facial abnormalities</b>	-	+	+
Wide nasal bridge	-	+	+
Long philtrum	-	+	+
Anteverted nares	-	+	+
Large ears	-	+	+
Epicanthal folds	-	+	+
Narrow palpebral fissures	-	+	-
Thick lower lip vermillion	-	+	-
Broad Philtrum	-	+	+
Lymphopenia	-	+	+
<b>Other</b>			
Recurrent infections	-	+	+
Ischiopubic hypoplasia	-	+	+
<b>Neurological Abnormalities</b>	+	+	+
Seizures	+	+	+
Seizure onset in the first year of life	+	NA	+
Seizure triggered by fever	+	+	+
Psychomotor development stagnates.	+	+	+
Mental decline	+	+	+
Behavioral problems	+	-	-
Learning disabilities	+	+	+
Global brain atrophy on MRI	+	+	+
EEG with irregular generalized spike and wave complexes	+	NA	-
Microcephaly	+	-	-
Ataxia	+	NA	-
Limited knee extension	+	+	-
Muscle Weakness	+	NA	+
Dysgenesis of the hippocampus	+	+	+

**Table S2:** In individual 4, both a heterozygous truncating variant in *SCN1A* as well as a genetic variant in *NAE1* were identified. To distinguish the clinical phenotype caused by each of the genetic variants, the phenotypic features of Dravet syndrome<sup>6</sup> (MIM: 607208) were compared to all phenotypic features observed in individual 4. Truncating *SCN1A* variants result mostly in Dravet syndrome. As individual 4 has a truncating variant in *SCN1A*, features of Dravet syndrome were used for comparison. The characteristic facial features, short stature, lymphopenia, frequent infections and ischiopubic hypoplasia have never been identified in Dravet disease, and therefore suggest an additional role for the genetic variants in *NAE1* in disease pathophysiology.

**Table S3: List of 24 most specific phenotypes (with the highest occurrence ratio).**

HPO code	HPO name	Associated genes	Individual1	Individual2	Individual3	Individual4	Percentage of cohort	Occurrence Ratio
HP:0008822	Hypoplastic ischiopubic rami	1	X	X	X	X	100	100
HP:0006834	Developmental stagnation at onset of seizures	1	X	-	X	X	75	75
HP:0410256	Infection associated lymphopenia	1	X	X	-	X	75	75
HP:0031397	Reduced proportion of naive T cells	1	X	X	NA	NA	50	50
HP:0030887	Increased lymphocyte apoptosis	1	X	X	NA	NA	50	50
HP:0410255	Transient lymphopenia	2	X	X	X	-	75	37.5
HP:0030374	Decreased proportion of	2	X	X	X	NA	50	25
HP:0025539	Abnormal B cell subset distribution	2	X	X	NA	NA	50	25
HP:0031869	Recurrent joint dislocation	4	X	X	NA	NA	50	12.5
HP:0007281	Developmental stagnation	12	X	X	X	X	100	8.3
HP:0002265	Large fleshy ears	11	X	X	-	X		6.81
HP:0003173	Hypoplastic pubic bone	15	X	X	X	X	100	6.66
HP:0010975	Abnormal B cell count	9	X	X	NA	NA	50	5.55
HP:0001041	Facial erythema	6	X	-	-	-	25	4.16
HP:0045025	Narrow palpebral fissure	39	X	X	X	X	100	2.56
HP:0007874	Almond-shaped palpebral fissure	41	X	X	X	X	100	2.44
HP:0002344	Progressive neurologic deterioration	43	X	X	X	X	100	2.32
HP:0200005	Abnormal shape of the palpebral fissure	44	X	X	X	X	100	2.27
HP:0002850	Decreased circulating total IgM	26	X	X	NA	NA	50	1.92
HP:0009103	Aplasia/hypoplasia involving the pelvis	57	X	X	X	X	100	1.754
HP:0025540	Abnormal T cell subset distribution	33	X	X	NA	NA	50	1.51
HP:0002180	Neurodegeneration	77	X	X	X	X	100	1.75
HP:0011839	Abnormal T cell count	46	X	X	X	X	50	1.08
HP:0001888	Lymphopenia	107	X	X	NA	NA	50	0.70

**Table S3:** Overview of the most specific phenotypes as depicted in Figure 3. The first two rows represent the phenotype and the HPO codes attached to the phenotype name. The third

column shows the number of genetic diseases associated with the phenotype, as assessed using the Human Phenotype Ontology.<sup>7</sup> Columns four to seven show which individuals display the phenotype, X means the phenotype is present, - means the phenotype is not present, and NA means the phenotype was not assessed. If the phenotype was not assessed, it was considered 'not present' for the calculation of column 8 (percentage). The occurrence ratio is the value of column 8 divided by the value of column 3.

**Table S4: Overview of primers used for this study.**

Construct	Targeting sequence
NAE1 Tet-PkLo-Puro	5'-CCGGAGTCCTATGATTTGGATCACTCGAGTGATCCAATCATAGGACTTTTTTG54-3'
pLenti-CMV-Puro NAE1	5'-GAATTCTGCAGTCGACATGGCGCAGCTGGGA-3' 3'-GCTGTCTAGACTCGAGCTACAACCTGGAAAGTTGCTGAAGT-5'
NAE1 sequencing primer	5'-GGCTCCAGAAGATGAAGAGAA-3'
Piko-tet-on sequencing Primer	5'-ATTACGCCAAGGTCGACTTAACCCT-3'



**Table S5: Overview of significantly up- and downregulated genes identified with RNA sequencing.**

Gene	Adjusted p-value	Z-Score HC1	Z-Score HC2	Z-Score HC3	Z-Score Father	Z-Score Mother	Z-Score Individual1	Z-score Individual2	Log2 Fold Change I1	Log2 Fold Change I2
ADA2	0.03585676	2.176	-0.55	0.03	-0	-0.364	-0.65	-0.637	-2.639	-2.542
ADAMTS8	0.02301275	-0.46	2.224	-0.093	-0.34	-0.154	-0.589	-0.589	-5.763	-5.763
ADAMTSL4	1.72E-05	1.018	-0.45	0.607	0.364	0.9949	-1.08	-1.45	-1.852	-3.202
AKAP6	0.02207786	0.955	-0.51	1.393	0.765	-0.873	-1.011	-0.72	-3.498	-1.815
AKR1C2	0.0456592	2.159	0.146	-0.443	-0.04	-0.604	-0.668	-0.555	-5.456	-2.796
AMOT	0.01333326	-0.2	1.246	-0.325	0.07	1.3758	-1.247	-0.922	-2.028	-1.354
AMPH	0.04072475	0.044	1.687	-0.47	1.026	-0.525	-1.041	-0.721	-7.565	-2.098
ARHGAP45	0.00015617	-0.14	-0.45	0.318	1.902	0.3394	-0.985	-0.985	-6.492	-6.492
ATP2A3	0.00727996	0.551	-0.43	1.644	0.781	-0.693	-0.94	-0.917	-6.185	-5.004
AXIN2	7.88E-05	1.456	-0.01	-0.693	1.262	-0.127	-0.995	-0.895	-7.993	-3.713
B4GAT1	0.03114516	0.877	0.481	0.665	-0.57	1.0486	-1.288	-1.215	-1.381	-1.29
BMPER	0.00775421	0.129	1.917	0.289	-0.27	0.0078	-1.041	-1.035	-1.391	-1.38
BOC	0.03355107	0.17	0.501	0.028	-0.14	1.7381	-1.307	-0.984	-1.381	-1.009
BTN3A2	0.04321401	0.16	0.479	-0.101	0.302	1.576	-1.555	-0.861	-6.624	-1.526
C20orf96	0.04361249	0.783	0.161	0.858	0.225	0.7691	-1.21	-1.587	-1.513	-2.238
CAMK2N1	1.10E-07	1.311	0.661	0.231	-0.04	0.4884	-1.469	-1.18	-2.948	-1.971
CASZ1	0.04958066	1.869	0.138	-0.167	0.326	-0.029	-1.253	-0.885	-5.171	-2.054
CD302	0.03355107	0.402	1.123	-0.255	0.533	0.728	-1.763	-0.768	-3.48	-1.032
CD82	0.0109587	-0.48	1.155	0.757	0.38	0.716	-1.309	-1.222	-2.01	-1.815
CDH4	0.00292178	1.496	0.196	0.567	0.445	-0.192	-1.338	-1.173	-1.572	-1.337
CDK18	0.0437208	-0.05	-0.45	2.194	0.018	-0.571	-0.579	-0.567	-7.312	-5.591
CDON	0.03061071	0.047	0.282	-0.07	-0.5	2.0023	-0.66	-1.106	-1.368	-3.08
CELSR1	0.04874031	-0.09	1.598	-0.73	0.048	1.0595	-0.966	-0.92	-4.376	-3.628
CHRD	0.00138544	0.509	0.241	-0.745	1.293	0.9565	-1.127	-1.127	-5.823	-5.823
CILP2	0.00281157	0.251	0.181	1.61	-0.45	0.6964	-1.146	-1.146	-6.088	-6.088
CLEC2A	0.01419896	0.816	-0.13	-0.691	1.902	-0.516	-0.691	-0.691	-8.302	-8.302
CLEC2B	0.00013394	1.331	-0.13	-0.603	1.504	-0.434	-0.892	-0.773	-5.977	-3.167
CLMN	0.01653896	-0.39	0.277	-0.228	2.129	-0.315	-0.737	-0.737	-3.946	-3.946
CNNM1	0.02807154	-0.93	0.906	1.501	0.544	-0.155	-0.932	-0.932	-5.224	-5.224
COL10A1	0.04153762	0.238	-0.02	-0.071	2.058	-0.493	-0.854	-0.854	-5.363	-5.363
COL6A3	0.00051898	0.45	1.023	0.89	-0.25	0.5322	-1.087	-1.559	-1.179	-1.843
COL7A1	0.01159841	1.196	-0.52	-0.273	0.799	1.0304	-0.99	-1.244	-1.426	-1.939
COL8A2	6.74E-05	0.3	1.03	1.232	0.39	-0.592	-1.032	-1.329	-1.895	-3.007
COX7A1	0.00021423	1.263	0.053	-0.003	1.37	-0.609	-1.005	-1.069	-2.699	-3.113
CPXM2	1.53E-06	1.858	-0.14	0.772	-0.34	-0.284	-0.896	-0.964	-3.008	-3.69
CRYBG1	1.25E-05	1.415	0.673	-0.477	0.157	0.6258	-1.331	-1.062	-3.856	-2.269
CSPG4	4.54E-06	1.455	0.557	-0.062	0.748	-0.279	-1.155	-1.264	-1.826	-2.093
CTSK	0.00991428	1.517	0.937	-0.392	-0.09	0.272	-1.313	-0.927	-1.732	-1.138
CYB5R2	0.00018635	0.077	-0.14	0.266	2.004	-0.315	-0.964	-0.927	-3.368	-3.039
DENND2A	1.57E-05	0.022	1.138	-0.357	1.584	-0.46	-0.963	-0.963	-7.599	-7.599
DGCR6	0.01241277	0.649	0.592	-0.447	0.856	0.9454	-1.175	-1.422	-2.489	-4.097
DHCR24	0.0036859	1.391	1.009	-0.86	0.036	0.4522	-0.858	-1.169	-1.653	-2.735
DHRS13	0.00074085	-0.01	-0.08	1.46	0.653	0.4879	-1.405	-1.106	-4.925	-2.439

# NAE1 VUS

DNM1	2.43E-05	-0.17	0.635	1.552	-0.45	0.6647	-1.206	-1.031	-3.422	-2.403
DPF3	0.02310761	-0.36	0.612	1.61	-0.6	0.7196	-0.803	-1.172	-1.717	-3.481
DPYSL3	0.00052457	1.565	0.385	0.227	0.638	-0.503	-1.065	-1.247	-1.48	-1.824
ECM1	0.00697725	1.849	0.074	0.096	-0.03	0.234	-0.973	-1.251	-1.14	-1.527
EFNA5	0.00839476	0.083	1.308	-0.642	-0.64	1.482	-0.796	-0.796	-5.849	-5.849
EGR2	0.0332212	-0.53	0.082	2.015	0.489	-0.651	-0.703	-0.703	-5.909	-5.909
ELOVL2	0.01862053	-0.39	1.233	-0.2	-0.32	1.5545	-1.012	-0.861	-6.66	-3.089
ENPP1	0.00292178	-0.66	1.1	-0.081	1.528	0.081	-1.174	-0.792	-4.632	-1.866
EPHB2	0.00697725	-0.47	1.723	0.152	-0.23	0.8284	-1.133	-0.876	-2.866	-1.828
ERMP1	0.00338071	0.918	0.855	-0.356	1.032	0.0769	-1.403	-1.122	-1.87	-1.395
FBLN7	1.66E-05	0.08	-0.29	-0.149	0.739	1.751	-1.047	-1.086	-2.601	-2.806
FGF9	0.00396068	-0.8	1.879	-0.116	0.656	0.0455	-0.834	-0.834	-6.476	-6.476
FHOD3	0.02506544	1.644	-0.43	0.432	0.827	-0.529	-0.785	-1.16	-1.301	-2.215
FMNL1	0.04321401	0.57	0.232	-0.196	1.356	0.6152	-1.434	-1.144	-2.831	-1.898
FST	0.01419896	-0.67	-0.44	0.115	1.445	1.303	-0.984	-0.772	-2.295	-1.599
GDF6	0.01862053	1.94	0.668	-0.122	-0.34	-0.442	-0.94	-0.761	-2.429	-1.739
GJA1	0.00164499	1.305	0.431	0.504	-0.06	0.4501	-1.015	-1.619	-1.103	-1.963
GJD3	0.04361249	0.547	-0.21	0.473	-0.16	1.6578	-1.153	-1.153	-7.004	-7.004
GPR153	0.01121289	0.473	-0.18	0.888	0.145	1.2314	-1.548	-1.012	-1.995	-1.165
GPR3	0.04432331	0.735	0.098	0.455	0.688	0.8556	-1.538	-1.293	-6.739	-3.001
GRIA1	4.54E-06	2.16	-0.35	0.136	-0.08	-0.508	-0.692	-0.674	-7.954	-5.479
HAS2	0.00775421	0.18	0.626	-0.43	1.703	0.0595	-0.749	-1.389	-1.178	-2.855
HECW1	0.0129608	0.61	0.89	-0.267	1.396	-0.293	-1.214	-1.122	-4.566	-3.398
HHIPL1	0.00164664	1.345	0.042	-0.058	0.079	1.0455	-1.428	-1.024	-2.485	-1.509
HLA-B	0.04072475	0.035	-0.91	1.304	-0.12	1.4044	-0.757	-0.952	-1.609	-2.261
HR	1.81E-06	0.705	-0.51	0.843	0.402	1.0836	-1.319	-1.209	-3.397	-2.739
ICAM5	0.01623189	-0.42	-0.47	1.543	-0.24	1.2971	-0.793	-0.926	-2.26	-3.101
IER5	0.00238366	-0.23	0.365	1.121	0.002	1.1973	-1.462	-0.993	-2.165	-1.288
IL15RA	0.0246276	0.462	-0.42	0.334	-0.3	1.8664	-1.098	-0.849	-3.658	-2.099
IL18	0.03631202	-0.18	-0.56	0.023	2.186	-0.167	-0.651	-0.651	-6.24	-6.24
IL1RAP	0.03585676	1.432	0.368	-0.751	0.437	0.706	-1.379	-0.812	-2.255	-1.132
IPMK	0.03013895	0.584	1.489	0.38	-0.19	0.2565	-1.382	-1.133	-1.683	-1.313
IRS2	0.01862053	0.023	-0.52	0.78	0.449	1.5347	-1.144	-1.118	-1.359	-1.323
ISM2	0.0202337	-0.72	-0.54	1.414	1.457	-0.168	-0.722	-0.722	-6.275	-6.275
KCNB1	0.01619268	1.485	0.518	0.644	0.337	-0.925	-1.14	-0.918	-5.846	-2.663
KCNC3	0.00021423	1.386	0.141	1.145	-0.14	-0.21	-1.159	-1.159	-6.319	-6.319
KCNIP3	0.01862053	1.441	0.255	1.003	-0.04	-0.334	-1.044	-1.284	-1.342	-1.745
KCNS1	6.95E-05	0.158	0.62	0.73	1.028	0.2673	-1.402	-1.402	-6.918	-6.918
KIAA1549	0.00991428	0.719	0.825	1.36	0.051	-0.831	-1.014	-1.11	-1.945	-2.252
KIAA1958	0.00309789	0.78	0.89	0.519	0.451	0.1639	-1.112	-1.692	-1.071	-1.766
KRTAP1-1	0.03197017	1.818	0.275	0.597	-0.32	-0.356	-1.073	-0.939	-8.311	-3.408
LAMB1	0.01862053	0.949	1.271	-0.777	0.08	0.6727	-1.167	-1.03	-1.278	-1.113
LAPTM5	0.00641507	-0.13	-0.45	-0.418	2.159	0.1857	-0.673	-0.673	-6.67	-6.67
LGALS9	0.00248602	-0.4	0.746	0.434	1.649	-0.29	-1.071	-1.071	-5.793	-5.793
LIN7A	0.04432331	2.073	-0.44	-0.389	-0.4	0.5102	-0.559	-0.788	-1.895	-3.897
LINC00707	0.00564295	0.873	1.275	-0.915	0.938	-0.256	-0.957	-0.957	-6.862	-6.862

## Chapter 3

LINC00900	0.04958066	2	0.236	-0.577	0.319	-0.29	-0.844	-0.844	-5.003	-5.003
LINC01139	0.03374528	-0.82	0.779	1.487	0.854	-0.66	-0.82	-0.82	-7.353	-7.353
LOC101927809	0.01513948	-0.1	-0.17	2.032	-0.09	0.2139	-0.943	-0.943	-8.35	-8.35
LOXL4	1.72E-05	-0.01	1.773	0.832	-0.12	-0.555	-0.925	-0.993	-2.493	-2.886
LRIG1	0.00543979	-0.91	0.971	0.164	1.12	0.7954	-1.182	-0.958	-2.612	-1.836
LRP11	0.00157294	0.043	1.164	-0.263	0.679	0.9164	-1.426	-1.113	-1.478	-1.111
LTBP4	1.26E-07	0.49	-0.08	1.188	0.147	0.9016	-1.231	-1.412	-2.246	-2.948
LUM	2.90E-05	0.085	0.692	0.879	0.72	0.4362	-1.204	-1.607	-1.198	-1.703
MAF	0.00011392	2.119	0.027	-0.444	0.2	-0.422	-0.769	-0.711	-7.528	-4.071
MAN1A1	0.01862053	-0.03	1.627	-0.37	-0.05	0.9217	-1.339	-0.754	-2.432	-1.13
MAOA	0.03061071	0.342	0.27	-0.721	2.01	-0.458	-0.721	-0.721	-6.003	-6.003
MARCH9	0.00569747	1.925	-0.69	0.298	-0.13	0.3667	-0.953	-0.819	-7.408	-3.208
MATN2	0.00056662	1.149	0.553	-0.709	0.053	1.1676	-0.942	-1.272	-1.804	-3.108
MC4R	0.01862053	2.244	-0.23	-0.446	-0.12	-0.46	-0.493	-0.493	-9.408	-9.408
MDFI	0.02506544	-0.65	1.288	-0.391	1.575	-0.261	-0.779	-0.779	-6.459	-6.459
MDK	0.03252576	-0.48	0.114	1.55	0.674	0.3615	-0.716	-1.503	-1.135	-3.544
MEIS2	0.00991428	0.349	0.827	-0.374	-0	1.5044	-0.896	-1.41	-1.048	-1.798
MFSD10	0.02858347	1.163	-0.46	0.776	0.853	0.1537	-1.213	-1.288	-1.054	-1.106
MGARP	0.02722563	1.846	-0.25	-0.042	-0.13	0.6218	-1.17	-0.868	-8.546	-2.366
MMP11	0.01544699	-0.35	-0	1.007	0.366	1.3574	-1.356	-1.026	-6.564	-2.409
MOCOS	3.81E-05	-0.01	-0.12	-0.022	2.126	-0.317	-0.81	-0.842	-3.02	-3.352
MPP4	0.00248602	2.104	0.216	-0.557	0.1	-0.446	-0.709	-0.709	-6.468	-6.468
MSL2	0.00874296	0.4	0.877	0.332	0.654	0.6091	-1.567	-1.306	-1.235	-1.014
MSTN	3.01E-06	-0.37	2.117	0.316	-0.27	-0.296	-0.748	-0.748	-9.181	-9.181
MTSS1L	0.00961871	0.4	-0.21	0.528	0.118	1.5675	-0.912	-1.487	-1.041	-1.871
MX1	0.00697725	1.941	-0.53	0.727	-0.08	-0.625	-0.756	-0.679	-6.608	-3.595
MXRA5	7.27E-05	0.767	1.428	-0.459	-0.01	0.6027	-0.964	-1.367	-1.851	-3.772
MYLK	0.02506544	2.085	0.075	0.124	-0.3	-0.279	-0.794	-0.915	-1.383	-1.654
MYRIP	0.01755076	2.242	-0.2	-0.241	-0.23	-0.518	-0.526	-0.526	-7.39	-7.39
NA	9.99E-06	-0.23	-0.27	0.585	1.639	0.5402	-1.107	-1.152	-3.073	-3.415
NA	0.00814197	1.089	-0.13	0.909	-0.44	0.958	-1.147	-1.242	-2.03	-2.318
NA	0.01898174	0.283	0.775	-0.35	0.559	1.2674	-1.451	-1.083	-7.581	-2.379
NA	0.04072475	-0.63	0.814	-0.814	0.676	1.5804	-0.814	-0.814	-5.782	-5.782
NES	4.24E-10	-0.34	1.538	-0.27	0.874	0.4306	-1.131	-1.105	-3.431	-3.215
NFATC2	0.00709268	2.09	-0.12	-0.538	0.381	-0.369	-0.777	-0.667	-6.689	-3.165
NFE2L3	7.12E-05	0.159	-0.6	0.815	1.3	0.6877	-1.212	-1.147	-3.654	-3.117
PBX3	0.02008894	1.62	0.751	-0.547	0.356	-0.076	-1.341	-0.763	-2.646	-1.199
PCOLCE	0.03518198	-0.13	0.027	0.989	-0.21	1.5631	-1.114	-1.131	-1.089	-1.107
PHLDA1	0.01862053	1.608	0.203	-0.472	1.025	-0.394	-0.947	-1.023	-1.391	-1.532
PITPNM3	0.00684464	-0.13	1.515	-0.616	0.098	1.1241	-1.171	-0.816	-2.514	-1.466
PKN3	0.03374528	0.149	-0.17	0.01	1.738	0.5438	-1.295	-0.979	-2.359	-1.557
PLTP	0.04958066	1.006	1.224	0.758	-0.19	-0.52	-1.196	-1.086	-1.469	-1.308
PPP2R2B	0.04762812	1.971	0.008	-0.134	0.484	-0.585	-0.872	-0.872	-4.657	-4.657
PRELP	0.02301275	0.102	-0.58	2.153	-0.19	-0.096	-0.708	-0.689	-3.732	-3.435
PRLR	0.01862053	0.417	1.443	-0.963	1.102	-0.24	-0.851	-0.907	-3.094	-3.71
PSG1	0.0025378	2.022	0.604	-0.233	-0.48	-0.485	-0.678	-0.756	-2.843	-3.842

# NAE1 VUS

PSG5	0.0089704	1.78	0.517	-0.756	-0.18	0.4725	-1.082	-0.752	-2.585	-1.488
RALGPS1	0.02881424	-0.52	-0.13	0.339	1.893	0.35	-1.076	-0.855	-5.3	-2.535
RGCC	0.01898174	-0.73	0.378	-0.15	2.055	-0.088	-0.732	-0.732	-8.162	-8.162
RIMS2	0.00540232	-0.02	0.415	-0.808	1.193	1.2763	-1.03	-1.03	-4.609	-4.609
RTN4RL1	0.04432331	2.139	-0.21	0.006	0.073	-0.536	-0.755	-0.722	-6.275	-4.509
RUNX2	0.00224238	1.51	-0.02	-0.014	0.47	0.5453	-1.029	-1.463	-1.625	-2.918
S1PR3	0.00557986	0.366	0.742	-0.706	-0.43	1.7607	-0.989	-0.745	-3.69	-2.023
SALL2	0.0129608	1.177	0.654	-0.15	-0.1	0.9364	-1.482	-1.04	-6.966	-2.129
SAMD14	0.03197017	2.044	-0.1	0.169	0.115	-0.48	-0.793	-0.955	-1.742	-2.327
SDC4	0.02506544	-0.86	0.287	1.428	0.393	0.8342	-0.794	-1.284	-1.188	-2.242
SERPINE2	0.0343186	1.949	0.348	-0.373	0.368	-0.675	-0.659	-0.958	-1.372	-2.326
SFTA1P	0.03252576	-0.5	-0.41	-0.418	2.037	0.6161	-0.665	-0.665	-8.078	-8.078
SHISAL1	0.01120488	0.72	-0.4	0.209	1.843	-0.728	-0.784	-0.856	-2.55	-3.087
SLC29A4	0.00697725	1.676	-0.29	0.073	0.686	0.1235	-1.286	-0.98	-6.802	-2.446
SLC43A1	0.00395203	0.672	0.134	1.079	-0.13	0.8821	-1.536	-1.102	-5.661	-2.147
SLC8A1-AS1	0.01121289	2.209	-0.3	-0.454	-0.01	-0.197	-0.627	-0.627	-5.9	-5.9
SOX9	0.03197017	1.306	-0.29	0.268	-0.58	1.3202	-0.936	-1.087	-1.764	-2.219
SPON2	7.88E-05	-0.53	-0.11	0.185	2.133	-0.202	-0.734	-0.734	-7.151	-7.151
STAP2	0.00874296	0.5	0.842	-0.115	1.295	0.0648	-1.343	-1.242	-6.871	-4.005
STEAP2	0.00243819	0.01	0.809	0.943	0.064	0.8259	-1.681	-0.971	-2.404	-1.154
STMN3	0.0456592	-0.22	-0.45	-0.514	2.164	0.2361	-0.532	-0.676	-2.086	-3.425
STX1B	0.00382025	0.813	-0.05	0.646	-0	1.2161	-1.363	-1.258	-2.409	-2.097
TCTN2	0.02881424	-0.05	0.886	-0.346	0.655	1.2486	-1.548	-0.841	-2.859	-1.189
TGFA	0.00091112	2.206	-0.31	-0.015	-0.25	-0.306	-0.708	-0.618	-6.479	-3.291
TGFBR3L	0.03895544	1.374	0.299	1.175	-0.53	-0.169	-1.174	-0.979	-3.467	-2.315
TLE2	0.01862053	1.331	0.846	0.514	-0.43	0.163	-1.427	-1.002	-7.287	-2.138
TMED1	0.00874296	0.543	0.465	0.036	1.076	0.6302	-1.648	-1.102	-1.818	-1.115
TMEM119	0.00074085	-0.4	0.466	-0.172	0.085	1.9367	-0.916	-0.996	-1.892	-2.158
TMEM25	0.00052457	1.266	-0.12	1.474	-0.17	-0.486	-1.045	-0.925	-4.096	-2.871
TMEM9B-AS1	0.04361249	-0.62	-0.45	0.534	1.565	0.9017	-0.966	-0.966	-7.031	-7.031
TNFRSF21	0.01648881	0.447	0.32	-0.663	-0.32	1.9225	-0.907	-0.797	-2.46	-1.978
TOR4A	0.03751673	0.482	-0.32	1.86	0.403	-0.708	-0.68	-1.038	-1.552	-3.178
TPP1	0.00049575	1.338	0.25	0.725	-0.37	0.5667	-1.306	-1.208	-1.601	-1.45
TRIM14	0.0083662	1.622	0.524	-0.185	0.658	-0.404	-1.184	-1.032	-1.813	-1.508
TRIM16	0.0056343	1.632	-0.24	0.085	0.604	0.2935	-1.238	-1.134	-1.926	-1.701
TRIM55	1.81E-06	1.027	-0.28	1.582	-0.66	0.2603	-0.968	-0.964	-9.965	-8.029
TRIM7	0.00488864	0.882	-0.59	-0.331	1.687	0.2711	-0.986	-0.935	-6.013	-4.26
TSPOAP1	0.00992749	-0.33	-0.11	1.204	0.904	0.7798	-1.226	-1.225	-2.031	-2.028
TYRO3	0.00082187	1.321	0.903	0.13	0.169	0.0306	-1.534	-1.02	-3.034	-1.545
VAT1L	0.03627585	0.487	-0.78	0.933	-0.52	1.5852	-0.705	-1.006	-1.857	-3.878
ZNF385D	0.02443378	1.144	0.729	1.1	-0.15	-0.619	-1.337	-0.87	-3.008	-1.496
ZNF521	0.0202337	1.498	-0.23	-0.91	0.325	1.0924	-0.875	-0.9	-2.01	-2.104
ZNF578	0.02998066	1.278	0.267	-0.343	1.119	0.0903	-1.266	-1.146	-5.181	-3.406
ZNF853	0.0021976	-0.31	0.44	1.33	1.147	-0.381	-1.114	-1.114	-6.393	-6.393

**Table S4:** Overview of significantly (adjusted p-value <0.05, log2foldchange >2 or <2) up- or downregulated genes identified with RNA sequencing in individuals with *NAE1* genetic variants and healthy control fibroblasts. Heterozygous carriers (parents of individual 1) fibroblasts were also included. The first column shows the adjusted (Bonferroni) p-value comparing individuals with healthy controls. The 3th to the 9th column show the Z-scores of all donors comparing the RPKM score of the gene to the RPKM of that gene in all other donors. The 10th and 11th columns show the log2foldchange in individual 1 and individual 2.

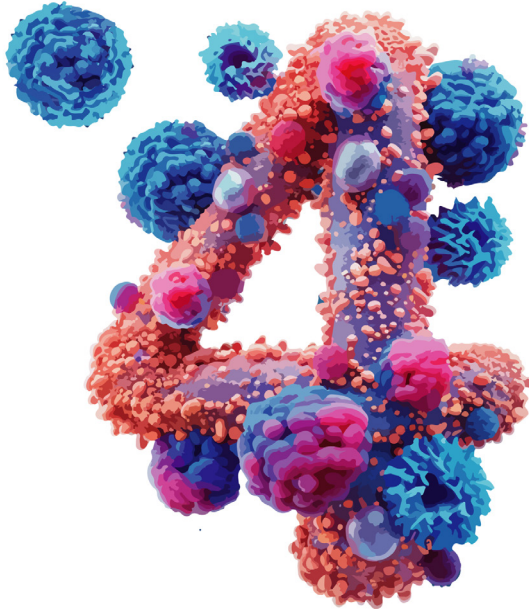
### References:

1. Richards S, Aziz N, Bale S, Bick D, Das S, Gastier-Foster J, et al. Standards and guidelines for the interpretation of sequence variants: A joint consensus recommendation of the American College of Medical Genetics and Genomics and the Association for Molecular Pathology. *Genet Med*. 2015;17(5):405–24.
2. Schwarz JM, Rödelberger C, Schuelke M, Seelow D. MutationTaster evaluates disease-causing potential of sequence alterations. *Nat Methods*. 2010;7(8):575–6.
3. Adzhubei IA, Schmidt S, Peshkin L, Ramensky VE, Gerasimova A, Bork P, et al. A method and server for predicting damaging missense mutations. *Nat Methods*. 2010;7(4):248–9.
4. Rentzsch P, Witten D, Cooper GM, Shendure J, Kircher M. CADD: Predicting the deleteriousness of variants throughout the human genome. *Nucleic Acids Res*. 2019;47(D1):D886–94.
5. Karczewski KJ, Francioli LC, Tiao G, Cummings BB, Alföldi J, Wang Q, et al. The mutational constraint spectrum quantified from variation in 141,456 humans. *bioRxiv* [Internet]. 2019;531210. Available from: <https://www.biorxiv.org/content/10.1101/531210v3>





# Chapter



***LIMK1* variants are associated with  
divergent endocrinological phenotypes  
aligning with  
divergently altered exocytosis dynamics.**



**LIMKI variants are associated with divergent endocrinological phenotypes aligning with divergently altered exocytosis dynamics.**

Irena J.J. Muffels<sup>1</sup>, Theodore Carter<sup>2</sup>, Holger Rehmann<sup>3</sup>, Sebastiaan J. Vastert<sup>4</sup>, Annemarie A. Verrijn Stuart<sup>5</sup>, Andreas C. Blank<sup>6</sup>, Aurore Garde<sup>7</sup>, Bert van der Zwaag<sup>8</sup>, Iris M. De Lange<sup>8</sup>, Jaques C Giltay<sup>8</sup>, Koen L.I. van Gassen<sup>8</sup>, Klaas Koop<sup>1</sup>, Cedric S. Asensio<sup>2</sup>, Peter M. van Hasselt<sup>1</sup>

<sup>1</sup> Department of Metabolic Diseases, Wilhelmina Children's Hospital, University Medical Center Utrecht; Utrecht, The Netherlands.

<sup>2</sup> Department of Biological Sciences, College of Natural Sciences and Mathematics; Denver, Colorado, United States of America.

<sup>3</sup> Department of Energy and Biotechnology, Flensburg University of Applied Sciences; Flensburg, Germany.

<sup>4</sup> Department of Pediatric Rheumatology and Immunology and Center for Translational Immunology, Wilhelmina Children's Hospital, University Medical Center Utrecht; Utrecht, The Netherlands.

<sup>5</sup> Department of Pediatric Endocrinology, Wilhelmina Children's Hospital, University Medical Center Utrecht; Utrecht, The Netherlands.

<sup>6</sup> Department of Pediatric Cardiology, Wilhelmina Children's Hospital, University Medical Center Utrecht; Utrecht, The Netherlands.

<sup>7</sup> Centre de Génétique et Centre de référence maladies rares, Fédération Hospitalo-Universitaire Médecine Translationnelle et Anomalies du Développement (FHU TRANSLAD), Hôpital d'Enfants, Centre Hospitalier Universitaire de Dijon; Dijon, France.

<sup>8</sup> Department of Medical Genetics, Wilhelmina Children's Hospital, University Medical Center Utrecht; Utrecht, The Netherlands.

Conditionally Accepted at iScience

## Abstract

*Background:* LIM kinase 1 (LIMK1) plays a pivotal role in dynamic actin remodeling through phosphorylation of cofilin. In turn, the dynamic remodeling of the actin cytoskeleton is involved in exocytosis, thereby contributing to tuned secretion of hormones and neurotransmitters, although the exact role of actin in these processes is still debated.

*Results:* We report two individuals with de novo variants in *LIMK1* with dissimilar clinical phenotypes: one individual exhibited epileptic encephalopathy and developmental delay, the other showed common variable immune deficiency, glucose dysregulation, and episodic sinus tachycardia. Given the intragenic localization of these variants, one impacting the highly conserved kinase domain, the other variant located in the auto-inhibitory LIM domain, we suspected that the phenotypic features could be explained by opposite effects of the *LIMK1* variants on LIMK1-mediated exocytosis dynamics. Indeed, we found significantly decreased actin polymerization in individual 1, contrasting with increased LIMK1 availability, cofilin phosphorylation, and actin polymerization in fibroblasts of individual 2. As compared to wildtype, significantly slower and decreased insulin exocytosis was observed in insulin-secreting cell lines expressing the *LIMK1* variant of individual 1 (harboring the catalytically dead variant), which contrasted with rapid and uncontrolled insulin exocytosis in case of a lack of auto-inhibition for individual 2.

*Conclusion:* This first report of two individuals with *LIMK1* variants harboring divergent effects on cofilin phosphorylation and actin polymerization, reveals novel and important roles for LIMK1 in tuned exocytosis. These distinct exocytosis defects may underlie the epileptic encephalopathy and glucose dysregulation observed.

## Introduction

The unique ability of actin to provide structural support to cells, whilst allowing dynamic adaptations, is essential for eukaryotic health. The cytoskeletal ability to change rapidly is utilized in many ways, including cellular migration, endocytosis, and exocytosis.<sup>1,2</sup> A set of actin-modifying proteins warrant appropriate tuning of the actin cytoskeleton when needed. The importance of these proteins is underlined by a growing number of monogenetic disorders causing dysfunction of these proteins, called actinopathies.<sup>3</sup>

LIM kinase 1 (LIMK1) is an example of an actin modifying protein that operates via phosphorylation of cofilin, which increases the elasticity of the actin cytoskeleton by severing actin filaments.<sup>4</sup> LIMK1 and cofilin operate in a complex signaling cascade, thought to allow rapid actin filament disassembly when needed.<sup>5</sup> Unusually, the two LIM domains and the PDZ domain directly mediate LIMK1 activity, which is thought to occur by interacting with the kinase domain directly.<sup>6,7</sup> LIMK1 can also transphosphorylate other LIMK1 proteins, thereby increasing their activity, half-life, and stability.<sup>8</sup> It is thought that these complex feedback dynamics promote unique protein kinetics, essential to facilitate cellular processes requiring rapidly changing morphology, such as endo- and exocytosis. However, the exact role of actin in these processes is still debated, as it can be either a positive or negative regulator, depending on the secretory system under investigation.<sup>9</sup>

The complex dynamics of the LIMK1-cofilin-actin signaling cascade suggests that pathogenic variants can derail the entire pathway in potentially unpredictable ways. We are the first to report two individuals with heterozygous *LIMK1* missense variants, showing divergent clinical phenotypes, ranging from epileptic encephalopathy to immunodeficiency and glucose regulation issues. Functional studies in patient-derived cells revealed opposite effects of variants on LIMK1 activity, allowing us to delineate how a broad range of altered LIMK1 activity leads to aberrant insulin exocytosis, glucose dysregulation, and the other clinical phenotypes observed.

## Materials and Methods

### *Patient Inclusion*

Two Dutch, unrelated children, both harboring *LIMK1* variants, were recruited in the Wilhelmina Children's Hospital in Utrecht. The patient with *LIMK1/ELN* hemideletion was recruited in Centre Hospitalier Universitaire (CHU) Dijon. Written informed consent was obtained from the parents of each child. Healthy adult donor Peripheral Blood Mononuclear Cells (PBMCs) (N=4) were obtained through the Minidonor Services, an ethics review board-approved blood donation facility at the UMC Utrecht (protocol number 18-774). Healthy fibroblast lines were recruited through the Wilhelmina Children's Hospital metabolic biobank (TCBio 19-489/B, <https://tcbio.umcutrecht.nl>). The identified *LIMK1* variants were submitted to the ClinVar repository under accession numbers SCV004190115 and SCVXXXXXX. All procedures performed in studies involving human participants were in accordance with the ethical standards of the institutional and/or national research committee(s) and with the Helsinki Declaration (as revised in 2013).

### *Exome Sequencing*

Exomes were enriched using Agilent SureSelect XT Human All Exon kit V5 and sequenced on a HiSeq sequencing system (Illumina). Reads were aligned to hg19 using Burrows–Wheeler Aligner. Variants were called using Genome Analysis Toolkit Variant Caller and annotated, filtered, and prioritized using the Bench NGS Lab platform (Agilent-Cartagenia, Leuven, Belgium) and/or an in-house designed “variant interface” and manual curation. The minimal coverage of the full target was >15 x 99%. All common polymorphisms with a minor allele frequency (MAF) higher than 0.5% were filtered out using several public databases including 1,000 genomes database<sup>10</sup>, Ensembl GRCh37 genome browser<sup>11</sup>, exome aggregation consortium database (ExAC)<sup>12</sup>, genome aggregation database (GnomAD)<sup>13</sup>, and database of single nucleotide polymorphisms (dbSNP)<sup>14</sup>. Variant calling was performed using the complete human reference genome (hg19, NCBI release GRCh37).

### *Glucose measurements*

Continuous glucose measurements were performed in individual 2 for a period of three consecutive years. In individual 1, glucose was measured for approximately one week. The glucose values were extracted from the Dexcom Clarity Professional portal. Additionally, data from six patients was extracted for comparison. Analysis was performed using R studio (Version 1.4.1106). ‘Non-hypoglycemic days’ were identified as days with all values  $>3.5$  mmol/L, while ‘Hypoglycemic days’ were quantified as days with one or more glucose values  $<3.5$  mmol/L. The derivative was calculated by dividing the absolute glucose difference between two time points by the number of minutes between the two time points. If the amount of time (in minutes) between two time points was more or less than five minutes, values were excluded.

### *Flow Cytometry*

PBMCs were isolated from the whole blood fraction using Ficoll (GE Healthcare). Cells were fixed with 4% formaldehyde and stained with live/dead fixable viability dye (Thermo Fisher), CD3 (Biolegend), CD19 (Sony Biotechnology), and phalloidin (Sigma Aldrich) for 1 hour at room temperature. Fibroblasts were harvested using Accutase (Gibco) and fixed with 4% formaldehyde.

### *Western Blotting*

Fibroblasts were harvested using TrypLE (Thermo Fisher) and lysed in laemli buffer with protease (Sigma Aldrich) and phosphatase (Sigma Aldrich) inhibitors. Immediately after harvesting, samples were boiled for 5 minutes at 100 degrees. Western blot was performed as described previously.<sup>15</sup> Membranes were probed with phosphorylated-Cofilin (Cell Signaling), Cofilin (Cell Signaling), LIMK1 monoclonal antibody directed against the PDZ domain (Enzo), or GAPDH antibodies (Novus Biologicals) overnight at 4 degrees. Ins-1 cells were probed with anti-HA-high-affinity (Roche) and anti- $\alpha$ -tubulin (Millipore).

*Overexpression of LIMK1 variants in Ins-1 cells*

LIMK1-WT, or LIMK1 harboring variants of individual 1 or 2 lentiviral plasmids were generated by Gibson (NEB) assembly using gene blocks (Twist Bioscience). All constructs were verified by Sanger sequencing (Quintarabio). Lentiviruses were produced by transfecting HEK293T cells with pLenti-CMV-puro, psPAX2, and pVSVG together with PEI at 1 µg/µL. HEK293T cells were maintained in DMEM with 10% fetal bovine serum under 5% CO<sub>2</sub> at 37°C. Rat Ins-1 cells, originally obtained from the laboratory of Dr. Peter Arvan (University of Michigan), were maintained in RPMI supplemented with 1mM sodium pyruvate, 10% fetal bovine serum and 50 µM β-mercaptoethanol under 5% CO<sub>2</sub> at 37°C. To generate stable Limk1 cell lines, Ins-1 cells were transduced with lentivirus. 24hr after virus transduction, Ins-1 cells were selected for ~24hr using 3µg/mL puromycin. Transient transfection of Ins-1 cells was performed using Lipofectamine 2000 (Invitrogen) according to the manufacturer's instructions.

*Exocytosis measurements in Ins-1 cells*

Prior to exocytosis assays, stable Ins-1 cells overexpressing LIMK1-WT constructs or LIMK1 harboring variants of individual 1 or 2 were transiently transfected with NPY-pHluorin (a pH-sensitive GFP whose fluorescence is quenched at acidic pH) and NPY-sfCherry3 (an RFP that fluoresces regardless of pH). When the granules fuse with the plasma membrane during exocytosis, the pH rapidly rises allowing pHluorin detection. Prior to running the exocytosis experiments, cells were incubated with a low KRB buffer (1.5mM glucose, 5.4mM KCl). Cells in focus were imaged for 15 seconds under these conditions before the low KRB was replaced with high KRB buffer (40mM KCL, 16.7mM Glucose) as described previously.<sup>16</sup> After changing the medium, images were acquired for another 60 seconds. Cells were visualized using total internal reflection fluorescence (TRIF) microscopy. Images were acquired every 0.2 seconds.

*Statistical Methods*

Statistical analyses were performed using Prism (Version 9.3.0, Graph-Pad Software) or R-studio (Version 2022.12.0.353). P values \*P<0.05;

\*\*P<0.01, \*\*\*P<0.001, \*\*\*\*P<0.0001 were considered significant. Flow cytometry analysis was performed using FlowJo (Version 10.6.2., Becton, Dickinson and Company, USA, 2019). Exocytosis images were analyzed using ImageJ. Western blots were analyzed using Image Lab software (Version 5.1, BioRad). Figures 1D-F, 5D, E, G were created using R (Version 4.2.3) and R-studio (Version 2022.12.0.353). Specifically, the `geom_smooth` function from the `ggplot2` package was employed to generate smoothed trend lines. The following formula was used within `geom_smooth`: `method="gam", formula = y ~ s(x, bs = "cs", fx = TRUE, k = 60)`. This formula specifies a generalized additive model (GAM) with a cubic spline basis (`bs = 'cs'`) and other relevant parameters.

## Results

### *Clinical Phenotype of individuals with LIMK1 variants*

In two individuals, *LIMK1* de novo missense variants were identified. Individual 1 is a five-year-old girl who presented with epileptic encephalopathy and developmental delay at the age of eight months. Individual 2 presented with a completely different phenotype. During his first year of life, recurrent upper- and lower respiratory infections, diarrhea and failure to thrive were noted. Decreased levels of immunoglobulins led to the diagnosis of Common Variable Immune Deficiency (CVID) (**Figure 1A**). During childhood, tiredness, exercise intolerance, enuresis nocturna and hypoglycemic events were noted. The hypoglycemic events were associated with the intake of fast-acting carbohydrates, but were always self-limiting. The hypoglycemia could lead to temporary unconsciousness at times. Additionally, he experienced bouts of sinus tachycardia during exercise or rest, that similarly normalized spontaneously (**Figure 1B, C**). Clinical descriptions are detailed in **Note S1**.

Repeated hypoglycemia observed in individual 2 led to continuous glucose measurements (CGM) being performed. In individual 2, hypoglycemic events were frequently recorded: 21% of GCM recorded days (>900) showed one or more hypoglycemic events, despite receiving hypercaloric





(B) Graph showing continuous heart rate measurements of individual 2. On the y-axis, the beats per minute (BPM) are shown, on a day with a tachycardic event. The x-axis shows the time of day.

(C) Holter ECG recording of individual 2 during an episode of inappropriate sinus tachycardia. During the tachycardic event, a maximum heart rate of 223 beats per minute during exercise was observed.

(E) Graphs showing glucose values on a representative day (24-hour) for one of the pediatric controls, individual 1 and individual 2. For individual 2, two separate graphs are shown. On the left, a normal day is shown, where individual 2 does not experience hypoglycemia. On the right, a ‘hypoglycemic day’ is shown, where individual 2 experiences a nocturnal hypoglycemic event. As can be seen, glucose values remained highly variable throughout the day after a nocturnal hypoglycemic event was recorded.

(F) Line graphs showing the average glucose variation throughout the day. For individual 2, two separate lines are shown, one for days where he does not experience hypoglycaemic events, and one for days where he experiences one or more hypoglycemic events. Glucose variation was calculated by measuring the absolute difference (delta) between consecutive glucose value measurements (measured every 5 minutes). Missing values were excluded. The dots indicate the mean glucose variation per hour. The error bars surrounding the grey line indicate the standard deviation for six different pediatric controls. A more detailed description of the pediatric controls can be found in **Table S1**.

intake (**Note S2**). Additionally, highly variable glucose values were seen, which were even higher on days where nocturnal hypoglycemic events were recorded (**Figure 1D, E**). We found individual 1 showed very little glucose variation compared to pediatric controls (**Figure 1D, E**). However, her ketogenic diet might in part explain this observation (**Note S2, Figure S2**).

Immuno-phenotyping revealed decreased percentages of naïve T cells and increased levels of memory T cells in individual 1. Intriguingly, individual 2 exhibited exactly opposite values, with high percentages of naïve T cells and low numbers of effector memory cells (**Figure 1A**).

### *In-Silico predictions*

LIMK1 shows intolerance against loss-of-function, with a pLI score of 1.0 and o/e ratio of 0.09.<sup>17</sup>

The *LIMK1* variant of individual 1 was located at a highly conserved residue in the kinase domain: c.(1532G>C);p.(Gly511Ala) (**Figure 2A, B**). The variant has not been reported in GnomAD. PolyPhen-218 predicts this variant

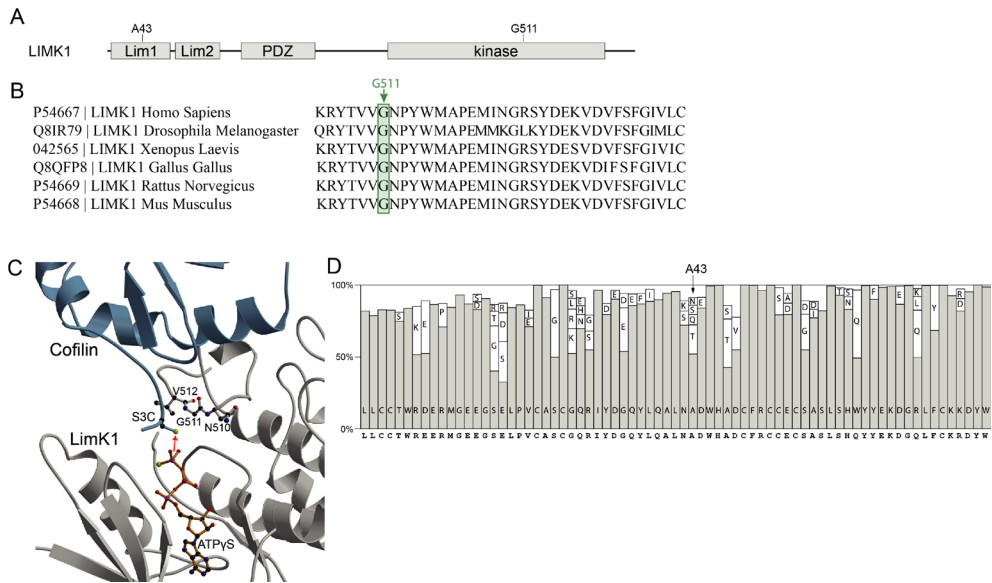


**Figure 2: In-silico predictions of *LIMK1* genetic variants.**

(A) Domain organization of LIMK1. The location of the genetic variants in individual 1 and 2 are indicated. Lim1, Lim domain 1; Lim2, Lim domain 2; PDZ, PDZ domain; kinase, kinase domain.

(B) Showing the conservation of the glycine at position 511 among species. The green square and arrow indicate the glycine at position 511. Gly511 and surrounding residues are highly conserved across species.

(C) Ribbon representation of the LimK1 kinase domain (grey) in complex with cofilin (light blue) and ATP $\gamma$ S, a hydrolysis resistant ATP analogue (orange, ball-and-stick representation). Gly511 and its neighboring residues are shown in ball-and-stick representation. The red arrow indicates the phosphoryl transfer to the substrate. For structure determination the receiving Ser3 in cofilin was mutated to Cys. The figure is based on the pdb entry 5HVK20 and was generated with the programs molscript 37 and raster3d38

(D) Sequence motif of the Lim1 domain of about 370 different species. Amino acid residues with a frequency lower than 4.5% are omitted for clarity of presentation. The most frequent residue is represented as a grey bar. The sequence of human LimK1 is shown underneath.

to be probably damaging (0.995), with a CADD score of 26.9.<sup>19</sup> Gly511 resides within the catalytic domain and is part of the activation segment, where the transfer of the phosphate from ATP to the substrate takes place.<sup>20</sup> The backbone conformation of Gly511 adopts  $\phi$ - and  $\Psi$ -angles, which are impossible for other amino acids to adopt (**Figure 2C**). The second individual harbored a variant in the first LIM domain: c.(127G>A);p.(Ala43Thr) (**Figure 2A**). The Ala43Thr variant has been reported with an allele frequency of 0.000009. PolyPhen predicts Ala43Thr to be benign, and the variant has a CADD score of 13.4. Ala43 is substituted for threonine in many species (**Figure 2D**). Interestingly, a shorter variant that lacks major parts of the first Lim domain including Ala43 exists, although it is not clear to what extent this isoform is biologically relevant. While structural information about the LIM domains is lacking, the LIM domains are known to act as an auto-inhibitor of the protein.<sup>6</sup> Thus, a destabilizing effect of the Ala43Thr on the Lim domain variant could result in increased activity of LIMK1.

#### *Functional assay results*

We set out to study the functional effects of *LIMK1* variants in patient-derived fibroblasts. We included a patient with heterozygous *LIMK1* deletion for comparison. The patient harbored a large deletion encompassing the entire *LIMK1* gene and the last exon of *ELN*. The patient showed verbal delay and learning disability, together with *ELN*-related phenotypic features (**Note S1**).

Overall, LIMK1 protein abundance varied between donors, but average LIMK1 protein levels in fibroblasts of individual 1 and the patient with *LIMK1* hemideletion were similar compared to healthy control fibroblasts. In contrast, fibroblasts of individual 2 showed increased LIMK1 protein levels (**Figure 3A, Figure S2**). To study LIMK1 functionally, we assessed phosphorylated cofilin protein levels in fibroblasts (**Figure 3B**). We found Individual 1 and the patient with LIMK1 hemideletion showed normal phosphorylated cofilin over cofilin ratios compared to healthy controls (**Figure 3C**). In support of overactive LIMK1, we found increased phosphorylated cofilin over cofilin ratio in fibroblasts of individual 2.

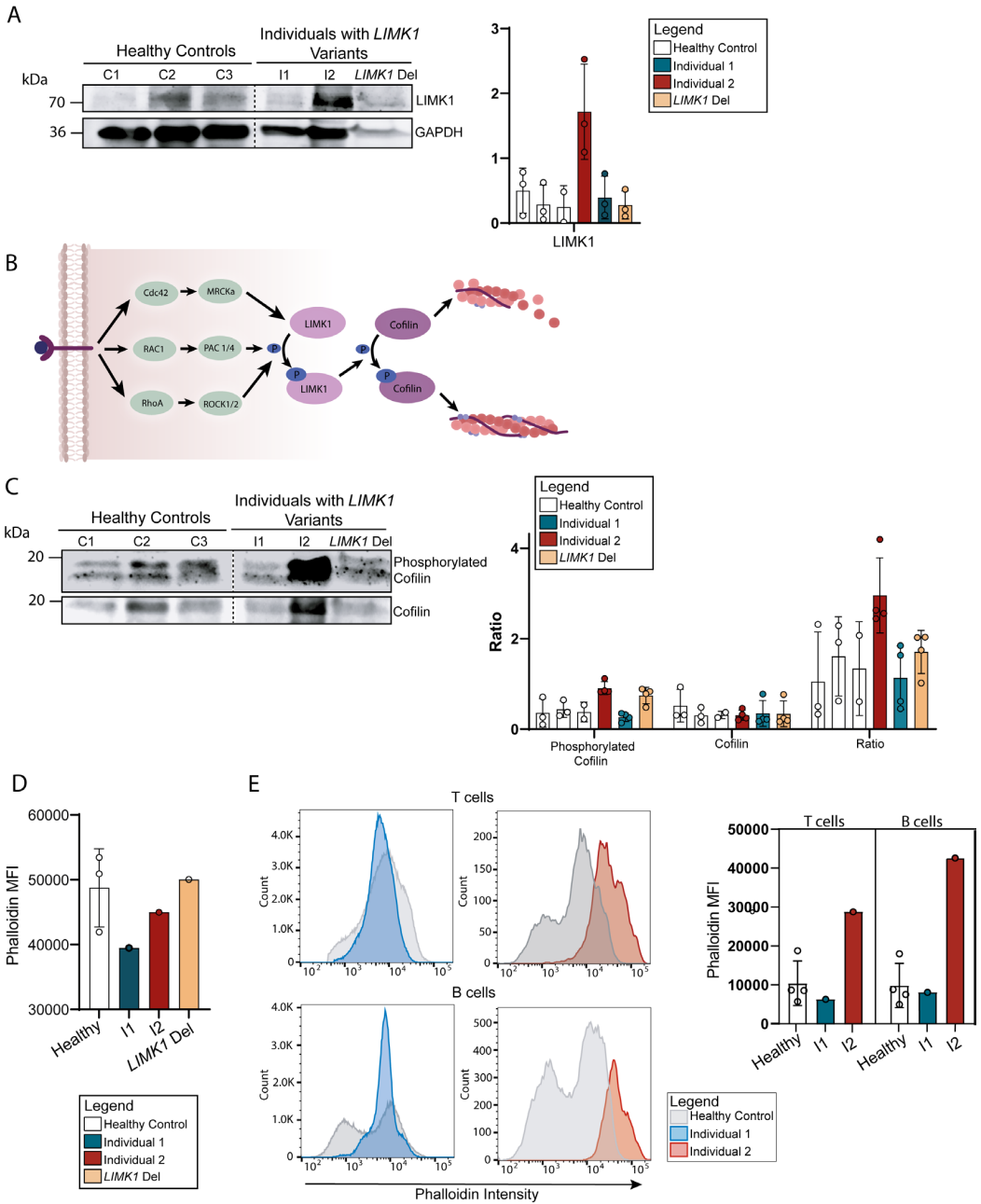


**Figure 3: Functional assessment of *LIMK1* variants in fibroblasts and lymphocytes.**

(A) Representative western blot showing LIMK1 protein levels in fibroblasts derived from three healthy controls and individual 1 (I1), individual 2 (I2), and a patient with *LIMK1/ELN* hemideletion (LIMK1 Del). GAPDH was used as housekeeper. The bar graphs show the ratio of LIMK1 band intensity normalized to GAPDH. For the bar graph, three independent western blot experiments were used (**Figure S2**). Each bar represents one biological replicate, each dot represents one technical replicate. The bar graphs show the mean values  $\pm$ SD.

(B) Graphical representation of LIMK1 and its downstream functions. On the far right, polymerized actin strands are visualized in red.

(C) Representative western blot showing cofilin and phosphorylated cofilin (Ser3) protein levels in fibroblasts derived from three healthy controls and individual 1,2 and a patient with *LIMK1/ELN* hemideletion. GAPDH (as visualized in **Figure 3A**) was used as housekeeper. The bar graph shows the ratio of cofilin or phosphorylated cofilin over GAPDH. For the bar graph, three independent western blot experiments were used (**Figure S2**). Each bar represents one biological replicate, each dot represents one technical replicate. The bar graphs show the mean values  $\pm$ SD.

(D) Bar graphs showing the mean fluorescence intensity (MFI)  $\pm$ SD from one representative flow cytometry experiment. In total, the experiment was performed three times. The gating strategy can be found in **Figure S4**.

(E) Representative histograms showing phalloidin fluorescence intensity distribution in healthy controls (N=2) and individual 1 and 2 B- and T cells. The bar graphs show the mean fluorescence intensity (MFI)  $\pm$ SD for four different healthy controls (N=4) and for individual 1 and 2 (N=1 each). The gating strategy can be found in **Figure S3**.

The increased levels of LIMK1 protein and LIMK1 activity indicate that the Ala43Thr variant might lead to increased half-life and stability, potentially due to increased phosphorylation by LIMK1 itself or upstream kinases.<sup>8</sup>

Next, we measured levels of polymerized actin in fibroblasts and PBMCs. Here, we found differences between individual 1 and the patient with *LIMK1* hemideletion, as individual 1 showed significantly decreased actin polymerization while the patient with *LIMK1* hemideletion did not (**Figure 3D**). In contrast, we found increased levels of actin polymerization in fibroblasts of individual 2, albeit not significant (**Figure 3D**). For individual 1, we found no significant difference in actin polymerization in T and B cells, however, the distribution seemed different between cells compared to healthy controls (**Figure 3E**). In line with the western blot results in individual 2, we observed a trend towards increased levels of actin polymerization for individual 2 in fibroblasts, T and B cells (**Figure 3E**).

Together, these results support the divergent effects of *LIMK1* variants. While absolute cofilin phosphorylation levels were not altered in fibroblasts of individual 1, cofilin phosphorylation dynamics could have been affected, illustrated by decreased actin polymerization. The significant difference in actin polymerization in comparison to the patient with *LIMK1* hemideletion indicates that the Gly511Ala variant might exert more severe effects on overall LIMK1 functioning than the mere loss of one functional LIMK1 copy.

Conversely, in individual 2, the increased cofilin phosphorylation and actin polymerization support the hypothesis of overactive LIMK1.

#### *Translation of cellular defects to clinical phenotype*

Given the aberrant glucose regulation observed in individual 2, and the role of LIMK1 in insulin exocytosis<sup>21</sup>, we studied Ins-1 cells, that release insulin upon stimulation with glucose, overexpressing either WT-LIMK1 or LIMK1 harboring Gly511Ala (individual 1) or Ala43Thr (individual 2) variants. We found different LIMK1 protein levels were reached after overexpression of these variants (**Figure 4A**). Visual inspection of the LIMK1-Gly511Ala ex-

# Chapter 4

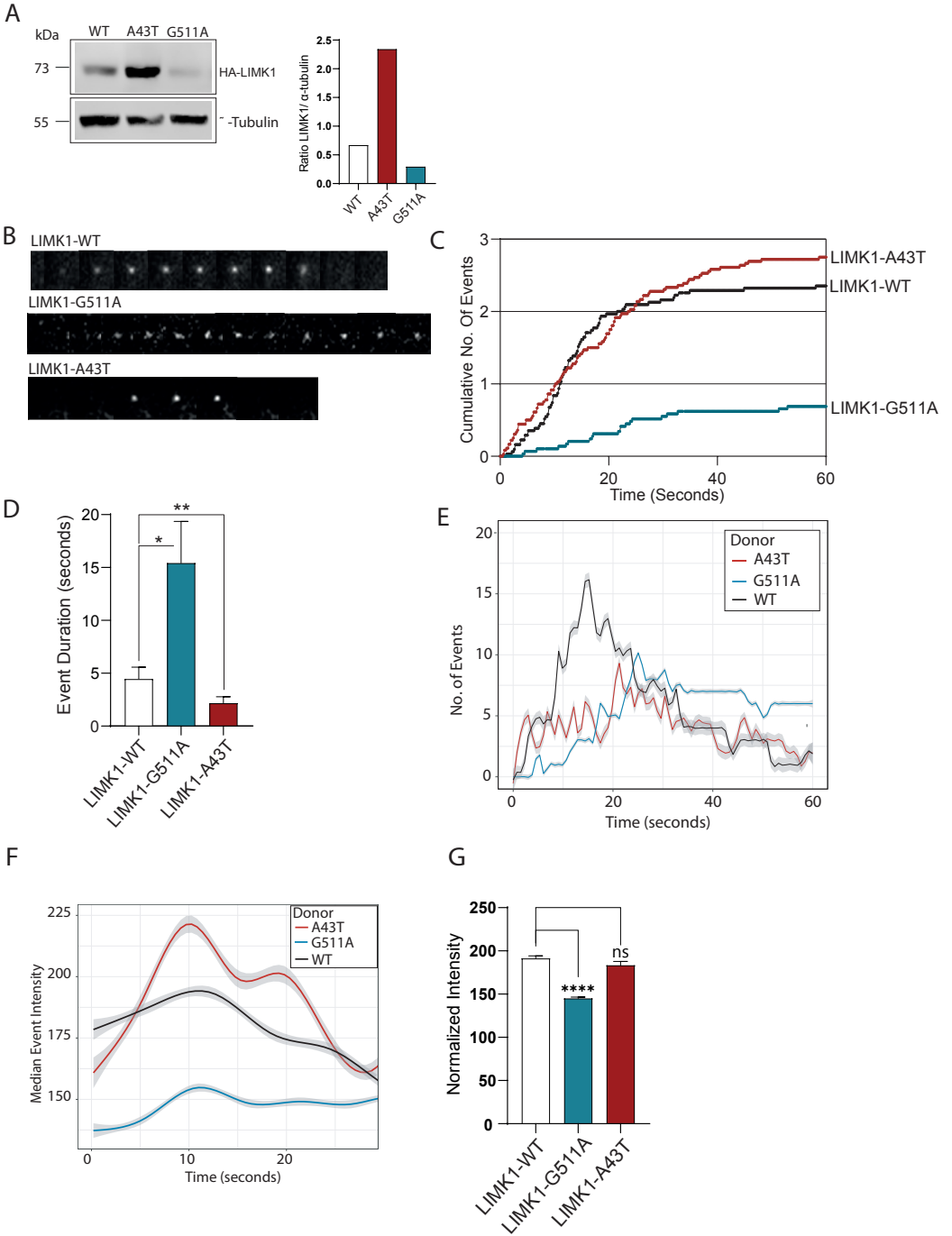


**Figure 4: Exocytosis measurements in Ins-1 cells after the introduction of different LIMK1 constructs.**

Exocytotic events were visualized by introducing NPY-pHluorin (a pH-sensitive GFP that fluoresces under higher pH) in cell lines. After stimulation of Ins-1 cells with medium containing high levels of glucose/potassium, exocytosis was measured for 60 seconds. Images were taken every 0.2 seconds.

(A) Western blot of Ins-1 cells overexpressing HA-WT-LIMK1, or HA-LIMK1 harboring variants of individual 1 and 2. The western blot shows increased LIMK1 protein levels for the Ins-1 cells expressing LIMK1-Ala43Thr, while Ins-1 cells overexpressing LIMK1-Gly511Ala seem to have decreased LIMK1 protein levels compared to overexpression of WT-LIMK1.

(B) Showing representative images of exocytotic events in Ins-1 cells expressing either the LIMK1-WT, LIMK1-Gly511Ala or LIMK1-Ala43Thr construct.

(C) Line graph showing the cumulative number of exocytosis events over time. The number of cumulative events was normalized for the total number of cells that were visualized. For each donor, approximately 30 cells were analyzed (WT=31, Ala43Thr=36, Gly511Ala=29).

(D) Box plot showing the mean duration of complete vesicle excretion for each exocytosis event. The box extends from the 25th to the 75th percentile. The whiskers extend to the minimal and maximal value. 2% of outliers were removed using the ROUT method.<sup>39</sup> Statistics were calculated using one-way ANOVA followed by Dunn's test. p-values were adjusted for multiple comparisons (Turkey's range test).

(E) Line graph showing the number of exocytosis events observed at each timepoint (Event rate/second). Ins-1 cells expressing the LIMK1-Ala43Thr construct had faster vesicle excretion, therefore less exocytosis events were observed at each timepoint, but the number of events fluctuated heavily over time. Ins-1 cells expressing the Gly511Ala variant showed slower vesicle excretion, and events started significantly later after potassium/glucose stimulation.

(F) Line graph showing the median intensity of vesicles over time. Intensity values were normalized for vesicle size (total area). Most events lasted between 1-30 seconds, and therefore the x-axis was adjusted accordingly. Every 0.2 seconds, the median intensity of the events present at that timepoint was calculated. The values were plotted using a generalized additive model (GAM) with a cubic spline basis (bs = 'cs'). The grey shades surrounding the lines represent the confidence intervals of the model.

(G) Box plots showing the median intensity values normalized for vesicle size (total area) per vesicle. The box extends from the 25th to the 75th percentile. The whiskers extend to the minimal and maximal value. 2% of outliers were removed using the ROUT method.<sup>39</sup> To calculate overall median intensity, all timepoints were pooled (0-60 seconds). Statistics were calculated using mixed effect models.



pressing cell line revealed significantly less, slow, and dim exocytosis events, while the LIMK1-Ala43Thr expressing Ins-1 cell line seemed to have a flashy appearance (**Figure 4B, Supplementary Video 1,2,3**). Upon quantification, we found LIMK1-Gly511Ala overexpression was associated with a decreased number of cumulative exocytotic events (**Figure 4C**). In contrast, Ins-1 cells expressing the Ala43Thr variant showed a higher number of cumulative exocytotic events after glucose stimulation (**Figure 4C**). Average exocytosis events normalized per cell were not significantly different for both individuals (data not shown). The entire process of vesicle secretion in Ins-1 cells expressing LIMK1-Gly511Ala lasted significantly longer (**Figure 4D**). Additionally, exocytosis commenced significantly later after glucose stimulation (**Figure 4E**). In contrast, vesicle secretion in Ins-1 cells expressing Ala43Thr lasted significantly shorter, started more rapidly after glucose stimulation and fluctuated heavily over time (**Figure 4D, E**). For Ins-1 cells expressing the WT-LIMK1 construct, we found that the dim appearance of the vesicles secreted by Ins-1 cells expressing the Gly511Ala variant correlated with significantly decreased intensity values over time (**Figure 4F**). In addition, the median event intensity was significantly decreased (**Figure 4G**). Ins-1 cells expressing the Ala43Thr variant showed a high intensity peak, in line with its flashy appearance (**Figure 4F**). However, the cumulative intensity of vesicles was not significantly altered (**Figure 4G**).

In conclusion, while overexpression of the Gly511Ala variant (individual 1) resulted in decreased exocytosis, longer vesicle excretion duration and lower intensity, faster vesicle excretion with higher peak intensity was observed upon overexpression of the Ala43Thr variant.

## Discussion

We present two individuals harboring *LIMK1* variants with divergent clinical phenotypes, and provide evidence that these differences align with divergent consequences on LIMK1 function. Individual 1 showed developmental delay and epilepsy, and decreased actin polymerization in patient-derived fibroblasts suggested loss of LIMK1 kinase activity. Upon overexpression

of this variant, significantly slower and decreased levels of exocytosis were found in insulin secreting (Ins-1) cell lines. Conversely, the genetic variant in individual 2, who exhibited common variable immune deficiency, disordered glucose regulation and bouts of exaggerated sinus tachycardia, showed defective auto-inhibitory function of LIMK1, leading to rapid, flashy, exocytosis events upon overexpression of this variant in Ins-1 cells. Together, these results indicate that heterozygous variants in *LIMK1* may give rise to neurological and hormonal disturbances, potentially through altered exocytosis dynamics.

The first aim of this study was to establish whether *LIMK1* variants were pathogenic and give rise to a novel syndrome. The variant of individual 1 was predicted to disrupt the local fold and the highly conserved catalytic site of LIMK. While normal levels of phosphorylated cofilin might argue against pathogenicity, the significantly decreased levels of polymerized actin, that were not identified in heterozygous loss of *LIMK1*, suggest that cofilin phosphorylation dynamics and downstream functions could have been affected. The severity of the clinical phenotype found in individual 1 suggests the variant exerts effects beyond the mere loss of one active *LIMK1* copy alone, although the mechanism remains to be studied. Potentially, the variant mimics the expression pattern of a specific LIMK1 isoform (ENST00000435201.1) lacking the catalytically active site. For LIMK2, a similar isoform (LIMK2d) has been identified, and was found to negatively affect neurite outgrowth in rats. The authors postulated that this isoform occupies the phosphorylation site of cofilin, masking it from other fully functional LIMK isoforms. The variant of individual 2 was associated with significantly increased LIMK1 and phosphorylated cofilin levels, suggesting that the Ala43Thr variant affects the auto-inhibitory function of the first LIM domain. Interestingly, a shorter LIMK1 isoform (ENST00000538333.3) exists, lacking part of the first LIM domain, including the Ala43Thr variant. While detailed information about this shorter isoform is lacking, it could be used to regulate overall LIMK1 expression by converging LIMK1 to a more open confirmation. Exploring the clinical relevance of these isoforms across different tissues and their impact on LIMK1 activity could provide an

exciting avenue for further research.

LIMK1 and cofilin are both activated upon glucose stimulation in pancreatic  $\beta$  cells (MIN6-K8).<sup>21</sup> The second phase of insulin secretion is characterized by a continuously high state of LIMK1 and cofilin phosphorylation, that favors the presence of F-actin, allowing insulin vesicles further away from the plasma membrane to be recruited.<sup>21</sup> Expression of a constitutively active form of cofilin, leading to a depletion of the G-actin pool preventing actin polymerization, inhibits overall insulin secretion<sup>21</sup>, potentially through a mechanism where distant vesicles cannot be recruited. Similarly, the *LIMK1* Gly511Ala variant could have limited the recruitment of distant vesicles, leading to the decreased exocytosis observed. However, the various roles of actin in several exocytotic processes (endocytosis, vesicle recruitment, docking, etc.) make it challenging to pinpoint specifically which steps would be most affected. We can only speculate why the profound exocytosis defects in Ins-1 cells are not associated with severe glucose regulation issues in individual 1. Possibly, as seen in patients with type II diabetes, pancreatic  $\beta$ -cells might compensate for defective insulin secretion up until a certain point.<sup>22</sup> Additionally, the exocytosis defects could extend to other endocrine cells and organs, making the prediction of glucose levels solely based on altered insulin secretion non-trivial. Finally, the slower exocytosis might be far more destructive to organs that require rapid kinetics, such as neurons, which concurs with the predominantly neurological phenotype of individual 1. Regarding individual 2, the hypoglycemic events observed shortly after ingestion of fast-acting carbohydrates resemble the rapid and uncontrolled insulin exocytosis observed in Ins-1 cells, after glucose stimulation, suggesting a functional link. Additionally, other characteristics of his clinical phenotype, such as enuresis nocturna and episodic tachycardia, make it tempting to speculate that uncontrolled exocytosis of vasopressin or catecholamines could similarly play a role in underlying pathophysiology.

The epileptic encephalopathy in individual 1 prompts consideration of defective neurotransmitter exocytosis as a potential contributor, given the established link between epilepsy and impaired neurotransmitter exocytosis.<sup>23</sup>

While *LIMK1* knockout mice exhibit disrupted neurotransmitter exocytosis, they primarily display decreased learning performance rather than epilepsy.<sup>24</sup> However, Cofilin knockout mice do show epilepsy, associated with impaired neuronal vesicle recruitment and exocytosis, resulting in decreased glutamate secretion.<sup>25,26</sup> Thus, the treatment-resistant epilepsy observed in individual 1 might similarly stem from significantly slower and decreased exocytosis of neurotransmitters, thereby contributing to the development and sustainment of epilepsy.

The phenotypic features in individuals with *LIMK1* variants align with those seen in other actinopathies<sup>3</sup>, where immunodeficiency is a common manifestation. Similarly, developmental delay and seizures have been observed in actinopathies, although to a lesser extent.<sup>15,27–30</sup> While many actin-modifying proteins have been linked to insulin exocytosis at the cellular level<sup>31–34</sup>, clinical glucose dysregulation has been reported only marginally.<sup>35,36</sup> However, this report of an actinopathy with a pronounced endocrinological phenotype, coupled with divergent exocytosis results in insulin-secreting cell lines, strongly suggest a critical role for LIMK1-mediated actin remodeling in exocytosis. Additionally, the individuals described in this study suggest that tight regulation and auto-inhibition of LIMK1 are essential to warrant appropriate actin tuning.

### **Author contributions**

Conceptualization: IM, CSA, PMH

Methodology: IM, CSA, PMH

Investigation: IM, TC, HR, SJV, AAVS, ACB, AG, BZ, IML, JCG, KLI, KK, CSA, PMH

Visualization: IM, TC, CSA, PMH

Supervision: CSA, PMH

Writing – original draft: IM, PMH

Writing – review & editing: IM, HR, SJV, AAVS, ACB, BZ, KLI, KK, CSA, PMH

### **Conflicts Of Interests**

The authors declare that no conflict of interest exists.

## References

1. Iman Mousavi S, Li X, Berro J. Fast actin disassembly and mechanosensitivity of the actin crosslinker fimbrin during clathrin-mediated endocytosis. *Biophys J*. 2022;121(3):519a. doi:10.1016/j.bpj.2021.11.2734
2. Kotila T, Wioland H, Selvaraj M, et al. Structural basis of rapid actin dynamics in the evolutionarily divergent *Leishmania* parasite. *Nat Commun*. 2022;13(1). doi:10.1038/s41467-022-31068-y
3. Sprenkeler EGG, Webbers SDS, Kuijpers TW. When Actin is Not Actin' like It Should: A New Category of Distinct Primary Immunodeficiency Disorders. *J Innate Immun*. 2021;13(1):3-25. doi:10.1159/000509717
4. Caroni P, Arber S, Barbayannis FA, et al. Regulation of actin dynamics through phosphorylation of cofilin by LIM-kinase. *Nature*. 1998;393(6687):805-809.
5. Ramirez-Munoz R, Castro-Sánchez P, Roda-Navarro P. Ultrasensitivity in the cofilin signaling module: A mechanism for tuning T cell responses. *Front Immunol*. 2016;7(FEB). doi:10.3389/fimmu.2016.00059
6. Nagata K, Ohashi K, Yang N, Mizuno K. The N-terminal LIM domain negatively regulates the kinase activity of LIM-kinase 1. *Biochemical Journal*. 1999;343(1):99-105. doi:10.1042/0264-6021:3430099
7. Casanova-Sepúlveda, G., Sexton JA, Turk BE et, Boggon TJ. Auto-regulation of the LIM kinases by their PDZ domain. *Nat Commun*. 2023;14:8441. doi:10.1038/s41467-023-44148-4
8. Li R, Soosairajah J, Harari D, et al. Hsp90 increases LIM kinase activity by promoting its homo-dimerization. *The FASEB Journal*. 2006;20(8):1218-1220. doi:10.1096/fj.05-5258fje
9. Porat-Shliom N, Milberg O, Masedunskas A, Weigert R. Multiple roles for the actin cytoskeleton during regulated exocytosis. *Cellular and Molecular Life Sciences*. 2013;70(12):2099-2121. doi:10.1007/s00018-012-1156-5
10. Donnelly P, Green ED, Knoppers BM, et al. A global reference for human genetic variation. *Nature*. 2015;526(7571):68-74. <http://www.nature.com/doifinder/10.1038/nature15393%0Apapers3://publication/>

doi/10.1038/nature15393

11. Zerbino DR, Achuthan P, Akanni W, et al. Ensembl 2018. *Nucleic Acids Res.* 2018;46(D1):D754-D761. doi:10.1093/nar/gkx1098
12. Karczewski KJ, Weisburd B, Thomas B, et al. The ExAC browser: Displaying reference data information from over 60 000 exomes. *Nucleic Acids Res.* 2017;45(D1):D840-D845. doi:10.1093/nar/gkw971
13. Karczewski KJ, Francioli LC, MacArthur DG. The mutational constraint spectrum quantified from variation in 141,456 humans. *Yearbook of Paediatric Endocrinology*. Published online 2020. doi:10.1530/ey.17.14.3
14. Sherry ST, Kholodov MH, Ward M, et al. dbSNP: the NCBI database of genetic variation. *Nucleic Acids Res.* 2001;29(1):308-311. <https://academic.oup.com/nar/article-abstract/29/1/308/1116004>
15. Muffels IJJ, Wiame E, Fuchs SA, et al. NAA80 bi-allelic missense variants result in high-frequency hearing loss, muscle weakness and developmental delay. *Brain Commun.* 2021;3(4). doi:10.1093/braincomms/fcab256
16. Burns CH, Yau B, Rodriguez A, et al. Pancreatic  $\beta$ -cell-specific deletion of VPS41 causes diabetes due to defects in insulin secretion. *Diabetes.* 2021;70(2):436-448. doi:10.2337/db20-0454
17. Samocha KE, Robinson EB, Sanders SJ, et al. A framework for the interpretation of de novo mutation in human disease. *Nat Genet.* 2014;46(9):944-950. doi:10.1038/ng.3050
18. Adzhubei I, Jordan DM, Sunyaev SR. Predicting functional effect of human missense mutations using PolyPhen-2. *Curr Protoc Hum Genet.* 2013;(SUPPL.76). doi:10.1002/0471142905.hg0720s76
19. Rentzsch P, Witten D, Cooper GM, Shendure J, Kircher M. CADD: Predicting the deleteriousness of variants throughout the human genome. *Nucleic Acids Res.* 2019;47(D1):D886-D894. doi:10.1093/nar/gky1016
20. Hamill S, Lou HJ, Turk BE, Boggon TJ. Structural Basis for Noncanonical Substrate Recognition of Cofilin/ADF Proteins by LIM Kinases. *Mol Cell.* 2016;62(3):397-408. doi:10.1016/j.molcel.2016.04.001
21. Uenishi E, Shibasaki T, Takahashi H, et al. Actin dynamics regulated by the balance of neuronal wiskott-aldrich syndrome protein (N-WASP) and cofilin activities determines the biphasic response of

- glucose-induced insulin secretion. *Journal of Biological Chemistry*. 2013;288(36):25851-25864. doi:10.1074/jbc.M113.464420
22. Kasuga M. Insulin resistance and pancreatic  $\beta$  cell failure. *Journal of Clinical Investigation*. 2006;116(7):1756-1760. doi:10.1172/JCI29189
  23. Cali E, Rocca C, Salpietro V, Houlden H. Epileptic Phenotypes Associated With SNAREs and Related Synaptic Vesicle Exocytosis Machinery. *Front Neurol*. 2022;12. doi:10.3389/fneur.2021.806506
  24. Meng Y, Zhang Y, Tregoubov V, et al. Abnormal spine morphology and enhanced LTP in LIMK-1 knockout mice. *Neuron*. 2002;35(1):121-133. doi:10.1016/S0896-6273(02)00758-4
  25. Wolf M, Zimmermann AM, Görlich A, et al. ADF/Cofilin controls synaptic actin dynamics and regulates synaptic vesicle mobilization and exocytosis. *Cerebral Cortex*. 2015;25(9):2863-2875. doi:10.1093/cercor/bhu081
  26. Bellenchi GC, Gurniak CB, Perlas E, Middei S, Ammassari-Teule M, Witke W. N-cofilin is associated with neuronal migration disorders and cell cycle control in the cerebral cortex. *Genes Dev*. 2007;21(18):2347-2357. doi:10.1101/gad.434307
  27. Martinelli S, Krumbach OHF, Pantaleoni F, et al. Functional Dysregulation of CDC42 Causes Diverse Developmental Phenotypes. *Am J Hum Genet*. 2018;102(2):309-320. doi:10.1016/j.ajhg.2017.12.015
  28. Verloes A, Di Donato N, Masliah-Planchon J, et al. Baraitser-Winter cerebrofrontofacial syndrome: Delineation of the spectrum in 42 cases. *European Journal of Human Genetics*. 2015;23(3):292-301. doi:10.1038/ejhg.2014.95
  29. Huang Y, Mao X, Van Jaarsveld RH, et al. Variants in CAPZA2, a member of an F-actin capping complex, cause intellectual disability and developmental delay. *Hum Mol Genet*. 2020;29(9):1537-1546. doi:10.1093/hmg/ddaa078
  30. Procaccio V, Salazar G, Ono S, et al. A mutation of  $\beta$ -actin that alters depolymerization dynamics is associated with autosomal dominant developmental malformations, deafness, and dystonia. *Am J Hum Genet*. 2006;78(6):947-960. doi:10.1086/504271
  31. Wang B, Lin H, Li X, et al. The adaptor protein APPL2 controls

- glucose-stimulated insulin secretion via F-actin remodeling in pancreatic  $\beta$ -cells. *Proc Natl Acad Sci U S A*. 2020;117(45):28307-28315. doi:10.1073/pnas.2016997117
32. Kepner EM, Yoder SM, Oh E, Kalwat MA, Wang Z, Quilliam LA. Cool-1  $\beta$  PIX functions as a guanine nucleotide exchange factor in the cycling of Cdc42 to regulate insulin secretion. *Physiol Endocrinol Metab*. 2011;301:E1072-E1080.
  33. Nevins AK, Thurmond DC. Caveolin-1 functions as a novel Cdc42 guanine nucleotide dissociation inhibitor in pancreatic  $\beta$ -cells. *Journal of Biological Chemistry*. 2006;281(28):18961-18972. doi:10.1074/jbc.M603604200
  34. Nie J, Sun C, Faruque O, et al. Synapses of amphids defective (SAD-A) kinase promotes glucose-stimulated insulin secretion through activation of p21-activated kinase (PAK1) in pancreatic  $\beta$ -cells. *Journal of Biological Chemistry*. 2012;287(31):26435-26444. doi:10.1074/jbc.M112.378372
  35. Böttcher Y, Schleinitz D, Tönjes A, Blüher M, Stumvoll M, Kovacs P. R1467H variant in the rho guanine nucleotide exchange factor 11 (ARHGEF11) is associated with impaired glucose tolerance and type 2 diabetes in German Caucasians. *J Hum Genet*. 2008;53(4):365-367. doi:10.1007/s10038-008-0252-8
  36. Harms FL, Kloth K, Bley A, et al. Activating Mutations in PAK1, Encoding p21-Activated Kinase 1, Cause a Neurodevelopmental Disorder. *Am J Hum Genet*. 2018;103(4):579-591. doi:10.1016/j.ajhg.2018.09.005
  37. Kraulis PJ. MOLSCRIPT. A program to produce both detailed and schematic plots of protein structures. *J Appl Crystallogr*. 1991;24(pt 5):947-950. doi:10.1107/s0021889891004399
  38. Merritt EA, Murphy MEP. Raster3D version 2.0 A program for photorealistic molecular graphics. *Acta Crystallogr D Biol Crystallogr*. 1994;50(6):869-873. doi:10.1107/S0907444994006396
  39. Motulsky HJ, Brown RE. Detecting outliers when fitting data with nonlinear regression - A new method based on robust nonlinear regression and the false discovery rate. *BMC Bioinformatics*. 2006;7. doi:10.1186/1471-2105-7-12



## Supplementary Files

### Note S1: Comprehensive Clinical Descriptions:

#### *Individual 1*

Individual 1 is a five-year-old girl born to non-consanguineous parents after an uneventful pregnancy and delivery. Development appeared normal during the first 8 months. Subsequently, parent noted sudden developmental decline: she lost the ability to laugh and did not respond to sounds anymore. She developed myoclonic epilepsy and focal epileptic seizures. An EEG confirmed epileptic encephalopathy. She has since been treated with different types of anti-seizure medication and a ketogenic diet. Brain MRI showed no abnormalities. Cerebral vision loss was suspected, but due to her severely delayed development this could not be assessed. In addition, frequent middle ear infections and bilateral conductive hearing loss were noted (~40dB, most prominent in the high-frequency area). Despite extensive diagnostic follow-up, no known cause for her symptoms was found. Trio Whole Exome Sequencing revealed a de novo heterozygous missense variant in *LIMK1*.

#### *Individual 2*

Individual 2 is a 16-year-old boy born to non-consanguineous parents. During the first year of life, recurrent upper- and lower respiratory infections were noted, as well as diarrhea and failure to thrive. At two years of age, the diagnosis of Common Variable Immune Deficiency was made based on decreased levels of IgA, total IgG, IgG2, and IgM in plasma (**Figure 1A main text**), after which intravenous immunoglobulin therapy was initiated. From the age of 4 years onwards, parents noted frequent (~daily) episodes of profuse sweating, sometimes leading to fainting that were more prone to occur after ingestion of foods containing fast-acting carbohydrates, such as apple juice. The events could lead to unconsciousness at times. For example, he would grab and eat several sugar cubes and faint minutes after. He would always recover spontaneously.

At five years of age parents noted that he was frequently tired, accompanied by exercise intolerance and enuresis nocturna. During hospital admission, an episode of excessive sweating occurred, and hypoglycemia (glucose value

of 1.8 mmol/L) was recorded. Interestingly, attempts to address the hypoglycemia with sugar (ingestion of apple juice and a sandwich) provoked an exaggerated rise of glucose followed by a fall of glucose to 0.9 mmol/L. Subsequent endocrine follow-up showed normal response to glucagon challenge tests (normal insulin, glucose, and cortisol values). Growth hormone secretion after glucagon challenge test was slightly decreased 15 mIU/L (normally >20 mIU/L), with normal levels of IGF1 (80 ng/ml, normally 42-143 ng/ml). ACTH challenge test results were normal. Saliva cortisol levels were normal. TSH and T4 values and catecholamine excretion in urine were normal as well. Based on the clinical history dietary advices were given, including avoidance of fast-acting carbohydrates and uniform distribution of carbohydrates during the day, which was associated with disappearance of episodes of excessive sweating and unconsciousness. Exercise tolerance also improved. Over time, his dietary restrictions were temporarily relaxed and reinstalled when complaints recurred. Parents noted glucose levels increased more rapidly during adrenaline rushes, when he gets startled or is stressed. For example, when individual 2 got startled by fireworks, his glucose levels rose from 4 to 12 within minutes. At the age of 11, a decline in cognitive development was noted by parents. He was unable to concentrate, his school performance declined, and impairments in short- and long-term memory were noted. Brain MRI revealed no abnormalities. This slowly normalized over the course of 2 years, and he is currently attending high school without major issues.

At the age of 12, individual 2 reported palpitations. Holter ECG showed episodes of inappropriate sinus tachycardia during exercise. Parents noted these episodes were more prone to occur when activity was suddenly initiated, for example when walking the stairs, and occurred less when activity levels were gradually increased. Continuous heart rate and event monitoring with a subcutaneous ECG loop recording revealed additional bouts of inappropriate sinus tachycardia, which could occur either in rest or during exercise, without any signs of cardiac conduction or rhythm abnormalities (**Figure 2B, C, main text**). Ivabradine treatment helped to relieve these complaints. Additionally at the age of 13, his enuresis nocturna spontaneously resolved.

Despite extensive diagnostic follow-up, no cause for his symptoms was found. Trio Whole Exome Sequencing did reveal a de novo heterozygous missense variant in *LIMK1*.

### *Patient with LIMK1/ELN Hemideletion*

The patient with *LIMK1/ELN* was 9 years old at the time of inclusion. He presented with a heart murmur after which echocardiography was performed, that showed supra-valvular pulmonary and aortic stenosis. During follow-up, almond-shaped palpebral fissures, epicanthus, mild puffy cheeks and flat feet were observed. His pulmonary stenosis resolved spontaneously by the age of five years. Glucose values were never assessed. Additionally, he showed learning disabilities and verbal dyspraxia. WPPSI-IV testing revealed low-to-average results: Verbal Comprehension index 92, Visual-spatial Index 82, Fluid reasoning index 83, Working memory index 100, processing speed index 82, intellectual quotient 82. Genetic testing revealed a 96 KB de novo deletion comprising the last exon of *ELN*, and the entire *LIMK1* gene (del7q11.23):

arr[hg19]7q11.23(73,482,417-73,578,265)x1,17p13.2(3,507,046-3,558,393)  
x1

### **Note S3: Details about dietary regimen of Individual 1 and 2.**

#### *Individual 1: Ketogenic Diet*

Total calories/day: 1230 kcal

Tube Feeding:

3 x 91 gr. Ketocal: 87% fat, 4% carbohydrates, 9% protein.

5 gr. Protifar: 4% fat, 1% carbohydrates and 95% protein.

70 ml whole milk.

Oral Intake:

1. Twice per day, 2.5 gr. carbohydrates (fruit) and 40 ml whipped cream.

2. Once per day 2.5 gr. carbohydrates vegetables/meat and 40 ml sour cream.

3. Once per day: 10 gr. bread + 3 gr. margarine (>60% fat). With 15 ml Li-  
quigen + 8 ml yoghurt drink.

*Intake Individual 2: High Caloric Diet*

Total calories/day: 3270 kcal

Carbohydrates: 250g, 32%

Fat: 180g, 50%

Protein 130g, 16%

Oral intake: 1800 kcal, Tube Feeding: 1470 kcal

Tube Feeding:

During the day (breakfast – lunch – dinner – before sleeping):

4x 20 mL (=80 mL) Calogen (Nutricia ©):

Fat: 40g.

4x 45mL sachet ProSource (Sorgente ©):

Carbohydrates: 44g. Protein: 60g.

4x 47 ml Nutrison Protein Plus Multifibre (Nutrilon ©):

Protein: 12g.

During the night, continuous feeding.

90 ml Calogen (Nutricia ©):

Fat: 45g.

160 ml Nutrison Protein Plus Multi Fibre

Protein: 10,1g.

**Figure S1: Comparison of pediatric patient controls on a ketogenic diet to individual 1 continuous glucose measurement values.**

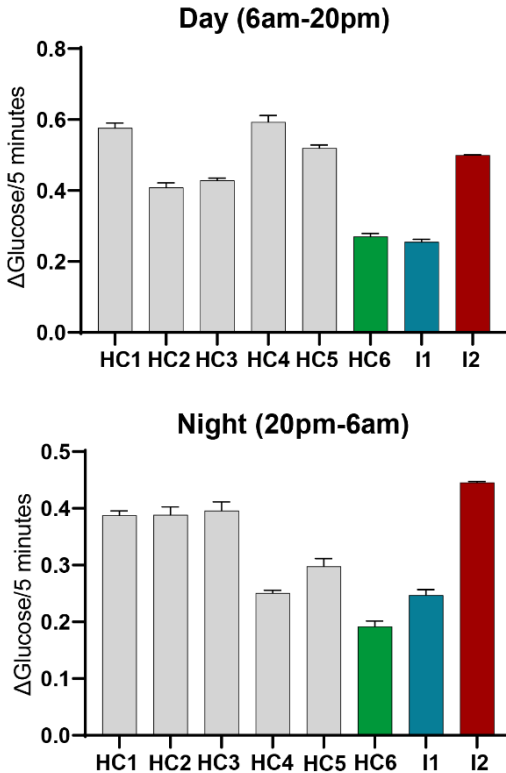


**Figure S1:** Glucose variation during the day and during the night in six pediatric donors and individual 1 and 2 harboring *LIMK1* genetic variants. The bars show the mean glucose variation during the day or during the night for six pediatric controls, individual 1 and individual 2. The green bar represents Healthy Control 6, who was on a ketogenic diet with limited carbohydrate intake when continuous glucose measurements were taken. In order to verify whether the glucose variation of individual 2 was similarly due to low carbohydrate ingestion, the glucose variation between these donors was directly compared. As can be seen, the low glucose variation is similar to a pediatric control on a ketogenic diet.

**Figure S2: Western blots as referred to in Figure 3A/C**

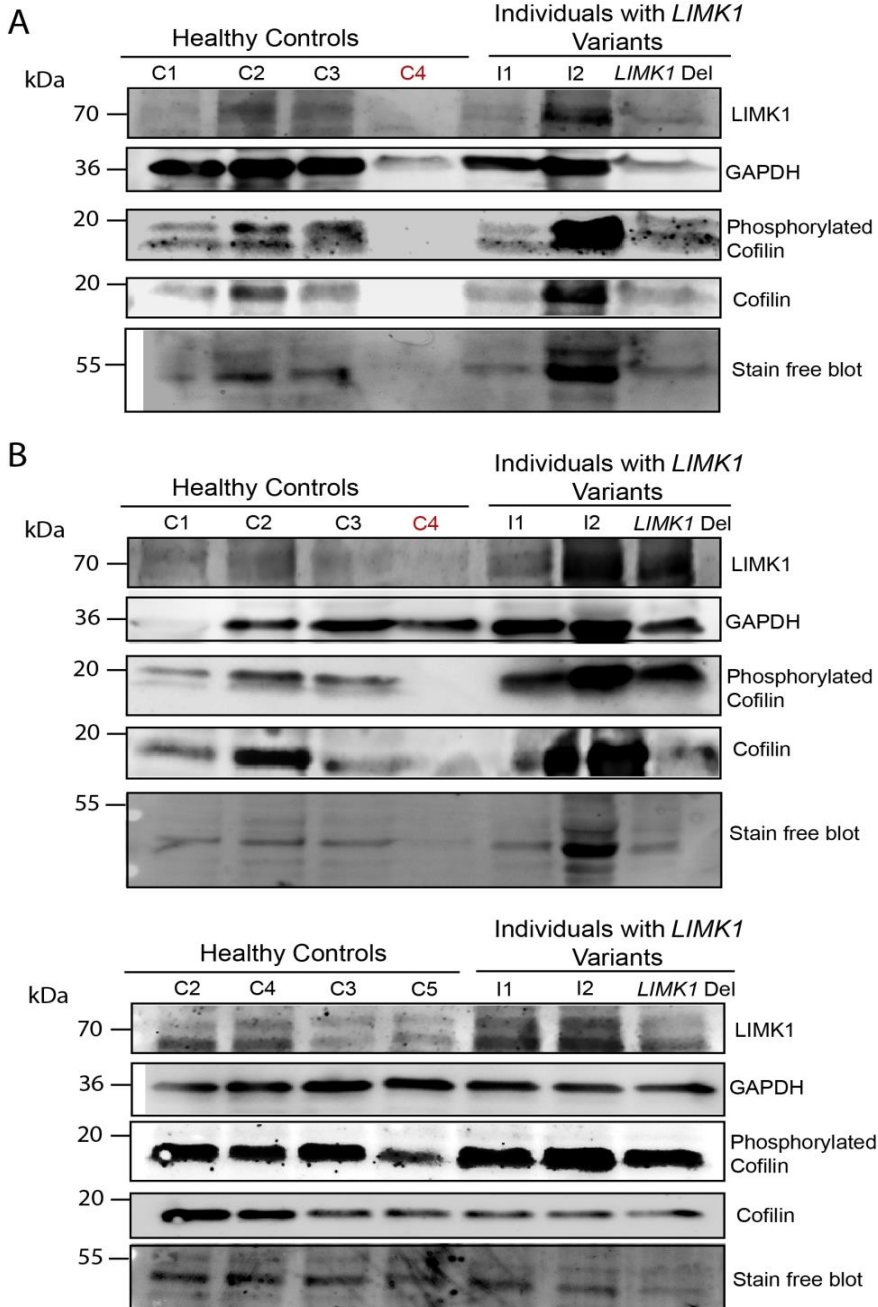


**Figure S2: Western blots as referred to in Figure 3A/C**

(A) Showing the uncropped version of the western blot which is also shown in Figure 3A/C found in the main body of the manuscript. Healthy control 4 was removed due to the low amount of protein that was present (most prominently visible in the stain-free blot).

(B) Showing the western blots used for quantification incorporated in the bar graphs shown in Figure 3A/C. Again, healthy control 4 was removed from the blot due to low protein levels. GAPDH was used as a housekeeper instead of the stain-free blots due to the inferior quality of the stain-free blots.

**Figure S3: Flow cytometry gating strategy used for B- and T cells**

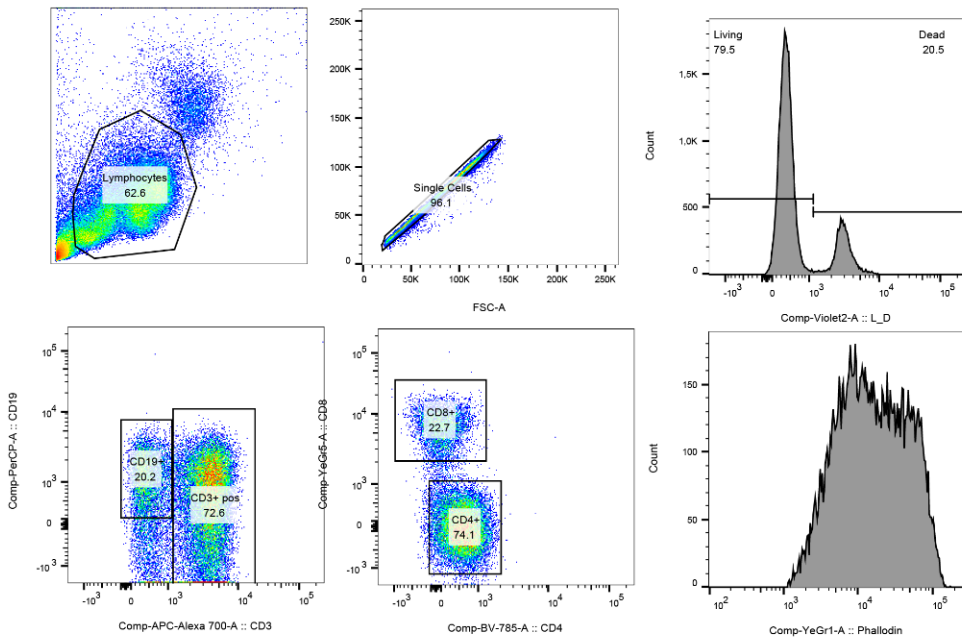


**Figure S3: Flow cytometry gating strategy used for B- and T cells**

Flow Cytometry Gating Strategy. Lymphocytes were gated using FSC-A and SSC-A. Single cells were gated using SSC-A and SSC-W. Dead cells

were excluded from analysis (using a fixable violet dead cell staining). Next, CD3-, CD4- and CD19- cells were gated.

**Figure S4: Flow cytometry gating strategy used for fibroblasts**

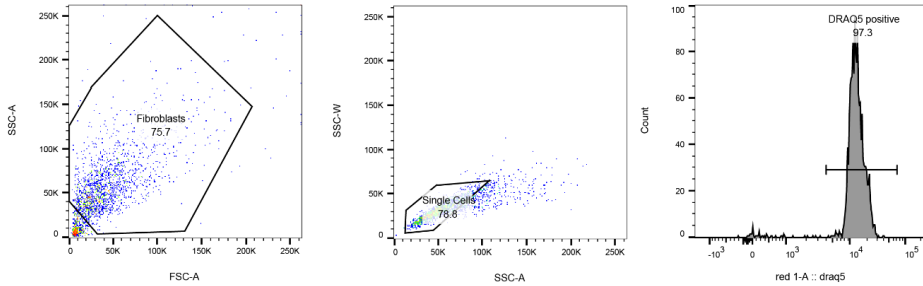


**Figure S4: Flow cytometry gating strategy used for fibroblasts**

Flow Cytometry Gating Strategy. Fibroblasts were separated from debris using FSC-A and SSC-A. Single cells were gated using SSC-A and SSC-W. Cells without nuclear staining were excluded from analysis.

**Table S1: Detailed information about diet, diagnosis and glucose measurements of pediatric controls and individuals with LIMK1 variants.**

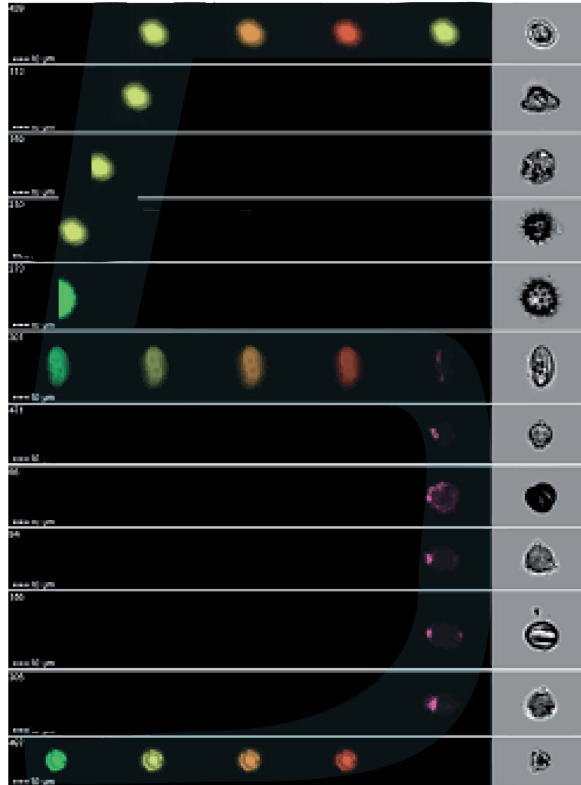
Donor Name	No. of days with continuous glucose measurement	Diagnosis	Diet	Hypoglycemic Days
Individual 2	>900	No Diagnosis	Hypercaloric diet, nightly feeding	Yes
Individual 1	8	No Diagnosis	Ketogenic Diet	No
HC1	18	GSD type 1	Continuous nightly feeding	Yes
HC2	9	Pediatric hypoglycemia	Normal Diet	Yes
HC3	8	Hypoglycemia ECI	Normal Diet	No
HC4	23	GSD type 1	Continuous nightly feeding	Yes
HC5	8	Fasting Intolerance ECI	Normal Diet	No
HC6	8	No Diagnosis	Ketogenic Diet	Yes

**Table S1:** Detailed information about the pediatric controls used as reference and individuals with *LIMK1* genetic variants used in **Figure 1C**.





# Chapter



**Imaging Flow Cytometry-based cellular screening elucidates pathophysiology in individuals with Variants of Uncertain Significance.**

## **Imaging Flow Cytometry-based cellular screening elucidates pathophysiology in individuals with Variants of Uncertain Significance.**

Muffels, I.J.J.,<sup>1</sup> Waterham, H.,<sup>2,3</sup> D'Allessandro, G.,<sup>4</sup> Zagnoli-Vieira, G.,<sup>5</sup> Sacher, M.,<sup>6,7</sup> Lefeber, D.J.,<sup>8</sup> Vinne, C.,<sup>1</sup> Roifman, C.,<sup>9</sup> Van Haaften-Visser, D.Y.,<sup>10</sup> Nieuwenhuis, E.E.S.,<sup>1,11</sup> Jackson, S.,<sup>4</sup> Fuchs, S.A.,<sup>1\*</sup> Wijk, F.,<sup>12\*</sup> Hasselt, P.M.<sup>1</sup>

<sup>1</sup>Department of Metabolic Diseases, division Pediatrics, Wilhelmina Children's Hospital University Medical Centre Utrecht, Utrecht University, Utrecht, the Netherlands.

<sup>2</sup>United For Metabolic Diseases (UMD).

<sup>3</sup>Department of Laboratory Medicine, Laboratory Genetic Metabolic Diseases, Amsterdam UMC - AMC, Amsterdam, the Netherlands.

<sup>4</sup>Cancer Research UK Cambridge Institute, University of Cambridge, Cambridge, United Kingdom

<sup>5</sup>The Gurdon Institute and Department of Biochemistry, University of Cambridge, Cambridge, United Kingdom

<sup>6</sup>Department of Biology, Concordia University, Montreal, Quebec, Canada.

<sup>7</sup>Department of Anatomy and Cell Biology, McGill University, Montreal, Quebec, Canada

<sup>8</sup>Translational Metabolic Laboratory, Department of Neurology, Department of Human Genetics, Donders Institute for Brain, Cognition and Behavior, Radboud University Medical Center, Nijmegen, the Netherlands

<sup>9</sup>The Hospital for Sick Children and Research Institute, The University of Toronto, Canada.

<sup>10</sup> Department of Pediatrics, Center for Lysosomal and Metabolic Diseases, Erasmus University Medical Center, Rotterdam, The Netherlands

<sup>11</sup> Center for Rare Diseases, Erasmus University Medical Center, Rotterdam, the Netherlands.

<sup>12</sup> Center for Translational Immunology (CTI), University Medical Center Utrecht (UMC), Utrecht University (UU), Utrecht, The Netherlands.

\* These authors contributed equally

**Manuscript under review at Genome Medicine**

### **Abstract:**

*Background:* Deciphering Variants of Uncertain Significance (VUS) represents a major diagnostic challenge, partially due to the lack of easy-to-use and versatile cellular readouts that aid the interpretation of pathogenicity and pathophysiology. To address this challenge, we propose a high-throughput screening of cellular functionality through an Imaging Flow Cytometry (IFC)-based platform.

*Methods:* Six assays to evaluate autophagic-, lysosomal-, Golgi- health, mitochondrial function, ER stress, and NF- $\kappa$ B activity were developed in fibroblasts. Assay sensitivity was verified with compounds (N=5) and positive control patients (N=6). Eight healthy controls and 20 individuals with VUS were screened.

*Results:* All molecular compounds and positive controls showed significant changes on their cognate assays, confirming assay sensitivity. Simultaneous screening of positive control patients on all six assays revealed distinct phenotypic profiles. In addition, individuals with VUS(es) in well-known disease genes showed distinct – but similar - phenotypic profiles compared to patients with pathogenic variants in the same gene, suggesting pathogenicity of their VUSes. For all individuals with VUSes in Genes Of Uncertain Significance (GUS), we found one or more of six assays were significantly altered. Broadening the screening to an untargeted approach led to the identification of two clusters that allowed for the recognition of altered cell cycle dynamics and DNA damage repair defects. Experimental follow-up of the ‘DNA damage repair defect cluster’ led to the discovery of highly specific defects in top2cc release from doublestrand DNA breaks in one of these individuals, harboring a VUS in the *RAD54L2* gene.

*Conclusion:* Our high-throughput IFC-based platform simplifies the identification of VUS pathogenicity through six assays and allows for the recognition of useful pathophysiological markers that structure follow-up experiments, thereby representing a novel valuable tool for precise functional diagnostics in genomics.

## Introduction

The ‘genetics first’ era has revolutionized the diagnostics of genetic disease. In its slipstream, genetic screening has offered hints for yet uncharacterized disease entities: Variants of Uncertain Significance (VUS). For these variants, a connection to human disease has yet to be established. Elucidating the significance of a VUS is painstakingly complex, as it requires *in silico*, *in vitro* and expert human analyses. It may take years to study the functional impact of a genetic variant on RNA levels, protein levels, and cellular pathways, and at significant costs, whereas the outcome of this endeavor is uncertain.<sup>1</sup> As a consequence, many VUS cases are left unexplored and unsolved. For patients, the absence of a diagnosis hampers prognosis prediction, family counseling, and treatment allocation, resulting in significant morbidity and mortality.<sup>2</sup>

An important part of VUS elucidation is establishing the impact of the VUS on intracellular pathway functionality. Even though this step is considered most challenging, these insights are crucial to unravel disease pathophysiology in relation to the clinical phenotype and to develop therapeutic strategies. Challenges arise mostly when there is limited functional data about a gene, there is no cellular read-out available, or when limited numbers of patients are included. Unless there is a clear-cut mechanism where the VUS is thought to interfere, it is almost impossible to decide which of the numerous potentially affected cellular pathways should be studied first, and which assays should be prioritized. We hypothesized that screening for morphological and functional cellular changes could help delineate the single culprit involved. By narrowing down the cellular pathways that could be studied, a functional cellular screening could provide a starting point to allow a more targeted set-up of subsequent experimental follow-up assays.

Microscopy has become increasingly popular to screen for cellular dysfunction in human diseases.<sup>3</sup> The largest benefit of microscopic screening is the fact that prior knowledge about underlying pathophysiology is not required, circumventing the need for expert-craft cellular assays.<sup>4,5</sup> However, this

approach has not been tested for individuals with VUS on a larger scale, and additionally, untargeted microscopic screening comes with its own set of challenges, especially in regard to extracting relevant phenotypic profiles. Imaging Flow Cytometry (IFC) combines flow cytometry with microscopy, and its high throughput potential combined with a simple analysis tool allows rapid extraction of relevant features and morphological profiles, without the need for deep learning models or computational scripts. These aspects make IFC highly suitable for untargeted screening for individuals with VUS.

Here, we developed a novel screening platform to identify functional cellular aberrancies in individuals with VUS using Imaging Flow Cytometry (IFC). We developed six assays to quantify morphology and function of six important cellular organelles and pathways (autophagy – Golgi – lysosomes – mitochondria – endoplasmic reticulum – NF- $\kappa$ B). We confirmed all molecular compounds and positive control patients showed significant changes on cognate assays. Next, we screened 20 patients with VUS(es) in well-known disease genes (N=7) and VUS in GUSes (Genes Of Uncertain Significance) (N=13). For all individuals with VUS, we found significant changes on one or more IFC assays, which were validated using additional functional assays, thereby unveiling the IFC-based platform as a valuable tool for the detection of relevant pathophysiological mechanisms for individual with VUS.

Methods:

### *Patient recruitment*

All patients without diagnosis despite an extensive diagnostic workup, including Whole Exome Sequencing seen at the outpatient clinic of the department of metabolic diseases, were eligible for inclusion in this study. All patients consented to use their residual material collected for diagnostic purposes in the Wilhelmina Children's Hospital metabolic biobank (TCBio 19-489/B, <https://tcbio.umcutrecht.nl>). Fibroblasts of a patients with pathogenic *ERCC1* variants was provided by the Genome Damage and Stability Centre Research Tissue Bank (GDSC-RTB), University of Sussex. The

GDSC-RTB is approved by the Wales REC 3 to release human cell lines for research (19/WA/0091).

All procedures performed in studies involving human participants were in accordance with the ethical standards of the institutional and/or national research committee(s) and with the Helsinki Declaration (as revised in 2013).

#### *Fibroblast cultures*

Fibroblasts had been obtained previously for diagnostic purposes, using forearm punch biopsies. Cells were cultured in fibroblast culture medium (HAM F12 with 10% fetal bovine serum, penicillin (100 UI/ml) and streptomycin (100 µg/ml)), in a humidified incubator at 37°C and 5% CO<sub>2</sub>. Medium was changed every 3-4 days. Cells were split at 80% confluency.

#### *Positive Controls - Molecular Compounds*

To validate the specificity of the assays and features used for this project, molecular compounds were used as positive controls. Cells were incubated with 25 ng/ml Ethidiumbromide (Sigma Aldrich) for 7 days to deplete mitochondrial mass and FCCP (TargetMol) for 5 minutes to abolish membrane potential (3µM). Bafalomycin (Sigma Aldrich) was added at 0.2 µM for 8 hours to stimulate autophagosome accumulation. For ER stress, cells were incubated with Brefeldin A (Bio Legend) for 16 hours at a concentration of 10 µg/ml. To induce NF-κβ translocation, cells were stimulated with TNF-α for 30 minutes at a concentration of 20 ng/ml. To induce Golgi fragmentation, cells were incubated with Nocodazole (Sigma Aldrich) for 16 hours at a concentration of 0.3 µM.

#### *Imaging Flow Cytometry Assays in Fixed cells*

For IFC analysis, cells were collected using Accutase (Stempro) and fixed immediately with fix/perm buffer containing methanol (BD Biosciences). For the autophagy assay, cells were harvested, incubated in 0.5% saponin in PBS0 for 30 minutes, spun down, and fixed with 4% formaldehyde. For the NF-κβ assay, 4% formaldehyde was used instead of fix/perm buffer. Cells were stained using: LAMP1 (Abcam), LC3B (MBL International), ATF6 (Novus Biologicals), GM130 (Abcam), p65 (Cell Signaling Technology)

and DRAQ5 (Biolegend) in perm/wash buffer (BD Biosciences). For the NF- $\kappa$ B assay, PBS0 with 1% FBS and 0.1% triton-X-100 was used. For IFC analysis, cells were resuspended in 20  $\mu$ L of 1% FBS in PBS0 at a concentration of approximately 5000 cells/ $\mu$ L. The laser power of the 488 and 642 laser were adjusted to avoid saturation (pixel intensity <1500) and consistent voltages were maintained throughout experiments. Cells were acquired using the 60X magnification and low speed fluidics using the MKII Imagestream with Inspire (Version 201.1.0.765, Cytex Biosciences). Cells with a nuclear intensity >1x10<sup>5</sup> were processed for downstream analyses.

### *Imaging Flow Cytometry Assay in Living cells (Mitochondrial Assay)*

Cells were plated in 6-well plates to reach 70-80% confluency at the day of the assay. At the day of the assay, cells were incubated with the following antibodies TMRM (30 nM, Sigma Aldrich), NAO (50 nM, Enzo Life Sciences), DRAQ5 (Biolegend) at 37 degrees in HBSS for 40 minutes. FCCP (3  $\mu$ M, TargetMol) was added the last 5 minutes of incubation. After incubation, cells were washed once with PBS0 and incubated with TrypLE (Gibco) for 2 minutes. Cells were harvested using 1 mL 10% dialyzed FBS (Gibco) in PBS0, spun down, resuspended in small volumes (<30  $\mu$ L) and immediately visualized using IFC. Since lipophilic cations like TMRM are extruded by Multi Drug Resistance (MDR) transporters<sup>43</sup>, TMRM fluorescence is not stable for prolonged periods.<sup>44</sup> Therefore, we included 4 samples per experiment (one healthy control and one patient, two samples per donor (with and without FCCP)) and measured each sample for 2 minutes. This set-up allowed us to perform each IFC experiment within 30 minutes after the initial staining procedure.

The laser power of the 488 and 642 laser were adjusted to avoid saturation (pixel intensity <1500) and consistent voltages were maintained throughout experiments. Compensation files were created using single staining for all channels. Compensation settings were calculated using IDEAS software (Version 6.2, Cytex Biosciences). Cells were acquired using the 60X magnification and low speed fluidics using the MKII Imagestream with Inspire (Version 201.1.0.765, Cytex Biosciences). Cells with a nuclear intensity >1x10<sup>5</sup> were processed for downstream analyses.



### *IFC Data Analysis - IDEAS*

Data was analyzed using IDEAS software (Version 6.2, Cytex Biosciences). Gating strategy and masks used for each experiment can be found in **Supplementary Figure 3**. For each donor, >200 cells were analyzed. For mitochondrial mass and membrane potential, median pixel intensity of the NAO and the TMRM staining, respectively, were extracted for each donor. Each patient was compared to one healthy control counterpart analyzed in the same experiment. For all other assays, patients were compared with at least three healthy controls. To quantify Golgi functionality, the percentage of cells with intact Golgi system was calculated. To quantify autophagy, the mean spot count was extracted. To quantify NF- $\kappa$ B activity and ER stress, the percentage of cells with translocated p65/AF6 were compared between donors.

### *IFC Data Analysis in R*

To create figure 1, raw feature values for single cells were extracted from IDEAS as excel files, and analyzed using using R (Version 4.2.3) and R-studio (Version 2022.12.0.353). Before extraction of raw data, compensation was applied, and out of focus cells and doublets were removed using IDEAS. The boxplot in Figure 1 shows the non-normalized feature values per cell per condition. For Figure 2 and 3, similarity was calculated using Manhattan distance, and clustering was performed using average linkage clustering. Clustering performance was determined using the Elbow Method, by plotting the total intra-cluster variation (WSS) for each additional cluster. We configured UMAP with specific parameters, setting the number of neighbors to 8 and the minimum distance to 0.01, which were determined through exploratory analysis. To create Figure 4, raw feature values were extracted as .txt files. The mean value for each patient for each feature was divided by the mean value of all three healthy controls analyzed within the same experiment. The healthy control feature values were divided by the means of all other healthy controls analyzed within the same experiment. Columns containing significantly large foldchange values (<0.15 or >6) were removed. Before UMAP and clustering, the entire data frame was scaled and centered. For clustering analyses using 1800 features, similarity was

calculated using Euclidean distance, and clustering was performed using Ward's method. We configured UMAP with specific parameters, setting the number of neighbors to 4 and the minimum distance to 0.01, which were determined through exploratory analysis.

'Cluster characteristics' were determined by extracting features with a fold-change  $<0.5$  and  $>1.5$  in individuals included in the cluster. Highly correlating features were removed from the graph (Pearson correlation coefficient  $>0.9$ ) to enhance graph readability.

### *Functional assays for individuals with VUS in gene*

To validate the specificity of the IFC assays, functional assays were used. To assess pathogenicity of *CLN3* variants, lymphocytes with vacuoles and the number of vacuoles per lymphocytes were assessed as described previously. Data was acquired using FACSCanto II and analyzed using FACS Diva Version 6.13 (BD Biosciences) or FlowJo version 7.6.5 software.<sup>45</sup>

Quantification of MLCL/CL levels in individuals with *TAZ* variants was performed in dried blood spots using UHPLC-mass spectrometry.<sup>46</sup>

For individuals with *DLPI* variants, peroxisomes were examined with the use of immunofluorescence microscopy with antiserum against peroxisomal catalase.<sup>47</sup> To examine mitochondria, fibroblasts were cultured on coverslips, incubated for 30 minutes with 50 nM of MitoTracker Green FM dye (Molecular Probes) and examined with the use of fluorescence microscopy at 488 nm.<sup>26</sup> Autophagy defects were assessed in individuals with *EPG5* variants using western blot probed against LC3-I, LC3-II and p62.<sup>48</sup>

### *Clonogenic survival assays and stainings to detect $\gamma$ H2AX foci*

For clonogenic assays, fibroblasts were plated and treated 24 hours later, and then stained and counted 14-21 days later, when visible colonies had formed. All clonogenics were carried in 10cm dishes containing a feeder layer of  $5 \times 10^4$  fibroblasts irradiated with 35Gy. Cells were treated with etoposide (VP-16, Cayman Chemicals) for the indicated timeframes or irradiated with indicated doses using CellRAD (Faxitron). For imaging purposes, cells were plated in 24-well imaging plates, treated with etoposide (30  $\mu$ M, 30 min), washed, and released for the indicated period of time. After

treatments, cells were fixed in 4% paraformaldehyde for 10 min, permeabilized in phosphate-buffered saline (PBS)–0.2% Tween for 10 min, and blocked in PBS–5% bovine serum albumin (BSA) for at least 30 min. After 1 hour of incubation at room temperature with primary antibodies ( $\gamma$ H2AX, Cell Signaling Technology, 2577 and cyclin A, BD Biosciences, 611268), cells were washed in PBS–0.2% Tween three times and incubated with secondary antibodies for 45 min. After three more washes in PBS–0.2% Tween, nuclei were stained with 4',6-diamidino-2-phenylindole for 10 min. Images were acquired and analyzed using the Opera Phenix microscope. All quantifications were done in cyclin A negative cells representing G1 population.

#### *Data Analysis and Statistics*

To calculate statistics in **Figure 1**, nonlinear mixed effect models were used. Statistical analyses were performed using Prism (Version 9.3.0, GraphPad Software). Statistics were only calculated if the number of patients exceeded three. If not shown, statistics were not assessed.

The following R packages were used for analysis: umap (0.2.10.0), dplyr (1.1.3), ggplot2 (3.4.3), ggfortify (0.4.16), ggforce (0.4.1), cluster (2.1.4), factoextra (1.0.7), misctools (0.6-28), caret (6.0-94).

## **Results**

#### *Assay selection*

For this study, we included six essential cellular pathways that could be morphologically assessed, and for which a reliable marker was available. Selection criteria can be found in **Supplementary Table 1**. Out of 10 pathways eligible for inclusion in this study, we included six assays, that quantified morphology and function of mitochondria, autophagosomes, lysosomes, Golgi and ER stress/NF- $\kappa$ B translocation (**Table 1**). All assays were set up in primary dermal fibroblasts since these could easily be obtained from patients and their large cytoplasm allowed proper visualization of organelles.

#### *Assay and feature validation*

After optimizing antibody concentrations and assay conditions, we set out to

## Imaging Flow Cytometry for individual with VUS

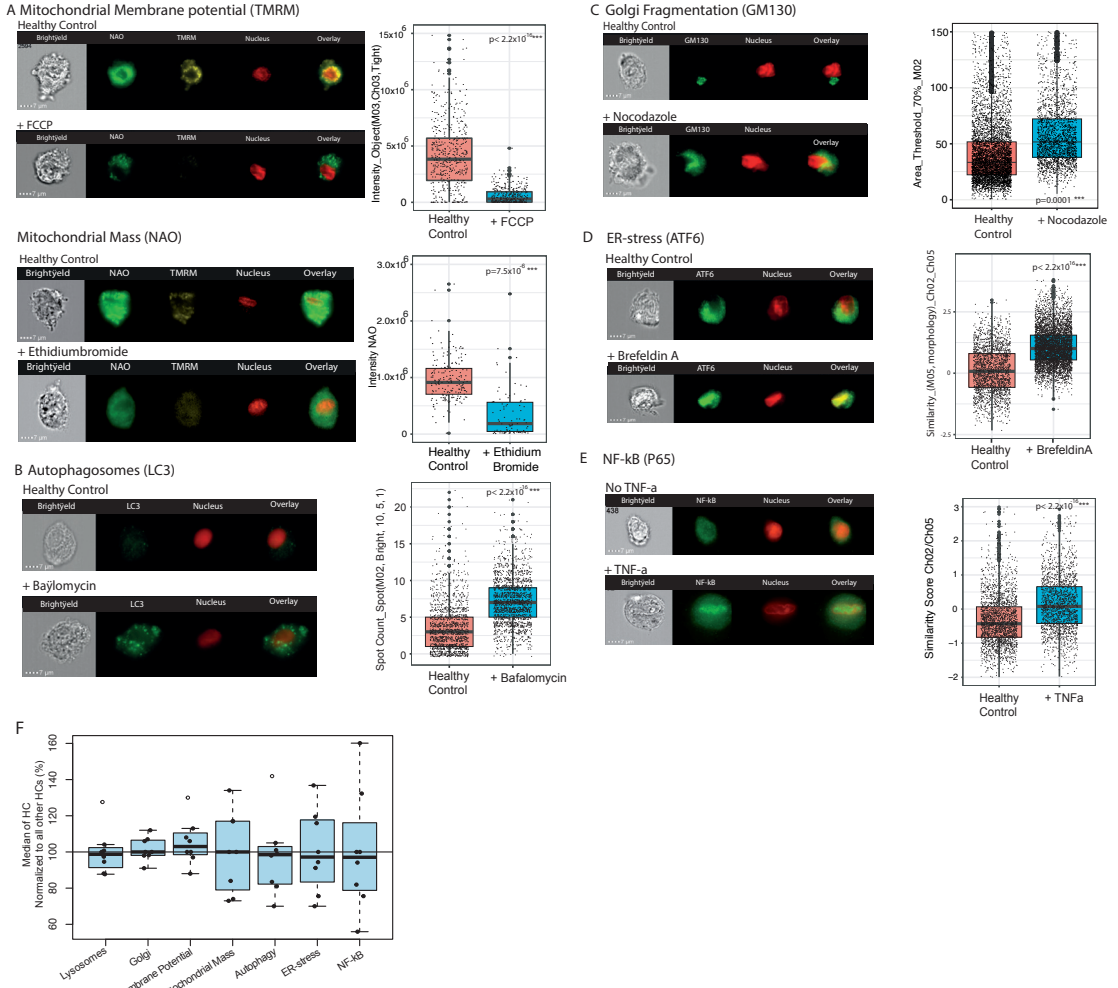
Primary assay	Marker	Molecular compound	Positive patient control
<b>Mitochondrial mass</b>	NAO	Valproic acid (Jang et al., 2021)	Polymerase- $\gamma$ pathogenic variants (Ashley et al., 2009)
<b>Membrane potential</b>	TMRM	FCCP (Park et al., 2002)	Mitochondrial disease patients with mt-TL1 or NDUSF4 pathogenic variants (Bakare et al., 2021; Distelmaier et al., 2009)
<b>Autophagy</b>	LC-3	Bafilomycin and starvation (Pugsley, 2017).	EPG5/Vici Syndrome (Cullup et al., 2013)
<b>Lysosomal Accumulation</b>	LAMP-1	NA	Batten Disease (Kuper et al., 2020)
<b>ER Stress</b>	ATF6	Brefeldin A (Di Pietro et al., 2017).	PMM2 pathogenic variants (Rita Lecca et al., 2005)
<b>Golgi fragmentation</b>	GM130	Nocodazole (Wortzel et al., 2017).	TRAPPC2L pathogenic variants (Scrivens et al., 2009)
<b>NF-<math>\kappa</math>B translocation</b>	p65	TNF- $\alpha$ (George et al., 2006)	NFKB1 pathogenic variants (Mandola et al 2021)

Table 1: Overview of the six IFtC assays quantifying six different aspects of cellular health. All assays were validated using compounds known to cause specific changes in the targeted pathway, serving as positive controls. Next, all assays were validated using patient cells, with diseases known to cause specific changes in the pathway of interest (Positive Patient Control)

evaluate whether the six assays were able to detect significant cellular changes in the selected pathways. As positive controls, we used a set of molecular compounds known to affect the specific pathways (**Figure 1A-E, Table 1**). For quantification, we used features and masks derived from literature (**Table 1**). For the LAMP1 assay, a novel feature and mask were designed based on two positive control patient fibroblasts. For each assay and feature, we found significant differences between healthy control fibroblasts with and without molecular compounds (**Figure 1A-E, Supplementary Table 2**), indicating specificity of assays and features. In the absence of a molecular compound known to induce lysosomal accumulation, validation of the LAMP1 assay was based on two positive control patients alone.

### *Establishing a healthy reference range and assessing the effect of passage number and confluence on IFC assays*

To assess interindividual variation and to set reference values as a benchmark, we included eight healthy control fibroblast lines (**Figure 1F**).



**Figure 1 Validation of assays using molecular compounds.** (A) Representative IFC images of the mitochondrial staining (NAO and TMRM). The top two images show NAO/TMRM staining before and after FCCP treatment. The boxplot shows the intensity of the TMRM staining within the Object mask, which was used to quantify membrane potential. The bottom two images show the NAO/TMRM staining before and after ethidium bromide treatment. The boxplot shows the intensity of the NAO staining for both conditions, which was used to quantify mitochondrial mass. (B) Representative IFC images of the autophagy staining (LC3). When autophagy is induced with bafilomycin, the autophagosomes become visible. The boxplot shows the number of autophagosomes per cell (Spot Count). (C) Representative IFC images of a cell with a healthy and intact Golgi and a cell with fragmented

Golgi after the addition of nocodazole. The boxplot shows the area of the Golgi staining after applying a 70% intensity threshold. During nocodazole treatment, the surface area of the Golgi system becomes larger, indicating that the Golgi system is fragmented. To quantify fragmentation, both surface area as well as minor axis were used (Supplementary Figure 3).

(D) Representative IFC images of the ATF6 staining. When ER-stress is triggered, ATF6 translocates to the nucleus. The boxplot shows the similarity between the nuclear staining and the ATF6 staining, which was used as a measure to quantify ER-stress.

(E) Representative IFC images of the NF- $\kappa$ B staining (p65). Upon NF- $\kappa$ B activation, p65 translocates to the nucleus. The boxplot shows the similarity between the nuclear staining and the p65 staining, which was used as a measure to quantify NF- $\kappa$ B translocation.

All boxplot represent one single experiment, and one treated and one untreated condition. The length and concentration of drug treatment are described in the Methods section. The boxplot upper and lower hinge reflect the 25% and 75% percentiles and the black line reflects the median. The upper and lower whisker extend to 1.5 \* IQR. Data beyond the end of the whiskers are plotted as large black circles. All statistics were calculated using nonlinear mixed effect models  $p < 0.001^{***}$ .

(F) Boxplots showing the natural variation of assays in healthy controls. The median value of the designated feature for each assay was compared to the mean all other healthy controls taken along in the same run and converted to percentages. The boxplot upper and lower hinge reflect the 25% and 75% percentiles and the black line reflects the median. The upper and lower whisker extend to 1.5 \* IQR. Data beyond the end of the whiskers are plotted as black circles.

For all assays, we found that variation in confluence - when kept within the advised confluence range (30%-80%) - did not significantly affect assay results ( $p > 0.05$ ). Passage number differences larger than five passages between donors were found to significantly affect Golgi fragmentation and mitochondrial function (Figure S2) (IQR < 25% or IQR > 75%). Therefore, for these two assays, we kept patient fibroblasts and healthy control fibroblasts at similar passage numbers (<5).

### *Cellular phenotypes are consistent among positive controls*

Next, we verified assay sensitivity through the inclusion of positive control patients. These individuals were chosen based on literature indicating that their respective diseases could trigger discernible alterations in one of the six assays (**Table 1**). We found all positive patient controls showed significant changes on the assays for which they were selected, indicating assay sensitivity (**Figure 2A, Supplementary Table 2**). Additionally, the similar changes observed in two siblings with Batten disease, both showing enlargement of the lysosomal compartment, and in fibroblasts of siblings

with Vici Syndrome, both displaying increased amounts of autophagosomes, indicates that assays are consistent among patients with the same disorder (**Figure 2A**). We suspected that aberrancies in positive patient controls extended beyond the cellular pathway for which they were primarily selected. For example, it is well-known that mitochondrial disease patients exhibit increased autophagy due to a pseudo-starvation response.<sup>23</sup> Indeed, we found that mitochondrial disease patients showed increased autophagy (**Figure 2B**). Moreover, patients with Vici syndrome (homozygous p.Arg1161\* variant in *EPG5*) showed decreased numbers of lysosomes (**Figure 2B**), corresponding with the pathophysiological mechanisms of Vici syndrome, associated with impaired autophagosome-lysosome transition.<sup>12</sup> Additionally, we found that patients with *EPG5* and *CLN3* pathogenic variants both showed increased ER stress (**Figure 2B**). Putatively, autophagic and lysosomal protein degradation is impaired in these patients, triggering ER stress.<sup>31</sup> Based on these results, we suspected that the combination of primary and secondary aberrancies would lead to more specific disease profiles. To evaluate the added benefit of using multiple assays, we assessed the performance of clustering algorithms when it comes to separating diseases from each other and from healthy controls. Indeed, we found that combining the six assays yielded specific clusters that corresponded with the specific diseases in the positive patient control cohort (**Figure 2C**). In contrast, clustering based on primary assay results alone did not allow separation of positive controls from healthy controls. Additionally, it mistakenly clustered the patient harboring *TRAPPC2L* pathogenic variants with mitochondrial disease patients.

#### *IFC screening of individuals with VUS(es) in well-known disease genes*

First, we assessed the potential of IFC assays for seven individuals with genetic variants classified as VUS(es) in well-known disease genes (VUS in gene) (**Supplementary Table 2**). For each fibroblast line of an individual with VUS (white rows in **Table 2**), fibroblasts of a patient with a pathogenic variant in the same gene (positive control counterpart) were included for comparison (green rows in **Table 2**). When using all six assays, we found that 6/7 individuals showed highly similar IFC profiles and clustered together with their positive control counterpart (**Figure 3A**). The two individuals with *CLN3* VUSes clustered towards pathogenic *CLN3* variants,

## Imaging Flow Cytometry for individual with VUS

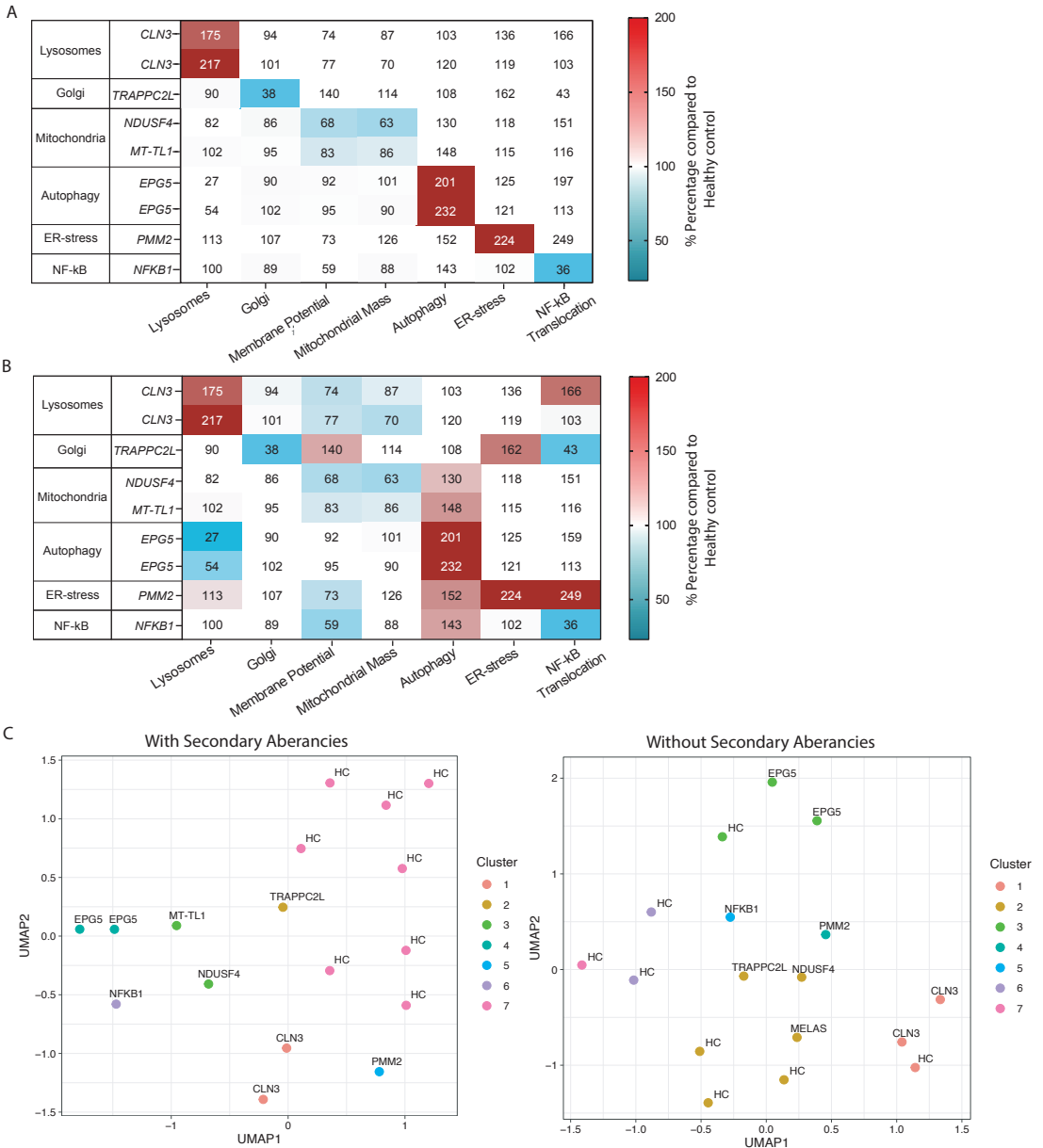


**Figure 2: Validation of assays in positive control patients.** (A) Heatmap showing the values for each assay for the positive control patients compared to healthy controls (N=3) taken along in the same experiment. Each experiment was performed once. The primary aberrancies



for the positive control patients are colored using a color gradient (0%-200%). (B) Showing a similar heatmap as in (A), but here the secondary aberrancies are also colored according to the same scale as in figure 2A. (C) UMAP plots (Manhattan distance, neighbors=8, minimal distance=0.01) showing the clustering performance when combining all six assays (left), or when only the primary assay aberrancies were used (right). Clustering was performed using Manhattan Distance followed by average linkage clustering. Input for the plots were the percentage values as shown in Figure 2C. For the UMAP plot and clustering based on the primary aberrancies only, secondary aberrancies were set to 100% (secondary aberrancies include all values shown in grey in Figure 2B).

all of whom showed increased lysosomal size (**Figure 3B**). The individual with *ACAD9* VUS and its positive control counterpart both showed increased Golgi fragmentation, increased ER stress and decreased autophagy, and clustered together (**Figure 3C**). Two individuals with *DLP1* VUSes clustered with the patient with pathogenic *DLP1* variants, based on

Patient ID	Gene	Golgi	ER-stress	Autophagy	LAMP1	Membrane Potential	Mitochondrial Mass	NFKB
33	<i>CLN3</i>	94%	136%	103%	175%	74%	87%	166%
34	<i>CLN3</i>	101%	119%	120%	217%	77%	70%	103%
31	<i>CLN3</i> VUS	106%	147%	111%	213%	84%	88%	234%
35	<i>CLN3</i> VUS	103%	108%	87%	167%	127%	122%	106%
07	<i>EPG5</i>	90%	125%	201%	27%	92%	101%	159%
08	<i>EPG5</i>	102%	121%	232%	54%	95%	90%	113%
250	<i>EPG5</i> VUS	97%	135%	152%	83%	85%	89%	98%
252	<i>DLP1</i>	99%	111%	99%	78%	79%	76%	140%
249	<i>DLP1</i> VUS	106%	114%	106%	97%	60%	62%	139%
253	<i>DLP1</i> VUS	89%	132%	94%	108%	90%	72%	146%
251	<i>TAZ</i>	116%	102%	116%	79%	87%	62%	58%
240	<i>TAZ</i> VUS	122%	160%	124%	112%	82%	67%	52%
261	<i>ACAD9</i>	51%	182%	77%	99%	103%	86%	65%
111	<i>ACAD9</i> VUS	39%	158%	46%	101%	116%	84%	57%

**Table 2:** Showing the IFC assays results in individuals with VUS in known disease genes and positive control patients. The white rows represent individuals with VUS, the green rows represent their positive control counterparts. The population means in individuals were compared to healthy controls and shown here as percentages.

# Imaging Flow Cytometry for individual with VUS

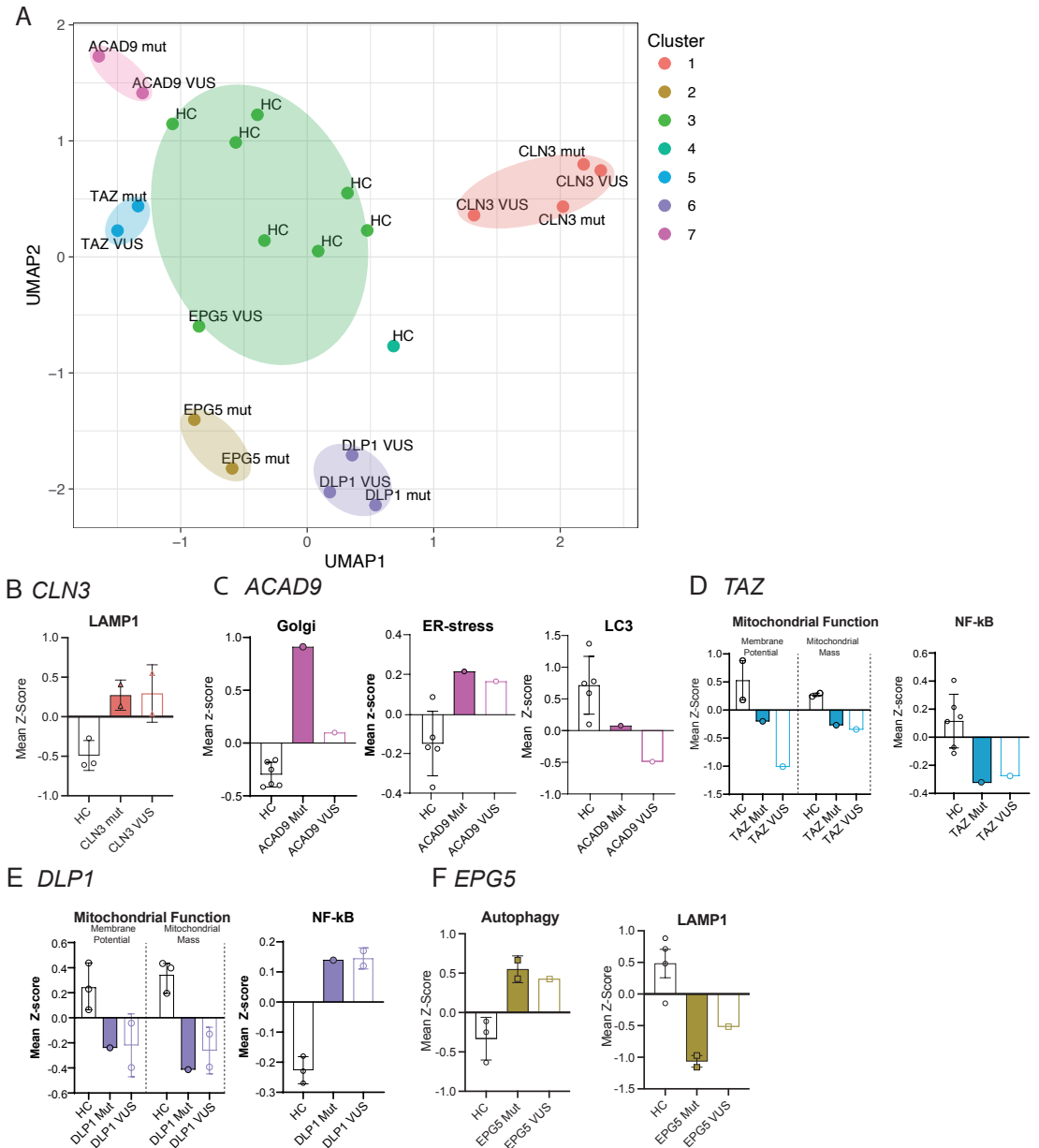


**Figure 3: Imaging Flow Cytometry (IFC) results of individuals with VUS in well-known disease genes.**

(A) UMAP plot (Manhattan distance, neighbors=8, minimal distance=0.01) showing the healthy controls (HC), individuals with VUS(es) and positive control counterparts matching the individuals with VUS in well-known disease genes. Normalized percentage values as shown in Table 2 were first scaled and used as input for UMAP. Most individuals with VUS clustered together with their positive control counterparts on UMAP, suggesting similar underlying mechanisms of disease. Only the individual with *EPG5* VUS clustered with healthy controls. (B) Bar graph showing aberrancies for two patients with pathogenic variants in *CLN3* (*CLN3* mut) and individuals with *CLN3* VUSes (*CLN3* VUS). (C) Bar graph showing the Z-scores of the individual with *ACAD9* VUS and its positive control counterpart (one patient with pathogenic *ACAD9* variants) for Golgi, NF- $\kappa$ B and mitochondrial assay. (D) Bar graph showing aberrancies for one patient with pathogenic variant in *TAZ* (*TAZ* mut) and one individual with *TAZ* VUS (*TAZ* VUS) for Golgi and mitochondrial assays. (E) Bar graph showing the Z-scores of the individuals with *DLPI* VUS and their positive control counterpart (one patient with pathogenic *DLPI* variant) for the NF- $\kappa$ B and the mitochondrial assay. (F) Bar graph showing the Z-scores for the individual with *EPG5* VUS and two patients harboring pathogenic *EPG5* variants for the autophagy assay (LC3 - Spot Count) and LAMP1 assay (LAMP1 - Internalization) For all bar charts, the raw values for each experiment were converted to Z-scores. The mean of all single cell Z-scores was calculated for each individual. The bars represent the mean and the error bars represent the range for healthy controls, individuals with VUS or patients with pathogenic variants. Each dot represents the mean z-score per donor. Each experiment was performed once, and at least three healthy controls were included for each experiment, except for the mitochondrial experiment, where only one healthy control was included.

mitochondrial dysfunction and decreased NF- $\kappa$ B translocation (**Figure 3E**). *TAZ* and *DLP1* dysfunction were expected to predominantly result in mitochondrial dysfunction<sup>11,32</sup>. While both cohorts indeed presented with mitochondrial dysfunction, differences in NF- $\kappa$ B activation helped separate the individuals with *DLPI* variants from individuals with *TAZ* variants (**Figure 3D/E**). The individual with *EPG5* VUS clustered with healthy controls instead of pathogenic *EPG5* variants, probably due to the mildly increased autophagy compared to patients with pathogenic *EPG5* variants (**Figure 3F**). Thus, IFC-based screening revealed highly specific phenotypic profiles for individuals with VUS, that allowed clustering with their positive control counterpart, indicative of pathogenicity. Only the individual with *EPG5* VUS showed similar – but much milder – aberrancies and was clustered with healthy controls.

In order to verify the performance of IFC-assay based clustering, we validated whether the VUS(es) were truly pathogenic using well-established diagnostic assays. With the inclusion of these well-established functional results (PS3), all VUS(es) could be classified as pathogenic or likely pathogenic according

to the ACMG guidelines, except for the *EPG5* VUS, that remained classified as VUS (**Supplementary Table 2**). Individuals with *CLN3* VUS harboring a large 1kb deletion in *CLN3* showed increased number of vacuoles per lymphocyte and increased percentage of lymphocytes with vacuoles, indicating pathogenicity (**Supplementary Figure 4**). The *TAZ* variant was classified as pathogenic due to its severely increased MLCL/CL ratio (**Supplementary Figure 4**). For the *ACAD9* VUS, functional studies showed that the mis-sense variant in this patient causes mildly decreased *ACAD9* activity (70% residual activity compared to WT-*ACAD9*)<sup>27</sup>. Individuals 249 and 253, both harboring heterozygous missense *DLP1* variants, showed mild mitochondrial fission and peroxisomal aberrancies upon microscopy, characteristic of *DLP1* dysfunction. Individual 253 lacked the peroxisomal aberrancies typically seen, suggesting that the variants in this patients might have a milder impact on overall protein function. Concurrently, IFC-screening revealed mild aberrancies for individual 253. All *DLP1* variants were considered pathogenic based on ACMG guidelines (**Supplementary Table 2**). Individual 250 harbored a homozygous missense *EPG5* variant. Western blot probed against p62/LC3 revealed only mildly increased autophagy for this individual. Based on these results and ACMG guidelines, the variant was classified as VUS (**Supplementary Table 2**).

Thus, IFC assays correctly clustered individuals with *CLN3*, *TAZ*, *DLP1* and *ACAD9* VUS with their positive control counterparts, based on diagnostic assay results and ACMG guidelines. The uncertain pathogenicity of the *EPG5* variants was reflected in IFC assays, indicating the variant might result in a very mild cellular phenotype or is not pathogenic.

### *IFC assays for individuals with VUS in GUS*

Next, we assessed the potential of our platform for individuals that did not harbor VUSes in well-known disease genes (**Supplementary Table 4**). We found all individuals in this group showed aberrancies on at least one of the six assays (**Table 3**). To allow better understanding of the IFC aberrancies found, we assessed whether fibroblasts of these individuals behaved analogously to any of the positive control patient fibroblasts used in this study.

As expected, we did not identify relevant cluster formation (**Figure 4A**). However, we did find seven individuals with VUS showing a unique combination of IFC aberrancies, leading to them being clustered individually. In contrast, all other individuals with VUS showed only very mild differences and clustered with healthy controls (**Figure 4A**).

To increase the possibility of relevant cluster formation, we introduced a novel patient control with a DNA damage repair defect, assumed to have a similar phenotype as one of the individuals harboring a VUS in a gene associated with DNA damage repair (106, VUS in *RAD54L2*<sup>28</sup>). To this aim, we included fibroblasts of a patient with a pathogenic variant in the *ERCC1* gene, c.693C>G<sup>29</sup>). We found that individual 106, but also individual 211, clustered with the patient with pathogenic *ERCC1* variants, based on decreased mitochondrial function and decreased Golgi fragmentation (**Figure 4B**). These similarities suggest that the VUSes identified in individual 106 and 211 might lead to defective DNA damage repair.

Patient ID	Gene	Golgi	ER-stress	Autophagy	LAMP1	Membrane Potential	Mitochondrial Mass	NFKB
143	<i>CSDE1</i>	32%	72%	112%	62%	47%	79%	149%
140	<i>LIMK1</i>	112%	173%	90%	153%	138%	66%	160%
093	<i>LIMK1</i>	98%	145%	95%	158%	98%	119%	111%
225	<i>ZNF806</i>	63%	186%	81%	135%	68%	48%	167%
227	<i>PDE3B</i>	112%	141%	154%	130%	119%	95%	167%
228	<i>MMS19</i>	112%	142%	99%	106%	96%	146%	201%
034	NA	99%	113%	126%	146%	63%	153%	183%
211	<i>DLGAP2, TNKS, BLM</i>	118%	107%	88%	75%	73%	48%	109%
106	<i>RAD54L2</i>	105%	111%	90%	106%	81%	77%	69%
226	<i>PDE4DIP</i>	90%	33%	124%	152%	127%	97%	66%
216	NA	114%	152%	111%	104%	124%	99%	79%
202	<i>MEIOC</i>	132%	78%	95%	81%	101%	101%	97%
217	<i>EIF4ENIF1</i>	109%	82%	106%	68%	100%	66%	111%

**Table 3:** Showing the individuals with VUS included in Group 2. The population means in these individuals were compared to healthy controls and shown as percentages. For each of the six assays, the features as shown in Table 2 were used for quantification. Red and blue values indicate the values are outside the reference range measured in healthy controls.

# Imaging Flow Cytometry for individual with VUS

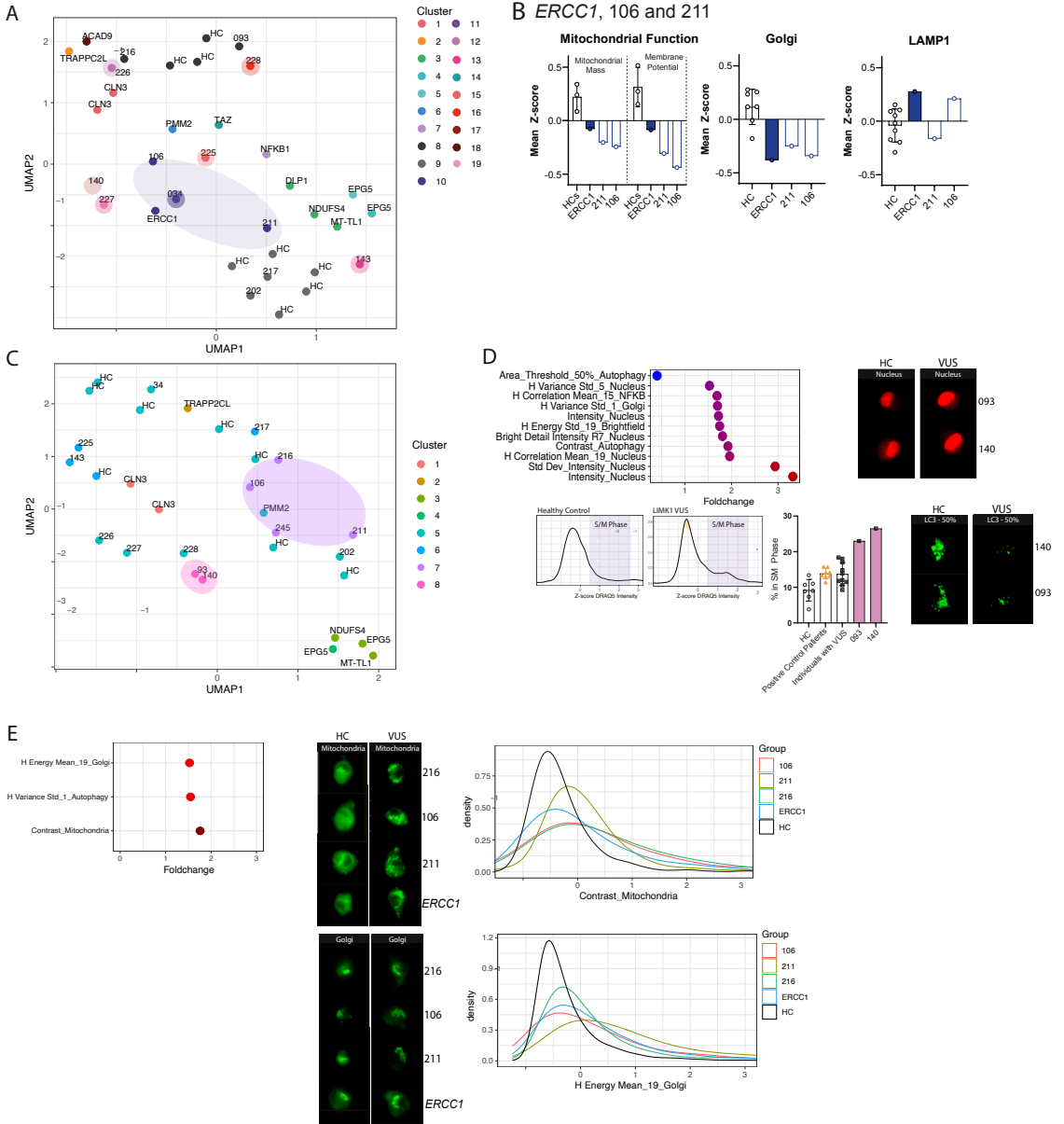


**Figure 4: Imaging Flow Cytometry results for individuals with VUS in GUS.** (A) UMAP showing clustering based on six assays for healthy controls (HC), positive control patients, and 13 individuals with VUS in GUS. Normalized percentage values as shown in Table 3 were scaled and used as input for UMAP.

(B) Bar graph showing the Z-scores of individual 106, 211 and patient with pathogenic ERCC1 variants, for the Golgi, LAMP1 and mitochondrial assay. For the bar charts, the raw values for each experiment were converted to Z-scores. The mean of all single cell Z-scores was calculated for each individual. The bars represent the mean and the error bars represent the range for healthy controls, individuals with VUS or patients with pathogenic variants. Each dot represents the mean z-score per donor. Each experiment was performed once, and at least three healthy controls were included for each experiment, except for the mitochondrial experiment, where only one healthy control was included. (C) UMAP of the healthy controls (HC), positive control patients, and the individuals with VUS in GUS. To create the plot, all 1800 features were used, including those quantifying nuclear and brightfield intensity and morphology. Each patient was normalized against three healthy controls taken along in the same experiment. The circles were drawn using the ggforce package. (D) Showing the cluster characteristics of the cluster with the individuals with LIMK1 genetic variants (093 and 140). The dot plot on the left shows the features with foldchange  $<0.5$  and  $>1.5$  in both individuals compared to healthy controls. The median foldchange values for the two individuals is shown. Highly correlating features were removed from the graph (Pearson correlation coefficient  $>0.9$ ) to enhance graph readability. The increased nuclear intensity observed in both individuals with LIMK1 genetic variants suggests increased numbers of cells in S/M phase. The histogram plot shows the distribution of nuclear intensity for single cells. For this plot, healthy controls (N=3) were merged, and individuals with LIMK1 VUS were merged (N=2). The purple square indicates the gating that was used to determine the percentage of cells that were in the S/M phase. The bar chart shows the percentage of cells in S/M phase for each patient. Each dot represents the percentage of cell in S/M phase per donor. On the right, two representative examples of the autophagy staining are shown. For the images, the intensity threshold was set at 50%. (E) Showing the cluster characteristics of the cluster of the patient with pathogenic ERCC1 variant and individuals 106, 211 and 216. The dot plot on the left shows the features with foldchange  $<0.5$  and  $>1.5$  in both individuals compared to healthy controls. The median foldchange values for the individuals is shown. Features with Pearson correlation coefficient  $>0.9$  were removed to enhance graph readability. The histogram plot shows the distribution of the Contrast feature for healthy controls (N=3) and individuals 106, 211 and 216. On the right, representative examples of IFC images of healthy control fibroblasts and individual 106 and 211 are shown. The histogram plot on the far right shows the distribution of the H Energy Std\_5 of the autophagy staining for healthy controls (N=3) and individuals 106 and 211. On the right, representative examples of IFC images of healthy control fibroblasts and individual 106 and 211 are shown.

The six selected features may offer only a limited representation of all quantifiable changes that can occur in individuals with VUS. For example, alterations in the distribution, size or shape of organelles may occur. Consequently, alongside a targeted analysis based on six assays, we employed a broadened, untargeted approach, that allowed quantification of many aspects of each of the six cellular pathways. To this aim, we extracted all built-in IDEAS features derived from all six assays (~300 features per assay, 1800 features in total), including those quantifying nuclear and brightfield images (**Supplementary Table 3**). To minimize batch effects, we normalized each individual to the healthy controls taken along in the same experiment (**Supplementary Figure 5**). Using all 1800 features, we identified three clusters of individuals with VUS that clustered away from healthy controls (**Figure 4C**).

The first cluster consisted of two individuals (093 and 140), both harboring *LIMK1* genetic variants. We found that this was mostly the result of altered nuclear morphology and intensity (**Figure 4D**). Most notably, nuclear intensity (DRAQ5 intensity) was increased in these individuals, suggesting increased DNA content, and thus an increased number of dividing cells (S/M phase). After quantification of the number of cells in G1/S/M phase using DRAQ5 nuclear intensity (2N/4N peaks), we found that the individuals with *LIMK1* genetic variants had increased percentages of dividing cells (S/M phase) (**Figure 4D**). Another characteristic of the cluster became visible when LC3 (autophagy staining) intensity threshold was set at 50%, revealing a lower total area of the autophagy staining.

The second cluster identified was similar as one of the clusters identified when using all six assays. Again, we found the cluster included the patient with pathogenic *ERCCI* variants and individuals 106 and 211. Additionally, individual 216 was added to this cluster (**Figure 4E**). The cluster was characterized by enhanced contrast of the mitochondrial staining (NAO) and altered texture of autophagosomes and the Golgi system (**Figure 4E**). Texture was quantified using Haralick (H) features<sup>30</sup>, using different pixel sizes. Notably, one of the finer texture attributes (pixel size 1, H Variance Standard Deviation) showed significant alterations in the autophagy assay. Moreover, there were notable changes for the larger texture attributes of the Golgi assay (pixel size 19, H



Energy Mean), corresponding to the observed disarray and irregular borders of the Golgi system, which were evident upon visual inspection (**Figure 4E**). These irregular borders could have potentially affected the quantification of Golgi area and diameter, particularly following the application of a 70% threshold, which might explain the diminished Golgi fragmentation that characterized this cluster when looking at six features only.

To study whether the second cluster indeed correlated with DNA damage repair diseases, we performed follow-up experiments. For individual 106 that harbored a VUS in *RAD54L2* (NM\_015106.2: c.389A>G, p.Gln130Arg) and clustered with the patient with pathogenic *ERCC1* variants, we assessed DNA damage repair capacity. We focused on DNA damage repair capacity after X-ray irradiation and etoposide treatment, a chemotherapeutic agent that stabilizes DNA topoisomerase II cleavage complexes (TOP2ccs), as *RAD54L2* is involved in TOP2cc resolution.<sup>28,31</sup> For comparison, we included patient fibroblasts of a patient with pathogenic *TDP2* variants, since *TDP2* is also involved in TOP2cc resolution and similarly shows increased sensitivity to etoposide.<sup>32</sup> While survival after X-ray irradiation was not appreciably affected, we observed decreased survival of fibroblasts from the individual with *RAD54L2* VUS upon etoposide treatment compared to control cells (**Figure 5A, B**). In addition, compared to control cells, we observed increased  $\gamma$ H2AX foci in patient-derived fibroblasts of individual 106 immediately after etoposide treatment (0 hour), which normalized after 4 and 8 hours (**Figure 5C**). Additionally, we did not observe any changes in  $\gamma$ H2AX foci levels in individual 106 upon treatment with ionizing radiations, in agreement to the survival data (**Figure 5D**). Based on these specific functional results, we concluded that the *RAD54L2* VUS was indeed pathogenic (ACMG: PS4, PS3, PM2, PP3).

The third cluster we observed consisted of individuals 225, 143, 217 and one healthy control. The cluster was characterized by slightly decreased mitochondrial mass values (data not shown). Due to the presence of a healthy control in the cluster we decided not to study this cluster in depth.

In conclusion, we found that integrating all available IFC features (N=1800) yielded two interesting clusters with distinct morphological aberrancies. In the individuals harboring *LIMK1* variants, we found increased mitosis and

## Imaging Flow Cytometry for individual with VUS

less bright autophagosomes. For individuals 211, 106 and 216, we found significant overlap with a patient harboring pathogenic ERCC1 variants, characterized by altered Golgi- and mitochondrial morphology, which could be related to underlying DNA Damage Repair defects. Indeed, we found that one individual in this cluster harboring a VUS in *RAD54L2* showed decreased survival and increased  $\gamma$ H2AX foci after treatment with the

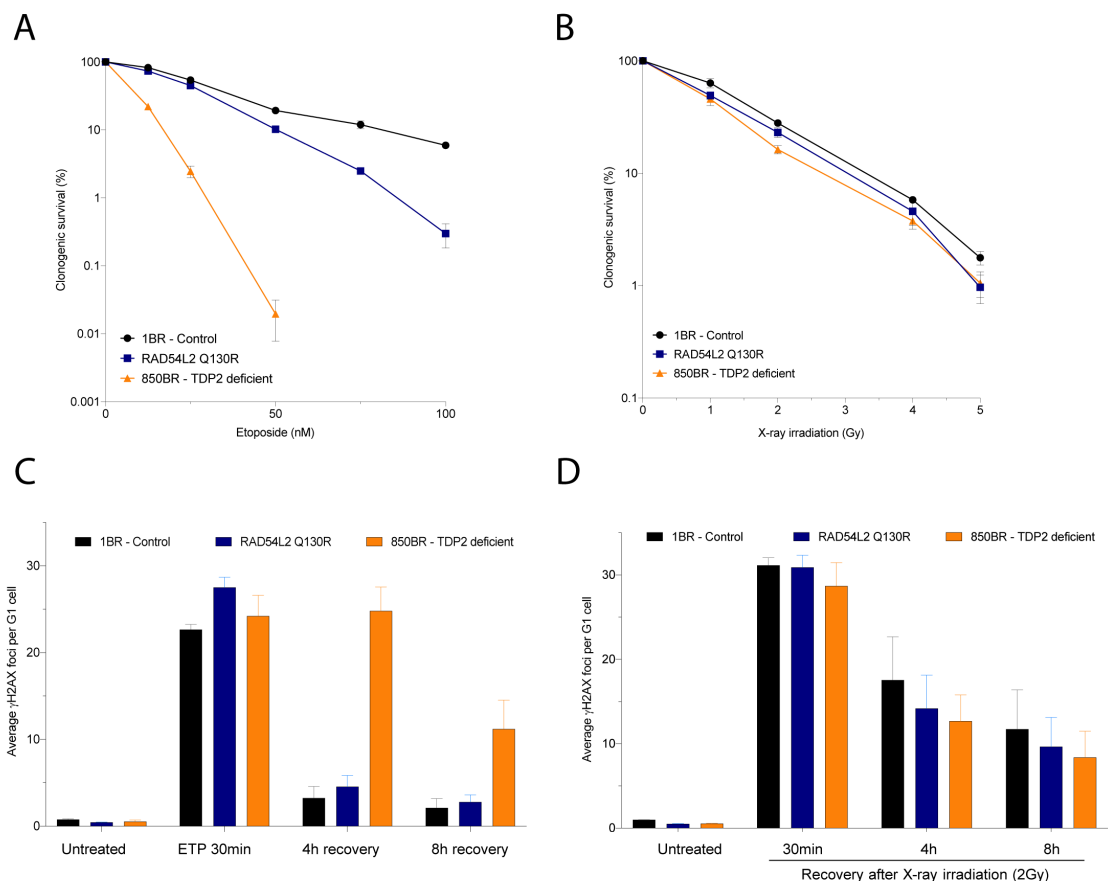


**Figure 5: Assessing pathogenicity of fibroblasts derived from individual 106.**

(A-B) Clonogenic survival assay of patient fibroblasts upon treatment with the indicated doses of etoposide (A) or X-ray irradiation (B). (C) Number of  $\gamma$ H2AX foci in G1 cells (cyclin A negative) untreated or treated with 30  $\mu$ M etoposide (ETP) for 30 min, washed, and left to recover for 4 or 8 hours. n = 3 independent experiments. Bars represent means  $\pm$  SEM. (D) Number of  $\gamma$ H2AX foci in G1 cells (cyclin A negative) untreated or irradiated with 2Gy X-rays and left to recover for 30 minutes, 4 or 8 hours. n = 4 independent experiments. Bars represent means  $\pm$  SEM.

chemotherapeutic agent etoposide, in agreement with its mechanism on TOP2 damage reversal recently elucidated.<sup>28</sup>

## Discussion

Here, we describe a novel Imaging Flow Cytometry (IFC)-based screening platform, aimed to delineate the clinical significance of Variants of Uncertain Significance (VUS) by providing insights into six pivotal cellular processes. We found that both compounds as well as positive control patients showed significant changes on cognate assays, indicating assay sensitivity, and combining the six assays enhanced clustering performance. For all individuals with VUS(es) in well-known disease genes, IFC-based screening identified similar aberrancies compared to corresponding positive controls, that aligned with diagnostic assay results, suggesting that IFC allows for accurate pathogenicity prediction. For individuals with VUS(es) in Genes of Uncertain Significance, we found significant changes for each individual on one or more of six assays, which could be used to structure follow-up assays. Additionally, we found two relevant clusters that granted insights into highly specific pathophysiological mechanisms, for example by uncovering mitosis defects or DNA damage repair defects. Based on these results, we propose that IFC-based functional screening allows for high-throughput characterization of cellular phenotypes, which can contribute to disease elucidation and subsequent diagnosis for individuals with VUS.

We found IFC aberrancies for all 13 individuals with VUS in GUS, all of which could serve as a basis to structure subsequent experiments. However, the inclusion of a relevant control (DNA damage repair defect) to complement individuals with VUS in genes associated with DNA damage repair, provided a clearer picture of the potential pathophysiology involved. Both the mitochondrial dysfunction and the altered Golgi morphology, that characterized the cluster, have been observed in patients with DNA damage repair defects, including *ERCCI* knockout models.<sup>33,34</sup> Thus, the combination of mitochondrial dysfunction and altered Golgi morphology might be specific for DNA damage repair defects. One of the individuals in

## Imaging Flow Cytometry for individual with VUS

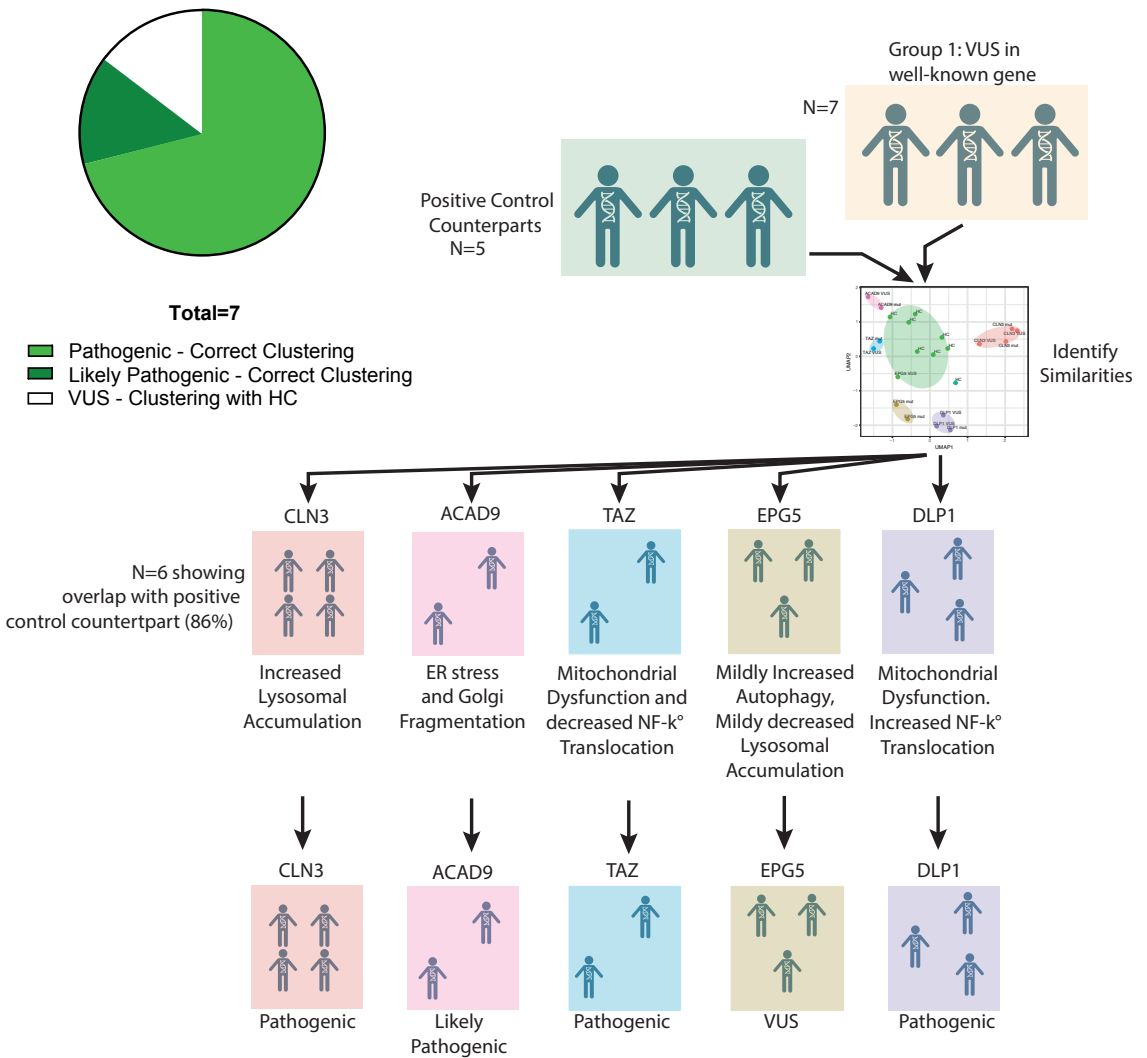


**Figure 5: Overview of Imaging Flow Cytometry results for individuals with VUS**

The Pie chart indicates the number on individuals with VUS in well-known disease genes that were correctly clustered with its pathogenic counterpart based on diagnostic assay results, leading to the VUSes being classified as pathogenic or probably pathogenic based on ACMG guidelines. Only one individual was clustered with Healthy Controls (HC). Diagnostic assays were inconclusive and the variant remained classified as VUS. The colored planes indicate the significant changes that were identified with IFC (upper row) and the ACMG classification of VUSes (lower row).

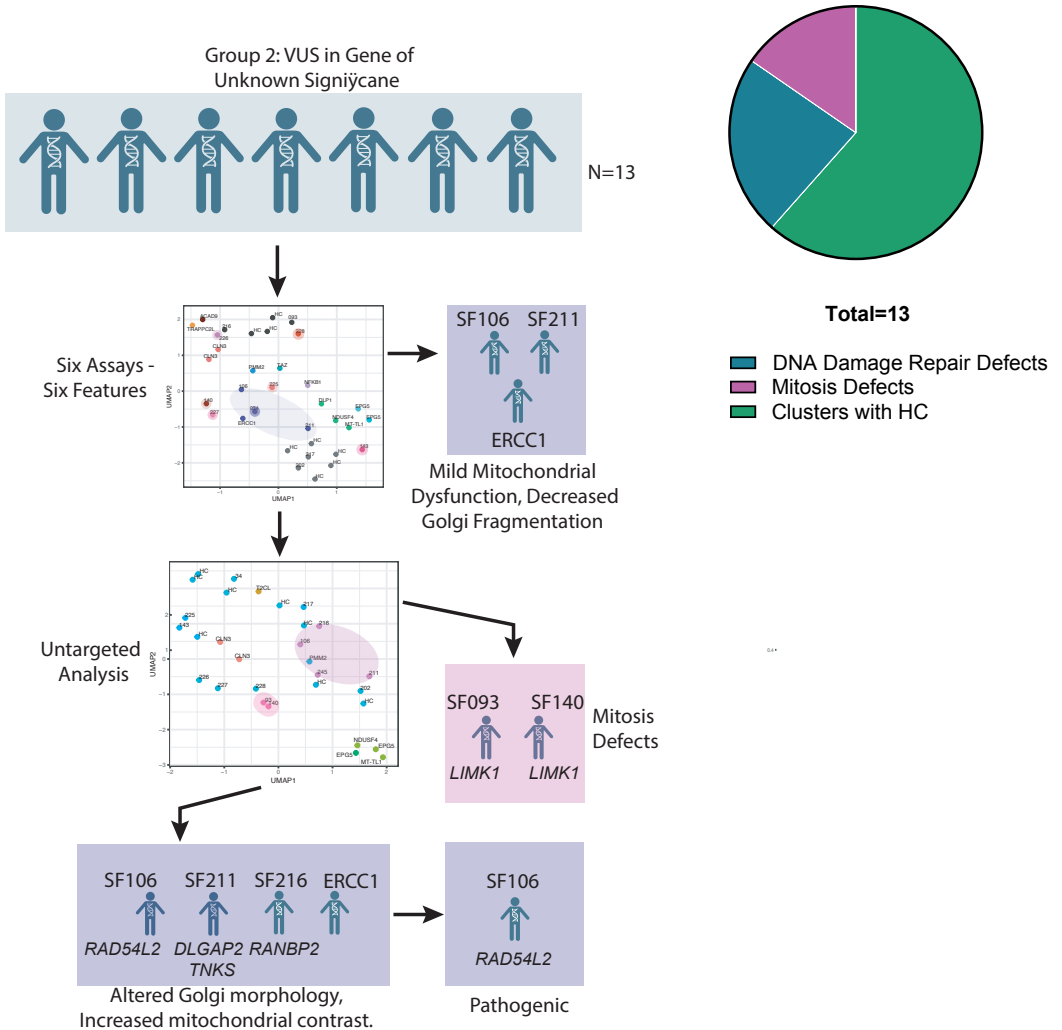


**Figure 5: Overview of Imaging Flow Cytometry results for individuals with VUS**

Pie chart indicating the clusters identified with IFC assays for individuals with VUS in Genes of Uncertain Significance (GUS). Three individuals clustered with the patient with pathogenic ERCC1 variants presumably based on altered DNA damage response, two individuals clustered together based on striking mitosis defects and the rest of the individuals clustered with healthy controls based on 1800 features. The colored planes indicate the significant changes found with IFC.

the cluster, individual 106, harbored a de novo variant in *RAD54L2*, which interacts with TOP2 to alleviate DNA damage.<sup>28,31</sup> Functional assays showed that fibroblasts from this individual displayed increased  $\gamma$ H2AX foci and decreased survival after treatment with etoposide, suggesting individual 106 indeed exhibits a DNA damage repair defect. Additionally, these results suggest that the VUS in *RAD54L2* is most likely causative of the patient's clinical phenotype. Another individual included in the cluster, individual 211, harbored multiple VUSes in the *DLGAP2*, *TNKS*, and *BLM* gene. Of these, *BLM* is a well-known disease gene, with bi-allelic variants leading to Bloom syndrome, a well-known DNA damage repair defect (OMIM #210900). While the patient was solely a carrier of a pathogenic *BLM* variant, carriers of *BLM* variants can also exhibit mild DNA damage repair defects.<sup>35</sup> Potentially, this explains its clustering with other DNA damage related diseases. However, *TNKS* also has a role in DNA damage repair, and could have contributed to the phenotype as well.<sup>36</sup> However, the similar cellular phenotypes observed in individuals 106, 211, and the patient with pathogenic *ERCC1* variants could reflect similar functional cellular changes in response to impeded DNA damage repair, providing a relevant basis for further functional exploration. Additionally, these results indicate that the inclusion of relevant positive controls increases the diagnostic yield of IFC assays.

To broaden the scope of the IFC-based assays, we included all 1800 predefined IDEAS software-included features instead of just six. This untargeted approach led to the identification of two novel clusters. The first cluster consisted of two individuals harboring *LIMK1* variants, showing increased intensity of the nuclear (DNA) staining, suggesting that there was an increased number of cells in SM phase. Concurrently, LIMK1 dysfunction has been associated with mitosis defects due to defective spindle positioning.<sup>35</sup> Therefore, the mitosis defects uncovered by IFC could indicate that the *LIMK1* variants identified in both individuals cause similar underlying pathophysiological defects. The second cluster identified when using the 1800 features was highly similar to the cluster found when using six features only, consisting of individuals 106, 211 and the patient with pathogenic *ERCC1* variants. Again, the cluster was characterized by altered Golgi and

mitochondrial features, although the inclusion of 1800 features led to more precise quantification of these aberrancies, showing enhanced contrast of the mitochondrial staining and disorganized Golgi integrity. Additionally, expanding the scope to 1800 features led to the addition of individual 216 to the ‘DNA damage cohort’, although the absence of candidate VUSes in this individual limited the interpretation of its relevance. Nonetheless, based on these results, we propose that studying all 1800 features leads to the identification of more specific cellular phenotypes, which could be exploited to structure follow-up studies in a more targeted fashion. The inclusion of additional positive controls and optimized feature extraction strategies might aid pathophysiology elucidation in a larger number of individuals.

So far, a limited number of studies have explored the potential of microscopy to determine the significance of VUS. Chao et al., quantified the cellular location of PTEN in Hela cells with different *PTEN* VUS to discern pathogenic variants from benign ones. Similarly, Ebrahimi-Fakhari et al. (2021) used microscopy to quantify ATG9A distribution, which helped to discern pathogenic *ATG9A* variants. While both studies seemed promising, their focus on a single gene limits general clinical applicability, since the genetic heterogeneity seen in most patient populations will require an untargeted approach. Fortunately, untargeted microscopic approaches have also been explored for VUS elucidation, although not in pediatric patients. Caicedo et al. (2022) found high accuracy when using microscopic screening to detect the pathogenicity of lung cancer variants using Cell Painting (RNA, ER, mitochondria, DNA and highly glycosylated proteins (AGPs) staining), while Ohya et al. (2005) and Rohban et al. (2017b) found highly specific microscopic phenotypes after introducing various genetic deletions, that correlated with underlying pathophysiology. While these results are promising, the strong phenotype induced by deletion of entire genes or the formation of lung cancer is relatively easy to capture with microscopy. The question remains whether untargeted microscopy would be able to classify milder phenotypes as well and can be used for diagnosis. While the higher resolution of microscopy in comparison to IFC could add another layer of information when studying individuals with VUS, the question remains whether the

enhanced complexity and computational skills needed to interpret microscopic data are proportionate to that.

For individuals with VUS in well-known disease genes, we found that IFC assays were able to detect relevant overlap with patients with pathogenic variants in the same gene, aiding the interpretation of pathogenicity. The differentiating power of IFC for these individuals was enhanced by combining the six assays, since certain diseases appeared similar when looking at single axes only. For example, patients with pathogenic *DLPI* or *TAZ* variants primarily showed mitochondrial dysfunction, however, the increased versus decreased NF- $\kappa$ B translocation made them cluster separately. These differentiating features are in line with previous work, showing decreased NF- $\kappa$ B activation in tafazzin knockout iPSCs, putatively as a consequence of altered mitochondrial ROS signaling.<sup>43</sup> In contrast, HEK293 cells expressing mutant *DLPI* showed increased mitochondrial fusion and increased NF- $\kappa$ B activity.<sup>44</sup> Thus, the integration of six assays provided enhanced discriminatory power, and revealed relevant underlying disease mechanisms for individuals with VUSes in well-known genes.

To formally assess diagnostic accuracy, the question remains whether solely the significant changes outside the healthy control range should be used to diagnose patients, or that diagnostic validation of complete disease profiles using trained classification models is needed, which will require the inclusion of substantial patient numbers. That being said, most genetic diseases are rare, and including sufficient numbers to allow accurate pathogenicity prediction will remain challenging. Potentially, the use of single cell results rather than bulk medians will help to gather sufficient numbers to train classification models, although this will require optimization of batch effects, normalization, and noise filtering steps. Regardless, we expect a combination of in-silico prediction tools, functional cellular models and the interpretation by expert clinicians will remain essential for the final judgement of pathogenicity prediction. Additionally, most endeavors to elucidate VUS nowadays exist of multiple experiments, where IFC-based assays could serve as the first step to structure these experiments. It will remain challenging



to accurately quantify the value of having a valid starting point, despite its relevance in establishing diagnosis.

IFC has the potential to streamline multiple aspects of the diagnostic workflow. Firstly, in cases where individuals have variants of uncertain significance (VUS) in well-known genes lacking diagnostic assays, IFC-based assays could assist in interpreting pathogenicity. Establishing a public IFC database could ultimately eliminate the need for including patients with similar pathogenic variants as positive controls. Additionally, even in cases where diagnostic assays are available, IFC could offer an alternative requiring fewer assays and resources, while simultaneously aiding in the recognition of unknown disease entities by serving as a positive control. Secondly, for individuals with VUS in GUS, IFC based assays can lead to a more targeted diagnostic workflow by providing researchers with a sense of direction. For example, the striking mitosis defects found in individuals with *LIMK1* variants suggest that mitosis should be studied more in depth. Beyond its diagnostic applications, the high-throughput potential of IFC assays could be used to predict disease severity and therapeutic response. Previously, we found that IFC assessed LAMP1 accumulation serves as a proxy for Batten disease severity.<sup>13</sup> The potential of the other IFC-based assays could be assessed in a similar manner. Moreover, once a specific phenotypic profile for an individual with VUS is established and validated for diagnostic- and prognostic purposes, it can be used to screen for relevant therapies. Using the entire platform of IFC, including all six assays, would ensure that all relevant phenotypes would improve, while also allowing for the uncovering of unexpected side effects.

Here, we explored the potential of IFC-based cellular screening for individuals with a variety of VUSes in patient-derived fibroblasts. We provide evidence that IFC is able to predict pathogenicity in individuals with VUS(es) in well-known genes, based on similar cellular phenotypes compared to ‘true patients’, on assays of known relevance for underlying pathophysiology. Even in the most challenging group of individuals with VUS that underwent IFC-based screening, we found significant changes for all

subjects and distinct disease signatures that offer novel insights into underlying pathophysiological mechanisms for 5 out of 13 patients. We anticipate that by broadening the spectrum of patients and diseases included in our study and implementing improved noise filtering steps and feature selection tools, the screening quality of IFC could be further enhanced. Given the versatility, simplicity, and high-throughput potential of our IFC-based screening platform, we believe its full capacity to elucidate pathophysiology and facilitate clinical applications in individuals with VUS and patients with genetic diseases is yet to be fully realized.

### **Acknowledgements**

This work was funded by the Wilhelmina Children's Hospital Stimulus Stipend and United For Metabolic Diseases Catalyst Grant. We thank Prof. Paul Coffey, Dr. Jorg Calis and Dr. Jorg van Loosdregt for their input during the project conceptualization. We would like to thank Dr. Arjan F. Theil and Prof. Dr. Wim Vermeulen for the relevant resources and advice on DNA Repair deficient disorders. Fibroblasts harboring ERCC1 pathogenic variants were kindly provided by the Genome Damage and Stability Centre Research Tissue Bank (GDSC-RTB), University of Sussex.

### **Author Contributions**

Conceptualization: IM, PMH

Data Collection/Patient Inclusion: IM, HW, SM, DJL, CR, DYHV, SJ

Methodology: IM, PMH, FvW, SAF

Investigation: IM, PMH, GZV, GD, CvV

Visualization: IM, GZV

Supervision: PMH, SAF, EN, FvW

Writing – original draft: IM, PMH

Writing – review & editing: IM, HW, GD, GZV, SM, DJL, SJ, SAF, FvW, PMH

### **References**

1. Richards S, Aziz N, Bale S, et al. Standards and guidelines for the interpretation of sequence variants: A joint consensus recommendation of the American College of Medical Genetics and Genomics and the Associ-

- ation for Molecular Pathology. *Genetics in Medicine*. 2015;17(5):405-424. doi:10.1038/gim.2015.30
2. Makhnoon S, Shirts BH, Bowen DJ. Patients' perspectives of variants of uncertain significance and strategies for uncertainty management. *Genet Couns*. 2019;28(2):313-325. doi:10.1002/jgc4.1075
  3. Gustafsdottir SM, Ljosa V, Sokolnicki KL, et al. Multiplex cytological profiling assay to measure diverse cellular states. *PLoS One* 2013;8(12):e80999
  4. Chandrasekaran SN, Ceulemans H, Boyd JD, Carpenter AE. Image-based profiling for drug discovery: due for a machine-learning upgrade *Nat Rev Drug Discov*. 2021;20(2):145-159. doi:10.1038/s41573-020-00117-w
  5. Rohban MH, Singh S, Wu X, et al. Systematic morphological profiling of human gene and allele function via cell painting. *Elife*. 2017;6 doi:10.7554/eLife.24060
  6. Jang EH, Lee JH, Kim SA. Acute valproate exposure induces mitochondrial biogenesis and autophagy with foxo3a modulation in sh $\square$ sy5y cells. *Cells*. 2021;10(10). doi:10.3390/cells10102522
  7. Ashley N, O'Rourke A, Smith C, et al. Depletion of mitochondrial DNA in fibroblast cultures from patients with POLG1 mutations is a co - sequence of catalytic mutations. *Hum Mol Genet*. 2009;18(24):4905-4906. doi:10.1093/hmg/ddp458
  8. Park KS, Jo I, Pak Y, et al. FCCP depolarizes plasma membrane potential by activating proton and Na<sup>+</sup> currents in bovine aortic endothelial cells. *Pflugers Arch*. 2002;443(3):344-352. doi:10.1007/s004240100703
  9. Bakare AB, Daniel J, Stabach J, et al. Quantifying mitochondrial dynamics in patient fibroblasts with multiple developmental defect and mitochondrial disorders. *Int J Mol Sci*. 2021;22(12). doi:10.3390/ijms22126263
  10. Distelmaier F, Koopman WJH, Van Den Heuvel LP, et al. Mitochondrial complex I deficiency: From organelle dysfunction to clinical disease. *Brain*. 2009;132(4):833-842. doi:10.1093/brain/awp058
  11. Pugsley HR. Assessing Autophagic Flux by Measuring LC3, p62, and LAMP1 Co-localization Using Multispectral Imaging Flow Cytometry.

J Vis Exp. 2017;(125):55637. doi:10.3791/55637

12. Cullup T, Kho AL, Dionisi-Vici C, et al. Recessive mutations in EPG5 cause Vici syndrome, a multisystem disorder with defective autophagy. *Nat Genet.* 2013;45(1):83-87. doi:10.1038/ng.2497
13. Kuper WFE, Oostendorp M, van den Broek BTA, et al. Quantifying lymphocyte vacuolization serves as a measure of CLN3 disease severity. *JIMD Rep.* 2020;54(1):87-97. doi:10.1002/jmd2.12128
14. Di Pietro N, Marcovecchio ML, Di Silvestre S, et al. Plasma from pre-pubertal obese children impairs insulin stimulated Nitric Oxide (NO) bioavailability in endothelial cells: Role of ER stress. *Mol Cell Endocrinol.* 2017;443:52-62. doi:10.1016/j.mce.2017.01.001
15. Rita Lecca M, Wagner U, Patrignani A, Berger EG, Hennet T. Genome-wide analysis of the unfolded protein response in fibroblasts from congenital disorders of glycosylation type-1 patients. *The FASEB Journal.* 2005;19(2):1-21. doi:10.1096/fj.04-2397fje
16. Wortzel I, Koifman G, Rotter V, Seger R, Porat Z. High Throughput Analysis of Golgi Structure by Imaging Flow Cytometry. *Sci Rep.* 2017;7(1):788. doi:10.1038/s41598-017-00909-y
17. Scrivens PJ, Shahrzad N, Moores A, Morin A, Brunet S, Sacher M. TRAPPC2L is a novel, highly conserved TRAPP-interacting protein. *Traffic.* 2009;10(6):724-736. doi:10.1111/j.1600-0854.2009.00906.x
18. George TC, Fanning SL, Fitzgerald-Bocarsly P, et al. Quantitative measurement of nuclear translocation events using similarity analysis of multispectral cellular images obtained in flow. *J Immunol Methods.* 2006;311(1-2):117-129. doi:10.1016/j.jim.2006.01.018
19. Mandola AB, Sharfe N, Nagdi Z, et al. Combined immunodeficiency caused by a novel homozygous NFKB1 mutation. *Journal of Allergy and Clinical Immunology.* 2021;147(2):727-733.e2. doi:10.1016/j.jaci.2020.08.040
20. Rajan R, Karbowniczek M, Pugsley HR, Sabnani MK, Astrinidis A, La-Beck NM. Quantifying autophagosomes and autolysosomes in cells using imaging flow cytometry. *Cytometry Part A.* 2015;87(5):451-458. doi:10.1002/cyto.a.22652
21. Ratinaud MH, Leprat P, Julien R. In situ flow cytometric analysis of

- nonyl acridine orange-stained mitochondria from splenocytes. *Cytometry*. 1988;9(3):206-212. doi:10.1002/cyto.990090304
22. Creed S, McKenzie M. Measurement of mitochondrial membrane potential with the fluorescent dye tetramethylrhodamine methyl ester (TMRM). *Methods in Molecular Biology*. 2019;1928:69-76. doi:10.1007/978-1-4939-9027-6\_5
23. Morán M, Delmiro A, Blázquez A, Ugalde C, Arenas J, Martín MA. Bulk autophagy, but not mitophagy, is increased in cellular model of mitochondrial disease. *Biochim Biophys Acta Mol Basis Dis*. 2014;1842(7):1059-1070. doi:10.1016/j.bbadis.2014.03.013
24. Ghosh AK, Mau T, O'Brien M, Garg S, Yung R. Impaired autophagy activity is linked to elevated ER-stress and inflammation in aging adipose tissue. *Aging*. 2016;8(10):2525-2537. doi:10.18632/aging.101083
25. Karkucinska-Wieckowska A, Trubicka J, Werner B, et al. Left ventricular noncompaction (LVNC) and low mitochondrial membrane potential are specific for Barth syndrome. *J Inher Metab Dis*. 2013;36(6):929-937. doi:10.1007/s10545-013-9584-4
26. Waterham HR, Koster J, van Roermund CWT, Mooyer PAW, Wanders RJA, Leonard J V. A Lethal Defect of Mitochondrial and Peroxisomal Fission. *New England Journal of Medicine*. 2007;356(17):1736-1741. doi:10.1056/nejmoa064436
27. Schiff M, Haberberger B, Xia C, et al. Complex I assembly function and fatty acid oxidation enzyme activity of ACAD9 both contribute to disease severity in ACAD9 deficiency. *Hum Mol Genet*. 2014;24(11):3238-3247. doi:10.1093/hmg/ddv074
28. D'Alessandro G, Morales-Juarez DA, Richards SL, et al. RAD54L2 counters TOP2-DNA adducts to promote genome stability. *Sci Adv*. 2023;9(49):eadl2108. doi:10.1126/sciadv.adl2108
29. Kashiyama K, Nakazawa Y, Pilz DT, et al. Malfunction of nuclease ERCC1-XPF results in diverse clinical manifestations and causes Cockayne syndrome, xeroderma pigmentosum, and Fanconi anemia. *Am J Hum Genet*. 2013;92(5):807-819. doi:10.1016/j.ajhg.2013.04.007
30. Haralick R, Shanmugam K, Its'Hak D. Textural features for image classification. *IEEE Trans Syst Man Cybern*. Published online 1993:610-

621.

31. Zhang H, Xiong Y, Sun Y, et al. RAD54L2-mediated DNA damage avoidance pathway specifically preserves genome integrity in response to topoisomerase 2 poisons. *Sci Adv.* 2023;9(49). doi:10.1126/sciadv.adi6681
32. Zagnoli-Vieira G, Bruni F, Thompson K, et al. Confirming TDP2 mutation in spinocerebellar ataxia autosomal recessive 23 (SCAR23). *Neurol Genet.* 2018;4(5). doi:10.1212/nxg.0000000000000277
33. Milanese C, Bombardieri CR, Sepe S, et al. DNA damage and transcription stress cause ATP-mediated redesign of metabolism and potentiation of anti-oxidant buffering. *Nat Commun.* 2019;10(1). doi:10.1038/s41467-019-12640-5
34. De Waard MC, Van Der Pluijm I, Zuiderveen Borgesius N, et al. Age-related motor neuron degeneration in DNA repair-deficient *Ercc1* mice. *Acta Neuropathol.* 2010;120(4):461-475. doi:10.1007/s00401-010-0715-9
35. De Voer RM, Hahn MM, Mensenkamp AR, et al. Deleterious Germ-line BLM mutations and the risk for early-onset colorectal cancer. *Sci Rep.* 2015;5. doi:10.1038/srep14060
36. Dregalla RC, Zhou J, Idate RR, Battaglia CLR, Liber HL, Bailey SM. Regulatory roles of tankyrase 1 at telomeres and in DNA repair: Suppression of T-SCE and stabilization of DNA-pkcs. *Aging.* 2010;2(10):691-708. doi:10.18632/aging.100210
37. Kaji N, Muramoto A, Mizuno K. LIM kinase-mediated cofilin phosphorylation during mitosis is required for precise spindle positioning. *Journal of Biological Chemistry.* 2008;283(8):4983-4992. doi:10.1074/jbc.M708644200
38. Chao JT, Roskelley CD, Loewen CJR. MAPS: machine-assisted phenotype scoring enables rapid functional assessment of genetic variants by high-content microscopy. *BMC Bioinformatics.* 2021;22(1). doi:10.1186/s12859-021-04117-4
39. Ebrahimi-Fakhari D, Alecu JE, Brechmann B, et al. High-throughput imaging of ATG9A distribution as a diagnostic functional assay for adaptor protein complex 4-associated hereditary spastic paraplegia. *Brain Commun.* 2021;3(4). doi:10.1093/braincomms/fcab221
40. Caicedo JC, Arevalo J, Piccioni F, et al. Cell Painting predicts impact of lung cancer variants. *Mol Biol Cell.* 2022;33(6). doi:10.1091/mbc.E21-11-

0538

41. Ohya Y, Sese J, Yukawa M, et al. High-dimensional and large-scale phenotyping of yeast mutants. *Proc Natl Acad Sci U S A*. 2005;102(52):19015-19020. doi:10.1073/pnas.0509436102
42. Rohban MH, Singh S, Wu X, et al. Systematic morphological profiling of human gene and allele function via cell painting. *Elife*. 2017;6 doi:10.7554/eLife.24060
43. Chowdhury A, Aich A, Jain G, et al. Defective Mitochondrial Cardiolipin Remodeling Dampens HIF-1 $\alpha$  Expression in Hypoxia. *Cell Rep*. 2018;25(3):561-570.e6. doi:10.1016/j.celrep.2018.09.057
44. Zemirli N, Pourcelot M, Ambroise G, Hatchi E, Vazquez A, Arnoult D. Mitochondrial hyperfusion promotes NF- $\kappa$ B activation via the mitochondrial E3 ligase MULAN. *FEBS Journal*. 2014;281(14):3095-3112. doi:10.1111/febs.12846
45. Diaz G, Diana A, Falchi AM, et al. Intra- and intercellular distribution of mitochondrial probes and changes after treatment with MDR modulators. *IUBMB Life*. 2001;51(2):121-126. doi:10.1080/15216540152122139
46. Bernardi P, Scorrano L, Colonna R, Petronilli V, Di Lisa F. Mitochondria and cell death. Mechanistic aspects and methodological issues. *Eur J Biochem*. 1999;264(3):687-701. doi:10.1046/j.1432-1327.1999.00725.x
47. Kuper WFE, Oostendorp M, van den Broek BTA, et al. Quantifying lymphocyte vacuolization serves as a measure of CLN3 disease severity. *JIMD Rep*. 2020;54(1):87-97. doi:10.1002/jmd2.12128
48. Vaz FM, van Lenthe H, Vervaart MAT, et al. An improved functional assay in blood spot to diagnose Barth syndrome using the monolysocardiolipin/cardiolipin ratio. *J Inherit Metab Dis*. 2022;45(1):29-37. doi:10.1002/jimd.12425
49. Van Grunsven EG, Van Berkel E, Mooijer PAW, et al. Peroxisomal bifunctional protein deficiency revisited: Resolution of its true enzymatic an molecular basis. *Am J Hum Genet*. 1999;64(1):99-107. doi:10.1086/302180
50. Hori I, Otomo T, Nakashima M, et al. Defects in autophagosome-lysosome fusion underlie Vici syndrome, a neurodevelopmental disorder with multisystem involvement. *Sci Rep*. 2017;7(1). doi:10.1038/s41598-017-02840-8

**Supplementary Files and Figures:**

**Table 1: Overview of assays included in the IFC platform for our pilot study.**

Category	Criteria
Relevant, included in manuscript	<ol style="list-style-type: none"> <li>1. Function can be assessed by visualization of morphology.</li> <li>2. Essential cellular pathway involved in a broad array of cellular functions.</li> <li>3. Altered morphology of the cellular compartment is associated with pathophysiology of disease(s).</li> <li>4. Reliable markers exist that aid visualization.</li> </ol>
Relevant, but not included in manuscript	<ol style="list-style-type: none"> <li>1. Assay meets all criteria of relevance, but has not yet been included for pilot project.</li> </ol>
Assay does not meet criteria of relevance	<ol style="list-style-type: none"> <li>1. Function cannot be assessed by visualizing morphology.</li> <li>2. Highly specific cellular pathway or only involved in a small subset of cellular functions.</li> <li>3. Altered morphology of the cellular compartment is not associated with disease.</li> <li>4. Reliable markers for the pathway do not exist</li> </ol>

Cellular component	Function	Marker	Diseases associated with dysfunction	Relevance.
Nucleus	DNA synthesis, repair, replication	BrdU incorporation (DNA synthesis) $\gamma$ -H2AX (double strand DNA breaks).	Ataxia telangiectasia, Nijmegen breakage syndrome, Werner syndrome, Bloom Syndrome, Fanconi anemia, xeroderma pigmentosum, Cockayne syndrome, trichothiodystrophy.	BrdU and EU incorporation measurements do not require morphologic assessment. $\gamma$ -H2AX staining requires visualization (distinction of foci in the nucleus). Increased $\gamma$ -H2AX staining is associated with disease. However, DNA damage first needs to be induced with DNA damaging agents or irradiation and the sensitivity to these agents differs per disease (radiation, chemotherapeutics, etc.)
	RNA synthesis, processing and transport	5-Ethynyl Uridine incorporation (RNA synthesis),	Mutations in RNA polymerase genes, the Mediator complex, the spliceosome, RNA editing, RNA export, etc.	
Endoplasmic Reticulum (ER)	Synthesis of lipids and proteins	ER Stress: ATF6 antibody translocation (ER-stress), etc.	Congenital disorders of glycosylation, neurodegenerative diseases, diabetes and cancer.	ATF6 translocation reflects ER-stress, is associated with disease and visualization of morphology is required to measure functionality.



## Chapter 5

		ER morphology: Calreticulin antibody (morphology) Calnexin antibody (morphology)		ER morphology reflects ER-function, is associated with disease and requires morphologic assessment.
Golgi	Modification, sorting, and packaging of proteins and lipids for secretion or delivery to organelles.	GM130 antibody (morphology) APIG1 antibody (protein sorting in the golgi) etc.	Congenital disorder of glycosylation (CDG), Menkes disease, Wilsons disease, neurodegenerative diseases.	Golgi fragmentation or swelling reflect golgi dysfunction, golgi morphology is involved in the pathophysiology of many diseases.
Mitochondria	ATP synthesis by oxidative phosphorylation	NAO (mitochondrial mass), TMRM (membrane potential), MitoSox (ROS production), etc.	Primary mitochondrial diseases, diseases associated with mitochondrial fission and/or fusion.	Mitochondrial mass and morphology are essential for mitochondrial function and involved in the pathophysiology of many diseases.
Lysosomes	Intracellular degradation	LAMP1 antibody, LysoTracker	Lysosomal storage disorders (Batten disease, Gaucher disease, Niemann Pick syndrome).	Enhanced lysosomal size correlates with lysosomal storage disorder disease pathophysiology and disease severity.
Autophagosomes	Degradation and recycling of cellular components.	LC3B or p62 antibodies.	Vici syndrome, X-linked myopathy with excessive autophagy (VMA21), Niemann Pick type C1.	LC3B visualization is essential to distinguish autophagosomes from background, and to distinguish micro- from macro autophagy. Autophagy is involved in the pathophysiology of many diseases.
Endosomes	Sorting of endocytosed material.	EEA1 antibody (early endosomes), RAB5a, RAB4A, RAB11, LAMP1 antibodies (late endosomes)	Niemann Pick syndrome, neurodegenerative diseases, TRAPPC mutations.	Enlarged size of endosomal compartment is associated with pathophysiology of several diseases.
The cytoskeleton	Maintains cellular shape and organization, provides mechanical support that enables cells to carry out essential functions like division and movement.	Phalloidin	Actinopathies, Wiskott-Aldrich syndrome (WAS), PFIT syndrome,	Alterations in actin cytoskeletal morphology have been associated with disease. Visualization is required to study the actin cytoskeleton.
		$\alpha$ -tubulin antibody, SiR-tubulin, Tubulin Tracker.	Tubulinopathies	Microtubules can better be studied dynamically, not statically.

## Imaging Flow Cytometry for individual with VUS

Peroxisome	Oxidative breakdown of toxic molecules	Catalase antibodies.	Peroxisome biogenesis disorders, Zellweger syndrome spectrum (PBD-ZSS)	Catalase scattering can be used as a marker for peroxisomal disorders. Visualization is required.
Cellular signaling pathways	Control of cellular processes in relation to internal or external triggers.	mTOR, NF-kB, JAK-STAT, NLRP3, MAPK, HIF1 antibodies.	Many genetic diseases are caused by defective intracellular signaling	If the signaling pathway involves (nuclear) translocation, assessment of morphology is essential. From all cellular signaling pathways, NF-kB was chosen as a proof of principle. In theory, any kind of signaling pathway can be measured.

**Table 1:** Overview of assays included in the IFC platform for our pilot study.

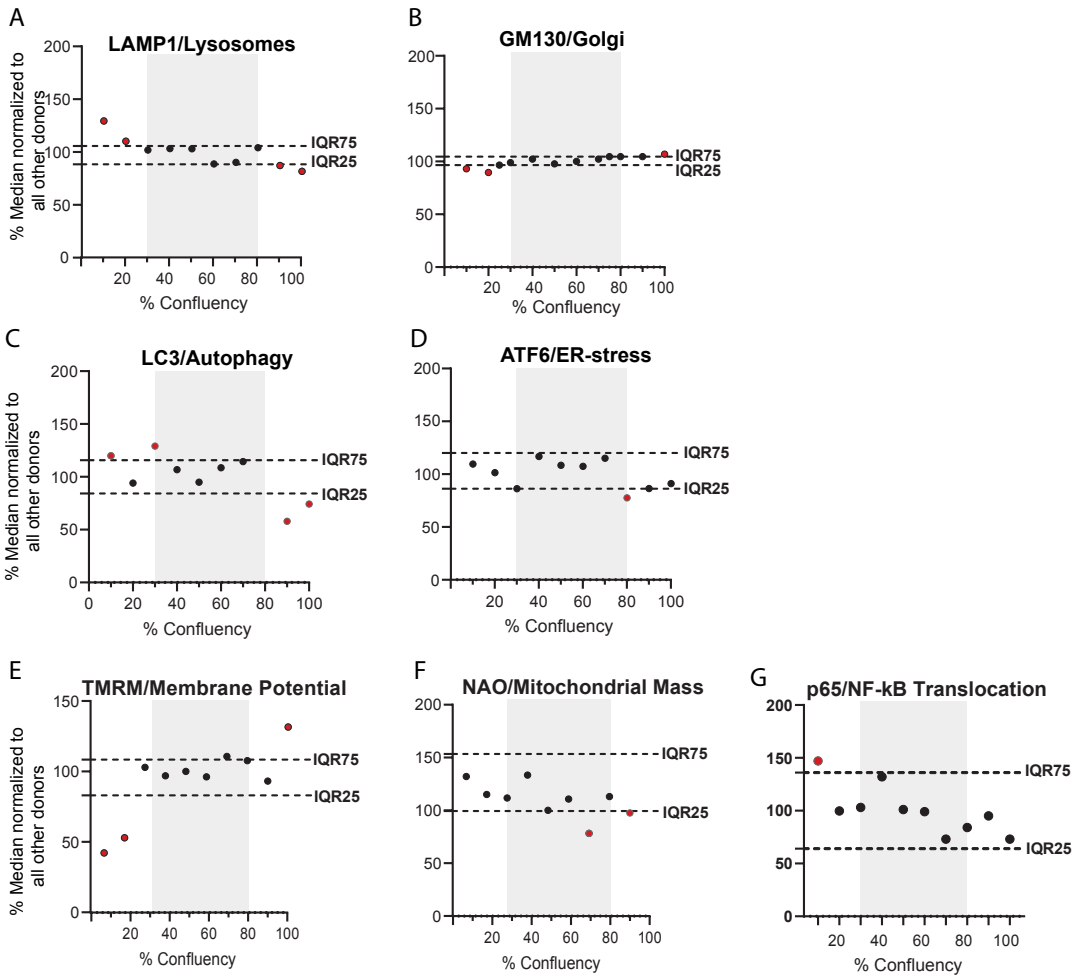
### Supplementary Table 2: Validation of Imaging Flow Cytometry Features

Assay	Feature	Mask	Compound		Patient Control	
			Log2 foldchange	P-value	Log2 foldchange	P-value
Mitochondrial Mass	NAO Intensity	NA	-1.44	7.475x10 <sup>-06</sup> ***	-0.63	0.02*
Membrane Potential	TMRM Intensity	NA	-1.01	< 2.2x10 <sup>-16</sup> ***	-1.04	9.81 x10 <sup>6</sup> ***
Autophagy	LC3 spot Count	Spot Bright Threshold: 10 Minimal size: 1 pixel Maximum size: 5 pixels	1.48	< 2.2x10 <sup>-16</sup> ***	1.02	< 2.2x10 <sup>-16</sup> ***
Lysosomal Accumulation	LAMP1 Area	Brightfield Adaptive Erode 70%	NA	NA	2.83	< 2.2x10 <sup>-16</sup> ***
ER Stress	Similarity ATF6 - Score nucleus	Morphology Nucleus	3.15	< 2.2x10 <sup>-16</sup> ***	1.17	3.33x10 <sup>6</sup> ***
Golgi Fragmentation	% Fragmented	Threshold Golgi 70%	0.67	0.004*	3.06	0.003*
NF-kB Translocation	Similarity Score p65 – nucleus.	Morphology Nucleus	2.00	< 2.2x10 <sup>-16</sup> ***	NA	NA

**Table 2:** Overview of the features used to quantify aberrancies on assays and their validation. All assays and features were validated with a compound known to cause aberrancies in the pathway of interest (‘Compound’) and in patient cells (‘Patient Control’). For each feature, the median value per patient or healthy control was calculated. The medians were compared between the patients serving as positive controls and all healthy

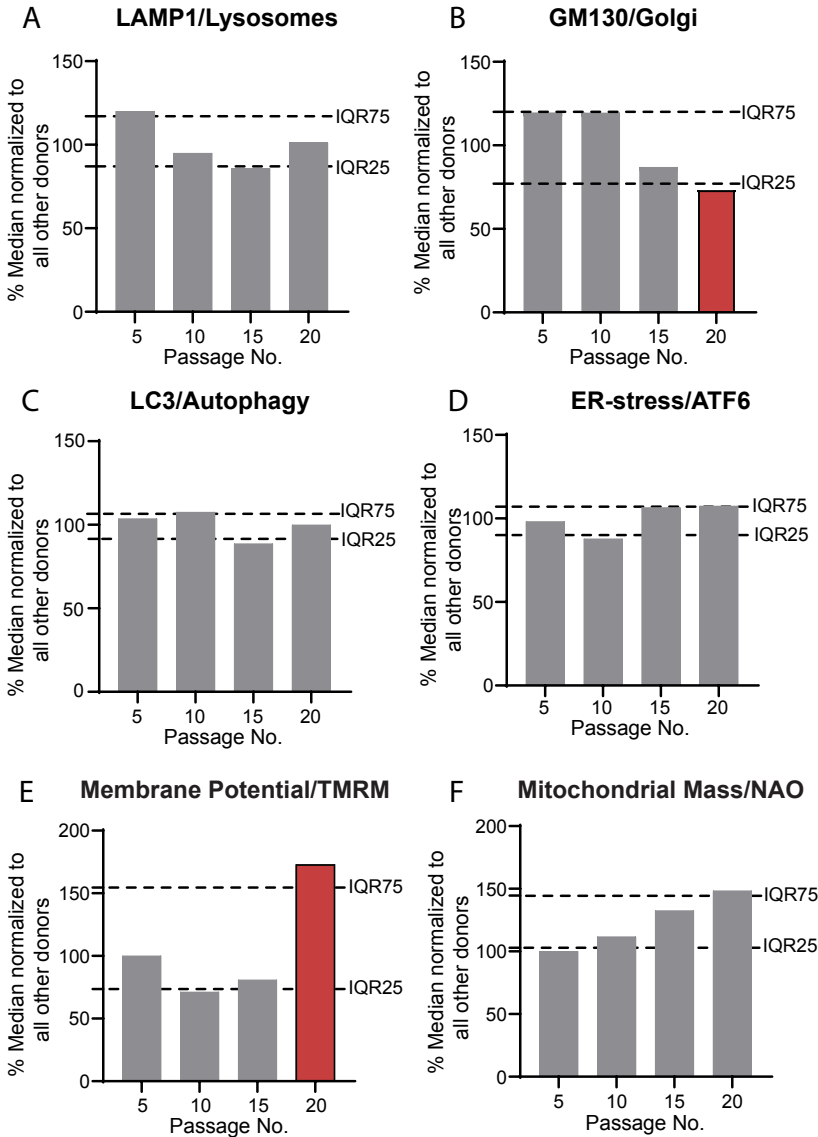
controls (N=3 for all assays, except for the mitochondrial assay) using fold change and converted to log<sub>2</sub> values. If positive patient controls groups consisted of two patients (CLN3, mitochondrial disease), the mean log<sub>2</sub> foldchange was taken. The p-value was calculated using non-linear mixed model analysis and ANOVA. A significant p-value and log<sub>2</sub> foldchange >1 or <-1 indicates the assay of interest is sensitive enough to pick up biological differences (log<sub>2</sub>foldchange >2).

**Supplementary Figure 1: Effect of fibroblast confluency on IFC assays.**



**Supplementary Figure 1: Effect of fibroblast confluency on IFC assays.**

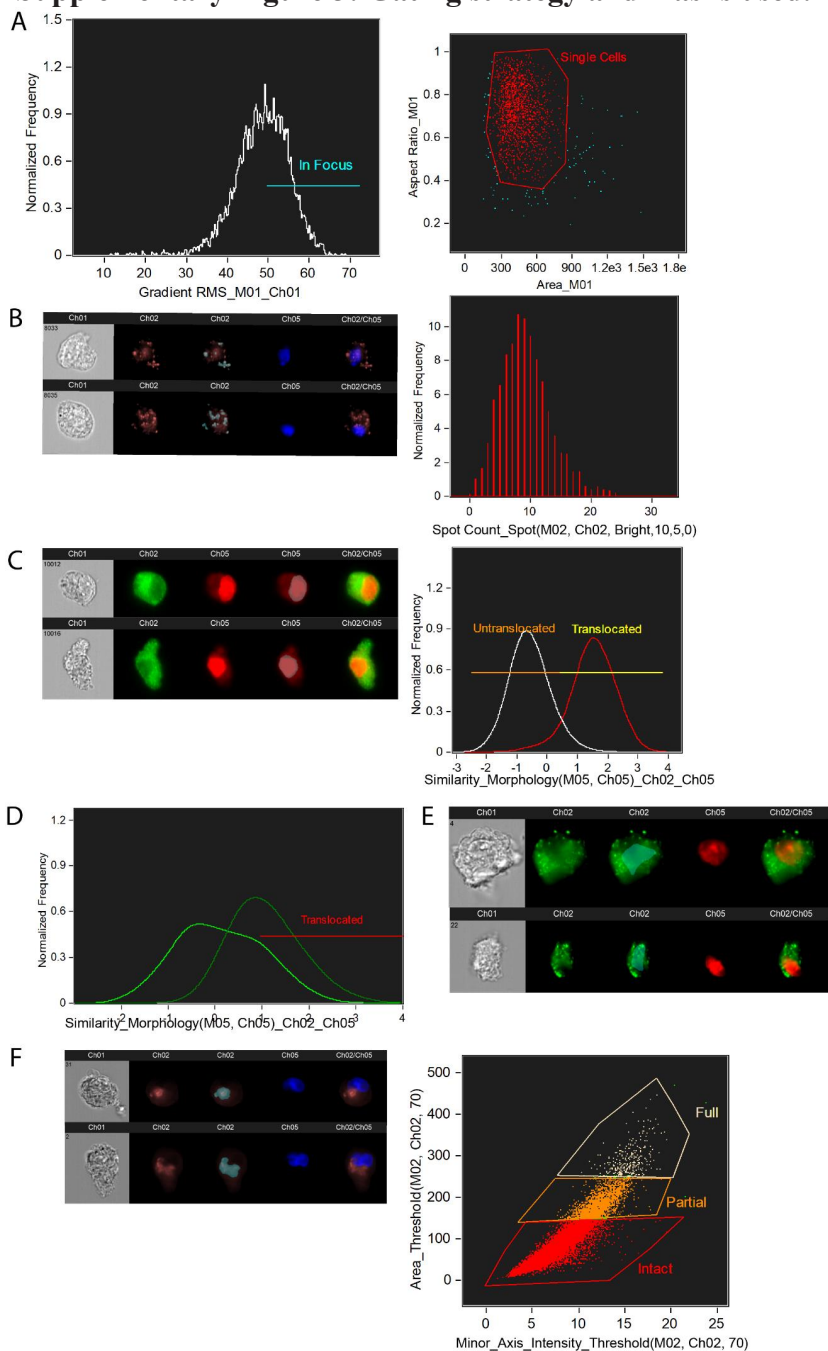
Cells were plated to reach the desired confluence rates on the day of the assay. Actual confluence was quantified on the day of the assay using ImageJ, calculating the fibroblast-covering surface in relation to the entire area. These percentages are shown on the X-axis. The median feature value for each confluency percentage was divided by all other medians and converted to a percentage, shown on the y-axis. (A) Showing the effect of fibroblast confluency on the LAMP1 assay. (B) Showing the effect of confluency on the Golgi assay. (C) Showing the effect of confluency on the autophagy assay. The 80% condition is missing. (D) Showing the effect of confluency on the ER-stress assay. (E) Showing the effect of confluency on the membrane potential assay. To calculate the percentages for this graph, each confluency percentage was directly compared to 50% and converted to a percentage (10% to 50%, 20% to 50%, etc.). Therefore, the IQR values are not centered around zero. (F) Showing the effect of confluency on the mitochondrial mass assay. To calculate the percentages for this graph, each confluency percentage was directly compared to 50% and converted to a percentage (10% to 50%, 20% to 50%, etc.). Therefore, the IQR values are not centered around zero.



**Supplementary Figure 2:** Effect of fibroblast passage number on IFC assays. For each individual analysis, the median feature value was divided by the median values of other replicates analyzed in the same experiment and converted to percentages. These percentages are shown on the Y-axis.

The X-axis shows the fibroblast passage number. (A) Showing the effect of passage number on the LAMP1 assay. (B) Showing the effect of passage number on the golgi assay. (C) Showing the effect of passage number on the autophagy assay. (D) Showing the effect of passage number on the ER-stress assay. (E) Showing the effect of passage number on the membrane potential assay. To calculate the percentages for this graph specifically, instead of comparing each value to all other values, each passage number was only compared to one other passage number and converted to a percentage (p5 to p10, p5 to p15, p5 to p20 etc). Therefore, the IQR values are not centered around zero. (F) Showing the effect of passage number on the membrane potential assay. To calculate the percentages for this graph, each passage number was directly compared to another passage number and converted to a percentage (p5 to p10, p5 to p15, p5 to p20 etc). Therefore, the IQR values are not centered around zero.

Supplementary Figure 3: Gating strategy and masks used.



### **Supplementary Figure 3:** Gating strategy and masks used.

(A) Showing the gating strategy used for all experiments. In Inspire, only cells having nuclear intensity  $>1 \times 10^5$  were captured. In IDEAS, cells in focus were gated using the Gradient\_RMS feature of the brightfield channel (Channel 1). Next, doublets were excluded by using the Area and Aspect Ratio of the brightfield image.

(B) Shows the specific gating for the autophagy assay. To count the number of autophagosomes, a Spot mask was created. On the left, the spot mask is shown as overlay (blue) over the LC3 staining (Channel 2, Ch02, light red). The nuclear staining (Channel 5, Ch05) is shown in blue. The graph on the right shows the Spot Count feature, which was combined with the spot mask, to quantify the number of autophagosomes.

(C) Shows the specific gating for the NF- $\kappa$ B translocation assay. To measure the amount of p65 in the nucleus, a nuclear mask was created (Morphology\_M05). The mask is shown as overlay (blue) over the nuclear staining (Channel 5, Ch05, red). In green, the p65 staining is shown (Channel 2, Ch02). The graph on the right shows the gating strategy to gate for p65 nuclear translocated and non-translocated cells. The pixel overlap between the p65 staining and the nuclear staining within the Morphology\_M05 mask were used to quantify translocation (Using the feature Similarity\_Morphology(M05, Ch05), Ch02\_Ch05).

(D) Showing the gating strategy for the ER-stress staining (ATF6 nuclear translocation). A similar strategy as for p65 translocation was used to quantify ER-stress (the Morphology\_M05 mask and Similarity\_Morphology(M05, Ch05), Ch02\_Ch05 feature).

(E) Shows the gating strategy for the LAMP1 staining. To measure the amount of lysosomes, the Adaptive Erode mask based on the brightfield image was used. In blue, the Adaptive\_Erode\_60 Mask of channel 1 is shown. To measure lysosomal accumulation within the entire cell, the Internalization of the LAMP1 staining within the Adaptive\_Erode\_60 mask was quantified.

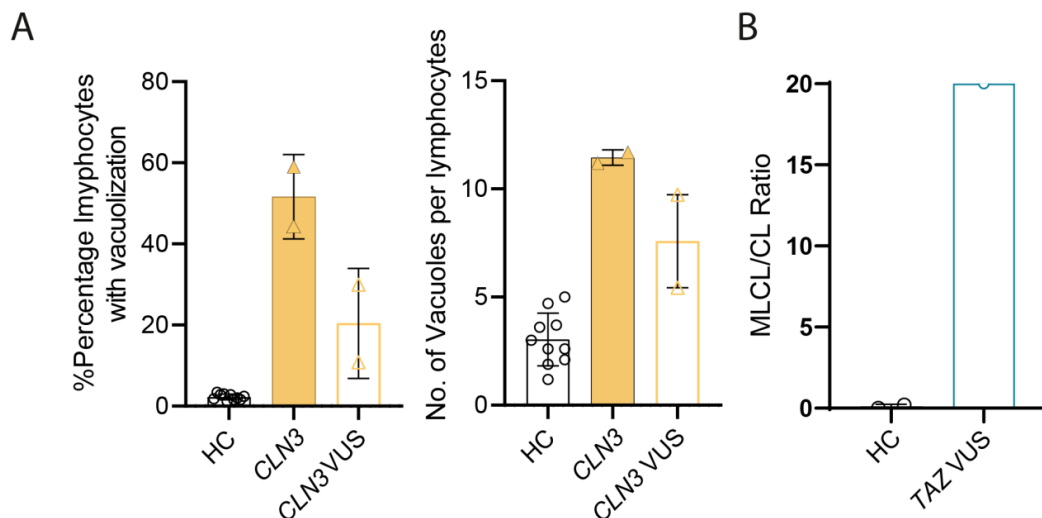
(F) To quantify golgi fragmentation, first, a 70% threshold mask of the golgi staining (Channel 2, Ch02) was created. The 70% Threshold mask is shown in blue. The Golgi/GM130 staining is shown in light red. In blue, the nuclear staining is shown (Channel 5, Ch05). The graph shows the gating strategy to gate for cells with intact-, partially fragmented- or a fully fragmented golgi system.



**Supplementary Table 3: Assessment of pathogenicity of VUSes in well-known disease genes**

Donor	Gene	In-silico predictions (MutationTaster)	In-silico predictions (CADD score)	Functional Assays	ACMG
CLN33	<i>CLN3</i> Homozygous 1kb deletion in exon 6	NA	NA	Increased vacuoles in lymphocytes and increased % lymphocytes with vacuolization ( <b>Supplementary Figure 4</b> )	PVS1, <b>PS3</b> , Pathogenic
CLN34	<i>CLN3</i> Homozygous 1kb deletion in exon 6	NA	NA	Increased vacuoles in lymphocytes and increased % lymphocytes with vacuolization ( <b>Supplementary Figure 4</b> )	PVS1, <b>PS3</b> , Pathogenic
240	<i>TAZ</i> De Novo variant	Disease Causing	29.1	Severely increase d MLCL/CL ratio ( <b>Supplementary Figure 4</b> )	PM6, PP2, PP3, PP4, PP5, <b>PS3</b> Pathogenic
111	<i>ACAD9</i> Homozygous missense variant	Polymorfism	20.5	Literature: 30% reduction of ACAD9 activity in protein extracts (Schiff et al., 2014)	PP5, PP4, <b>PS3</b> Likely pathogenic
249	<i>DLPI</i> De Novo variant	Disease Causing, splice site changes	25.1	Mildly aberrant peroxisomal staining (beads on a string). Peroxisomal fission defect.	PS2, PP4, <b>PS3</b> , PP5, PM2 Pathogenic
				Mildly aberrant mitochondrial staining.	
253	<i>DLPI</i> De Novo variant	Disease Causing, splice site changes	22.6	No peroxisomal aberrancies. Mildly aberrant mitochondrial staining.	PM2, PP3, PS2, <b>PS3</b> Pathogenic
250	<i>EPG5</i> Homozygous missense variant	Disease Causing, splice site changes	25.5	No differences observed with p62/LC3 western blot	PS2, PP4, PM2, Uncertain Significance

**Supplementary Figure 4: Diagnostic assays performed in individuals with VUS**



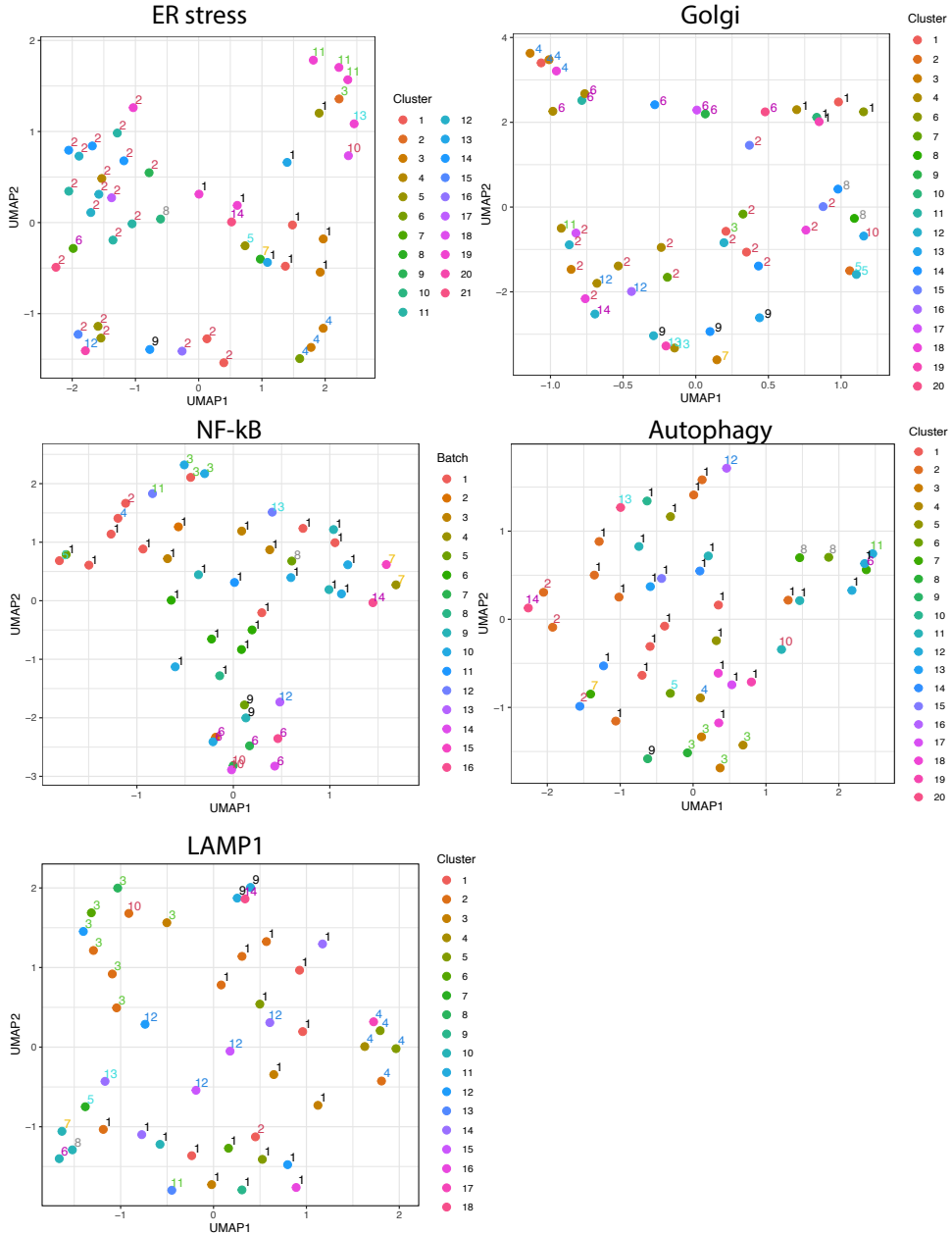
**Supplementary Figure 4:** (A) Bar graphs showing the mean number of vacuoles per lymphocyte as well as the number of lymphocytes with vacuole  $\pm$ SD. Both measures are the current gold standard to establish diagnosis of Batten disease. *CLN3* refers to the two patients with pathogenic variants, while *CLN3 VUS* refers to the two individuals with VUSes in *CLN3*. The increased values in the individuals with *CLN3* VUSes indicate pathogenicity of variants.

(B) Bar graph showing the monolysocardiolipin:cardiolipin (MCLC:CL) ratio for the individual with VUS in *TAZ*.

**Supplementary Table 4: Assessment of pathogenicity of VUSes in GUS.**

Donor	Gene	ACMG	In-silico predictions (MutationTaster)	In-silico predictions (CADD score)
143	<i>CSDE1</i> De Novo missense variant	PM2, PS2, PP3 VUS	Disease Causing	28.6
	<i>ZFYVE16</i> De Novo missense variant	PS2, PP3 VUS	Disease Causing	21.1
140	<i>LIMK1</i> De Novo missense variant	PS2, PM2, PP3 VUS	Disease Causing	26.9
093	<i>LIMK1</i> De Novo missense variant	PS2, PP3 VUS	Polymorphism	13.3
225	No VUSes identified			
227	<i>BRWD3</i> Hemizygous De Novo variant	PS2, PM2, PP3 VUS	Disease Causing	23.5
	<i>PDE3B</i> Homozygous deletion	PM4, PS2, PP3 VUS	Disease Causing, frameshift	NA
228	<i>MMS19</i> De Novo missense variant	PM2, PS2, PP3 VUS	Disease Causing	31
211	<i>DLGAP2</i> De Novo duplication	PP3, PS2, PM4 VUS	Disease Causing, frameshift	NA
	<i>TNKS</i> De Novo missense variant	PP3, PM2 VUS	Disease Causing, splice site changes	21
106	<i>RAD54L2</i> De Novo missense variant	PP3, PS2, PM2 VUS	Disease Causing	25.7
226	<i>PDE4DIP</i> Compound Heterozygous missense variant	BP4, VUS	Polymorfism, Polymorfism	14.41, 1.9
202	<i>MEIOC</i> De Novo missense variant	PM2, PS2, PP3 VUS	Disease Causing, splice site changes	23.4
	<i>SLC4A2</i> De Novo missense variant	PS2, PP3 VUS	Disease Causing, splice site changes	28.1
217	<i>EIF4ENIF1</i> De Novo missense variant	PS2, PP3, PM2 VUS	Disease Causing	31

**Supplementary Figure 5: Assessment of batch effects with the implementation of 1800 IFC features.**



**Supplementary Figure 5:** To assess batch effects, average linkage clustering based on Manhattan distance was used. UMAP was used for visualization. Batch effects were considered if donors analyzed within one single experiment clustered together. The experiment numbers /batch numbers are shown as actual numbers right next to the colored dots. The color of the dot indicates the outcome of the Manhattan clustering. Number of clusters were determined using elbow plots. As can be seen, the batch numbers do not correlate with cluster numbers in any of the assays, indicating the biological variation rather than batch effect contribute to differences between donors. Batch effects were assessed separately for (A) ER-stress, (B) Golgi, (C) NF-kB translocation, (D) Autophagy, (E) LAMP1.

### References:

1. Schiff M, Haberberger B, Xia C, et al. Complex I assembly function and fatty acid oxidation enzyme activity of ACAD9 both contribute to disease severity in ACAD9 deficiency. *Hum Mol Genet.* 2014;24(11):3238-3247. doi:10.1093/hmg/ddv074





# Chapter



**Imaging Flow Cytometry identifies divergent responses to mitochondrial pathology in patients with mitochondrial disease.**



## **Imaging Flow Cytometry identifies divergent responses to mitochondrial pathology in patients with mitochondrial disease.**

Muffels, I.J.J.,<sup>1</sup> Rodenburg, R.,<sup>2</sup> Willemen, H.L.D.M.,<sup>3</sup> Van Haaften-Visser, D.Y.,<sup>4</sup> Waterham, H.,<sup>5,6</sup> Eijkelkamp, N.,<sup>3</sup> Fuchs, S.A.,<sup>1</sup> Hasselt, P.M.<sup>1</sup>

<sup>1</sup> Department of Metabolic Diseases, Wilhelmina Children's hospital, University Medical Center Utrecht, Utrecht, The Netherlands.

<sup>2</sup> Nijmegen Center for Mitochondrial Disorders, Radboud University Nijmegen Medical Center, The Netherlands.

<sup>3</sup> Center for Translational Immunology (CTI), Wilhelmina Children's hospital, University Medical Center Utrecht, Utrecht, The Netherlands.

<sup>4</sup> Department of Pediatrics, Center for Lysosomal and Metabolic Diseases, Erasmus University Medical Center, Rotterdam, The Netherlands

<sup>5</sup> United For Metabolic Diseases (UMD).

<sup>6</sup> Department of Laboratory Medicine, Laboratory Genetic Metabolic Diseases, Amsterdam UMC - AMC, Amsterdam, the Netherlands.

### Abstract

*Background:* Mitochondrial disease heterogeneity greatly complicates diagnosis, prognosis, and treatment allocation. Traditional classification based on oxidative phosphorylation (OXPHOS) complex deficiencies often falls short in elucidating the complexity of genotype-phenotype correlations. A multi-modal functional assessment of mitochondrial function could help identify novel disease patterns, allowing insights into the complex genotype-phenotype correlation in mitochondrial disease.

*Methods:* We simultaneously assessed a broad range of mitochondrial functions in fibroblasts of 31 mitochondrial disease patients using Imaging Flow Cytometry (IFC) by quantifying five pivotal features: mitochondrial fragmentation, mitochondrial swelling, membrane potential, ROS production and mitochondrial mass.

*Results:* We found 29/31 of patients (94%) showed significant changes on one or more assays. Clustering analysis identified two disease-overarching groups characterized by distinct responses to mitochondrial pathology, reflective of either a hypo- or hypermetabolic state. The first cluster showed low-to-normal membrane potential and increased ROS production, while the other cluster showed elevated membrane potential and mitochondrial swelling. Literature-supported analyses linked these clusters to assembly defects in complex I stability (cluster 1) and proton pumping activity (cluster 2). Clinically, we found that epilepsy was predominantly observed in patients in the first cluster, while neuropathy was almost exclusively seen in cluster 2.

*Conclusion:* The IFC-based platform allows for high-throughput, simultaneous assessment of mitochondrial morphology and function, aiding the identification of disease-overarching clusters corresponding with underlying pathophysiology and clinical phenotypes. These assays open up a new avenue for the identification of disease-specific patterns based on similar functional responses to mitochondrial pathology, that can be used to optimize diagnostic- and therapeutic approaches.

## Introduction

Mitochondrial diseases encompass a group of rare disorders characterized by dysfunctional energy metabolism, resulting from pathogenic genetic variants in nuclear- or mitochondrial genes. For most genetic diseases, patients harboring the same disease subtype show similar phenotypes. Mitochondrial diseases appear to be an exception to this phenomenon, as patients with the same disease subtype or dysfunctional gene can present with completely different clinical and cellular phenotypes.<sup>1-4</sup> Even more striking, patients harboring the exact same pathogenic variant can present with highly heterogeneous clinical features, best illustrated by patients harboring the prevalent m.3243A>G variant in MT-TL1 (mitochondrial leucine tRNA), that can result in either isolated myopathy, diabetes, deafness or ataxia, but also in the syndromic combination of mitochondrial encephalomyopathy, lactic acidosis and stroke-like episodes (MELAS).<sup>5</sup> The substantial heterogeneity and complex genotype-phenotype correlations greatly complicate diagnosis, prognosis prediction and therapy development for mitochondrial diseases.

To understand genotype-phenotype correlations in mitochondrial disease, patients have been characterized according to their deficient oxidative phosphorylation (OXPHOS) complex. Nonetheless, heterogeneity persists among patients with similar complex deficiencies, illustrated by patients with isolated complex I deficiency that can have either increased- or decreased membrane potential, mitochondrial number and/or mitochondrial fragmentation.<sup>6</sup> Similar discrepancies were observed in fibroblasts of patients harboring complex V deficiency.<sup>3</sup> This may relate to the fact that most OXPHOS complexes establish interactions with other complexes to allow supercomplex formation<sup>7</sup>, to facilitate optimal electron transfer and limited Reactive Oxygen Species (ROS) formation.<sup>8</sup> Supercomplex formation is especially important for complex I, as 80% of all complex I is usually present in supercomplexes, and its presence in supercomplexes significantly promotes complex I stability.<sup>9-11</sup> Characterization based on complex deficiency is further complicated by the fact that complex specific subunits or assembly factors are generally not as specific as once thought.

For example, NDUFA4, previously known as a complex I assembly factor, has also been identified as a complex IV associating factor.<sup>12</sup> TMEM70, which was thought to be primarily a complex V assembly factor, is also involved in complex I assembly.<sup>13</sup> The interdependency of oxidative phosphorylation complexes implies that complex-directed disease subtyping may not be ideal to understand the complex genotype-phenotype relationships in mitochondrial disease.

Mitochondria have many functions that go beyond OXPHOS complex mediated ATP production, which involve ROS production, mitochondrial morphology, lipid oxidation, lipid synthesis, redox homeostasis, Fe/S cluster synthesis, copper metabolism, cardiolipin metabolism, calcium uptake and amino acid metabolism.<sup>14</sup> Similar to the interdependency of oxidative phosphorylation complexes, all of these functional aspects are closely intertwined. Thus, understanding mitochondrial pathophysiology asks for a comprehensive approach, omitting the traditional characterization based on one single functionality, and taking into account the various aspects of mitochondrial function.

Here, we developed a multifaceted assessment of mitochondrial morphology and function using Imaging Flow Cytometry (IFC). We selected five features to assess aberrancies in mitochondrial morphology and function, validated specificity of these features using molecular compounds, and applied these features to 31 different patient-derived fibroblast lines. We identified two disease subtype-overarching clusters, characterized by either a hyper- or hypometabolic response to pathogenic variants. Additionally, the two clusters correlated with specific clinical phenotypes. These results demonstrate that mechanistic exploration of cellular responses to mitochondrial disruptions are essential for understanding distinct genotype-phenotype relationships in mitochondrial diseases. Additionally, these divergent defense mechanisms may require their own unique diagnostic- and therapeutic strategies, paving the way for a more targeted approach of mitochondrial diseases.

## Materials and methods

### *Patient inclusion*

Patients harboring a broad range of mitochondrial diseases were recruited in the Wilhelmina Children's Hospital Utrecht and in the Radboud Medical Center in Nijmegen. Informed consent was obtained to use residual material collected for diagnostic purposes to include in the Wilhelmina Children's Hospital metabolic biobank (TCBio 19-489/B, <https://tcbio.umcutrecht.nl>) and we filed an additional protocol that allowed us to use these samples (TCBio 22-538). By using the same biobank, we included residual material of six different pediatric healthy fibroblast lines. All procedures performed in studies involving human participants were in accordance with the ethical standards of the institutional and/or national research committee(s) and with the Helsinki Declaration (as revised in 2013).

### *Fibroblast Cultures*

Cells were cultured in fibroblast culture medium (HAM F12 with 10% fetal bovine serum, penicillin (100 UI/ml) and streptomycin (100 µg/ml)), in a humidified incubator at 37°C and 5% CO<sub>2</sub>. Medium was changed every 3-4 days. Cells were split at 80% confluency.

### *Enzyme activity Assays*

OXPPOS enzyme and citrate synthase activities in muscle tissue or fibroblasts were assessed spectrophotometrically using standard procedures.<sup>54-56</sup> Thirty-seven and 100 internal control samples were used in the experiments with muscle and fibroblasts, respectively.

### *Seahorse-based Oxygen Consumption Rate Measurements*

Oxygen consumption rates (OCRs) were measured using the Seahorse XFe96 Extracellular flux analyzer (Agilent). Detailed methods have been described elsewhere.<sup>57</sup>

### *Imaging Flow Cytometry Assays*

Cells were plated in 6-well plates to reach 70-80% confluency. At the day of the assay, cells were incubated in the antibody mixture containing TMRM

(30 nM, Sigma Aldrich), NAO (50 nM, Enzo Life Sciences) and DRAQ5 (Biolegend) at 37 degrees in HBSS for 40 minutes. FCCP (3  $\mu$ M, Target-Mol) was added during the final 5 minutes. After incubation, cells were washed once and incubated with TrypLE (Gibco) for 2 minutes. Cells were harvested using 1 mL 10% dialyzed FBS (Gibco) in PBS0, washed once, and immediately visualized using Imaging Flow Cytometry. Since lipophilic cations like TMRM are extruded by Multi Drug Resistance (MDR) transporters<sup>58</sup>, TMRM fluorescence is not stable for prolonged periods.<sup>59</sup> Therefore, we included a total of 4 samples per assay. All experiments were performed within 30 minutes after the staining procedure, and each assay was performed in the exact same order to keep the duration between staining and imaging similar.

### *Imaging Flow Cytometry Features*

To quantify mitochondrial morphology and function, six features were selected. TMRM intensity reflects the absolute mitochondrial membrane potential. The normalized membrane potential is calculated by subtracting TMRM intensity (Intensity\_Ch03) in cells treated with FCCP (a potent mitochondrial uncoupler) from total TMRM intensity. FCCP response was calculated by dividing the intensity of TMRM of the non-treated sample by the intensity of TMRM in the treated sample. NAO intensity was used to indicate mitochondrial mass, correlating with the ability of cells to produce and maintain mtDNA. We calculated NAO intensity in the FCCP treated sample, to limit the effect of membrane potential on NAO intensity. For mitochondrial morphology, we used Form Factor, a measure reflective of mitochondrial fragmentation (decreased form factor) or compensatory branching (increased form factor). For the form factor, the spot mask on the TMRM staining was used (Bright, threshold 10, minimal area 0, maximal area 2). The median values derived from the Area\_Spot\_M03(10-0-2) and Perimeter Spot\_M03(10-0-2) features were used for the calculation of the form factor:  $[(\text{perimeter}^2)/(4\pi \cdot \text{surface area})]$ . Mitochondrial swelling was calculated by measuring total Area of the TMRM staining and reflects the mitochondrial permeability transition pore functionality (mPTP). Mitochondrial ROS production was assessed by quantifying the cytoplasmic MitoSox intensity, to

exclude intensity related to nonspecific binding of MitoSox to nucleic acids. For MitoSox intensity, a binary mask was created, that excluded the nuclear surface (DRAQ5 – Ch05 Morphology Mask), but included the cytoplasm (Ch01 Morphology).

### *Molecular compounds used for assay validation*

To validate the specificity of the membrane potential assay, we incubated cells with 10 ng/ml (25  $\mu$ M) Rotenone (Cayman Chemicals) 4 hours prior to the assay. To stimulate mitochondrial biogenesis, we incubated cells with 10 mM Valproic acid (Santa Cruz Biotechnology) for 4 days. To deplete mitochondrial mass, we incubated cells with 25 ng/ml Ethidiumbromide (Sigma Aldrich) for 7 days. To induce mitochondrial fusion, we treated fibroblasts with 50  $\mu$ M MDIVI1 (Sigma Aldrich) for 16 hours. To induce mitochondrial fragmentation, we incubated cells with 1.2  $\mu$ M Staurosporine (Adipogen) for 2 hours prior to the assay. To induce mitochondrial ROS production, we stimulated cells with 1  $\mu$ M antimycin A (Sigma Aldrich) for 40 minutes.

### *Data analysis – Statistics and R*

Data was collected with Amnis Imaging Flow Cytometry MkII Imaging Flow Cytometer (Luminex, Austin, US) and data analysis was performed with IDEAS version 6.0 software. Gating strategy can be found in Figure S2. Briefly, nucleated cells, cells in focus and single cells were gated. To create figure 1, raw values were extracted from IDEAS as excel files and analyzed using using R (Version 4.2.3) and R-studio (Version 2022.12.0.353).

For Figure 2B, normalized percentage values were used, for which the median value of each sample was extracted from IDEAS. Subsequently, the median values of each patient were normalized against a healthy control sample analyzed within the same experiment. All graphs and UMAP plots were created using R-studio, except for the line chart of Figure 2A, which was created with GraphPad Prism version 6 for Windows (GraphPad Software, USA). The following R packages were used for analysis: umap (0.2.10.0), dplyr (1.1.3), ggplot2 (3.4.3), ggfortify (0.4.16), gridExtra (2.3),

corrplot (0.92), factoextra (1.0.7), ggradar (0.2).

## Results

### *Assay selection*

To quantify mitochondrial function and morphology in a multifaceted way, we first selected dyes and features that would reflect a broad spectrum of functional, morphological and molecular domains of mitochondrial functionality. Dyes and features were based on the five most important qualifiers of mitochondrial function as described by Monzel et al.<sup>14</sup> (**Table 1**).

Mitochondrial Function	Fluorescent Dye	Feature	Positive Control
Mitochondrial Mass	Nonyl Acridine Orange (NAO)	NAO Intensity	Valproic acid (Mitochondrial Mass ↑) <sup>15</sup> Ethidiumbromide (Mitochondrial Mass ↓) <sup>16</sup>
Mitochondrial Swelling	Tetramethylrhodamine, Methyl Ester, Perchlorate (TMRM)	Mitochondrial Area	Ethidiumbromide (Mitochondrial Swelling ↓) <sup>16</sup>
Membrane potential	Tetramethylrhodamine, Methyl Ester, Perchlorate (TMRM)	TMRM Intensity (Normalized to FCCP)	Rotenone (Membrane Potential ↓) <sup>17</sup>
Reactive Oxygen Species (ROS)	MitoSox	Non-nuclear MitoSox Intensity	Antimycin-A (ROS Production ↑) <sup>18</sup>
Mitochondrial Fission/Fusion/Fragmentation	Tetramethylrhodamine, Methyl Ester, Perchlorate (TMRM)	Form Factor: Perimeter <sup>2</sup> / (4π*Area)	Staurosporine (Fragmentation ↑) <sup>19</sup> MDIVI (Mitochondrial Fusion ↑) <sup>20</sup>

**Table 1: Showing Imaging Flow Cytometry (IFC) dyes and features.** The ↑ sign indicates that the molecular compound selected as positive control heightens the feature value. The ↓ sign indicates that the molecular compound selected as positive control decreases the feature value.

### *Impact of Fibroblast Confluency and Passage Number on mitochondrial function*

First, we evaluated the effect of fibroblast confluency and passage number on IFC features. When confluency dropped below 30% or exceeded 90%, four out of five assays showed significant aberrancies (IQR <25th percentile or >75th percentile) (**Supplementary Figure 1A**). Similarly, high passage number (>15) affected membrane potential and ROS production significantly (IQR <25th percentile or >75th percentile) (**Supplementary Figure 1B**).



To minimize confluency- and passage-induced effects, we ensured that confluency was kept between 30% and 90%, and passage number differences between donors were kept at a minimum (preferably <5, but at least <15).

### *Assay Validation*

For validation of IFC dyes and features, we used five different compounds each known to affect one of the five selected features (**Table 1**). All compounds affected the corresponding feature as expected, indicating that IFC features reflected their corresponding mitochondrial function (**Figure 1A-G**). For rotenone, hyperpolarization was observed for FCCP-normalized membrane potential values, whereas a drop in membrane potential was evident in non-FCCP treated cells (**Figure 1A**). These highly variable effects of rotenone ranging from hypo- to hyperpolarization concur with results from literature.<sup>21</sup> Next, we evaluated the effect of the compounds on other features. We found that all compounds affected multiple features (**Figure 1H**), supporting the notion that all mitochondrial functions are mutually dependent.

### *Characteristics of the Patient Cohort*

We included fibroblasts of 31 patients encompassing a range of different disease subtypes including isolated complex deficiencies (complex I, II, III, IV and V), as well defects of translation, mtDNA maintenance, and cardiolipin remodeling (**Figure 2A**). Clinical characteristics of the cohort are detailed in **Supplementary Table 1**. Additionally, we included six healthy control fibroblast lines: four pediatric donors and two adult donors aged 20 and 23 years. The results for the healthy controls on each of the six features were taken as reference. Specifically, the values found in the controls were normalized against the individual means and converted to percentages, and the lowest and highest percentage values were used as upper and lower reference values (**Supplementary Table 1**). For mitochondrial disease patients, values were normalized against the mean of the healthy control taken along within the same experiment. Values were considered abnormal when they exceeded the lower- or upper reference range established in six healthy controls.

# Imaging Flow Cytometry for Mitochondrial Diseases

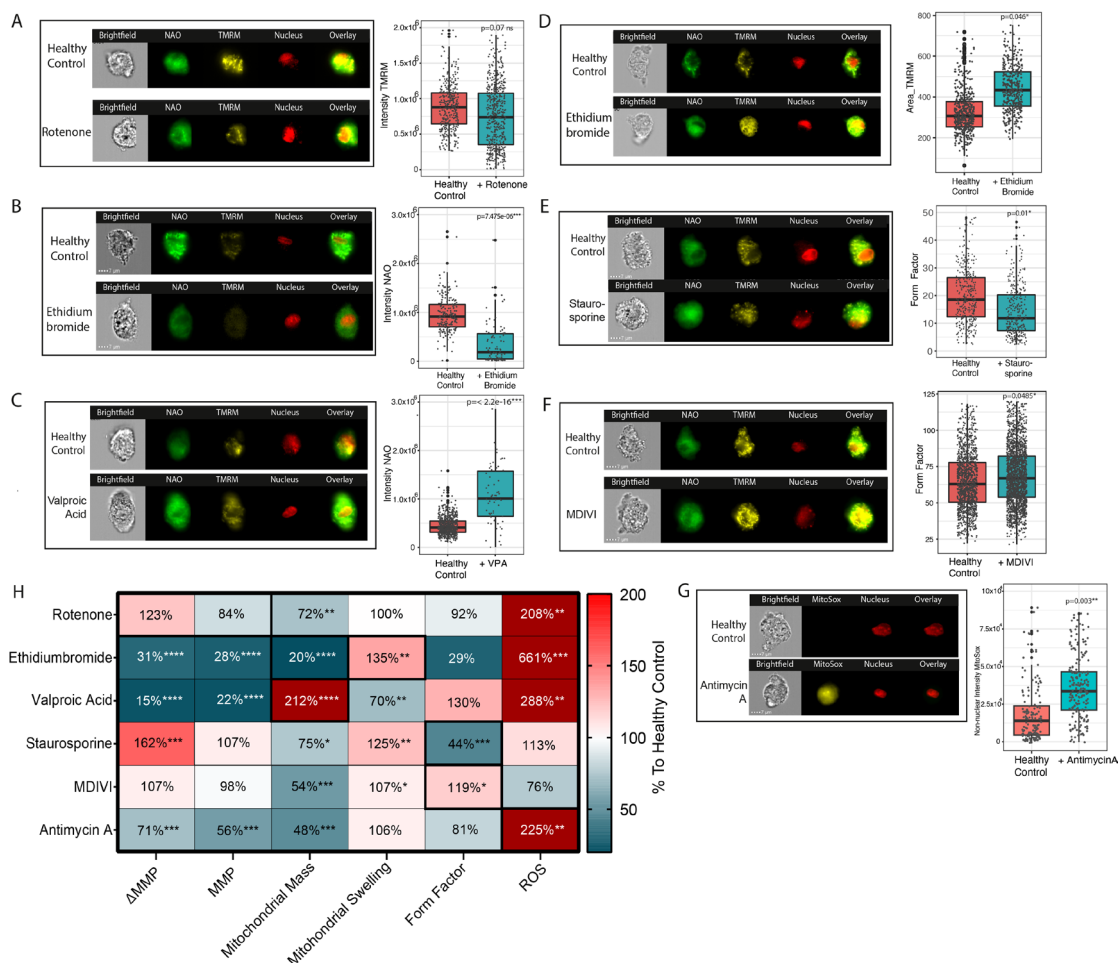


**Figure 1: Assay validation using molecular compounds.**

For all boxplots, the black line indicates the mean value, the lower and upper hinges correspond to the 25th and 75th percentiles. The upper and lower whisker extend to 1.5\*IQR. Linear mixed model analysis was used to calculate significance (\* $P < 0.05$ , \*\* $P < 0.01$ , \*\*\* $P < 0.001$ , \*\*\*\* $P < 0.0001$ ). Figures A-G show a representative example of a healthy control fibroblasts and the same healthy donor treated with:

(A) Rotenone for 4 hours (10 ng/ml). The boxplot shows the non-normalized TMRM Intensity for both conditions.

(B) Ethidiumbromide for 7 days (25 ng/ml). The boxplot shows the NAO Intensity in the FCCP treated condition for both conditions.

(C) Valproic acid for 4 days (10 mM). The boxplots show the NAO Intensity in the FCCP treated condition for both conditions.

(D) Ethidiumbromide for 7 days (25 ng/ml). The boxplot shows the non-normalized TMRM Area for both donors.

(E) Staurosporine for 2 hours (1.2  $\mu$ M). The boxplot shows the Form Factor (Mean Perimeter<sup>2</sup>)/(4 $\pi$  \* Mean Area) for both conditions.

(F) MDIVI1 for 16 hours (50  $\mu$ M). The boxplot shows the Form Factor for both conditions.

(G) Antimycin A for 5 minutes (10  $\mu$ M) causing mitochondrial reactive oxygen species production. The boxplot shows the Intensity of the MitoSox staining for both conditions.

(H) Heat Map showing experimental results for healthy controls treated with molecular compounds on all axes. Similar treatment conditions and features were used as stated in Fig 1A-G to create the graph. The mean value of the compound-treated fibroblast donor was normalized to the healthy control analyzed within the same experiment and converted to percentages. Percentages corresponding to the color coding are shown on the right. The black squares indicate the primary feature for which the compound was selected. Membrane potential was quantified by subtracting the background TMRM intensity in a sample treated with FCCP from that in a non-FCCP treated sample ( $\Delta$ MMP). The absolute membrane potential without subtraction of the FCCP sample is indicated as MMP.

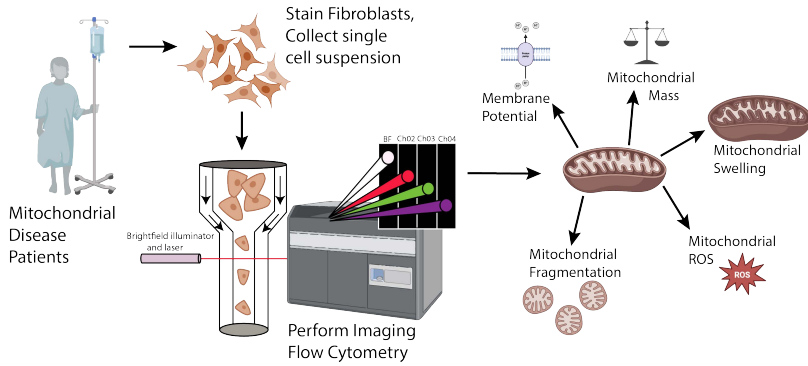
### *Imaging Flow Cytometry in Mitochondrial Disease Patients*

In patient-derived fibroblasts, we found that all five features could be either increased or decreased compared to healthy control fibroblasts (**Supplementary Table 1**). When using one feature in isolation, 20-60% of patients showed significant differences compared to healthy controls, depending on the feature used (**Figure 2B**). When considering all five features, 94% of patients showed significant changes on at least one of the five assays (**Figure 2B**).

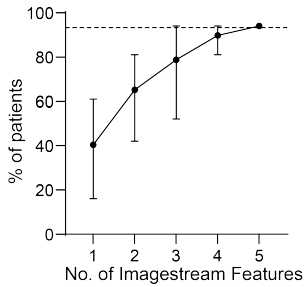
We then assessed the correlation of IFC features with traditional diagnostic testing for mitochondrial disease. In 19% of patients (6/31), Seahorse experiments were performed as part of their diagnostic follow up, although in none of these patients, significant differences in basal- or maximal respiration (OCR) were found (**Supplementary Table 1**). In contrast, all patients showed significant changes on at least one of six IFC features (**Supplementary Figure 2B**). We found no significant correlations between IFC features and specific isolated OXPHOS complex deficiencies in fibroblasts (**Supplementary Figure 2B**). We did observe a strong correlation between certain IFC features and complex I and IV deficiency in muscle, however, these measurements were only performed in a small number of patients (**Supplementary Figure 2C**).

# Imaging Flow Cytometry for Mitochondrial Diseases

A



B



C



# Chapter 6

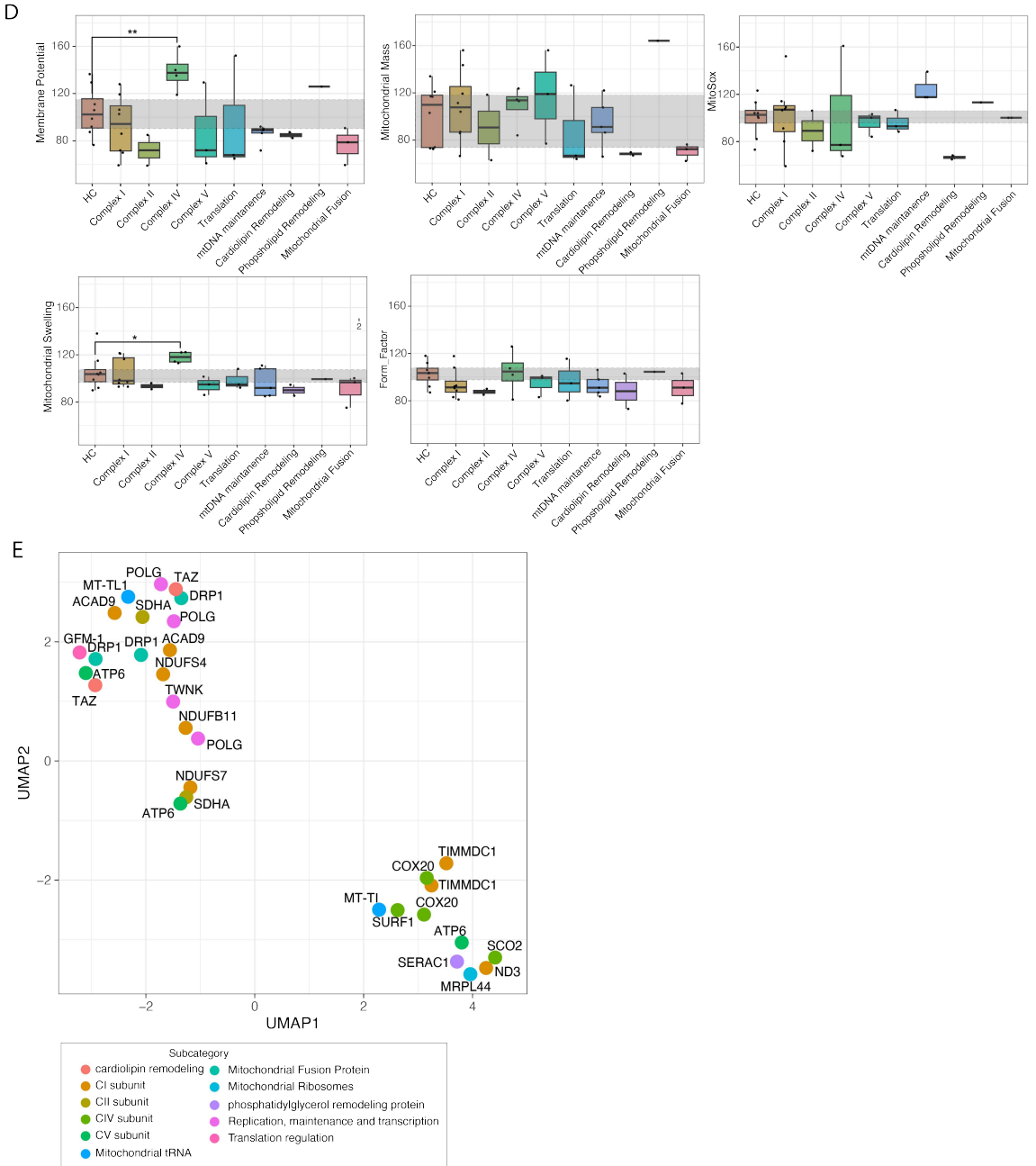


**Figure 2: Results of Imaging Flow Cytometry (IFC) assays for patients with mitochondrial disease.**

(A) Graphical representation of the IFC workflow. Fibroblasts derived from mitochondrial disease patients were cultured, plated, collected and stained with NAO, TMRM, MitoSox and DRAQ5. Living cells were analyzed using IFC and the five different mitochondrial features were extracted from the software.

(B) The percentage of patients showing significant changes on one or more assays was assessed for single features and for feature combinations. The Y-axis shows the percentage of patients with significant changes on either one, two, three, four or all five IFC assays. The dots represent the mean percentage for all possible combinations, the error bar represents the range.

(C) Radar plots showing the results for each patient on the five IFC assays. Patients harboring genetic variants in the same gene are grouped together. The light grey planes indicate the range of aberrancies in healthy control (lowest-highest). The line in the middle of the grey plane indicates the mean values in healthy controls. The red lines refer to the patients. All radar plots are scaled from 0 to 200%.

(D) Boxplots showing IFC assay results for all five assays. The Y-axis refers to the percentage observed in that specific donor normalized against the healthy control taken along in the same run. All six healthy controls (HC) were normalized against one healthy control. Each dot represents one donor. The grey planes indicate the reference values, based upon the entire range of assay results of six healthy controls (lowest-highest). The black line indicates the mean value, the lower and upper hinges correspond to the 25th and 75th percentiles. The upper and lower whisker extend to  $1.5 \times \text{IQR}$ . Statistics were only calculated when disease subgroups consisted of three patients or more. Mann Whitney U test was used to calculate significance. Each group was compared to the healthy control reference range. Only the significant values are indicated.

(E) UMAP (Euclidean distance, neighbors = 8, minimal distance = 0.01) showing IFC results for all patients with mitochondrial disease. The dots are colored according to the disease subtypes. The text refers to the name of the mutated gene.

### *Correlation of IFC characteristics with disease subtypes*

First, we assessed whether IFC aberrancies correlated with specific genetic defects or disease subtypes. **Figure 2C** shows an overview of the significant changes for each of the five features for all 31 patients, grouped per gene. The majority of patients with pathogenic variants in the same gene showed similar changes. In addition, we found that a small subset of disease subtypes showed similar changes on single axes (**Figure 2D**). Patients with complex IV deficiency showed increased membrane potential, while patients with *TAZ* variants, affecting cardiolipin remodeling, showed decreased mitochondrial mass and ROS production. However, most disease subtypes did not show similar phenotypes, and did not cluster together on UMAP (**Figure**

2E). Instead, there appeared to be two large disease-overarching clusters encompassing multiple disease subtypes.

Next, we sought to identify disease subtype-overarching clusters showing similar changes on IFC assays. Hierarchical clustering revealed that mitochondrial disease patients could be divided into two clusters (**Figure 3A**). Cluster 1 was characterized by decreased membrane potential, while cluster 2 was characterized by increased membrane potential, increased mitochondrial swelling and increased mitochondrial mass (**Figure 3B**). The first cluster consisted of complex I, II or V deficiencies, transcriptional deficits, and variants in mitochondrial tRNA, DRP1 or TAZ genes. The second cluster consisted of all patients harboring isolated complex IV deficiency, three patients with isolated complex I deficiency (TIMMDC1, mt-ND3), and one patient with complex V deficiency. Three patients in whom multiple complexes were affected were also part of cluster 2.<sup>22,23</sup> While background-subtracted TMRM values differed significantly between clusters, the non-background subtracted membrane potential appeared similar (**Figure 3C**). The heightened membrane potential may therefore be associated with an enhanced response to FCCP rather than an absolute disparity in membrane potential (**Figure 3C**). Notably, heightened sensitivity to FCCP has been previously documented in patients harboring pathogenic complex IV variants.<sup>24</sup> Similarly, we found that all patients with complex IV deficiency included in this study showed heightened membrane potential, potentially through increased FCCP sensitivity.

Patients with isolated complex I deficiencies were clustered separately, concurring with literature.<sup>25,26</sup> The disparate phenotypes are thought to correlate with the location of the affected subunits within holo-complex I.<sup>27</sup> Pathogenic variants leading to a disconnected N module cause increased ROS production, while pathogenic variants in the proton pumping module lead to decreased proton pumping activity and NADH accumulation. To assess whether these findings aligned with our clusters, we verified the location of the pathogenic variants within holo-complex I (**Figure 3E**). Since cluster 1 was associated with increased ROS production, we hypothesized that

# Imaging Flow Cytometry for Mitochondrial Diseases

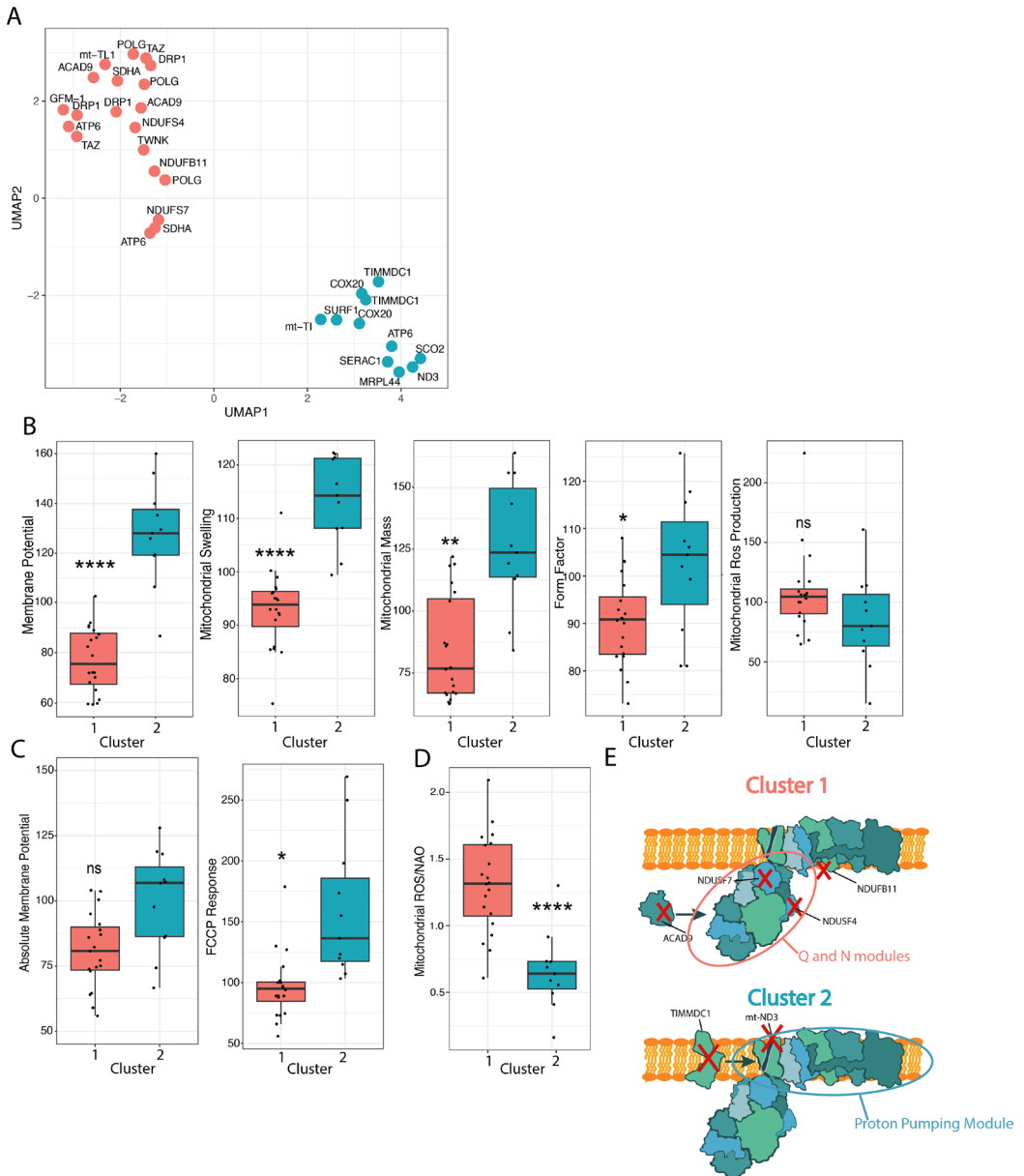


**Figure 3: Clustering of mitochondrial disease patients**

(A) Showing the same UMAP as in Figure 2C, however, now the nodes are colored



according to the clusters. Distance was calculated using Euclidean distance, and Ward's method was used to identify clusters.

(B) Boxplots showing the IFC characteristics for each of the two clusters. Statistics were calculated using Welsch t-test. For all boxplots, the black line indicates the mean value, the lower and upper hinges correspond to the 25th and 75th percentiles. The upper and lower whisker extend to 1.5\*IQR.

(C) Boxplot showing the FCCP response for each of the two clusters. The FCCP response was calculated by dividing the mean TMRM intensity of the untreated sample by the mean TMRM intensity of the FCCP treated sample. This ratio was then compared to the healthy control taken along in the same run and converted to percentage values.

(D) Boxplot showing mitochondrial ROS production normalized against mitochondrial mass for the two clusters. Since MitoSox and TMRM were analyzed in two separate experiments, intensity values were first normalized against healthy controls, and these normalized values were then converted to ratios by dividing the normalized MitoSox values by the normalized NAO intensity values. This ratio is shown on the Y-axis.

(E) Graphical representation of complex I and the location of the pathogenic variants of patients harboring isolated complex I deficiency (indicated with a red cross). In Cluster 1, patients with mutations affecting the N or Q module are included, leading to defective complex I assembly and stability (red circle). In Cluster 2, patients with mutations affecting the P module are included, affecting proton pumping activity (blue circle).

this cluster would show complex I assembly defects and disconnection of the N module. Indeed, for patients with pathogenic *NDUFS4* and *NDUFS7* variants, disconnection of the N module has been observed.<sup>27,28</sup> Similarly, pathogenic *NDUFB11* variants are associated with impaired assembly of the peripheral subunits, (including the N module) corresponding with the pre-sense of this patient in cluster 1 (**Figure 3E**).<sup>29,30</sup> Finally, pathogenic variants in *ACAD9* have been associated with accumulation of late-stage complex I assembly intermediates lacking the N module, explaining their presence in the first cluster (**Figure 3E**).<sup>31,32</sup>

In contrast, pathogenic *ND3* variants, part of cluster 2, generally affect proton translocation without accumulation of late-stage complex I assembly intermediates.<sup>33</sup> Patients harboring pathogenic variants in *TIMMDC1* (part of cluster 2) are similarly thought to have dysfunctional proton pumping activity due to *TIMMDC1*'s involvement in the membrane arm of complex I (ND1) and lack of colocalization with late-stage intermediates.<sup>34,35</sup>

In conclusion, the separation of complex I deficient patients into two separate clusters could be related to functional defects caused by either disconnected N module or defective proton pumping activity.

## Imaging Flow Cytometry for Mitochondrial Diseases

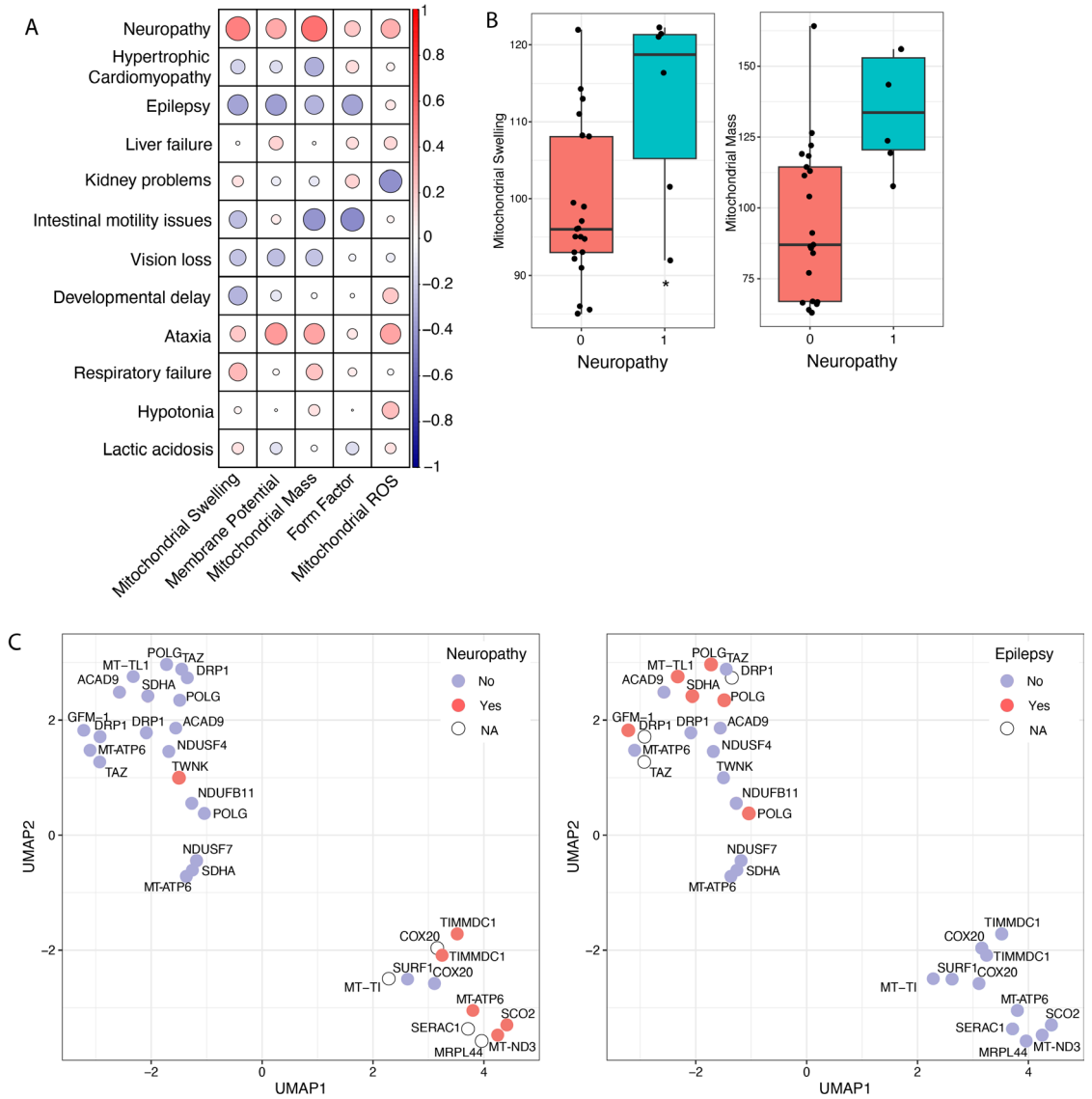


**Figure 4: Correlation of IFC features with phenotypic features.**

(A) Correlation plot showing the correlation between IFC features and clinical phenotype. All clinical features were converted to binary parameters (1=Present, 0=Not present) and correlation was calculated using Point-Biserial Correlation Coefficient.

(B) The only significant correlation between neuropathy and mitochondrial swelling is plotted as a boxplot. Statistics were calculated using Point-Biserial Correlation Coefficient. The

patient with *TWINK* mutation is highlighted separately.

(C) Showing the UMAP Plots from Figure 2C and 3A. The nodes are colored according to the presence of certain clinical phenotypic features (Yes, No, NA). NA means that the specific feature was not assessed in patients.

### Correlation of mitochondrial phenotype with clinical phenotype

Next, we assessed whether IFC features correlated with specific clinical phenotypes (**Figure 4A**). We found only one significant correlation, between neuropathy and mitochondrial swelling (**Figure 4B**). Intriguingly, all except one patient (harboring a pathogenic *TWINK* variant) showing neuropathy were part of cluster 2 (**Figure 4C**, Fisher's Exact test,  $p=0.0027^{**}$ ). Similarly, epilepsy was exclusively seen cluster 1, although this difference was not statistically significant (Fisher's Exact test,  $p=0.0549$ ). For a subset of patients that were part of cluster 2, neuropathy was not assessed (NA) due to lethality at a very young age.

## Discussion

It has long remained challenging to capture mitochondrial disease pathophysiology by focusing on similar genetic mutations or OXPHOS complex deficiencies. We hypothesized that multifaceted functional screening of mitochondria in many different disease subtypes could provide novel insights in the complex genotype-phenotype correlation of mitochondrial diseases. To this aim, we developed five Imaging Flow Cytometry (IFC) assays, using three mitochondrial dyes and five pivotal features, which we validated using molecular compounds known to disrupt one of these five features. We found that 94% of patients with mitochondrial disease showed significant changes on one or more of these five assays. While we did not observe disease subtype-specific phenotypes, we did identify two disease-overarching clusters, based on increased ROS production (Cluster 1) or increased membrane potential, mitochondrial mass and mitochondrial swelling (Cluster 2). Literature-supported analyses revealed that all genes in cluster 1 were associated with decreased complex I stability, whereas cluster 2 consisted of patients

associated with decreased proton pumping activity. At the clinical level, we found that epilepsy was predominantly observed in cluster 1, whereas neuropathy was predominantly observed in cluster 2.

In conclusion, we here found that multifaceted quantification of mitochondrial features using IFC allows detection of specific functional defects in nearly all patients with mitochondrial disease. Additionally, the identification of disease subtype-overarching clusters based on similar responses to mitochondrial injury grants relevant insights into pathology, suggesting that functional characterization of mitochondrial diseases might be superior compared to genetic- or complex based characterization.

The past decade, several attempts to perform high-throughput quantification of multiple aspects of mitochondrial morphology and function in patients with mitochondrial disease using live-cell imaging, microscopic screening or flow cytometry have been made.<sup>32,42–45</sup> While microscopy can quantify mitochondrial morphology with higher resolution, the data analysis of microscopic images is notoriously complex and often based on machine- and deep learning approaches. IFC is straightforward, equipped to analyze a large number of cells (>5000 cells) in a limited amount of time (5 minutes), allowing statistical analysis of large populations<sup>46</sup>. Until now, most studies that use microscopy have only been applied to small patient groups, focusing on one subtype of disease, for example isolated complex I deficiency<sup>32,33,45,47,48</sup>, MFN2 variants<sup>49</sup>, or isolated complex V deficiency.<sup>3,50</sup> Studies that did focus on multiple disease subtypes have only used small patient groups, which limits the reliable detection of disease-overarching clusters.<sup>51,52</sup> Thus, the potential of microscopy for detecting mitochondrial pathology in different disease subtypes remains uncertain. However, our study shows that the straightforward assessment of mitochondrial morphology and function using IFC is a suitable method to rapidly identify patient groups showing similar mitochondrial dysfunctionality.

If membrane potential is compromised due to oxidative phosphorylation (OXPHOS) deficiencies, complex V may exhibit partial compensatory activity by utilizing ATP to uphold membrane potential.<sup>53,54</sup> The administration

of FCCP, known for inducing a substantial H<sup>+</sup> current and abolishing the reversed action of complex V, provides an opportunity to unveil patients who rely on this compensatory mechanism. Notably, all patients within cluster 1 exhibited a FCCP response similar to that of healthy controls, suggesting the absence of this compensatory mechanism. In support, the absence of reversed complex V activity has been observed in *NDUFS4* knockout mice.<sup>55</sup> In contrast, all patients included in cluster 2 showed increased FCCP response, correlating with data obtained using SURF1-deficient fibroblasts.<sup>30</sup> Together, these results indicate that the presence or absence of compensatory action of complex V could correlate with heightened membrane potential and increased FCCP response, contributing to the functional separation of the two clusters.

In this study, we attributed shared functional defects based on the location of affected genes within holo-complex I. However, phenotypic heterogeneity is known to persist for pathogenic variants within the same gene, even for pathogenic variants at the exact same location. This was recapitulated in our study, where we found that patients with pathogenic mt-*ATP6* variants could be part of either cluster 1 or 2, although the position of the mt-*ATP6* genetic variants differed between clusters. Regardless, Ganetzky et al found that patients with the pathogenic MT-*ATP6* variants at the exact same location can show highly heterogeneous cellular phenotypes. The authors attributed this heterogeneity to secondary deficits. It is thought that mitochondrial heterogeneity originates through a combination of genetic background, heteroplasmy levels and epigenetic modifications, making certain individuals more prone to specific secondary mitochondrial responses to primary injury. Therefore, we hypothesize that mitochondrial diseases should be regarded as entities that can potentially show any given phenotype, regardless of their primarily affected gene or complex. Building on this premise, assessment of mitochondrial diseases thus demands a functional and multifaceted approach, capturing all secondary responses to primary mitochondrial injury.

We used fibroblasts for our IFC assays. Although easily obtained and expanded, their glycolytic dependency might fail to unveil relatively mild

mitochondrial disorders. However, our study shows that 94% of patients present with aberrancies on at least one of five assays, indicating that even in fibroblasts, mitochondrial aberrancies are recapitulated to some degree. Only two patients showed no significant changes on the IFC assays, although one patient with pathogenic *DRP1* variants showed borderline abnormal mitochondrial mass reduction. For the patient with pathogenic *NDUFS4* variants, all values were within normal range. Nonetheless, the degree of patients showing aberrancies exceeds the percentages seen for most other methods.<sup>56,57</sup> Additionally, many patients with mitochondrial disease exhibit aberrancies not confined to one or multiple complex deficiencies, which will be missed when diagnostic techniques focus on complex specific deficiencies alone. Formal testing of IFC assays using larger cohorts can help determine the absolute diagnostic value of single- and combined IFC assays compared to other diagnostic techniques currently used.

The two clusters identified in this study reflect two convergent functional responses to mitochondrial pathology, which might best be characterized as either a hypo- or hypermetabolic response. While a hypermetabolic response to mitochondrial injury may seem controversial, it has been frequently observed in mitochondrial disease animal models<sup>58,59</sup>, and patient-derived cells.<sup>60,61</sup> While the exact reason for this hypermetabolic state is not entirely clear, it is considered potentially damaging for mitochondrial disease patient cells, that struggle to maintain sufficient energy levels in the first place.<sup>60</sup> Therefore, direct targeting of this potential harmful compensatory mechanism by decreasing hypermetabolism could be beneficial. However, patients exhibiting a primarily hypometabolic state should not be exposed to these kinds of treatments. Instead, since cluster 1 was characterized by increased ROS production, these patients might benefit primarily from anti-oxidant treatment. Thus, our functional-based screening of mitochondrial disease patient cells could aid the optimization of personalized treatment strategies, aiming to normalize potentially harmful secondary deficits associated with primary pathology.

In conclusion, we here provide a high-throughput approach to quantify

mitochondrial function in patients with mitochondrial disease using Imaging Flow Cytometry. This approach enabled identification of abnormal mitochondrial features in nearly all patients with mitochondrial disease, and clustered patients based on similar functional responses to primary mitochondrial pathology. Our results indicate that functional classification of mitochondrial diseases may outperform genetic-based classifications, and can provide a novel basis to improve personalized diagnostic and therapeutic approaches for mitochondrial disease patients, based on shared secondary responses to mitochondrial injury.

### Acknowledgements

This work was funded by the Wilhelmina Children's Hospital Stimulus Stipend and United For Metabolic Diseases Catalyst Grant.

### References

1. López-Gallardo E, Emperador S, Solano A, Llobet L, Martín-Navarro A, López-Pérez MJ osé, et al. Expanding the clinical phenotypes of MT-ATP6 mutations. *Hum Mol Genet.* 2014;23(23):6191–200.
2. Capiiau S, Smet J, De Paepe B, Yildiz Y, Arslan M, Stevens O, et al. Clinical Heterogeneity in MT-ATP6 Pathogenic Variants: Same Genotype—Different Onset. *Cells.* 2022;11(3).
3. Ganetzky RD, Stendel C, McCormick EM, Zolkipli-Cunningham Z, Goldstein AC, Klopstock T, et al. MT-ATP6 mitochondrial disease variants: Phenotypic and biochemical features analysis in 218 published cases and cohort of 14 new cases. *Hum Mutat.* 2019;40(5):499–515.
4. Budde SMS, van den Heuvel LPWJ, Smeets RJP, Skladal D, Mayr JA, Boelen C, et al. Clinical heterogeneity in patients with mutations in the NDUF54 gene of mitochondrial complex I. *J Inherit Metab Dis.* 2003;26(8):813–5.
5. Nesbitt V, Pitceathly RDS, Turnbull DM, Taylor RW, Sweeney MG, Mudanohwo EE, et al. The UK MRC Mitochondrial Disease Patient Cohort Study: Clinical phenotypes associated with the m.3243A>G mutation - Implications for diagnosis and management. *J Neurol Neurosurg Psychiatry.* 2013;84(8):936–8.
6. Distelmaier F, Koopman WJH, Van Den Heuvel LP, Rodenburg RJ, Mayatepek E, Willems PHGM, et al. Mitochondrial complex I deficiency: From organelle dysfunction to clinical disease. *Brain.* 2009;132(4):833–42.
7. Schägger H. Blue-native gels to isolate protein complexes from mitochondria. *Methods Cell Biol.* 2001;(65):231–44.
8. Maranzana E, Barbero G, Falasca AI, Lenaz G, Genova ML. Mitochondrial respi-

ratory supercomplex association limits production of reactive oxygen species from complex I. *Antioxid Redox Signal*. 2013;19(13):1469–80.

9. Lopez-Fabuel I, Le Douce J, Logan A, James AM, Bonvento G, Murphy MP, et al. Complex I assembly into supercomplexes determines differential mitochondrial ROS production in neurons and astrocytes. *Proc Natl Acad Sci U S A*. 2016;113(46):13063–8.
10. Protasoni M, Pérez-Pérez R, Lobo-Jarne T, Harbour ME, Ding S, Peñas A, et al. Respiratory supercomplexes act as a platform for complex III-mediated maturation of human mitochondrial complexes I and IV. *EMBO J*. 2020;39(3).
11. Schägger H, Pfeiffer K. The Ratio of Oxidative Phosphorylation Complexes I-V in Bovine Heart Mitochondria and the Composition of Respiratory Chain Supercomplexes. *Journal of Biological Chemistry*. 2001;276(41):37861–7.
12. Balsa E, Marco R, Perales-Clemente E, Szklarczyk R, Calvo E, Landázuri MO, et al. NDUFA4 is a subunit of complex IV of the mammalian electron transport chain. *Cell Metab*. 2012;16(3):378–86.
13. Sánchez-Caballero L, Elurbe DM, Baertling F, Guerrero-Castillo S, van den Brand M, van Strien J, et al. TMEM70 functions in the assembly of complexes I and V. *Biochim Biophys Acta Bioenerg*. 2020;1861(8).
14. Monzel AS, Enríquez JA, Picard M. Multifaceted mitochondria: moving mitochondrial science beyond function and dysfunction. *Nat Metab*. 2023;5(4):546–62.
15. Feichtinger RG, Oláhová M, Kishita Y, Garone C, Kremer LS, Yagi M, et al. Biallelic C1QBP Mutations Cause Severe Neonatal-, Childhood-, or Later-Onset Cardiomyopathy Associated with Combined Respiratory-Chain Deficiencies. *Am J Hum Genet*. 2017;101(4):525–38.
16. Charif M, Gueguen N, Ferré M, Elkarhat Z, Khiati S, Lemaou M, et al. Dominant ACO2 mutations are a frequent cause of isolated optic atrophy. *Brain Commun*. 2021;3(2).
17. Gueguen N, Piarroux J, Sarzi E, Benkirane M, Manes G, Delettre C, et al. Optic neuropathy linked to ACAD9 pathogenic variants: A potentially riboflavin-responsive disorder? *Mitochondrion*. 2021;59:169–74.
18. Panneman DM, Wortmann SB, Haaxma CA, van Hasselt PM, Wolf NI, Hendriks Y, et al. Variants in NGLY1 lead to intellectual disability, myoclonus epilepsy, sensorimotor axonal polyneuropathy and mitochondrial dysfunction. *Clin Genet*. 2020;97(4):556–66.
19. Diaz G, Diana A, Falchi AM, Gremo F, Pani A, Batetta B, et al. Intra- and intercellular distribution of mitochondrial probes and changes after treatment with MDR modulators. *IUBMB Life*. 2001;51(2):121–6.
20. Bernardi P, Scorrano L, Colonna R, Petronilli V, Di Lisa F. Mitochondria and cell death. Mechanistic aspects and methodological issues. *Eur J Biochem*. 1999;264(3):687–701.
21. Sitarz KS, Elliott HR, Karaman BS, Relton C, Chinnery PF, Horvath R. Valproic acid triggers increased mitochondrial biogenesis in POLG-deficient fibroblasts. *Mol Genet Metab*. 2014;112(1):57–63.
22. Stewart JD, Schoeler S, Sitarz KS, Horvath R, Hallmann K, Pyle A, et al. POLG



- mutations cause decreased mitochondrial DNA repopulation rates following induced depletion in human fibroblasts. *Biochim Biophys Acta Mol Basis Dis.* 2011;1812(3):321–5.
23. De Paepe B, Smet J, Vanlander A, Seneca S, Lissens W, De Meirleir L, et al. Fluorescence imaging of mitochondria in cultured skin fibroblasts: a useful method for the detection of oxidative phosphorylation defects. *Pediatr Res.* 2012;72(3):232–40.
24. Wang L, Duan Q, Wang T, Ahmed M, Zhang N, Li Y, et al. Mitochondrial respiratory chain inhibitors involved in ROS production induced by acute high concentrations of iodide and the effects of sod as a protective factor. *Oxid Med Cell Longev.* 2015;2015.
25. Frank S, Gaume B, Bergmann-Leitner ES, Leitner WW, Robert EG, Catez F, et al. The Role of Dynamin-Related Protein 1, a Mediator of Mitochondrial Fission, in Apoptosis. *Dev Cell.* 2001;1(4):515–25.
26. Wang X, Chen Z, Fan X, Li W, Qu J, Dong C, et al. Inhibition of DNMI1 and mitochondrial fission attenuates inflammatory response in fibroblast-like synoviocytes of rheumatoid arthritis. *J Cell Mol Med.* 2020;24(2):1516–28.
27. Barrientos A, Moraes CT. Titrating the effects of mitochondrial complex I impairment in the cell physiology. *Journal of Biological Chemistry.* 1999;274(23):16188–97.
28. Viering D, Schlingmann KP, Hureaux M, Nijenhuis T, Mallett A, Chan MMY, et al. Gitelman-Like Syndrome Caused by Pathogenic Variants in mtDNA. *Journal of the American Society of Nephrology.* 2022;33(2):305–25.
29. Friederich MW, Geddes GC, Wortmann SB, Punnoose A, Wartchow E, Knight KM, et al. Pathogenic variants in MRPL44 cause infantile cardiomyopathy due to a mitochondrial translation defect. *Mol Genet Metab.* 2021;133(4):362–71.
30. Pecina P, Čapková M, Chowdhury SKR, Drahota Z, Dubot A, Vojtišková A, et al. Functional alteration of cytochrome c oxidase by SURF1 mutations in Leigh syndrome. *Biochim Biophys Acta Mol Basis Dis.* 2003;1639(1):53–63.
31. Koopman WJH, Verkaart S, Visch HJ, Van Emst-De Vries S, Nijtmans LGJ, Smeitink JAM, et al. Human NADH:ubiquinone oxidoreductase deficiency: Radical changes in mitochondrial morphology? *Am J Physiol Cell Physiol.* 2007;293(1).
32. Koopman WJH, Visch HJ, Verkaart S, Van Den Heuvel LWPJ, Smeitink JAM, Willems PHGM. Mitochondrial network complexity and pathological decrease in complex I activity are tightly correlated in isolated human complex I deficiency. *Am J Physiol Cell Physiol.* 2005;289(4 58-4).
33. Leman G, Gueguen N, Desquirit-Dumas V, Kane MS, Wettervald C, Chupin S, et al. Assembly defects induce oxidative stress in inherited mitochondrial complex I deficiency. *International Journal of Biochemistry and Cell Biology.* 2015;65:91–103.
34. Lazarou M, McKenzie M, Ohtake A, Thorburn DR, Ryan MT. Analysis of the Assembly Profiles for Mitochondrial- and Nuclear-DNA-Encoded Subunits into Complex I. *Mol Cell Biol.* 2007;27(12):4228–37.
35. Van Rahden VA, Fernandez-Vizarra E, Alawi M, Brand K, Fellmann F, Horn D, et al. Mutations in NDUFB11, encoding a complex I component of the mitochondrial respiratory chain, cause microphthalmia with linear skin defects syndrome. *Am J Hum Genet.*

2015;96(4):640–50.

36. Torraco A, Bianchi M, Verrigni D, Gelmetti V, Riley L, Niceta M, et al. A novel mutation in NDUFB11 unveils a new clinical phenotype associated with lactic acidosis and sideroblastic anemia. *Clin Genet*. 2017;91(3):441–7.

37. McKenzie M, Ryan MT. Assembly factors of human mitochondrial complex I and their defects in disease. *IUBMB Life*. 2010;62(7):497–502.

38. Guerrero-Castillo S, Baertling F, Kownatzki D, Wessels HJ, Arnold S, Brandt U, et al. The Assembly Pathway of Mitochondrial Respiratory Chain Complex I. *Cell Metab*. 2017;25(1):128–39.

39. Bruhn H, Samuelsson K, Schober FA, Engvall M, Lesko N, Wibom R, et al. Novel Mutation m.10372A>G in MT-ND3 Causing Sensorimotor Axonal Polyneuropathy. *Neurol Genet*. 2021;7(2).

40. Alston CL, Heidler J, Dibley MG, Kremer LS, Taylor LS, Fratter C, et al. Bi-allelic Mutations in NDUF6 Establish Its Role in Early-Onset Isolated Mitochondrial Complex I Deficiency. *Am J Hum Genet*. 2018;103(4):592–601.

41. Fuhrmann DC, Wittig I, Dröse S, Schmid T, Dehne N, Brüne B. Degradation of the mitochondrial complex I assembly factor TMEM126B under chronic hypoxia. *Cellular and Molecular Life Sciences*. 2018;75(16):3051–67.

42. Iannetti EF, Smeitink JAM, Beyrath J, Willems PHGM, Koopman WJH. Multiplexed high-content analysis of mitochondrial morphofunction using live-cell microscopy. *Biochimica et Biophysica Acta (BBA) - Bioenergetics*. 2016;1857:e124.

43. Bennett NK, Lee M, Orr AL, Ken N. Systems-level analyses dissociate genetic regulators of reactive oxygen species and energy production. *bioRxiv*. 2023;

44. Iannetti EF, Prigione A, Smeitink JAM, Koopman WJH, Beyrath J, Renkema H. Live-imaging readouts and cell models for phenotypic profiling of mitochondrial function. *Front Genet*. 2019;10(MAR).

45. Leipnitz G, Mohsen AW, Karunanidhi A, Seminotti B, Roginskaya VY, Markantone DM, et al. Evaluation of mitochondrial bioenergetics, dynamics, endoplasmic reticulum-mitochondria crosstalk, and reactive oxygen species in fibroblasts from patients with complex I deficiency. *Sci Rep [Internet]*. 2018;8(1):1165. Available from: <https://pubmed.ncbi.nlm.nih.gov/29348607/>

46. Zuba-Surma EK, Kucia M, Abdel-Latif A, Lillard JW, Ratajczak MZ. The ImageStream system: A key step to a new era in imaging. *Folia Histochem Cytobiol*. 2007;45(4):279–90.

47. Koopman WJH, Verkaart S, Visch HJ, Van Emst-De Vries S, Nijtmans LGJ, Smeitink JAM, et al. Human NADH:ubiquinone oxidoreductase deficiency: Radical changes in mitochondrial morphology? *Am J Physiol Cell Physiol*. 2007;293(1).

48. Verkaart S, Koopman WJH, van Emst-de Vries SE, Nijtmans LGJ, van den Heuvel LWPJ, Smeitink JAM, et al. Superoxide production is inversely related to complex I activity in inherited complex I deficiency. *Biochim Biophys Acta Mol Basis Dis*. 2007;1772(3):373–81.

49. Yenkin AL, Bramley JC, Kremitzki CL, Waligorski JE, Liebeskind MJ, Xu XE, et al. Pooled image-base screening of mitochondria with microrraft isolation distinguishes pathogenic mitofusins 2 mutations. *Commun Biol.* 2022;5(1).
50. Bugiardini E, Bottani E, Marchet S, Poole O V., Beninca C, Horga A, et al. Expanding the molecular and phenotypic spectrum of truncating MT-ATP6 mutations. *Neurol Genet.* 2020;6(1).
51. Blanchet L, Smeitink JAM, Van Emst - De Vries SE, Vogels C, Pellegrini M, Jonckheere AI, et al. Quantifying small molecule phenotypic effects using mitochondrial morpho-functional fingerprinting and machine learning. *Sci Rep.* 2015;5:1–7
52. Guillery O, Malka F, Frachon P, Milea D, Rojo M, Lombès A. Modulation of mitochondrial morphology by bioenergetics defects in primary human fibroblasts. *Neur - muscular Disorders.* 2008;18(4):319–30.
53. Nicholls DG, Lindberg O. Inhibited respiration and ATPase activity of rat liver mitochondria under conditions of matrix condensation. *FEBS Lett.* 1972;25(1):61–4.
54. Chinopoulos C. Mitochondrial consumption of cytosolic ATP: Not so fast. *FEBS Lett.* 2011;585(9):1255–9.
55. Valsecchi F, Monge C, Forkink M, De Groof AJC, Benard G, Rossignol R, et al. Metabolic consequences of NDUFS4 gene deletion in immortalized mouse embryonic fibroblasts. *Biochim Biophys Acta Bioenerg.* 2012;1817(10):1925–36.
56. Ebihara T, Nagatomo T, Sugiyama Y, Tsuruoka T, Osone Y, Shimura M, et al. Neonatal-onset mitochondrial disease: clinical features, molecular diagnosis and prognosis. *Arch Dis Child Fetal Neonatal Ed.* 2022;107(3):F329–34.
57. Ogawa E, Shimura M, Fushimi T, Tajika M, Ichimoto K, Matsunaga A, et al. Clinical validity of biochemical and molecular analysis in diagnosing Leigh syndrome: a study of 106 Japanese patients. *J Inherit Metab Dis.* 2017;40(5):685–93.
58. Celotto AM, Chiu WK, van Voorhies W, Palladino MJ. Modes of metabolic compensation during mitochondrial disease using the drosophila model of ATP6 dysfunction. *PLoS One.* 2011;6(10).
59. Chung HK, Ryu D, Kim KS, Chang JY, Kim YK, Yi HS, et al. Growth differentiation factor 15 is a myomitokine governing systemic energy homeostasis. *Journal of Cell Biology.* 2017;216(1):149–65.
60. Sturm G, Karan KR, Monzel AS, Santhanam B, Taivassalo T, Bris C, et al. OxPhos defects cause hypermetabolism and reduce lifespan in cells and in patients with mitochondrial diseases. *Commun Biol.* 2023;6(1).
61. Ganetzky RD, Markhard AL, Yee I, Clever S, Cahill A, Shah H, et al. Congenital Hypermetabolism and Uncoupled Oxidative Phosphorylation. *New England Journal of Medicine.* 2022;387(15):1395–403.

## **Supplementary Files**

### **Overview**

*Table S1:* Overview of IFC results, clinical data and biochemical data for all healthy control and patient fibroblast lines.

*Figure S1:* Effect of passage number and cellular density on IFC features.

*Figure S2:* Correlation of IFC features with other diagnostic approaches

*Figure S3:* Gating strategy

## Chapter 6

Gene	Category	Mitochondrial Swelling	Membrane Potential	Mitochondrial Mass	Form Factor	ROS
Healthy Control		90	111	117	87	113
Healthy Control		115	88	116	103	104
Healthy Control		90	77	72	99	82
Healthy Control		115	92	103	92	101
Healthy Control		104	106	74	118	73
Healthy Control		99	99	73	104	123
<i>NDUFS7</i>	Complex I	97	72	111	93	91
<i>NDUFS4</i>	Complex I	93	86	87	92	106
<i>NDUFB11</i>	Complex I	99	59	104	108	152
<i>ACAD9</i>	Complex I	96	103	86	83	109
<i>ACAD9</i>	Complex I	93	70	67	91	107
<i>MT-ND3</i>	Complex I	121	128	156	118	114
<i>TIMMDC1</i>	Complex I	116	106	143	81	80
<i>TIMMDC1</i>	Complex I	121	119	119	89	59
<i>SDHA</i>	Complex II	96	59	118	85	72
<i>SDHA</i>	Complex II	91	85	63	90	106
<i>COX20</i>	Complex IV	113	160	84	81	77
<i>COX20</i>	Complex IV	114	135	114	102	67
<i>SURF1</i>	Complex IV	122	119	113	107	46
<i>SCO2</i>	Complex IV	122	140	124	126	161
<i>MT-ATP6</i>	Complex V	86	61	119	83	103
<i>MT-ATP6</i>	Complex V	95	72	77	101	84
<i>MT-ATP6</i>	Complex V	102	129	156	99	102
<i>SERAC1</i>	Mitochondrial Translation	99	126	164	105	113
<i>MT-TI</i>	Mitochondrial Translation	108	87	91	106	15
<i>MT-TL1</i>	Mitochondrial Translation	102	104	102	80	107
<i>GFM-1</i>	Mitochondrial Translation	92	65	67	95	88
<i>MRPL44</i>	Mitochondrial Translation	108	152	126	116	93
<i>TWINK</i>	mtDNA maintenance	92	72	108	91	225
<i>POLG</i>	mtDNA maintenance	85	92	66	87	117
<i>POLG</i>	mtDNA maintenance	86	90	86	84	117
<i>POLG</i>	mtDNA maintenance	111	89	122	98	139
<i>DRP1</i>	Mitochondrial Fission	100	91	72	91	NA
<i>DRP1</i>	Mitochondrial Fission	75	79	76	78	NA
<i>DRP1</i>	Mitochondrial Fission	97	60	62	103	NA
<i>TAZ</i>	Cardiolipin Remodeling	85	87	70	73	65
<i>TAZ</i>	Cardiolipin Remodeling	95	82	67	103	68

## Imaging Flow Cytometry for Mitochondrial Diseases

Gene	Seahorse XF	OXPHOS Activity Measurements	Age of onset (Months)	Neuropathy	Hypertrophic Cardiomyopathy	Epilepsy
Healthy Control						
Healthy Control						
Healthy Control						
Healthy Control						
Healthy Control						
Healthy Control						
<i>NDUFS7</i>		Isolated complex 1 deficiency in fibroblast	42	0	0	0
<i>NDUFS4</i>		Isolated complex 1 deficiency in muscle	2	0	0	0
<i>NDUFB11</i>		NA	1	0	1	0
<i>ACAD9</i>		Isolated complex I deficiency in fibroblasts		0	0	0
<i>ACAD9</i>	Normal	Unaffected complex activity in fibroblasts	60	0	0	0
<i>MT-ND3</i>		Isolated complex I deficiency in fibroblasts	552	1	0	0
<i>TIMMDC1</i>		NA	1	1	0	0
<i>TIMMDC1</i>		Isolated complex 1 deficiency in muscle	1	1	0	0
<i>SDHA</i>		Isolated complex II deficiency in fibroblasts	1	0	0	1
<i>SDHA</i>		NA	6	0	1	0
<i>COX20</i>		Isolated complex IV deficiency in fibroblasts	13	0	0	0
<i>COX20</i>		NA	24	0	0	0
<i>SURF1</i>		NA	72	0	0	0
<i>SCO2</i>		NA	3	1	0	0
<i>MT-ATP6</i>	Normal	Normal	14	0	0	0
<i>MT-ATP6</i>	Normal	Normal	108	0	0	0
<i>MT-ATP6</i>	Normal	Normal	24	1	0	0
<i>SERAC1</i>		NA	1	0	0	0
<i>MT-TI</i>		Isolated complex IV deficiency		0	0	0
<i>MT-TL1</i>	Normal	Complex I and IV deficiency in muscle, unaffected complex activity in fibroblasts	72	0	1	1
<i>GFM-1</i>		Complex I/IV deficiency in fibroblasts, unaffected complex I and IV activity in muscle	1	0	0	1
<i>MRPL44</i>		NA	14	0	1	0
<i>TWNK</i>	Normal	Unaffected complex activity in fibroblasts and muscle	6	1	0	0
<i>POLG</i>		NA	14	0	0	1
<i>POLG</i>		NA	144	0	0	1
<i>POLG</i>		NA	36	0	0	1
<i>DRP1</i>		NA				
<i>DRP1</i>		Unaffected complex activity in fibroblasts and muscle	1	0	0	0
<i>DRP1</i>		NA				
<i>TAZ</i>		NA				
<i>TAZ</i>	Normal	Unaffected complex activity in fibroblasts	108	0	1	0

## Chapter 6

Gene	Liver Failure	Kidney Disease	Intestinal Motility Issues	Vision Loss	Developmental Delay	Ataxia	Respiratory failure	Hypotonia
Healthy Control								
Healthy Control								
Healthy Control								
Healthy Control								
Healthy Control								
Healthy Control								
<i>NDUFS7</i>	0	0	0	1	0	1	1	0
<i>NDUFS4</i>	0	0	0	0	0	0	1	0
<i>NDUFB11</i>	0	0	0	0	0	0	0	0
<i>ACAD9</i>	0	0	0	0	1	1	0	0
<i>ACAD9</i>	0	0	0	0	0	0	0	0
<i>MT-ND3</i>	0	0	0	0	0	0	0	0
<i>TIMMDC1</i>	0	0	0	0	0	0	1	0
<i>TIMMDC1</i>	0	0	0	0	0	0	1	0
<i>SDHA</i>	0	0	0	0	1	0	1	1
<i>SDHA</i>	0	0	0	1	1	0	0	1
<i>COX20</i>	0	0	1	0	0	1	0	1
<i>COX20</i>	0	0	0	0	1	1	0	0
<i>SURF1</i>	0	0	0	0	1	0	0	1
<i>SCO2</i>	0	0	0	0	1	1	1	1
<i>MT-ATP6</i>	0	0	0	0	1	0	0	1
<i>MT-ATP6</i>	0	0	0	1	1	0	0	0
<i>MT-ATP6</i>	0	0	0	0	1	1	0	0
<i>SERAC1</i>	0	0	0	0	1	1	0	1
<i>MT-TI</i>	0	1	0	0	0	0	0	0
<i>MT-TL1</i>	0	0	1	0	0	0	0	0
<i>GFM-1</i>	0	0	0	0	1	0	1	1
<i>MRPL44</i>	1	0	0	0	0	0	1	0
<i>TWINK</i>	0	0	0	0	1	1	0	1
<i>POLG</i>	1	0	1	0	1	0	0	0
<i>POLG</i>	0	0	1	0	1	0	0	0
<i>POLG</i>	1	0	0	0	1	1	1	1
<i>DRP1</i>								
<i>DRP1</i>					1		0	1
<i>DRP1</i>								
<i>TAZ</i>								
<i>TAZ</i>	0	0	0	0	1	0	0	0

## Imaging Flow Cytometry for Mitochondrial Diseases

Gene	CI activity in muscle (%)	CII activity in muscle (%)	CIII activity in muscle (%)	CIV activity in muscle (%)	CV activity in muscle (%)	ATP in Muscle (%)	CI activity in fibroblast (%)	CII activity in fibroblast (%)
Healthy Control								
Healthy Control								
Healthy Control								
Healthy Control								
Healthy Control								
Healthy Control								
<i>NDUFS7</i>							93.91%	249.07%
<i>NDUFS4</i>	12.77%	150.00%	108.48%	102.98%		10.39%		
<i>NDUFB11</i>								
<i>ACAD9</i>								
<i>ACAD9</i>							215.77%	379.20%
<i>MT-ND3</i>							87.46%	204.53%
<i>TIMMDC1</i>								
<i>TIMMDC1</i>	50.88%	188.00%	143.00%	123.00%		32.00%		
<i>SDHA</i>								
<i>SDHA</i>								
<i>COX20</i>							203.51%	134.33%
<i>COX20</i>								
<i>SURF1</i>								
<i>SCO2</i>	276.60%	100.00%	89.37%	26.60%	104.76%	20.00%	244.21%	138.81%
<i>MT-ATP6</i>							366.00%	334.00%
<i>MT-ATP6</i>							265.95%	211.73%
<i>MT-ATP6</i>								
<i>SERAC1</i>								
<i>MT-TI</i>								
<i>MT-TL1</i>	12.00%	140.00%	62.77%	47.65%	228.75%	18.84%	182.00%	234.00%
<i>GFM-1</i>	112.86%	144.78%	97.77%	136.17%		30.95%	34.00%	114.42%
<i>MRPL44</i>								
<i>TWNK</i>								
<i>POLG</i>								
<i>POLG</i>								
<i>POLG</i>								
<i>DRP1</i>								
<i>DRP1</i>	250%	280%	280%	121%				
<i>DRP1</i>								
<i>TAZ</i>								
<i>TAZ</i>							196.77%	442.13%



**Table S1: Additional Details**

Overview of IFC results, clinical data and biochemical data for all healthy control and patient fibroblast lines. Blank columns indicate that values were not assessed (NA).

The column 'Seahorse' describes the results of Mitochondrial Stress Test experiments using Agilent Seahorse equipment. All measurements were performed in a diagnostic setting at the Radboud MC, Nijmegen. Each patient was compared to at least three healthy controls. 'Normal' indicates that no significant reduction in basal- or maximal respiratory capacity was observed for patients compared to healthy controls.

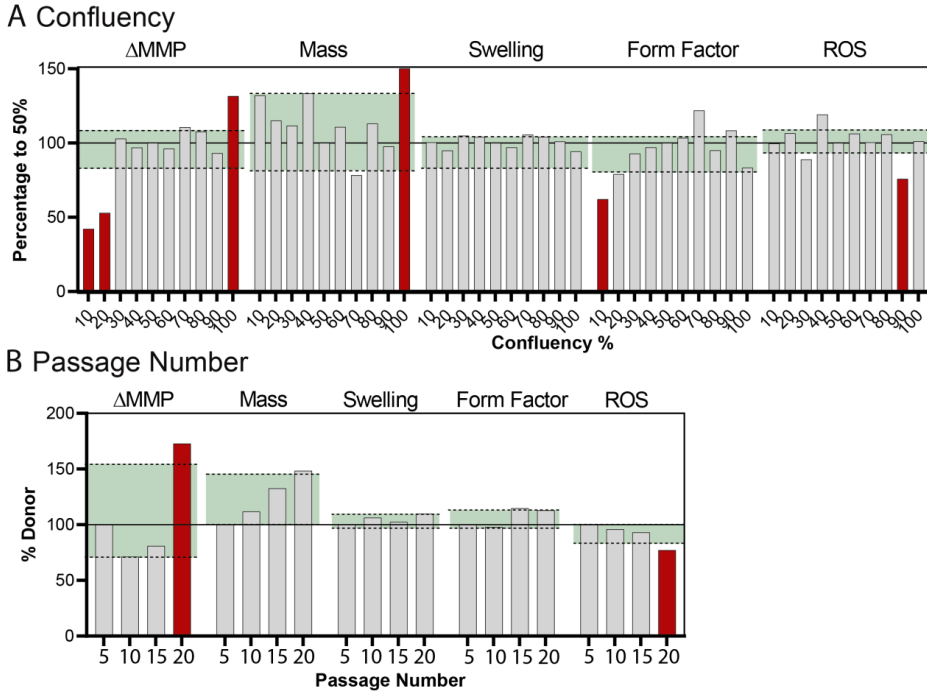
The 'Oxphos Activity Measurement Column' summarizes the results of the OXPHOS activity measurements, also performed in a diagnostic setting at the Radboud MC, Nijmegen.

The results of these measurements are shown in the columns Y t/m AI. Absolute values were normalized to the lower reference range of healthy controls and depicted as percentage.

The column 'Age of Onset' refers to the age where first symptoms were seen (shown in months).

The columns K-V indicate the presence (1) or absence (0) of specific clinical features.

**Supplementary Figure 1: Effect of passage number and cellular density on IFC features.**

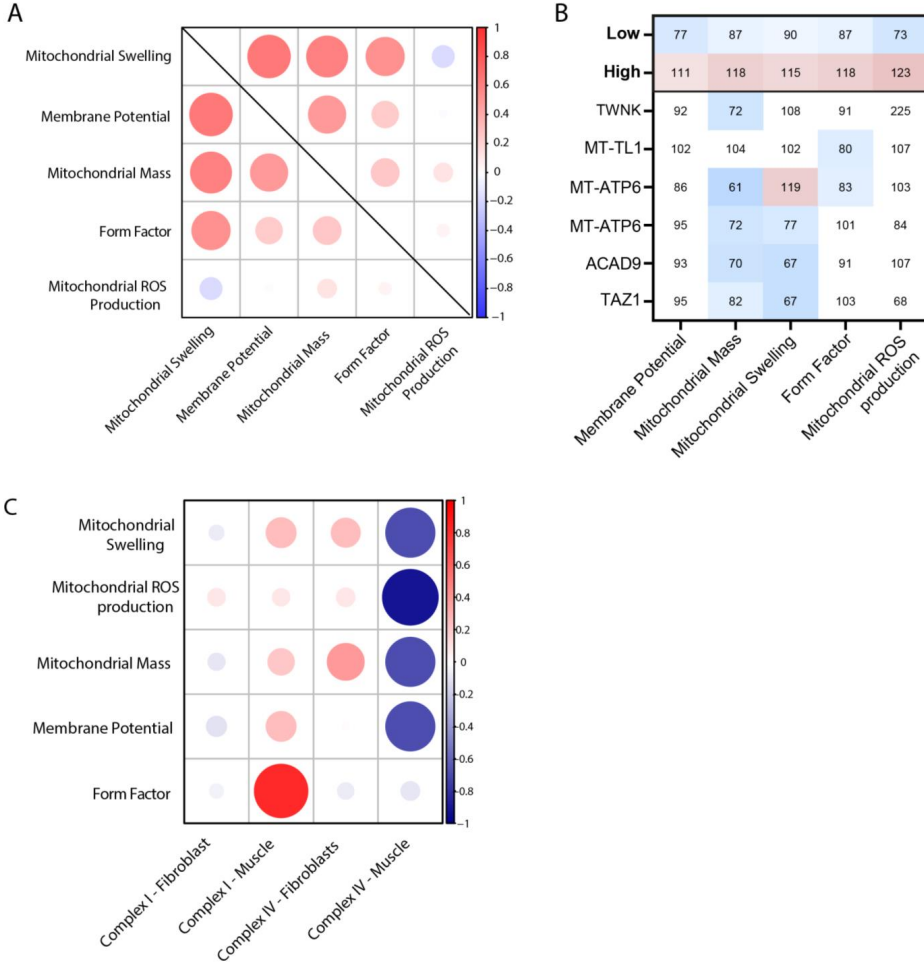


**Supplementary Figure 1:**

(A) Bar chart showing the effect of fibroblast confluency right before harvesting on assay results. Each value was normalized to the feature value observed at 50% confluency taken along in the same run and converted to percentages. The green planes indicate the IQR25-IQR75 range. The red colored bars indicate that the values fall outside (>5%) the IQR25-IQR75 range.

(B) Bar chart showing the effect of fibroblast passage number on assay results. Each value was normalized to passage number 5, taken along in the same run and converted to percentages. The green planes indicate the IQR25-IQR75 range. The red colored bars indicate that the values fall outside (>5%) the IQR25-IQR75 range.

**Supplementary Figure 2: Comparison of IFC assays with other diagnostic tools**



**Supplementary Figure 2:**

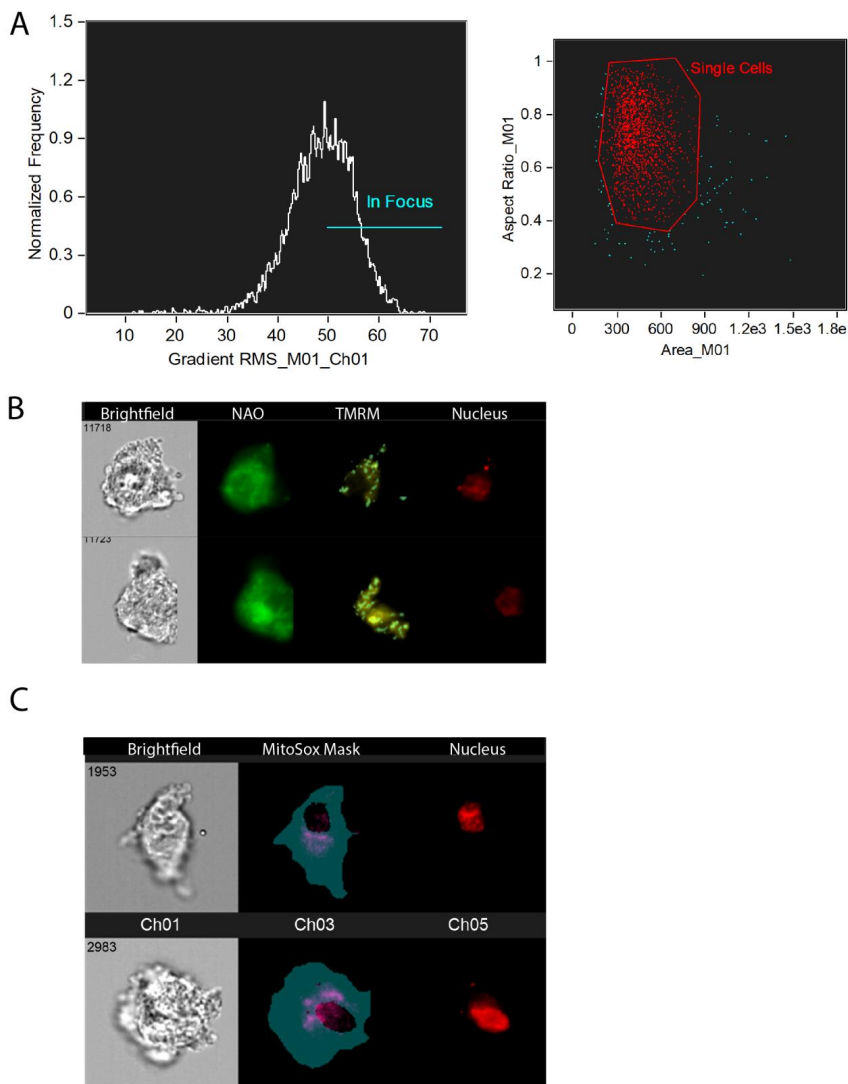
(A) Correlation plot showing correlation between IFC assays. Correlation was calculated using Spearman statistics. None of the rho correlation statistics was  $>0.7$ . However, correlation between mitochondrial swelling and membrane potential was high, with rho 0.64 and  $p=0.0001$ .

(B) Heat map showing assay results in mitochondrial disease patients where

seahorse respirometry was performed. All patients had normal basal, spare- and maximal respiratory capacity (N=6). All values are shown as percentage normalized against the healthy control taken along in the same run. The top two rows indicate the lowest- and highest reference values found in six healthy controls. The color coding refers to the severity of the aberrancies. White boxes indicate that the value falls within the range (lowest-highest value) of healthy controls. Colored boxes indicate that the value falls outside the range observed in healthy controls.

(C) Correlation plot showing the correlation between IFC features and OXP-HOS complex activities measured in fibroblast or muscle. All patients where OXP-HOS complex activity was measured were included for analysis (N=6 for muscle, N=13 for fibroblasts). Correlation was calculated using Spearman. None of the correlations was statistically significant.

**Supplementary Figure 3: Gating Strategy**



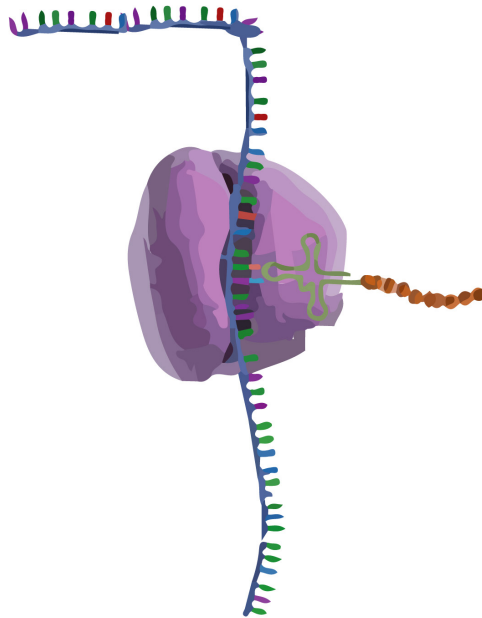
**Supplementary Figure 3: Gating strategy for IFC assays.**

(A) Primary gating applied on all samples. Cells out of focus and doublets were removed.  
 (B) Showing TMRM mask used to calculate the form factor. The Spot mask was used to remove the background of the TMRM staining. The threshold

was set to 10, the minimum size to 0 pixels and maximum size to 2 pixels. (C) Showing the mask used to quantify mitochondrial ROS production. A mask excluding the nuclear pixels was created by combining the morphology mask of the brightfield image and excluding the morphology mask of the nuclear staining.



# Chapter



**Tailored amino acid treatment for mitochondrial Aminoacyl-tRNA synthetase deficiencies.**



## **Tailored amino acid treatment for mitochondrial Aminoacyl-tRNA synthetase deficiencies.**

Irena J.J. Muffels,<sup>1,11</sup> Gautam Kok,<sup>1,11</sup> Ziqin Tang,<sup>2,3</sup> Leonardo Simão Medeiros,<sup>4</sup> Fabiano Oliveira Poswar,<sup>4</sup> Wilbert P. Vermeij,<sup>2,3</sup> Richard Rodenburg,<sup>5</sup> Kimberley Smit<sup>2,3</sup> Suresh K. Sukumaran,<sup>6</sup> Anne M.K. Kwok,<sup>7</sup> Edward E.S. Nieuwenhuis,<sup>8</sup> Peter M. van Hasselt,<sup>1</sup> Ida V.D. Schwartz,<sup>4</sup> Charlotte M.A. Lubout,<sup>9</sup> Annet M. Bosch,<sup>10</sup> Klaas Koop,<sup>1</sup> Eva M.M. Hoytema van Konijnenburg,<sup>1</sup> Sabine A. Fuchs,<sup>1,11</sup>

<sup>1</sup> Department of Metabolic Diseases, division Pediatrics, Wilhelmina Children's Hospital University Medical Centre Utrecht, Utrecht University, Utrecht, The Netherlands.

<sup>2</sup> Princess Máxima Center for Pediatric Oncology, Utrecht, The Netherlands.

<sup>3</sup> Oncode Institute, Utrecht, The Netherlands.

<sup>4</sup> Postgraduate Program in Genetics and Molecular Biology, Federal University of Rio Grande do Sul, Porto Alegre, Brazil.

<sup>5</sup> Department of Clinical Genetics, Radboud UMC, Nijmegen, The Netherlands.

<sup>6</sup> Department of Cardiology, Jawaharlal Institute of Postgraduate Medical Education and Research, Puducherry, India.

<sup>7</sup> Department of Pediatrics, The Hong Kong Children's Hospital, Hong Kong SAR, China.

<sup>8</sup> Department of Biomedical and Life Sciences, University College Roosevelt, Middelburg, The Netherlands.

<sup>9</sup> Department of Metabolic Diseases, Beatrix Children's Hospital, University of Groningen, University Medical Center Groningen, Groningen, The Netherlands

<sup>10</sup> Department of Pediatrics, Division of Metabolic Diseases, Amsterdam Gastroenterology Endocrinology and Metabolism, Emma Children's Hospital, Amsterdam UMC-AMC, Amsterdam, the Netherlands

<sup>11</sup> On behalf of United for Metabolic Diseases, Nijmegen, The Netherlands

**Manuscript in preparation**

## Abstract

*Background:* Aminoacyl-tRNA synthetases (ARS) facilitate loading of transfer RNAs with cognate amino acids in the cytosol (ARS1), mitochondria (ARS2) or both (dual ARS). ARS deficiencies cause severe disease affecting different organs, depending on the type and location of the dysfunctional ARS. Supplementation with cognate amino acids is effective to treat ARS1 deficiencies, but this remains to be established for ARS2 deficiencies.

*Methods:* First, the effects of amino acid depletion and supplementation were tested in fibroblasts from seven patients with ARS2 deficiencies to mimic treatment response. Second, we treated nine patients with AARS2, SARS2, EARS2, WARS2 and VARS2 deficiencies with amino acids for a period ranging from 6 months to 3 years.

*Results:* Fibroblasts of dual ARS and ARS2 – but not ARS1 – deficient patients show decreased mitochondrial membrane potential, and reduced basal- and maximal respiratory capacity during amino acid depletion. Clinical observations in nine patients revealed that amino acid supplementation was well-tolerated in all patients. Five patients showed beneficial effects of treatment in terms of more energy, accelerated development, decreased lactate values and improved cardiac function. In one patient, treatment discontinuation coincided with severe neurological regression.

*Conclusion:* We found that mitochondrial function depends on the availability of cognate amino acids in fibroblasts of ARS2 and dual ARS deficiencies. Our clinical observations show that amino acids are well-tolerated and can be beneficial for patients with ARS2 deficiencies. This study is the first example of a treatment for different mitochondrial ARS2 deficiencies beyond supportive care. Furthermore, the specific response of ARS2 deficiencies to amino acid depletion represents a novel diagnostic read-out for a group of diseases devoid of effective diagnostic assays.

## Introduction

Aminoacyl-tRNA synthetases (ARS) are essential for translating messenger RNA to proteins by coupling amino acids to their cognate transfer RNAs (tRNAs) in the cytosol (ARS1), mitochondria (ARS2) or both (Glycyl-RS, GARS1 or Lysyl-RS, KARS1). The clinical phenotype of patients with ARS deficiencies differs per ARS and its location.<sup>1-4</sup> In ARS1-deficient patients, it is generally conceptualized that aminoacylation often suffices in homeostatic conditions, but falls short during increased translational demands (rapid growth, illness) or decreased amino acid availability (starvation, vomiting).<sup>5</sup> In fibroblasts of ARS1 deficient patients, we found that low cognate amino acid concentrations were detrimental for cellular growth.<sup>5</sup> To prevent amino acid deficiencies, we decided to supplement ARS1-deficient patients with cognate amino acids<sup>5</sup>, resulting in significant clinical improvements in growth, head circumference, development, gastrointestinal and pulmonary symptoms.<sup>5-7</sup>

The beneficial effects of amino acid supplementation in ARS1 deficiencies prompted us to explore the effects in dual ARS- and ARS2 deficiencies. Although starvation and illness similarly are triggers for clinical deterioration for mitochondrial ARS-deficiencies, it is not obvious that amino acid deficiency would lead to similar pathophysiological defects, as the regulation of mitochondrial translation differs from the regulation of cytosolic translation.<sup>8</sup> Moreover, due to the versatile function of mitochondria, supplemented amino acids may be used for other pathways than mitochondrial translation, for example to fuel the TCA cycle. Recently, preliminary beneficial effects on clinical symptoms have been observed during amino acid treatment in a patient with pathogenic *FARS2* variants.<sup>9</sup> In four patients with RARS2 deficiency, brief administration of arginine led to improved EEG and higher energy levels, although seizure frequency did not change.<sup>10</sup>

Here, we tested the effects of amino acid supplementation and depletion in fibroblasts derived from seven patients with various ARS2 deficiencies. Primarily, we studied mitochondrial function and growth rates in fibroblasts

derived from patients with ARS2, ARS1 and dual ARS deficiencies. Building on the beneficial effects found on mitochondrial function in patient-derived fibroblasts, we supplemented nine ARS2 deficient patients with cognate amino acids for a period ranging from 6 months to 3 years, and report on the effects that were observed.

## Methods

### *Patient inclusion*

All patients from The Wilhelmina Children's hospital (WKZ) with bi-allelic genetic variants in mitochondrial ARS genes were recruited for this study. Additionally all patients seeking second opinion at the WKZ were asked to participate, P1<sup>EARS2</sup> and P2<sup>EARS2</sup> were recruited from Brazil, P1<sup>WARS2</sup> was recruited from the UMC Groningen, P3<sup>VAR2</sup> and P4<sup>VAR2</sup> were recruited from China, and P1<sup>SARS2</sup> from India. Genetic variants were identified using Whole Exome Sequencing.<sup>11</sup> Patients signed informed consent for the use of their medical data and storage and expansion of their cells in the Wilhelmina Children's Hospital metabolic biobank (TCBio 19-489/B, <https://tcbio.umcutrecht.nl>). All procedures performed in studies involving human participants are in accordance with national and local institutional review boards (IRBs) of the participating centers.

### *Amino acid supplementation*

Oral amino acid supplementation protocols, including dosing strategy, safety assessment and outcome parameters are added as **File S2**.

### *Fibroblast cultures*

Fibroblasts were obtained from forearm skin biopsies and cultured in Ham's F-12 supplemented with 10% Fetal Bovine Serum (FBS) and 1% penicillin–streptomycin (PS). For amino acid sensitivity experiments, amino acid free DMEM/F-12 with HEPES and NaHCO<sub>3</sub> (US Biological) was supplemented with 1% PS, 1% GlutaMAX (Gibco), 10% dialyzed FBS (ThermoFisher) and amino acids. For amino acid sensitivity tests, patient- and healthy donor derived fibroblasts were treated with the specific amino acid, with normal plasma concentrations defined as 100% (L-Valine 223 μmol/L, L-Alanine

350  $\mu\text{mol/L}$ , L-Glutamate 550  $\mu\text{mol/L}$ , L-Lysine 129  $\mu\text{mol/L}$ , L-Tryptophane 43  $\mu\text{mol/L}$ , L-leucine 114  $\mu\text{mol/L}$ , L-isoleucine 57  $\mu\text{mol/L}$ ) and in deprivation conditions as 1% of these concentrations.

### *Seahorse Mitochondrial Stress Test*

Dermal fibroblasts were plated at 10,000 cells/well in Seahorse XF24 V7 Cell Culture Microplates (Agilent) and treated with the desired amino acid concentrations for 48 hours. Afterwards, cells were incubated with Seahorse XF DMEM Medium (Agilent) for 1 hour in a non-CO<sub>2</sub> incubator. Mitochondrial respiration was measured as oxygen consumption rate (OCR) using the Seahorse XFe24 Extracellular Flux Assay Kit (Mito Stress Test, Agilent) and XFe24 Seahorse Analyzer (Agilent) with 1  $\mu\text{M}$  oligomycin, 1.5  $\mu\text{M}$  FCCP, 1  $\mu\text{M}$  Rotenone (All MedChemExpress) and 1  $\mu\text{M}$  antimycinA (Sigma-Aldrich) following manufacturer's protocol and with three or four technical replicates per condition.<sup>12</sup> After analysis, nuclei were stained with Hoechst 33342 (1:1000, Thermo Fisher Scientifics), visualized with Leica Thunder Live Imager (Leica Microsystem) with intensive computational clearance method, and counted using ImageJ v1.53o (NIH) for normalization.

### *Membrane potential measurements*

Fibroblasts were incubated with Tetramethylrhodamine, methyl ester (TMRM, Sigma Aldrich) in Hank Balanced Salt Solution (HBSS, Gibco) for 35 minutes. To assess TMRM background, Carbonyl cyanide-p-trifluoromethoxyphenylhydrazone (FCCP, Sigma Aldrich) was added during the final 5 minutes in 50% of the wells. Cells were harvested using TrypLE and visualized using the Amnis Imagestream Mk II (Luminex).

### *Cell proliferation*

Cell proliferation was measured using a real-time-cell-analyzer (xCELLigence MP) as described previously.<sup>5</sup>

### *Statistical analyses*

Imaging Flow Cytometry data analysis was performed using IDEAS soft-

ware (version 6.2, Amnis). Seahorse data were analyzed using Agilent Wave software (version 2.6, Agilent).

## Results

15 patients were eligible for inclusion in this study (**Figure 1**). For two patients (twins), pathogenicity of their genetic variants could not be established, and therefore they were not included in this study (**Supplemental Note 1 and 3**). Clinical data of three older siblings of treated ARS2 deficient patients were included to compare clinical disease course of treated versus non-treated patients that harbored similar genotypes. These three patients are not included in the clinical treatment cohort nor in our in-vitro studies (**Figure 1**). P1<sup>KARS</sup> was included post-mortem for in-vitro analysis (**Figure 1**).

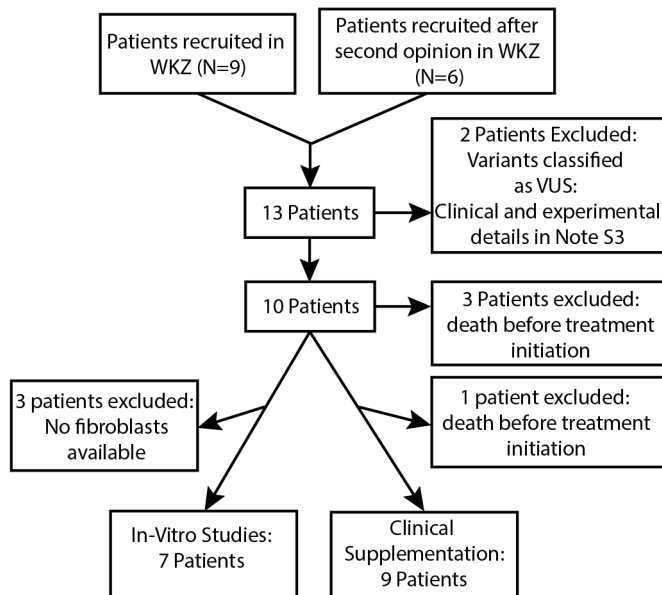


**Figure 1:** Flow Chart. Showing the inclusion process of ARS2 deficient patients for in-vitro and clinical studies.

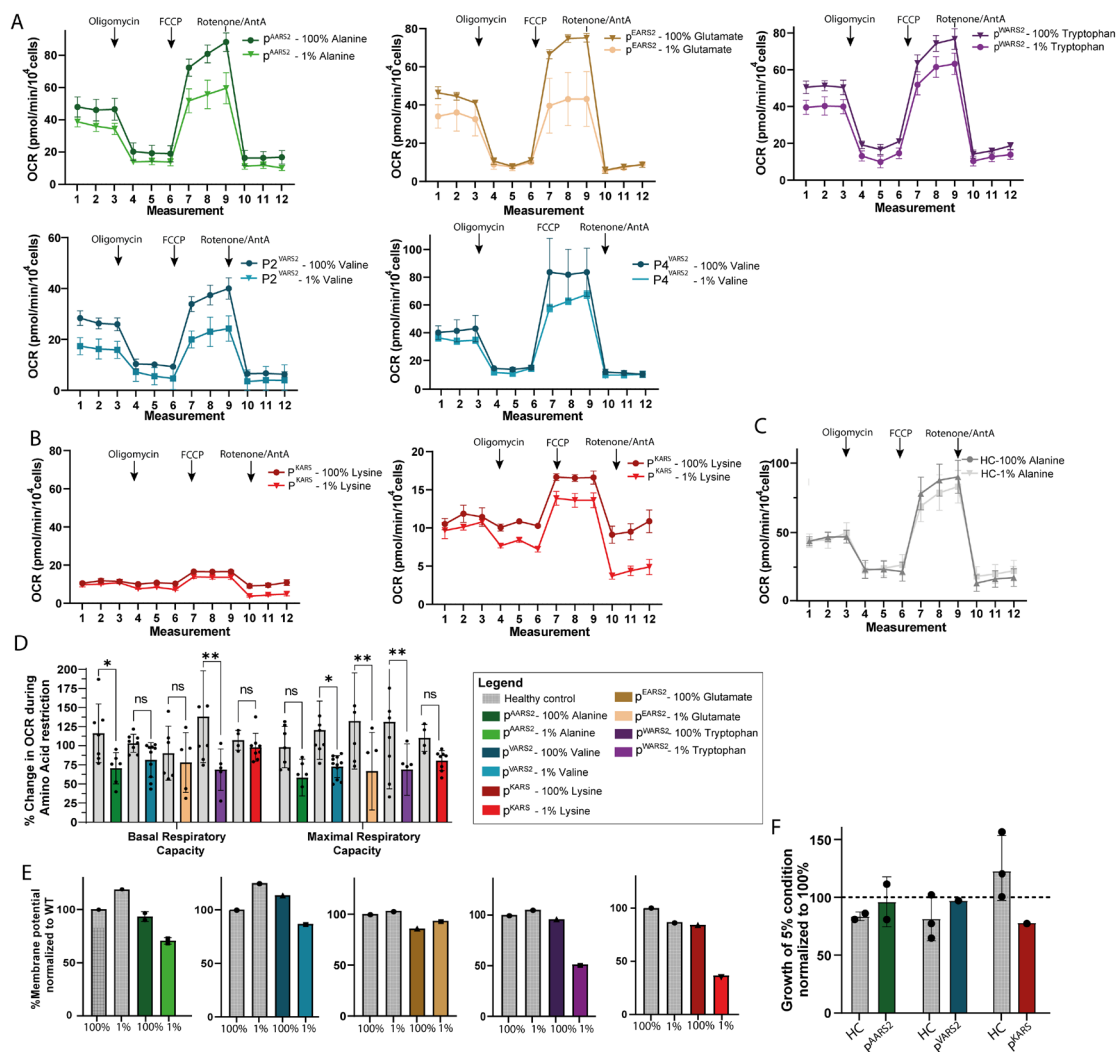


**Figure 2: ARS2- and dual ARS-deficient patients show mitochondrial dysfunction during amino acid deprivation.**

(A) Oxygen Consumption Rate (OCR; Y-axis) for each measurement (X-axis) with the injection of different compounds (Oligomycin, FCCP, Rotenone/AntimycinA, arrows) in VARS2- (2 patients, 3 and 4 replicates each), AARS2- (2 patients, 3 and 4 replicates), EARS2- (1 patient, 5 replicates), WARS2- (1 patient, 5 replicates) deficient fibroblast lines during treatment with normal blood plasma amino acid concentrations (indicated at 100%) and amino acid deprivation conditions (indicated as 1%). The dots represent the average of

all donors and technical replicates combined. Error bars represent SEM.

(B) Oxygen Consumption Rate (OCR; Y-axis) for each measurement (X-axis) with the injection of different compounds (Oligomycin, FCCP, Rotenone/AntimycinA, arrows) in 100% and 1% amino acid conditions for 2 days in a patient with KARS-deficiency (3 replicates). The dots represent the average of all donors and technical replicates combined. Error bars represent SEM. The graph on the left has an y-axis ranging from 0 to 80 pmol/min, similar as figure 2A. The graph on the right has an adjusted y-axis ranging from 0 to 20 pmol/min.

(C) OCR of one representative healthy control fibroblasts line treated with 100% alanine and 1% alanine for 2 days. The dots represent the average of three technical replicates. Error bars represent SEM.

(D) Bar graphs showing the average basal and maximal OCR of healthy controls, ARS2- and dual ARS-deficiency patients. The OCR values of the 1% condition are normalized to the 100% condition and depicted as a percentage. The bars represent the mean percentage of all donors and technical replicates combined  $\pm$ SD, the dots represent the percentage per technical replicates per donor. The bar represents the mean of all healthy donors and all conditions combined. Statistics were calculated using two-way repeated measures ANOVA.

(E) Mitochondrial membrane potential during 1% and 100% conditions. In the patients, the bars represent membrane potential normalized to healthy controls treated with the same condition  $\pm$ SD. In the healthy control, the 1% condition is normalized to the 100% condition of the same healthy control. All bars represent one healthy control or patient, using one technical replicate.

(F) Real-time-cell-analyzer results of ARS2- and dual-ARS deficiency patients. Relative impedance was taken as a measure for cellular proliferation after 96 hours of culture with 1% and 100% of cognate amino acids. Bars represent mean of biological replicates  $\pm$  standard deviation (SD). Dots represent mean values of all technical replicates of individual donors.



*Mitochondrial dysfunction upon amino acid deprivation in mitochondrial ARS deficiencies*

For our in-vitro studies, fibroblasts of seven ARS2 deficient patients were included: AARS2 (N=2), VARS2 (N=2), EARS2 (N=1), WARS2 (N=1) and KARS (N=1). All ARS2 deficient patient fibroblast lines showed reduced basal and maximal respiration during cognate amino acid deprivation, which was not observed in healthy controls nor in four patients with IARS1 and LARS1 deficiencies (**Figure 2A-D** and **Figure S1**). For P4<sup>VARS2</sup>, we observed only a small decrease in normalized maximum respiration, compared to the large decrease in non-normalized maximum respiration (**Figure S1**), which might be related to significant growth deficits in during amino acid deprivation specific to this patient.

Fibroblasts of all mitochondrial ARS-deficient patients showed decreased mitochondrial membrane potential during amino acid deprivation, except for P2<sup>EARS2</sup> (**Figure 2E**). Decreased membrane potential during amino acid deprivation was not observed in healthy controls nor ARS1 deficiencies.

*Impaired growth upon amino acid deprivation in dual ARS deficiencies but not in ARS2 deficiencies*

Cellular growth, which was the main cellular phenotypic read-out in patients with ARS1 deficiencies, was not significantly altered in patients with AARS2- or VARS2 deficiencies, but was significantly stunted in the patient with dual KARS-deficiency during amino acid deprivation. These results suggest that growth impairment is specific for cytosolic- and dual ARS-deficiencies (**Figure 2F**).

*Clinical observations of amino acid supplementation*

The mitochondrial dysfunction observed in fibroblasts of patients with ARS2 deficiencies during amino acid depletion, suggested that amino acid availability correlated with mitochondrial function. Therefore, we initiated cognate amino acid supplementation in nine patients (**Figure 1**). **Figure 3A** describes individual treatment regimens and duration for each patient. We aimed to treat patients with double daily dosages of WHO amino acid intake standards at first, which were increased to three times if well-tolerated.

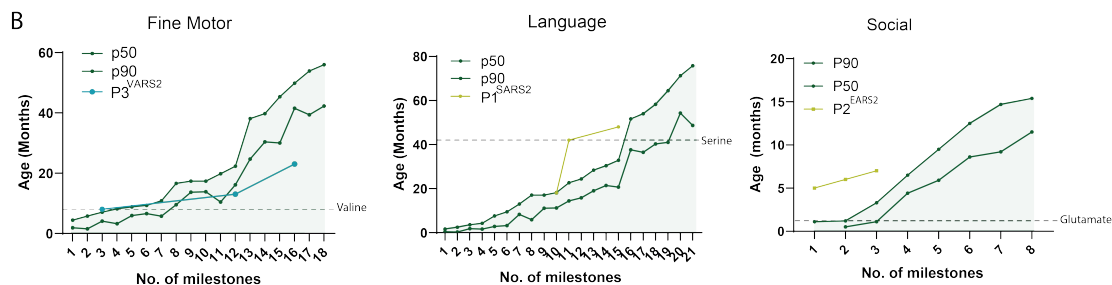
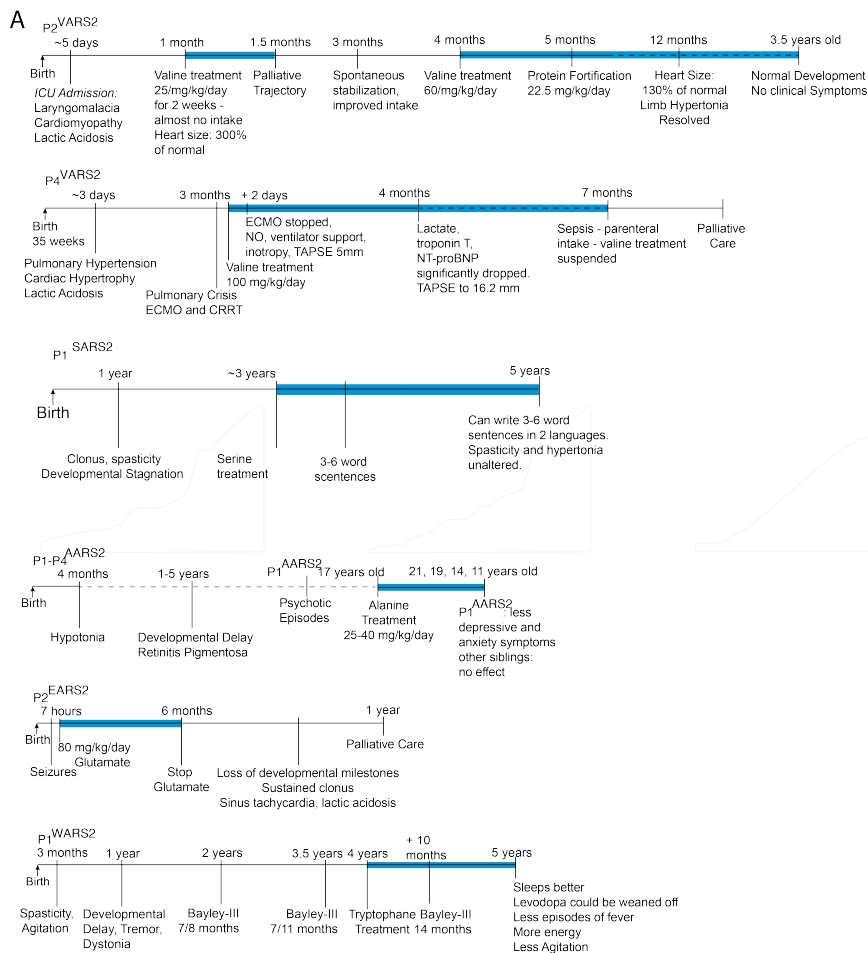
## Amino Acid Treatment for ARS2 deficiencies

**Table 1: Clinical characteristics of ARS deficient patients**

Patient ID	P1 <sup>VAR</sup> S2 and P2 <sup>VAR</sup> S2	P3 <sup>VAR</sup> S2 and P4 <sup>VAR</sup> S2	P1 <sup>SAR</sup> S2	P1, P2, P3, P4 <sup>AAR</sup> S2	P1 <sup>EARS</sup> 2 and P2 <sup>EARS</sup> 2	P1 <sup>WAR</sup> S2
Genetic variant	NM_001167734 c.1258G>A; c.1973G>A; p.Ala420Thr; p.Arg658His;	NM_001167734 c.1940C>T;c.763A>G p.Thr647Met; Lys255Glu	NM_017827 c.1347G>A; c.1347G>A	NM_020745 c.749+235_1150-88delins59; c.2255+8A>C p.?.p.?	NM_001083614 c.322C>T; c.920T>C; p.Arg108Trp p.Leu307Ser	NM_015836 c.938A>T; c.797delC; p.Lys313Met; p.Pro266Argfs*
Current age	P1 <sup>VAR</sup> S2 †7 weeks P2 <sup>VAR</sup> S2 3 years	P3 <sup>VAR</sup> S2 †4 months P4 <sup>VAR</sup> S2 9 months	5 years	21, 19, 14, 11 years	P1 <sup>EARS</sup> 2 †30 days P2 <sup>EARS</sup> 2 11 months	4 years
Age of onset	P1 <sup>VAR</sup> S2: 1 day P2 <sup>VAR</sup> S2: 7 days	P3 <sup>VAR</sup> S2: During pregnancy P4 <sup>VAR</sup> S2: During pregnancy	1 month	4 months	P1 <sup>EARS</sup> 2: 3 weeks P2 <sup>EARS</sup> 2: 6 hours	3 months
Phenotype	P1 <sup>VAR</sup> S2: Hypertrophic cardiomyopathy P2 <sup>VAR</sup> S2: Hypertonia, hypertrophic cardiomyopathy, bilateral vocal cord paralysis	P3 <sup>VAR</sup> S2: Chorioamniotitis, pulmonary hypertension, hypertrophic cardiomyopathy P4 <sup>VAR</sup> S2: Lactic acidosis, hypertrophic cardiomyopathy, pulmonary hypertension	Spasticity and weakness of lower limbs, developmental delay, clonus, ataxia.	Developmental delay, retinitis pigmentosa, dystonia, tremor. P1 <sup>AAR</sup> S2: Psychotic episodes, anxiety, depression	P1 <sup>EARS</sup> 2: feeding difficulties, lactic acidosis, enterocolitis, sepsis. P2 <sup>EARS</sup> 2: Seizures, feeding difficulties, axial hypotonia, limb hypertonia, hyperreflexia.	Developmental delay, dystonia, tremor, sleeping difficulties and feeding difficulties necessitating PEG-J feeding.
Treatment duration	~3 years	6 months	22 months	6 months	3 months, currently 8 months without treatment	10 months
Dosage	100 mg/kg/day valine	100 mg/kg/day valine	100 mg/kg/day serine	P1 <sup>AAR</sup> S2: 25 P2 <sup>AAR</sup> S2: 30 P3 <sup>AAR</sup> S2: 50 P4 <sup>AAR</sup> S2: 40 mg/kg/day alanine	80 mg/kg/day glutamate	60 mg/kg/day tryptophane
Additional medication	Magnesium-Malate, 50mg/day. Levocarnitine, 150mg/day.	3.5 g/kg/day protein supplementat ion, Milrinone 0.5 ug/kg/min, Sildenafil 10mg Q6H, Bosentan 7mg BD, Selexipag 75 ug BD, frusemide 6 mg Q4H, and	3.5 g/kg protein supplementat ion, Thiamine 100mg/day	P1 <sup>AAR</sup> S2: Olanzapine.	P2 <sup>EARS</sup> 2: Phenobarbital 5mg/kg/day, Levetiracetam 36mg/kg/day, Baclofen 2.5mg PRN, Domperidone 2,1mg Q8h, Esomeprazol 15mg BD	Biotin 20mg/day, Thiamine 15 mg/day Omeprazol BD, Macroglol 4-8mg BD, Melatoninine 1mg/day. Chloralhydrate PRN. Iron supplementation

**Table 1:** Clinical characteristics of ARS deficient patients. NA = Not Assessed

# Chapter 7



# Amino Acid Treatment for ARS2 deficiencies

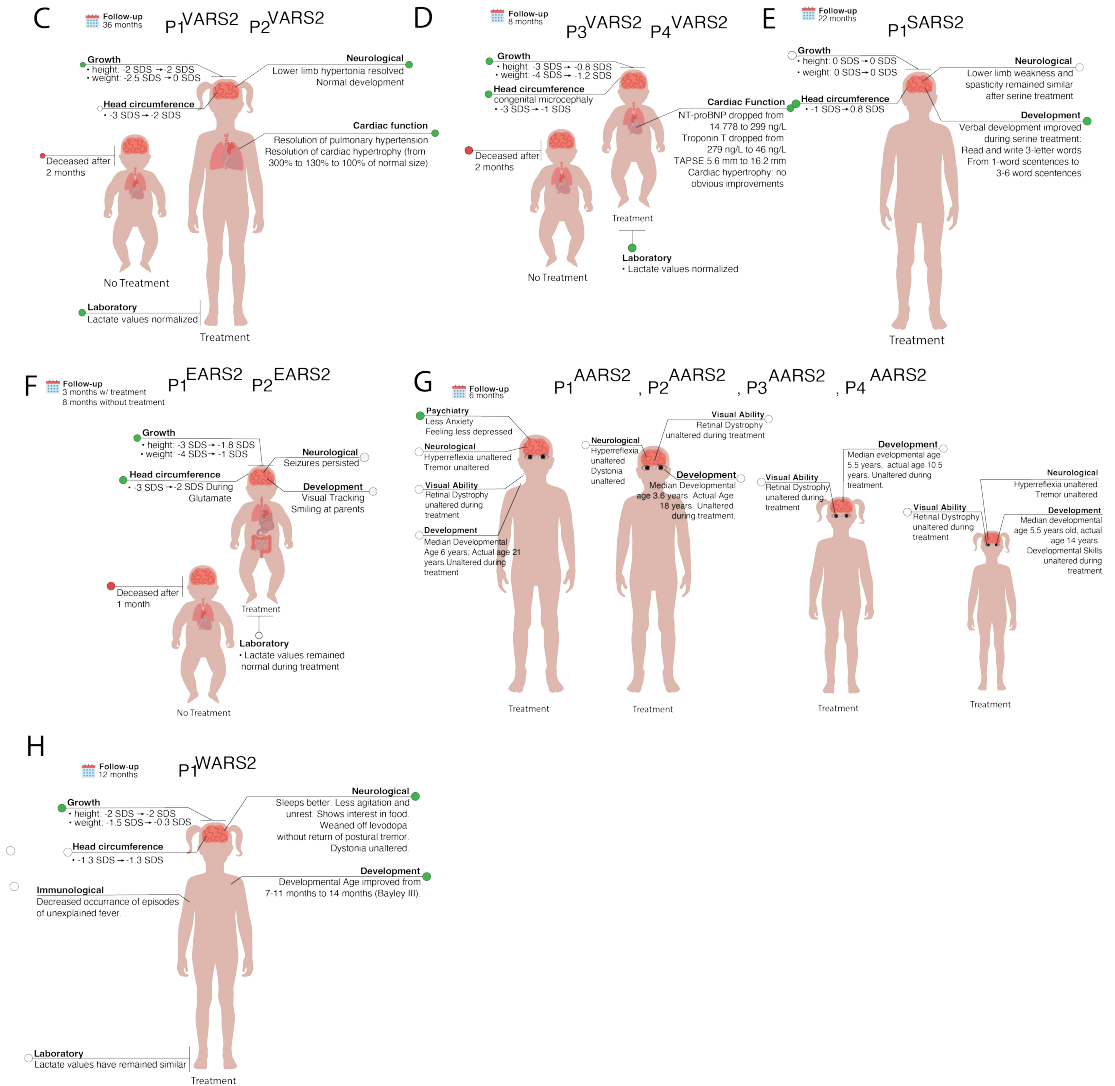


**Figure 2: Summary of clinical symptoms and treatment effects.**

(A) Graphical representation of clinical disease course over time before and during treatment for each patient. Blue colored bars indicate the time during which amino acid treatment was given. (B) Showing the Denver development scale for patients where developmental milestones were recorded before and during treatment (P3<sup>VARS2</sup>, P1<sup>SARS2</sup>, P2<sup>EARS2</sup>). AARS2 deficient patients (aged >8 years) had already acquired all developmental milestones before treatment initiation and are not included in this graph.

P4<sup>VARs2</sup> was on ventilator support and did not develop any developmental milestones before or during treatment. P1<sup>WARs2</sup> her developmental progression was recapitulated in the KIDN-III assessment and not shown in these graphs. The green lines and planes indicate the p50-p90 ranges for developmental progression. The black dotted lines indicate the age where treatment was initiated. Representative domains are shown for each of the three patient, a comprehensive overview of the Denver development scales on all domains can be found in **Table S1**.

(C-H) For each patient, the top left corner shows the treatment duration. Siblings are grouped together. For each patient, the bottom row indicates who was treated ('Treatment' or not ('No Treatment'). Colors indicate the generalized treatment effect on the specific symptom (green: improved; white: stable or stabilized; red: progressed). Standard deviation scores (Z) were used for height, weight, and head circumference. Z-scores were calculated using Dutch (NL) reference charts (P1/P2<sup>VARs2</sup>, P1/P2/P3/P4<sup>AARS2</sup>, P1<sup>WARs2</sup> or World Health Organization (WHO) reference charts (P3/P4<sup>VARs2</sup>, P1/P2<sup>EARS2</sup>, P1<sup>SARS2</sup>).

Since similar dosage increments resulted in clinical improvements in ARS1-deficient patients, and our in-vitro work showed that healthy reference range blood plasma amino acid levels were sufficient to improve mitochondrial function in patient-derived fibroblasts, we hypothesized these dosage increments would be sufficient to elicit a clinical response. Clinical characteristics of the patient cohort are summarized in **Table 1**.

Amino acid supplementation was well tolerated in all patients, since adverse effects were not reported and all laboratory values stayed within normal range during treatment (**File S2**). In a subset of patients, laboratory values improved during treatment, specifically lactate values (P2<sup>VARs2</sup> and P4<sup>VARs2</sup>), troponin and NT-proBNP values (P4<sup>VARs2</sup>). In P1<sup>SARS2</sup>, language development was delayed at first but significantly accelerated after treatment (**Figure 3B**). Similarly, P1<sup>WARs2</sup> showed improved language and social development during tryptophane treatment, as measured using Bayley-III. While P2<sup>VARs2</sup> showed mild developmental delay during infancy (p90), her development significantly accelerated during valine treatment, as she now reached her milestones within the 50th percentile (**Figure 3B**). In contrast, the majority of reported VARs2 deficient patients show developmental delay (86%).<sup>2</sup> Clinical improvements of patients during treatment are summarized in **Figure 3C**.

*VARs2 deficient patients*

P1<sup>VARs2</sup> presented with respiratory insufficiency and hypertrophic cardiomyopathy immediately after birth. He died at the age of 7 weeks. Post-mortem autopsy revealed pathogenic *VARs2* variants. Three years later, P2<sup>VARs2</sup> was born. Two days after birth, P2<sup>VARs2</sup> was diagnosed with laryngomalacia, for which she was admitted to the hospital. She developed cardiomyopathy, lactic acidosis and respiratory insufficiency, requiring mechanical ventilation and tracheotomy. Brain MRI showed a thalamic infarction in the right hemisphere. At the age of one month, valine supplementation (25 mg/kg/day) was briefly administered but feeding difficulties limited her intake. As her condition worsened, a palliative trajectory was initiated, and valine supplementation was stopped. At the age of three months, her symptoms stabilized spontaneously and her intake improved. At the age of four months, valine supplementation (60 mg/kg/day) was reinitiated. One month later, protein fortification was added (22.5g protein/day). Compared to 6 weeks of age, her condition has significantly improved; her pulmonary hypertension completely resolved; her hypertrophic cardiomyopathy completely resolved (heart size: 300% to 130% of normal within 1 year). Her lower limb hypertonia resolved. She never developed microcephaly or epilepsy, and reached all developmental milestones at a normal age (**Figure 3B**).

P3<sup>VARs2</sup> presented with hypertrophic cardiomyopathy and pulmonary hypertension shortly after birth. He died at the age of four months. Genetic testing was not performed. P4<sup>VARs2</sup> was born prematurely at 35 weeks due to restricted fetal movement and growth deficits. Shortly after birth, pulmonary hypertension, cardiac hypertrophy and lactic acidosis were noted, for which he required mechanical ventilation. At three months of corrected age, a severe pulmonary hypertensive crisis, requiring cardiopulmonary resuscitation, led to ICU admission and ECMO together with Continuous Renal Replacement Therapy (CRRT). At the same time, exome sequencing revealed *VARs2* variants, and valine supplementation was initiated. Two days after treatment initiation, ECMO treatment could be discontinued, and was replaced by Nitric Oxide, ventilator support and inotropy, which was slowly weaned down. His lactate values normalized during treatment (**File S2**).

Additionally, troponin T and NT-proBNP levels dropped significantly (**File S2**). All of his growth parameters improved during treatment (**File S3**). His biventricular cardiac hypertrophy persisted with no obvious improvements. While LVEF was normal before treatment and has remained normal, TAP-SE values have been improving from ~5-6 mm to 16.2mm. At the age of 7 months, he became septic, impeding the intake of enteral valine, as he was now completely dependent on parenteral nutritional- and ventilator support. During this time, his cardiac hypertrophy worsened significantly, and palliative care was initiated.

#### *SARS2 deficient patient*

P1<sup>SARS2</sup> presented in the first year of life with clonus and lower limb spasticity, accompanied by developmental stagnation after one year of age. At the age of 2 years and 8 months, *SARS2* genetic variants were identified, and serine treatment was started shortly afterwards. Before treatment, he had delayed speech development consisting of one-word sentences and non-verbal communication (**Figure 3B**). During treatment, he showed catch-up language development and was able to formulate 3-to-6-word sentences (development within p50-p90), allowing him to attend regular preschool, only six months after treatment initiation (**Figure 3B**). At preschool, he started to read 3-letter words and learned the English alphabet. Currently, he is attending kindergarten where he has learned to write 3-letter words. His lower limb weakness and spasticity have not changed since treatment.

#### *AARS2-deficient patients*

P1/P2/P3/P4<sup>AARS2</sup> are siblings that presented with feeding difficulties during infancy. All patients developed retinal dystrophy, optic nerve atrophy and progressive mental retardation. The oldest sibling (P1<sup>AARS2</sup>) additionally shows (nightly) agitation and psychotic episodes. All affected siblings started with low-dose  $\beta$ -alanine supplementation for six months (30-55 mg/kg/day), without clinical improvements. However, as  $\beta$ -alanine is only marginally converted to L-alanine, they were switched to low dosage L-alanine supplementation (25-40 mg/kg/day). These lower dosages were the result of swallowing difficulties related to the large capsules, that limited their

daily alanine intake. They have now used alanine supplementation for seven months, without obvious changes in visual performance or development. However, the oldest sibling experienced less anxiety and depression during alanine supplementation.

#### *EARS2 deficient patient*

P1<sup>EARS2</sup> was born to non-consanguineous parents. She was admitted at the ICU at three weeks of age, with COVID-19 infection, severe lethargy and lactic acidosis (lactate: 24 mmol/L). A ketogenic diet was initiated, but one week later, she died due to enterocolitis and sepsis. Genomic sequencing revealed *EARS2* variants. Her younger brother, P2<sup>EARS2</sup>, was diagnosed with the same *EARS2* variants antenatally. Six hours after birth, he had his first seizure, after which anti-epileptic medication, 40mg/kg/day glutamate and a high protein diet (3g/kg/day) were initiated. At one month of age, glutamate dosage was increased to 80mg/kg/day. The following two months, his seizures persisted and he developed proximal hypotonia and brief clonus upon neurological examination. He showed some developmental progression, moving both arms and legs, smiling at parents and being able to visually track objects. Severe nausea and feeding difficulties limited his intake, and glutamate treatment was discontinued at three months of age by parents, to see whether nausea would decrease, but it did not. At the age of 6 months, protein fortification was changed to Neocate LCP (a hypoallergenic protein formula lacking L-glutamate). After switching to Neocate LCP and discontinuing glutamate, the patient developed sinus tachycardia, cyclic vomiting, and progressive lactic acidosis within three months (**Figure S2**). His spasticity worsened and he showed sustained clonus upon examination. He lost previously acquired developmental skills, as he could not smile at parents, move arms or legs, or track faces anymore. He developed uncontrolled epilepsy and somnolence, requiring admission and initiation of palliative care.

#### *WARS2-deficient patient*

P1<sup>WARS2</sup> presented with spasticity and agitation at the age of 3 months. MRI showed a thin corpus callosum and frontal lobe atrophy, with normal myelination pattern. Her development was significantly delayed. Additionally, she



had developed a complex movement disorder consisting of tremor and dystonia. She had severe sleeping difficulties. She is completely dependent on tube feeding and vomits frequently. After initiation of tryptophane (60mg/kg/day), the vomiting stopped. Parents noted her to have more energy and she was less agitated. Before treatment, she could not join family dinners due to her agitation, but she is now able to. She sleeps better through the night; where she used wake up several times without being able to sleep thereafter, she now sleeps continuously. She only needs her chloralhydrate right before bedtime instead of several times per night. Where she used to have a fever several times a month, this now occurs now less frequently. Her development has improved: right before treatment, her developmental age was estimated at 7-11 months (Bayley-III, actual age: 42 months), whereas 10 months into treatment, her developmental age improved significantly to 14 months (actual age: 52 months). In contrast; the 2 years before tryptophan treatment initiation her development did not improve (developmental age 7-8 months at age 20 months). She now engages in pretend play and can point at objects in a book and leaf through it. While her dystonia has not changed, she was able to wean off levodopa, which was used to control tremors before tryptophane initiation. After weaning off levodopa, her tremor did not return.

## Discussion

We here present evidence for significant mitochondrial dysfunction during cognate amino acid deprivation in fibroblasts of mitochondrial ARS deficiencies, and show that this can be rescued by amino acid supplementation in patient-derived cells. Subsequently, we treated VARS2, AARS2, SARS2, WARS2 and EARS2 deficient patients with cognate amino acids to prevent mitochondrial dysfunction and subsequent clinical deterioration. Amino acid supplementation was well-tolerated in all patients. Our clinical observations show that during amino acid supplementation, a subset of symptoms improved, including cardiomyopathy, development, sleeping problems, agitation and feeding difficulties, while certain neurological symptoms (epilepsy, spasticity, dystonia), remained stable. Our preliminary results concur with

recently published case reports showing beneficial effects of amino acids in patients with pathogenic FARS2 and RARS2 variants.<sup>9,13</sup>

In all patients, we suspected that their clinical deterioration was aggravated by a combination of high amino acid expenditure and/or feeding difficulties, leading to a decrease in (local) amino acid availability. Our fibroblast studies confirm the correlation between amino acid availability and mitochondrial function, suggesting that amino acid supplementation might prevent amino acid shortages, thereby aiding mitochondrial translation during catabolism. Furthermore, the distinct mitochondrial abnormalities identified could potentially serve as a diagnostic marker for ARS2 deficiencies, addressing the current absence of targeted diagnostic assays for this condition. However, assessing the severity and amenability to treatment based on mitochondrial dysfunction observed in patient-derived cells during amino acid deprivation may pose challenges, as the extent of dysfunction might be influenced by the ability to synthesize non-essential amino acids endogenously or by patients' genetic background.

The small number of patients, differences in clinical presentation, and fluctuating disease course made it difficult to discriminate treatment effects from disease course fluctuations and ongoing development. Specifically, P2<sup>VARS2</sup> already showed clinical improvement before valine supplementation was reintroduced. However, her clinical improvement concurred with better oral (valine) intake. A comparison to her untreated sibling does suggest efficacy of treatment, as she survived well beyond the age where the untreated sibling passed away, similarly as the other patients that were compared to their older sibling (N=2). Although N-of-1 trials with standardized outcome measures would allow direct comparison of clinical improvement within the same patient, certain considerations should be taken into account. First of all, ethical considerations play a role, as discontinuation of amino acid supplementation in P2<sup>EARS2</sup> was followed by neurological deterioration and a palliative trajectory. Second, the adoption of standardized measures applicable across the diverse clinical phenotypes observed should be taken into account, to enhance the interpretability and generalizability of trial results.

In conclusion, our study shows that amino acid depletion leads to mitochondrial dysfunction in fibroblasts derived from patients with ARS2 deficiencies, suggesting that prevention of amino acid shortages by supplementation could represent an effective strategy to prevent deterioration in patients. Although anecdotal, our clinical observations show beneficial effects for the majority of patients and no unwanted side-effects of treatment with cognate amino acids. N-of-1 studies would help to objectify these treatment effects, however, the clinical heterogeneity of ARS2 deficiencies and their fluctuating disease course should be taken into account when designing these studies.

### **Acknowledgements**

The authors would like to thank Oncode for the Seahorse Equipment. The authors would like to thank Dominic Lenz for conceptualization of treatment protocols for ARS1 patients which were used as template for ARS2-deficient patients in this study. This work was funded by the Tjalling Roorda Foundation.

### **Author Contributions**

I.M., G.K. and S.A.F. conceptualized and wrote the original draft of the manuscript. G.K., I.M., Z.T. K.S., did the laboratory investigation, validation, and analysis. I.M. performed the visualization of results (figures, tables). K.K., P.v.H., C.M.A.L., I.V.D.S. L.S.M., F.O.P., S.K.K., A.M.K.K., R.R., M.B., S.H., R.J., A.M.B., E.H.K. and S.A.F. were involved in clinical investigation. I.M., G.K., W.V., K.K., E.H.K and S.A.F. reviewed and edited the final version of the manuscript.

### **References:**

1. Konovalova S, Tynismaa H. Mitochondrial aminoacyl-tRNA synthetases in human disease. *Mol Genet Metab.* 2013;108(4):206-211. doi:10.1016/j.ymgme.2013.01.010
2. Bruni F, Di Meo I, Bellacchio E, et al. Clinical, biochemical, and genetic features associated with VARS2-related mitochondrial disease. *Hum*

Mutat. 2018;39(4):563-578. doi:10.1002/humu.23398

3. Kok G, Schene I, Nikkels P, et al. Aminoacyl-tRNA synthetase deficiencies: in search of common themes. *Genetics in Medicine*. Published online 2018:1-12.
4. Botta E, Theil AF, Raams A, et al. Protein instability associated with AARS1 and MARS1 mutations causes trichothiodystrophy. *Hum Mol Genet*. 2021;30(18):1711-1720. doi:10.1093/hmg/ddab123
5. Kok G, Tseng L, Schene IF, et al. Treatment of ARS deficiency with specific amino acids. *Genetics in Medicine*. Published online 2021 doi:10.1038/s41436-021-01249-z
6. Lenz D, Stahl M, Seidl E, et al. Rescue of respiratory failure in pulmonary alveolar proteinosis due to pathogenic MARS1 variants. *Pediatr Pulmonol*. 2020;55(11):3057-3066. doi:10.1002/ppul.25031
7. Hadchouel A, Drummond D, Pontoizeau C, et al. Methionine supplementation for multi-organ dysfunction in MetRS-related pulmonary alveolar proteinosis. *European Respiratory Journal*. Published online 2021:2101554. doi:10.1183/13993003.01554-2021
8. Koripella RK, Sharma MR, Haque ME, Risteff P, Spremulli LL, Agrawal RK. Structure of Human Mitochondrial Translation Initiation Factor 3 Bound to the Small Ribosomal Subunit. *iScience*. 2019;12:76-86. doi:10.1016/j.isci.2018.12.030
9. Oswald S, Steinbruecker K, Achleitner M, et al. Treatment of Mitochondrial Phenylalanyl-Trna-Synthetase Deficiency (Fars2) With Oral Phenylalanine. *Neuropediatrics*. Published online 2023. doi:10.1055/a-2008-4230
10. Shen YW. Correspondence on “Treatment of ARS deficiencies with specific amino acids” by Kok et al. *Genetics in Medicine*. 2022;24(2):503-505. doi:10.1016/j.gim.2021.10.001
11. Muffels IJJ, Wiame E, Fuchs SA, et al. NAA80 bi-allelic missense variants result in high-frequency hearing loss, muscle weakness and developmental delay. *Brain Commun*. 2021;3(4). doi:10.1093/braincomms/fcab256
12. Milanese C, Bombardieri CR, Sepe S, et al. DNA damage and transcription stress cause ATP-mediated redesign of metabolism and poten-

tiation of anti-oxidant buffering. *Nat Commun.* 2019;10(1). doi:10.1038/s41467-019-12640-5

13. Shen YW, Zhou XL, Zou L ping. Correspondence on “treatment of ARS deficiencies with specific amino acids” by Kok et al. *Genetics in Medicine*. Published online 2021. doi:10.1016/j.gim.2021.10.001

14. Muffels IJJ, Schene IF, Rehmann H, et al. Bi-allelic variants in NAE1 cause intellectual disability, ischiopubic hypoplasia, stress-mediated lymphopenia and neurodegeneration. *Am J Hum Genet.* 2023;110(1):146-160. doi:10.1016/j.ajhg.2022.12.003

Supplementary Files and Figures

Figure S1: Seahorse and membrane potential assessment in healthy controls and ARS1/ARS2-deficient patients.

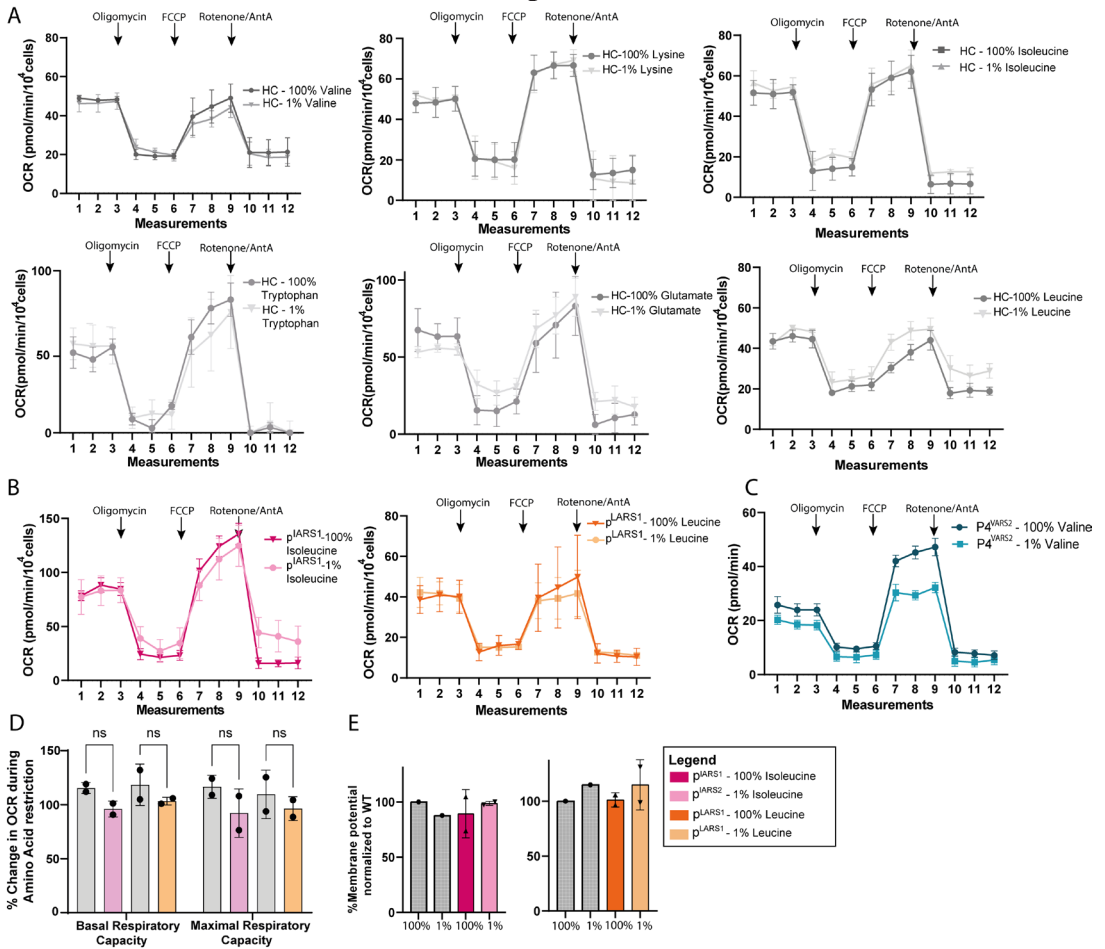


**Figure S1:** (A) Seahorse analyses in healthy controls treated with normal (100%) valine, lysine, leucine, isoleucine, glutamate and tryptophane, or depletion medium (1%) for two days. The graphs represent one representative experiment with one healthy donor. The error bars represent the SEM of three or four technical replicates.

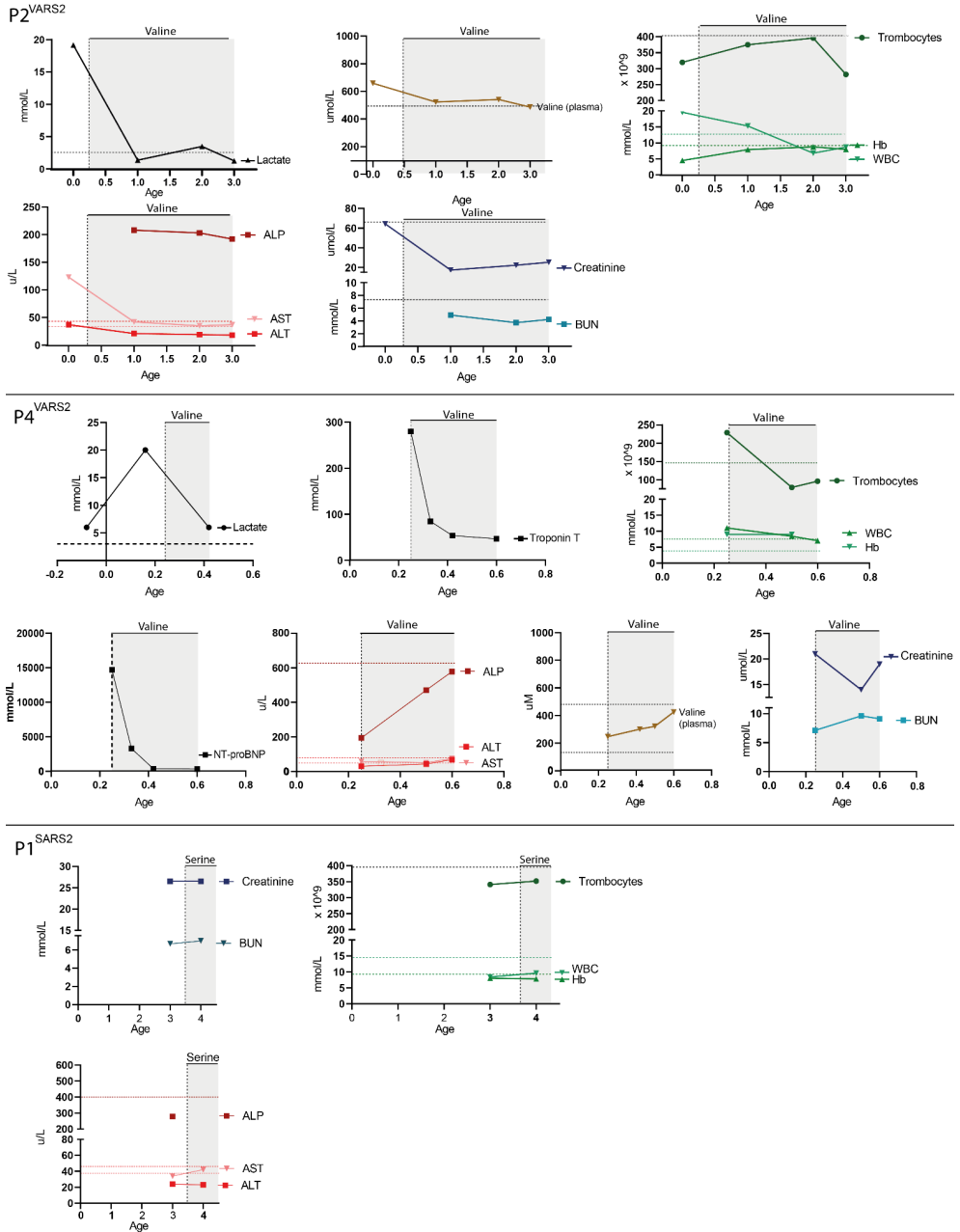
(B) Seahorse analyses performed in fibroblasts of patients with LARS1 (N=2) and IARS1 (N=2) deficiency, treated with normal (100%) leucine or isoleucine (respectively) or depletion medium (1%) for two days. The graphs represent one representative experiment with one donor. The error bars represent the SEM of three or four technical replicates.

(C) Seahorse analyses showing the non-normalized OCR in P4<sup>VARs2</sup> treated with normal (100%) valine or depletion medium (1%) for two days. The error bars represent the SEM of three or four technical replicates.

(D) Bar graphs showing the average basal and maximal OCR of healthy controls, ARS2 and dual ARS deficient patients. The OCR values of the 1% condition are normalized to the 100% condition and depicted as a percentage. The bars represent the mean percentage of all donors and technical replicates combined  $\pm$ SD, the dots represent the percentage per technical replicates per donor. The bar represents the mean of all healthy donors and all conditions combined. Statistics were calculated using two-way repeated measures ANOVA.

(E) Membrane potential measurements in patients with LARS1 (N=2) or IARS1 (N=2) deficiency. In the patients, the bars represent membrane potential normalized to healthy controls treated with the same condition  $\pm$ SD. In the healthy control, the 1% condition is normalized to the 100% condition of the healthy control.

**Figure S2: Laboratory Values before and after amino acid treatment.**





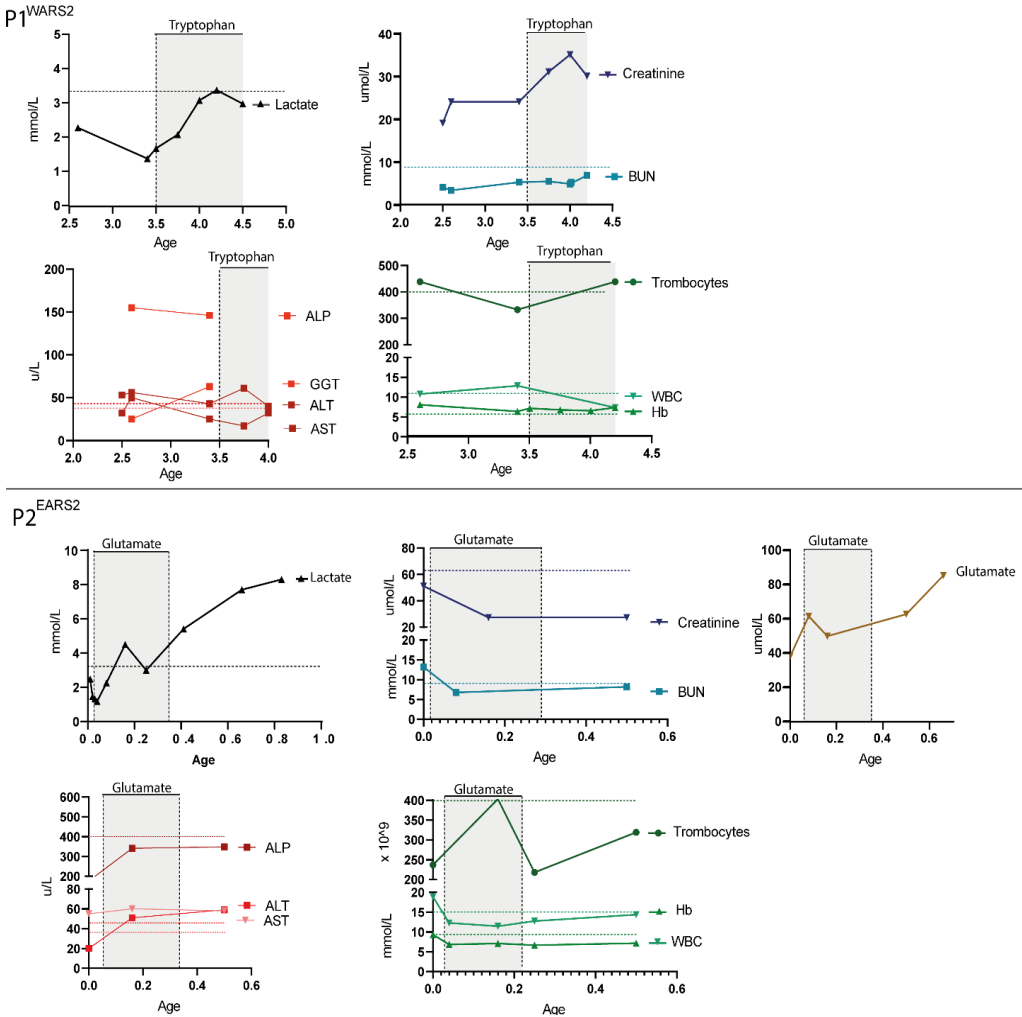


**Figure S2:** Laboratory values of patients before and after amino acid treatment. Grey areas indicate the period where amino acid treatment was given. The dotted horizontal lines indicate reference values in the healthy pediatric population. The vertical dotted lines indicate the age of treatment initiation. BUN = Blood Urea Nitrogen, ALP = Alkalic Phosphatase, GGT = Gamma Glutamyl Transpeptidase , ALT = Alanine Aminotransferase , AST = Aspartate Aminotransferase, Hb = Hemoglobin, WBC = White Blood Cell Count.

**Figure S3: Growth values before and after treatment**

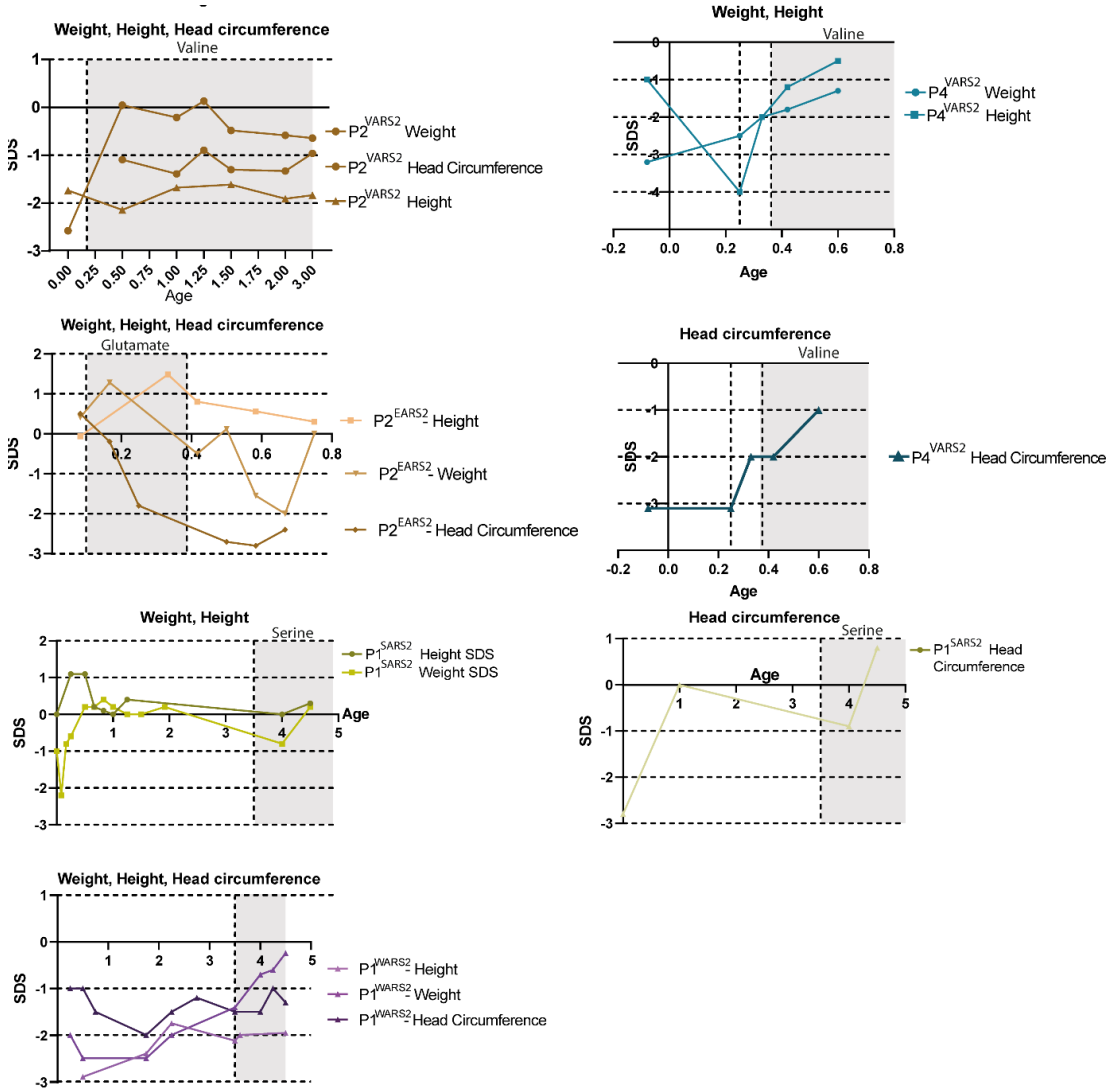


**Figure S3: Growth parameters (in SDS) for patients before and after amino acid** before and after amino acid supplementation. Grey areas indicates the period where amino acid treatment was given.

given. The vertical dotted lines indicate the age of treatment initiation. The SDS for Dutch patients was calculated by using Dutch reference values (TNO, <https://tnochildhealthstatistics.shinyapps.io/JGZRichtlijnLengte-groei>).

For patients included outside the Netherlands WHO reference values were used <https://www.who.int/tools/child-growth-standards/standards/weight-for-age>

### **Supplementary Note 1: Pathogenicity assessment of *VARS2*, *AARS2*, *SARS2*, *EARS2*, *WARS2* and *KARS* genetic variants.**

Some of the patients reported in this study had Variants of Uncertain Significance in ARS genes. Before amino acid treatment initiation, we assessed the pathogenicity of these variants. For ARS1 and dual ARS genetic variants, we used the gold standard to diagnose patients: ARS aminoacylation activity measurements. Unfortunately, aminoacylation measurements are not yet validated for ARS2 proteins. Thus, for *VARS2*, *AARS2*, *SARS2*, *WARS2* and *EARS2* genetic variants, we used different methods. First of all, we predicted the impact of the genetic variants on protein 3D structure and function. Next, we employed in-silico prediction tools (MutationTaster, PolyPhen2, CADD scores) (Adzhubei et al., 2013; Rentzsch et al., 2019; Schwarz et al., 2010). Finally, we assessed protein and RNA availability. In the end, pathogenicity was assessed using the ACMG criteria. (Richards et al., 2015) Patients harboring variants that were considered likely pathogenic or pathogenic are included in the main body of this manuscript.

### **P1<sup>VARS2</sup> and P2<sup>VARS2</sup>: NM\_001167734 c.(1258G>A); c.(1973G>A), p.(Arg658His); p.(Ala420Thr)**

#### *Whole Exome Sequencing*

With trio-whole Exome Sequencing (WES), no other genetic variants were identified in P2<sup>VARS2</sup>. P1<sup>VARS2</sup> and P2<sup>VARS2</sup> both harbored the same compound heterozygous *VARS2* variants.

#### *Predictions*

The Arg658 residue resides in the transfer domain and is rather close to

the substrate binding site and the editing domain, which are essential for VARS2 function. Arginine658 is part of the protein core, and thus a change of arginine to cysteine could destabilize the protein. Several in-silico prediction tools show that this variant is predicted to be damaging (PolyPhen2) or disease causing (MutationTaster). The residue is highly conserved among phylogenetically distant organisms.

The other variant, Ala420Thr, has been reported as pathogenic. It was observed in three different patients with a highly similar phenotype as P2<sup>VAR<sub>S2</sub></sup>, characterized by hypertrophic cardiomyopathy, respiratory failure, feeding difficulties and hypotonia (Bruni et al, 2010). It is located in a region important for the interaction of VARS2 with its cognate tRNA. The residue is highly conserved among phylogenetically distant organisms.

*Functional Studies*

Western blot of fibroblasts showed low-to-normal VARS2 expression in fibroblasts compared to three healthy controls (**Figure S4**). Additionally, complex activities of complex I and complex II were slightly reduced compared to healthy controls.

**Figure S4: VARS2 western blot.**

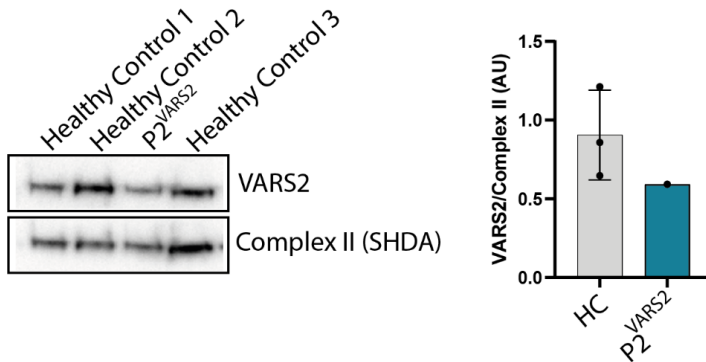


**Figure S4: VARS2 western blot**

Western blot of P2<sup>VAR<sub>S2</sub></sup> isolated mitochondria from fibroblasts. The patient was compared to three different healthy control fibroblast lines. Membranes were probed with VARS2 antibody (ProteinTech).

Western blot of P2<sup>VAR<sub>S2</sub></sup> isolated mitochondria from fibroblasts. The patient was compared to three different healthy control fibroblast lines. Membranes

mU/U CS	complex I	complex II	complex III	complex IV	complex V
P2 <sup>VAR2</sup>	<b>161</b>	492	743	<b>205</b>	637
Reference Values	163 – 599	335 – 888	570 – 1983	288 – 954	193 - 819
values.	mU/U CS	mU/U CS	mU/U CS	mU/U CS	mU/U CS

were probed with VARS2 antibody (ProteinTech).

*ACMG Criteria*

Together, these results indicate that both variants are pathogenic, based on ACMG criteria. While pathogenicity of Ala420Thr variant has been assessed previously. The Arg658His variant qualifies as pathogenic based on PS3, PM3, PP4, PP1, PP3.

**P3<sup>VAR2</sup> and P4<sup>VAR2</sup>: NM\_001167734 c.(1940C>T);c.(763A>G) p.(Thr-647Met);(Lys255Glu)**

*Whole exome sequencing*

Trio-whole exome sequencing revealed compound heterozygous VARS2 variants in P4<sup>VAR2</sup>. His older brother passed away at young age with a highly similar clinical phenotype. However, genetic testing was not performed in P3<sup>VAR2</sup>.

*Literature studies*

The Thr647Met variant has been reported previously in a patient with a similar phenotype as P3<sup>VAR2</sup> and P4<sup>VAR2</sup> together with a p.Arg773Gln variant. Thr647 is highly conserved across species. Substitution with methionine could destabilize binding with the ATP intermediate. Introduction of the individual variants in yeast led to growth deficits when grown on oxidative carbon sources. Additionally, respiration rate was reduced for both variants. (Chin et al., 2019)

*Predictions*

The Lys255Glu variant is located in a highly conserved acceptor splice site (PhyloP=3.9, PhastCons=1). MutationTaster predicts this variant to be disease

causing (0.99) and PolyPhen predicts this variant to be probably damaging (0.99). The residue is conserved among phylogenetically distant organisms.

#### *ACMG Criteria*

Together, these results indicate that both variants are pathogenic, based on ACMG criteria. While pathogenicity of p.Thr647Met variant has been assessed previously. The Lys255Glu variant qualifies as likely pathogenic based on PS3, PM3, PP4, PP3.

#### **P5<sup>VAR2</sup> and P6<sup>VAR2</sup>: NM\_001167734 c.(1972C>T);(c.-190C>G) p.(Arg-658Cys);p.(?)**

The genetic variants of monozygotic twins P5<sup>VAR2</sup> and P6<sup>VAR2</sup> were classified as Variants of Uncertain Significance based on ACMG guidelines. Despite extensive diagnostic workup including RNA analysis, we could not establish pathogenicity of variants. Therefore, we decided not to report these individuals in the main body of this work.

#### *Whole Exome Sequencing*

The bi-allelic variants in *VAR2* were not identified in an older brother of the twins who was not affected. With whole Exome Sequencing (WES), no other genetic variants that could explain the symptoms of P5<sup>VAR2</sup> and P6<sup>VAR2</sup> were identified.

#### *Predictions*

The Arg658 residue resides in the transfer domain and is rather close to the substrate binding site and the editing domain, both essential for *VAR2* function. The arginine at position 658 is part of the protein core, and a substitution of arginine to cysteine could destabilize the entire protein. Several in-silico prediction tools predict that this variant is damaging (PolyPhen2) or disease causing (MutationTaster). The residue is conserved among phylogenetically distant organisms.

The other variant, the c.-190C>G, might reside in the 5-UTR site. Structural information about this site is not available.

#### *Functional Studies*

Patients showed equal *VAR2* expression in fibroblasts compared to four healthy controls (**Figure S5A**). In muscle lysates of patient 2, *VAR2* expression appeared to be slightly decreased compared to healthy controls

**(Figure S5B).**

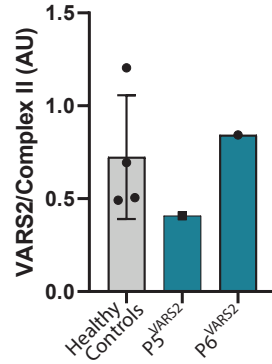
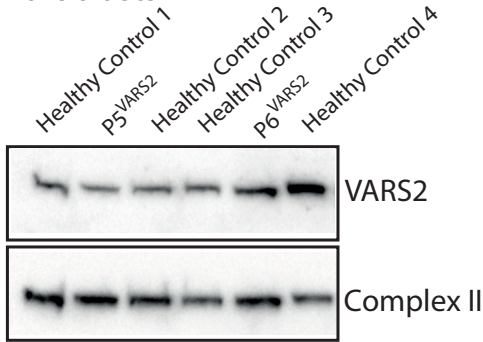
RNA sequencing data showed normal expression of the VARS2 isoform with the c.-190C>G variant compared to the allele with the p.Arg658Cys variant (data not shown).

*Biochemical Studies*

Biochemical studies showed normal activity of mitochondrial complexes in fibroblasts.

<b>mU/U CS</b>	<b>complex I</b>	<b>complex II</b>	<b>complex III</b>	<b>complex IV</b>	<b>complex V</b>
P5 <sup>VARS2</sup>	278	476	768	466	677
P6 <sup>VARS2</sup>	345	611	1036	475	918
Reference Values	163 – 599 mU/U CS	335 – 888 mU/U CS	570 – 1383 mU/U CS	288 – 954 mU/U CS	193 - 819 mU/U CS

A Fibroblasts



B Muscle

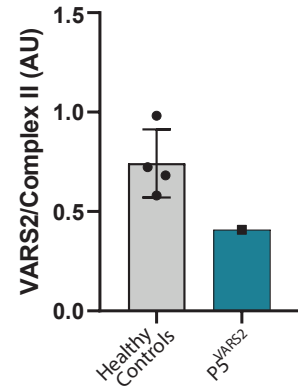
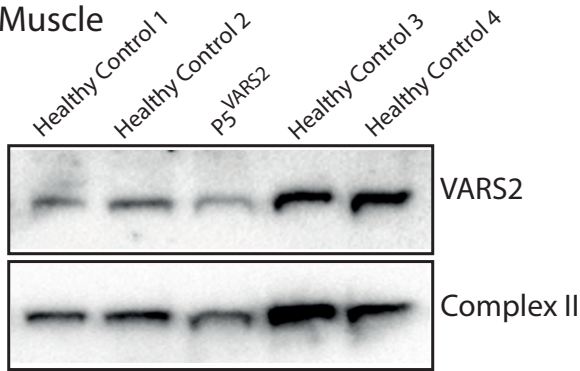


**Figure S5:** (A) Western blot of P5<sup>VARS2</sup> and P6<sup>VARS2</sup> isolated mitochondria from fibroblasts. Patients were compared to four different healthy control fibroblast lines

(B) Western blot of P5<sup>VARS2</sup> whole muscle lysate. For whole muscle lysate, 600 mg of tissue was loaded. P5<sup>VARS2</sup> was compared to whole muscle lysate of four pediatric controls.

**P1<sup>SARS2</sup> NM\_017827c.1347G>A; c.1347G>A**

P1<sup>SARS2</sup> has a homozygous synonymous variant in SARS2. Trio exome sequencing revealed both parents were heterozygous for the SARS2 variant. The variant has been reported previously. It is located in the splice site



of exon 14, and the variant has been shown to cause altered splicing and retainment of intron 14, leading to a frameshift after exon 14 an premature stopcodon, affecting the c-terminal part of the protein. It leads to severely decreased expression of SARS2 protein levels and tRNA<sup>Ser</sup> levels.(Linnan-kivi et al., 2016) This variant is thus classified as pathogenic based on PVS1 and PS1.

**P1<sup>EASRS2</sup> and P2<sup>EASRS2</sup> NM\_001083614 c.322C>T; p.(Arg108Trp) ; c.920T>C; p.(Leu307Ser)**

P1<sup>EASRS2</sup> has compound heterozygous missense variants in *EARS2*, that were also present in his deceased sister. Both variants have been reported previously.

The Arg108Trp is frequently observed in patients with *EARS2* variants, usually together with another heterozygous missense variant. It has been observed in at least six patients (Steenweg et al., 2012) with a similar phenotype. Additionally, the Arg108Trp in combination with other variants is associated with significantly reduced maximal respiratory rate.(Steenweg et al., 2012). It is considered pathogenic based on PS4, PS1. The Leu307Ser variant has also been reported in combination with the c.184A>T variant in a patient with similar phenotype.(Barbosa-Gouveia et al., 2021) It is considered likely pathogenic based on PM3, PP3, PP1, PP4, PP5.

**P1, P2, P3, P4<sup>AARS2</sup> NM\_020745.3: c.(749+235\_1150-88de-lins59);(2255+8A>C). p.(?);(?)**

*Whole Exome Sequencing*

The *AARS2* genetic variants were identified in a large family with eleven siblings. In total, four out of eleven siblings harbored compound heterozygous *AARS2* genetic variants, all with a similar phenotype. The unaffected siblings did not harbor the *AARS2* genetic variants.

*Predictions*

The *AARS2* genetic variants - a large deletion on one allele and an insertion resulting in a frameshift on the other - are both expected to cause severely decreased *AARS2* protein availability.

### Western Blot

Western blot analysis showed severely decreased AARS2 availability in P1<sup>AARS2</sup> and P2<sup>AARS2</sup> fibroblasts compared to healthy control fibroblast (**Figure S6**).

### ACMG Criteria

Together, these results indicate the homozygous deletion is pathogenic, based on ACMG criteria (PVS1, PS3, PP1 (based on segregation data in 11 siblings), PP3, PP4).

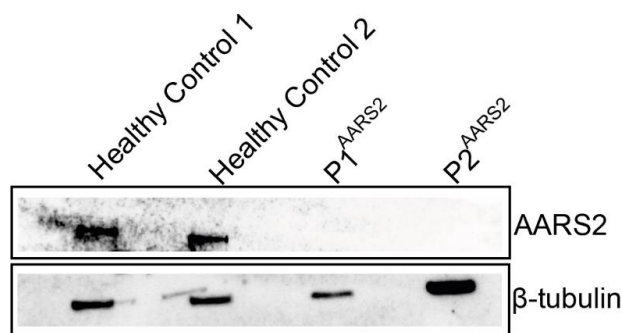


**Figure S6:** Western blot of fibroblasts of P<sup>AARS2</sup> and P2<sup>AARS2</sup> and two healthy controls. Membranes were probed with AARS2 antibody (HPA035636, Atlas) and β-tubulin (CST 2128S, Cell Signaling).

### P1<sup>KARS</sup> NM\_001130089 c.(1732\_1744delGGCATTGATC-GAG);(c.683C>T) p.(Gly578SerfsX20);p.(Pro228Leu)

The pathogenicity of the p.(Pro228Leu) has been assessed previously with functional assays.(Scheidecker et al., 2019). The Gly578SerfsX20 variant has not been reported in literature. It is expected to result in a frameshift and a premature stop codon. The frameshift might induce nonsense mediated decay or a truncated protein, affecting KARS protein function.

### Aminoacylation Activity measurements

The amino acylation activity of KARS was significantly reduced, to 52% compared to healthy controls. Therefore, the *KARS* genetic variants in these patients are considered pathogenic based on PVS1, PS3, PM4 (frameshift variant) and likely pathogenic based on PS1, PS3, PM3, PP4, PP3, PP5.

**P1<sup>WARS2</sup> NM\_015836 c.938A>T p.(Lys313Met) and c.797delC p.(Pro266Argfs\*10)**

The pathogenicity of the p.(Lys313Met) and p.(Pro266Argfs\*10) variants have been assessed previously (Wortmann et al., 2017). A patient harboring the same mutations as P1<sup>WARS2</sup> showed decreased WARS2 expression and decreased loading of mt-tRNA<sup>Trp</sup> with tryptophane (Wortmann et al., 2017). The frameshift variant is classified as pathogenic based on PVS1, PS1, PS3 while the missense variant is classified as likely pathogenic based on PS1, PS3, PM3, PP3, PP5, PP4.

## Amino Acid Treatment for ARS2 deficiencies

Amino Acid treatment			Interval
<b>Treatment</b>	Amino acid	Initiate treatment by giving two times the recommended dose of amino acid as stated in WHO guidelines.(FAO Join, 2007) Increase to three times if well tolerated. Divide the total dose over three time points (every 8 hours)	Evaluate tolerability every 6 weeks
	Protein Supplementation	Follow protein intake according to WHO guidelines. (FAO Join, 2007)	
<b>Safety parameters</b>	Laboratory	Determine creatinine, BUN, albumin, AST, ALT, $\gamma$ GT, ALP, complete blood count, plasma amino acids levels.	Every 6 months
<b>Clinical outcome parameters</b>	General	General assessment/wellbeing (history), including reaction to infections (history)	Every 3 months
	Growth	Weight, head circumference and height	Every 3 months
	Intake	Oral intake and tolerance, assess gastrointestinal complaints	Initially every 6 weeks, later every 3 months
	Development	Developmental index (using the appropriate tool for age)  Behavior (subjective, objective) and communicative skills (subjective, objective)	Every 2 years
			Every 3 months
	Cardiac function	In case cardiac dysfunction was present at baseline, monitor cardiac function.	Yearly
	Neurological	Assessment of neurological function Seizure frequency  Repeat EEG (if seizures were reported)	Every 3 months
Every 2 years			
During fever/infections	Focus on intake of cognate amino acid. Aim for intake of at least 2 g/kg/day of protein. Ensure anabolic state. Initiate antipyretic treatment (paracetamol 90mg/kg/day)		

**File S3: Treatment of P5<sup>VAR2</sup> and P6<sup>VAR2</sup>**

We treated two individuals with *VAR2* genetic variants with valine. However, since the *VAR2* genetic variants of these patients were classified as Variants of Uncertain Significance, it is uncertain whether the benefits seen after valine treatment are due to increased efficacy of *VAR2* mediated amino acylation or the result of natural disease course fluctuation or ongoing development. In this note, we describe treatment effects. Their fibroblasts were included for Seahorse and membrane potential analysis (**Figure S9**).

At the age of one month, twin brothers P5<sup>VAR2</sup> and P6<sup>VAR2</sup> were admitted to the hospital due to severe agitation, feeding difficulties and seizures. At the age of five months, their seizures and encephalopathy worsened, resulting in a palliative trajectory. In the weeks following, their symptoms stabilized spontaneously as their seizure frequency decreased. Valine treatment was initiated four months after symptom-stabilization. After valine supplementation, fenobarbital could be stopped, and the patients were less agitated, more comfortable, and made better contact with parents. However, patients did not reach any new developmental milestones, continued to show seizures - albeit decreased in frequency - and still showed severe axial hypotonia and spastic tetraparesis. Weight for height and laboratory values did not change significantly after valine initiation (**Figure S7, Figure S8**). Currently, patients have been using 53 mg/kg/day valine for over 3 years.

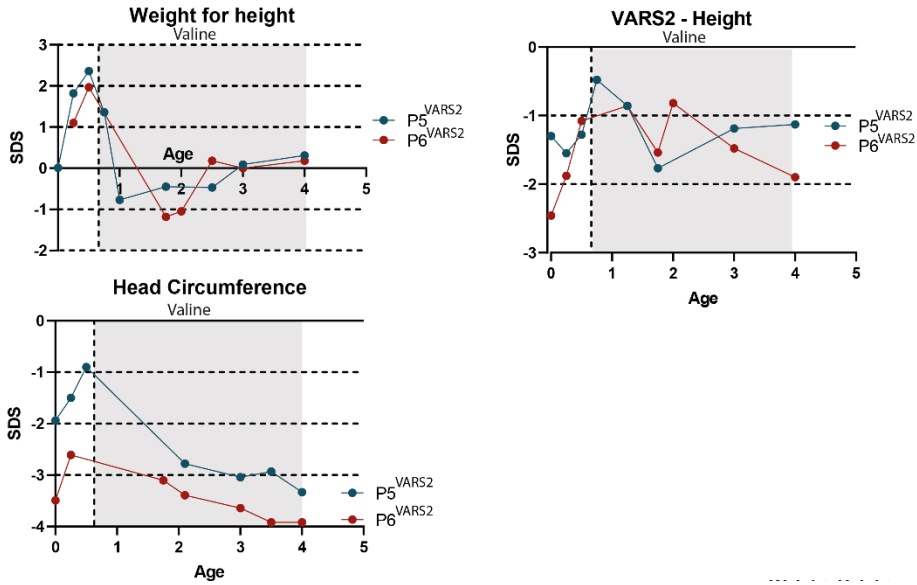


**Figure S7:** Growth values of P5<sup>VARS2</sup> and P6<sup>VARS2</sup>. Grey areas indicates the period where amino acid treatment was given. The vertical dotted lines indicate the age of treatment initiation. For P5<sup>VARS2</sup> and P6<sup>VARS2</sup> weight-for-height ratio was deviant (> 2 SDS) right before valine treatment onset, and therefore caloric restriction was started concordantly with enhanced protein intake and valine supplementation to normalize weight, explaining the weight drop at 6 months of age

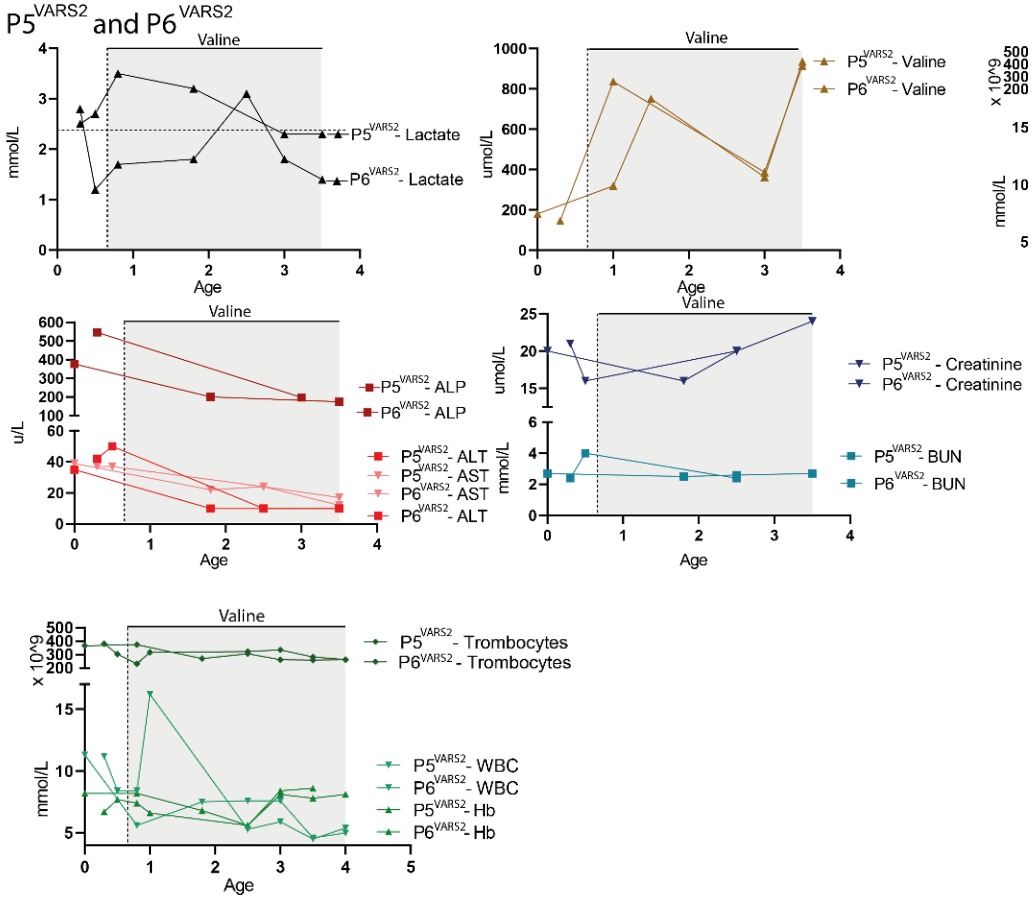


**Figure S8:** Laboratory values of P5<sup>VAR52</sup> and P6<sup>VAR52</sup> before and after valine treatment. Grey area indicates the period where amino acid treatment was given. Horizontal dotted lines indicate the upper limits of a healthy reference population. Vertical dotted lines indicate the age of treatment initiation.

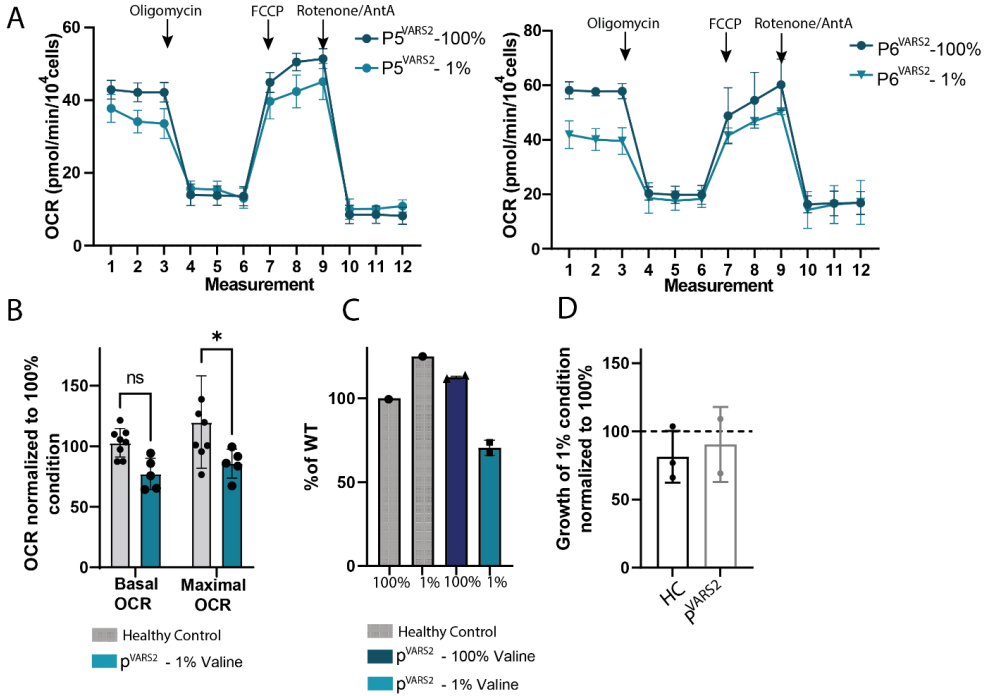


**Figure S9:** (A) Oxygen Consumption Rate (OCR; Y-axis) for each measurement (X-axis) with the injection of different compounds (Oligomycin, FCCCP, Rotenone/AntimycinA, arrows) in 100% and 1% amino acid conditions for 2 days in P5<sup>VAR2</sup> (left) and P6<sup>VAR2</sup> (right). Dots represent the mean of 3 technical replicates. Error bars represent SEM.

(B) Bar graphs showing the average basal and maximal OCR of healthy controls and P5<sup>VAR2</sup> and P6<sup>VAR2</sup>. The OCR values of the 1% condition are normalized to the 100% condition and depicted as a percentage. The bars represent the mean percentage of all donors combined  $\pm$ SD, the dots represent the mean percentage of all technical replicates per donor.

(C) Mitochondrial membrane potential during 1% and 100% conditions. In the patients, the bars represent membrane potential normalized to healthy controls treated with the same condition  $\pm$ SD. In the healthy control, the 1% condition is normalized to the 100% condition of the healthy control.



(D) Real-time-cell-analyzer results of P5<sup>VARs2</sup> and P6<sup>VARs2</sup>. Relative impedance was taken as a measure for cellular proliferation after 96 hours of culture with 5% and 100% of cognate amino acids. Bars represent mean of biological replicates  $\pm$  standard deviation (SD). Dots represent mean values of all technical replicates of individual donors.

### Bibliography

Adzhubei, I., Jordan, D. M., & Sunyaev, S. R. (2013). Predicting functional effect of human missense mutations using PolyPhen-2. *Current Protocols in Human Genetics*, SUPPL.76. <https://doi.org/10.1002/0471142905.hg0720s76>

Barbosa-Gouveia, S., Vázquez-Mosquera, M. E., González-Vioque, E., Al-varez, J. V., Chans, R., Laranjeira, F., Martins, E., Ferreira, A. C., Avila-Al-varez, A., & Couce, M. L. (2021). Utility of gene panels for the diagnosis of inborn errors of metabolism in a metabolic reference center. *Genes*, 12(8). <https://doi.org/10.3390/genes12081262>

Chin, H. L., Goh, D. L. M., Wang, F. S., Tay, S. K. H., Heng, C. K., Donni-ni, C., Baruffini, E., & Pines, O. (2019). A combination of two novel VARs2 variants causes a mitochondrial disorder associated with failure to thrive and pulmonary hypertension. *Journal of Molecular Medicine*, 97(11), 1557–1566. <https://doi.org/10.1007/s00109-019-01834-5>

FAO Join. (2007). WHO Technical Report Series Protein and Amino Acid Requirements in Human Nutrition. WHO Int, 935, 9–47.

Linnankivi, T., Neupane, N., Richter, U., Isohanni, P., & Tyynismaa, H. (2016). Splicing Defect in Mitochondrial Seryl-tRNA Synthetase Gene Causes Progressive Spastic Paresis Instead of HUPRA Syndrome. *Human Mutation*, 37(9), 884–888. <https://doi.org/10.1002/humu.23021>

Rentzsch, P., Witten, D., Cooper, G. M., Shendure, J., & Kircher, M. (2019). CADD: Predicting the deleteriousness of variants throughout the human genome. *Nucleic Acids Research*, 47(D1), D886–D894. <https://doi.org/10.1093/nar/gky1016>

Richards, S., Aziz, N., Bale, S., Bick, D., Das, S., Gastier-Foster, J., Grody, W. W., Hegde, M., Lyon, E., Spector, E., Voelkerding, K., & Rehm, H. L. (2015). Standards and guidelines for the interpretation of sequence variants: A joint consensus recommendation of the American College of Medical Genetics and Genomics and the Association for Molecular Pathology. *Genetics in Medicine*, 17(5), 405–424. <https://doi.org/10.1038/gim.2015.30>

Scheidecker, S., Bär, S., Stoetzel, C., Geoffroy, V., Lannes, B., Rinaldi, B., Fischer, F., Becker, H. D., Pelletier, V., Pagan, C., Acquaviva-Bourdain, C., Kremer, S., Mirande, M., Tranchant, C., Muller, J., Friant, S., & Dollfus, H. (2019). Mutations in KARS cause a severe neurological and neurosensory disease with optic neuropathy. *Human Mutation*, 40(10), 1826–1840. <https://doi.org/10.1002/humu.23799>

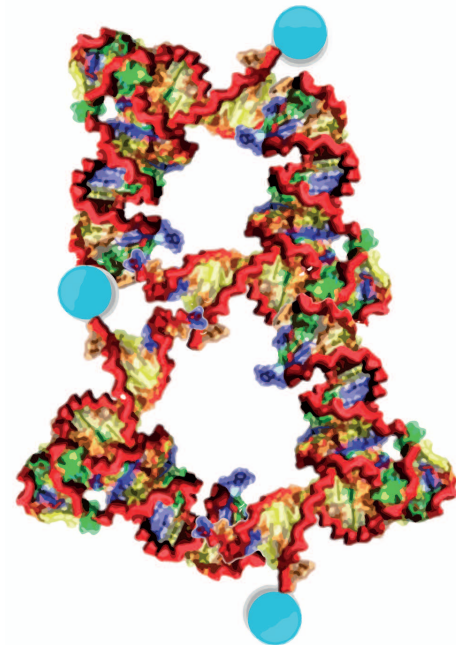
Schwarz, J. M., Rödelberger, C., Schuelke, M., & Seelow, D. (2010). MutationTaster evaluates disease-causing potential of sequence alterations. *Nature Methods*, 7(8), 575–576. <https://doi.org/10.1038/nmeth0810-575>

Steenweg, M. E., Ghezzi, D., Haack, T., Abbink, T. E. M., Martinelli, D., Van Berkel, C. G. M., Bley, A., Diogo, L., Grillo, E., Te Water Naudé, J., Strom, T. M., Bertini, E., Prokisch, H., Van Der Knaap, M. S., & Zeviani, M. (2012). Leukoencephalopathy with thalamus and brainstem involvement and high lactate “LTBL” caused by EARS2 mutations. *Brain*, 135(5), 1387–1394. <https://doi.org/10.1093/brain/aws070>

Wortmann, S. B., Timal, S., Venselaar, H., Wintjes, L. T., Kopajtich, R., Feichtinger, R. G., Onnekink, C., Mühlmeister, M., Brandt, U., Smeitink, J. A., Veltman, J. A., Sperl, W., Lefeber, D., Pruijn, G., Stojanovic, V., Freisinger, P., v Spronsen, F., Derks, T. G. J., Veenstra-Knol, H. E., ... Rodenburg, R. J. (2017). Biallelic variants in WARS2 encoding mitochondrial tryptophanyl-tRNA synthase in six individuals with mitochondrial encephalopathy. *Human Mutation*, 38(12), 1786–1795. <https://doi.org/10.1002/humu.23340>



# Chapter



**QARS1 deficiencies: unveiling mitochondrial dysfunction, impaired tRNA<sup>Gln</sup> import and therapeutic insights of glutamine supplementation.**

**QARS1 deficiencies: unveiling mitochondrial dysfunction, impaired tRNA<sup>Gln</sup> import and therapeutic insights of glutamine supplementation.**

Muffels, I.J.J.,<sup>1</sup> Siegal, L.,<sup>1</sup> Tang, Z.,<sup>2,4</sup> Vermeij, W.,<sup>2,4</sup> Jones, H.,<sup>4,5</sup> Balasubramaniam, S.,<sup>6</sup> Mohammad, S.,<sup>7</sup> Kok, G.,<sup>1</sup> Fuchs, S.A.<sup>2</sup>

<sup>1</sup> Department of Metabolic Diseases, Wilhelmina Children's Hospital, Utrecht Medical Center, Utrecht, The Netherlands.

<sup>2</sup> Prinses Maxima Center for Pediatric Oncology, Utrecht, The Netherlands.

<sup>3</sup> Oncode Institute, Utrecht, The Netherlands.

<sup>4</sup> Neurology Department, The Children's Hospital at Westmead Clinical School, Faculty of Medicine and Health, University of Sydney, New South Wales, Australia

<sup>5</sup> Starship Hospital, Centre for Brain Research, Faculty of Medical and Health Sciences, University of Auckland, New Zealand

<sup>6</sup> Metabolic Genetics Service, The Sydney Children's Hospitals Network, Westmead, NSW, Australia; Discipline of Genomic Medicine, Sydney Medical School, University of Sydney, Sydney, Australia

<sup>7</sup> TY Nelson Department of Neurology and Neurosurgery, The Children's Hospital at Westmead, Sydney, NSW, Australia; Discipline of Child and Adolescent Health, Faculty of Medicine and Health, University of Sydney, Sydney, Australia.

## Abstract

*Background:* Aminoacyl-tRNA synthetases (ARS) facilitate loading of transfer RNAs with cognate amino acids in the cytosol (ARS1), mitochondria (ARS2), or both (dual ARS). QARS1 is the only cytosolic ARS enzyme lacking a mitochondrial counterpart. Theoretically, mitochondrial thiolation of glutamine tRNA's renders them susceptible to translation errors, necessitating import of cytosolically charged tRNA<sup>Gln</sup>. It is still unclear whether QARS1 thus contributes indirectly to mitochondrial translation, and if glutamine supplementation elicits similar effects compared to other ARS deficiencies.

*Methods:* We evaluated mitochondrial function and cellular growth in QARS1-deficient patient-derived fibroblasts during various glutamine concentrations, and validated the clinical efficacy of glutamine supplementation in patients.

*Results:* We found that glutamine depletion led to significant growth deficits in QARS1-deficient patients. Additionally, fibroblasts of QARS1-deficient patients, but not of other ARS1-deficient patients and healthy controls, showed decreased mitochondrial membrane potential and decreased basal- and maximal respiratory capacity during glutamine depletion. As a potential mechanism underlying mitochondrial dysfunction, we found cytosolic tRNA<sup>Gln</sup> was imported into mitochondria in healthy controls, but this seemed to be lacking for QARS1-deficient patients. Clinically, glutamine supplementation in three QARS1-deficient patients was safe and well-tolerated. After glutamine treatment, seizures decreased or transiently stopped in most patients.

*Discussion:* Our study shows that cytosolic QARS1 deficiency is associated with mitochondrial dysfunction during glutamine depletion, potentially through decreased mitochondrial import of cytosolically loaded tRNA<sup>Gln</sup>. In patients, we found clinical improvements after glutamine supplementation.

## Introduction

Aminoacyl-tRNA synthetases (ARS) are essential for translating messenger RNA to protein by coupling amino acids to their cognate transfer RNAs (tRNAs). ARS1 enzymes perform this function in the cytosol, ARS2 enzymes in the mitochondria, and Glycyl-RS (GARS1) and Lysyl-RS (KARS1) in both. The absence of a mitochondrial Glutamyl-RS (QARS2) counterpart led to the initial categorization of QARS1 as a dual ARS. However, studies have shown QARS1 does not have a mitochondrial import sequence, nor is it present in mitochondria, and should thus be regarded a cytosolic ARS.<sup>1</sup> Instead, glutamyl mt-tRNA (mt-tRNA<sup>Gln</sup>) in mitochondria is aminoacylated by the glutamyl-tRNA<sup>Gln</sup> amidotransferase (GATC) protein complex, that transamidates Glu-mt-tRNA<sup>Gln</sup> into Gln-mt-tRNA<sup>Gln</sup>.<sup>2,3</sup> This mechanism of mitochondrial tRNA charging through transamidation is unique in its kind.

Mitochondria contain only a limited number of tRNA species compared to the cytoplasm. Despite the limited amount of tRNA species present, mitochondria do not lose the ability to decode any of their codons. This is the result of the unmodified U in the first position of the tRNA anticodon, that allows tRNA species to decode four codons, which are degenerate in the third position.<sup>4</sup> However, upon thiolation of the first anticodon nucleotide of mitochondrial tRNA<sub>UUG</sub><sup>Gln</sup>, the ability of the tRNA to interact efficiently with the glutamine codon GAG may be compromised.<sup>5</sup> Thiolation of Gln-tRNA<sup>Gln</sup> in mitochondria is facilitated by TMRU<sup>6-8</sup>, whose dysfunction leads to a severe type of mitochondrial disease (OMIM 613070).<sup>9</sup> Hypothetically, mitochondrial import of a cytoplasmic glutamine isoacceptor (tRNA<sub>CUG</sub><sup>Gln</sup>) could support protein translation when mitochondrial thiolation would occur. Recently, it was found that tRNA<sub>CUG</sub><sup>Gln</sup> is indeed imported into human and rat mitochondria, which requires both ATP and an ATPase.<sup>10</sup> However, the functional consequences of mitochondrial tRNA<sup>Gln</sup> import have remained elusive.

Additionally, the sequence of events regarding the charging and import of cytosolic tRNA<sup>Gln</sup> remains unresolved. If uncharged tRNA<sub>CUG</sub><sup>Gln</sup> would be

imported into mitochondria, it could not be charged, due to the absence of a mitochondrial QARS counterpart and the fact that tRNA<sub>CUG</sub><sup>Gln</sup> exhibits poor substrate suitability for GATC.<sup>11</sup> Alternatively, QARS1 could facilitate loading of tRNA<sub>CUG</sub><sup>Gln</sup> species in the cytoplasm prior to mitochondrial import, suggesting a direct functional role for QARS1 in supporting mitochondrial translation. While we have found beneficial effects of amino acid supplementation for cytosolic- and mitochondrial ARS deficiencies.<sup>12</sup> However, this has not yet been studied for QARS1 deficiencies. Concerns have been raised regarding glutamine supplementation, as its dual function as an excitatory neurotransmitter might worsen intractable epilepsy.<sup>13</sup>

In this work, we studied mitochondrial function in QARS1-deficient patient-derived fibroblasts exposed to normal glutamine levels and glutamine depletion. Surprisingly, we found glutamine depletion led to significant mitochondrial dysfunction in QARS1-deficient patients, but not in healthy controls nor in patients with other ARS1 mutations. We verified whether the mitochondrial involvement of QARS1 was based on mitochondrial import of tRNA<sub>CUG</sub><sup>Gln</sup>, and found high levels of tRNA<sub>CUG</sub><sup>Gln</sup> import in healthy controls, which seemed to be decreased in QARS1-deficient patients. Following up on previous work in ARS1 and ARS2 patients, we treated three QARS1-deficient patients with glutamine showing beneficial effects of treatment.

### **Materials and methods**

#### *Patient inclusion*

P1<sup>QARS1</sup> was recruited at the Wilhelmina Children's hospital in The Netherlands, and P2<sup>QARS1</sup> and P3<sup>QARS1</sup> at the Children's Hospital at Westmead in Australia. Genetic variants were identified using Whole Exome Sequencing, performed as described previously.<sup>14</sup>

#### *Amino acid supplementation*

Glutamine oral supplementation protocols, including dosing strategy, safety assessment and outcome parameters were described previously.<sup>12</sup>

#### *Fibroblast cultures*



Fibroblasts were obtained from forearm skin biopsies and cultured in Ham's F-12 supplemented with 10% Fetal Bovine Serum (FBS) and 1% penicillin-streptomycin (PS). For amino acid sensitivity experiments, amino acid free DMEM/F-12 with HEPES and NaHCO<sub>3</sub> (US Biological) was supplemented with 1% Penstrep, 1% GlutaMAX (Gibco), 10% dialyzed FBS (ThermoFisher) and different concentrations of the specific amino acids relative to physiological plasma concentrations (100%: L-glutamine 550 μmol/L, L-leucine 114 μmol/L, L-isoleucine 57 μmol/L).

### *Aminoacylation measurements*

Aminoacylation measurements were performed in fibroblast extracts as previously described.<sup>15</sup> [<sup>13</sup>C<sub>5</sub> Gln] was used as substrate, and [D<sub>3</sub>] Glu and [<sup>13</sup>C<sub>6</sub> Arg] were used as internal standard.

### *Seahorse Mitochondrial Stress Test*

Cultured fibroblasts were plated at 10,000 cells/well in Seahorse XF24 V7 Cell Culture Microplates (Agilent) and treated with the desired amino acid concentrations for 48 hours. Afterwards, cells were incubated with Seahorse XF DMEM Medium (Agilent) for 1 hour in a non-CO<sub>2</sub> incubator. Mitochondrial respiration was measured as oxygen consumption rate (OCR) using the Seahorse XFe24 Extracellular Flux Assay Kit (Mito Stress Test, Agilent) and XFe24 Seahorse Analyzer (Agilent) with 1 μM oligomycin, 1.5 μM FCCP, 1 μM Rotenone (All MedChemExpress) and 1 μM antimycinA (Sigma-Aldrich) following manufacturer's protocol with three or four technical replicates per condition.<sup>16</sup> After analysis, nuclei were stained with Hoechst 33342 (1:1000, Thermo Fisher Scientifics), visualized with Leica Thunder Live Imager (Leica Microsystem) with intensive computational clearance method, and counted using ImageJ v1.53o (NIH) for data normalization.

### *Membrane potential and mitochondrial mass/swelling*

Fibroblasts were incubated with Tetramethylrhodamine, methyl ester (TMRM, Sigma Aldrich) in Hank Balanced Salt Solution (HBSS, Gibco) for 35 minutes. To assess TMRM background, Carbonyl cyanide-p-trifluorome-

thoxyphenylhydrazone (FCCP, Sigma Aldrich) was added during the final 5 minutes in 50% of the wells. Cells were harvested using TrypLE and visualized using the Amnis Imagestream Mk II (Luminex).

### *Cell proliferation*

Cell proliferation was measured using a real-time-cell-analyzer (xCELLigence MP) as described previously.<sup>15</sup>

### *Northern Blot*

Mitochondrial RNA isolation has been described in detail elsewhere.<sup>17,18</sup> RNA was loaded on a Bis-Tris-Glycine gel, blotted on PVDF membrane and probed with biotin labeled probes at 68 degrees for 12 hours (**Table S1**). Membranes were incubated with streptavidin-HRP (GenScript) for 1 hour and visualized with Femto (BioRad).

### *Statistical analyses*

Imaging Flow Cytometry data analysis was performed using IDEAS software (version 6.2, Amnis). Seahorse data was analyzed using Agilent Wave software (version 2.6, Agilent).

Statistical analyses were performed using Prism (Version 9.3.0, GraphPad Software). P values \*P<0.05; \*\*P<0.01, \*\*\*P<0.001 were considered significant; when not indicated, comparisons were non-significant.

## **Results**

### *Glutamine deprivation causes mitochondrial dysfunction in QARS1-deficient patient-derived fibroblasts*

First, we assessed pathogenicity of *QARS1* variants using diagnostic testing. In patient-derived fibroblasts, we found significant reduction of QARS1 aminoacylation activity for all three patients compared to healthy controls (**Figure 1A**). Similar to observations in other patients with ARS1 deficiencies<sup>12</sup>, we noted significant growth reduction in two QARS1-deficient patients compared to healthy controls under glutamine deprivation (**Figure 1B**).

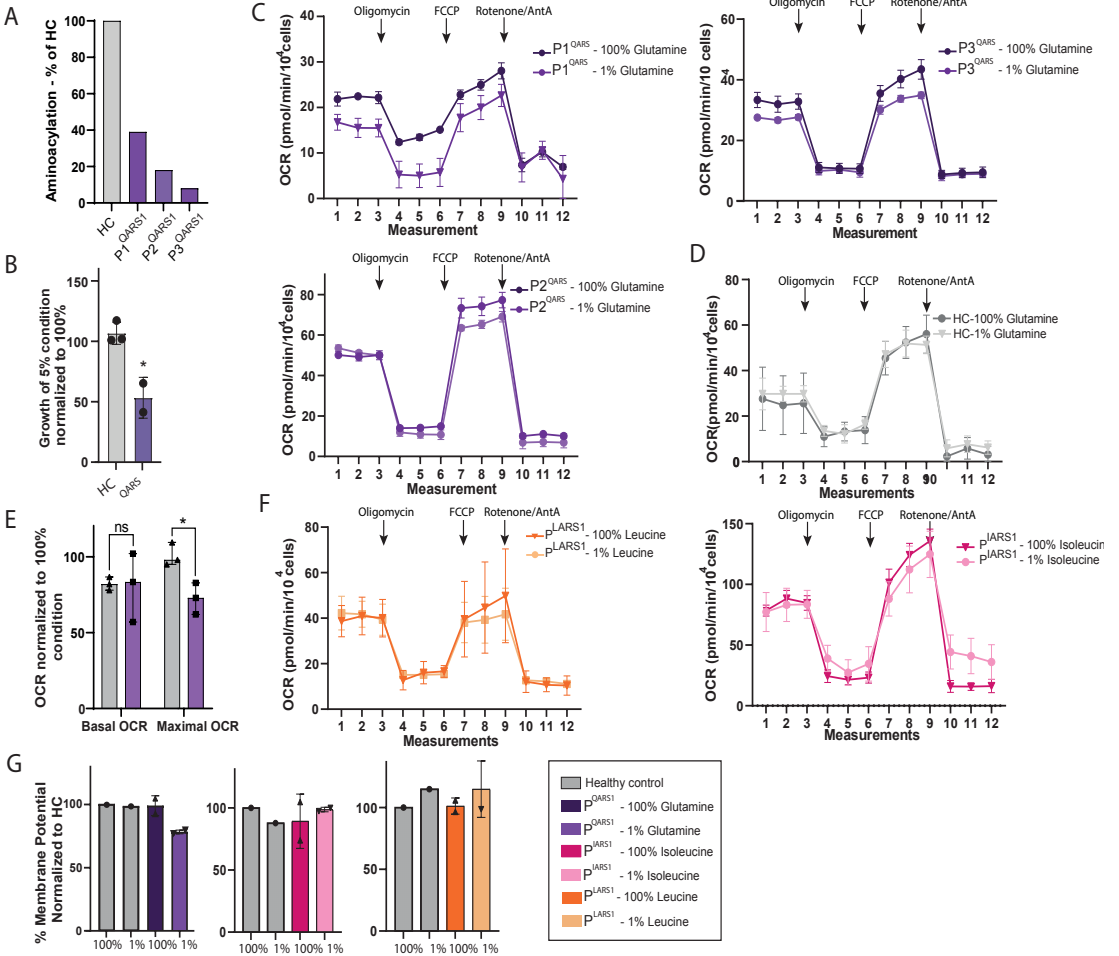


**Figure 1: Glutamine deprivation causes decreased growth and mitochondrial dysfunction in fibroblasts derived from QARS1-deficient patients.**

(A) Aminoacylation measurements performed in P1<sup>QARS1</sup>, P2<sup>QARS1</sup> and P3<sup>QARS1</sup> fibroblasts, presented as percentage compared to age matched controls, who are indicated as 100%.

(B) Real-time-cell-analyzer results of QARS1-deficient patients and healthy controls. Relative impedance was taken as a measure for cellular proliferation after 96 hours of culture with 1% and 100% of cognate amino acids. Bars represent mean of biological replicates ± standard deviation (SD). Dots represent mean values for the technical replicates of individual donors. Mann Whitney U test (p<0.05\*, p>0.05, ns).

(C) Oxygen Consumption Rate (OCR; Y-axis) for each measurement (X-axis) with the injection of different compounds (Oligomycin, FCCP, Rotenone/Antimycin A, arrows) in

QARS1-deficient patients (4 replicates each) during treatment with normal blood plasma amino acid concentrations (indicated at 100%) and amino acid deprivation conditions (indicated as 1%). QARS1-deficient patients show a significant reduction of oxygen consumption rates during deprivation (1%) conditions. Error bars represent SEM.

(D) Oxygen Consumption Rate (OCR; Y-axis) for each measurement (X-axis) with the injection of different compounds (Oligomycin, FCCP, Rotenone/Antimycin A, arrows) for one representative healthy control fibroblasts line treated with 100% glutamine and 1% glutamine for 2 days. The dots represent the average of three technical replicates. Error bars represent SEM.

(E) Bar graphs showing the average basal- and maximal OCR for healthy controls and QARS1-deficient patients. The OCR values of the 1% condition are normalized to the 100% condition and depicted as a percentage. The bars represent the mean percentage of all donors combined  $\pm$ SD, the dots represent the mean percentage of all technical replicates per donor. The bar represents the mean of all healthy donors and all conditions combined. Statistics were calculated using two-way repeated measures ANOVA.

(G) Oxygen Consumption Rate (OCR; Y-axis) for each measurement (X-axis) with the injection of different compounds (Oligomycin, FCCP, Rotenone/AntimycinA, arrows) in 100% and 1% amino acid conditions for 2 days in a patient with IARS1 and LARS1 deficiency. The dots represent the average of all three technical replicates. Error bars represent SEM.

(H) Mitochondrial membrane potential during 1% and 100% conditions. In the patients, the bars represent membrane potential normalized to healthy controls treated with the same condition  $\pm$ SD. In the healthy control, the 1% condition is normalized to the 100% condition of the healthy control.

Subsequently, we assessed mitochondrial function in QARS1-deficient patients. We found that fibroblasts of QARS1-deficient patients showed reduced basal and maximal respiration during glutamine acid deprivation (**Figure 1C,E**), which was not observed in healthy controls (**Figure 1D, E**) nor in patients with LARS1 and IARS1 deficiencies (**Figure 1F**). Additionally, fibroblasts of QARS1-deficient patients showed significantly decreased mitochondrial membrane potential during amino acid deprivation, which was not observed in healthy controls nor patients with IARS1- and LARS1 deficiency (**Figure 1G**).

*QARS1 might support mitochondrial translation through import of cytosolic glutamine-loaded tRNA<sup>Gln</sup>*

We hypothesized that the mitochondrial dysfunction observed in QARS1-deficient patients might be due to decreased mitochondrial import of cytosolic tRNA<sub>CUG</sub><sup>Gln</sup>. Therefore, we measured levels of cytosolic versus mitochondrial tRNA<sup>Gln</sup> in isolated mitochondria using northern blot. We identified cytosolic tRNA<sub>CUG</sub><sup>Gln</sup> species in isolated mitochondria of healthy control fibroblasts (**Figure 2A-D**), which seemed to be less pronounced for P1<sup>QARS</sup> and P2<sup>QARS</sup> (**Figure 2A,B, supplementary Figure 1**). However, the poor quality of the northern blots made it difficult to discern significant differences between the two groups.

*Treatment of QARS1-deficient patients with glutamine*

Both ARS1- and ARS2 deficient patients were shown to benefit from amino acid treatment.<sup>12,19</sup> However, this has not yet been tested for QARS1 deficiencies. We supplemented three QARS1-deficient patients with glutamine (**Table 1**). Glutamine was well-tolerated in moderate doses, while higher doses ( $\geq 100\text{mg/kg/day}$ ) caused itching and bruising in one patient and tiredness in another patient. All laboratory values stayed within normal range during treatment (**Figure S1**). Patients showed slightly increased glutamine levels in blood plasma during treatment (while remaining within the normal reference range). Growth remained stable for P1<sup>QARS1</sup>, improved in P2<sup>QARS1</sup>, and was not assessed for P3<sup>QARS1</sup> (**Figure S2**).

## Mitochondrial dysfunction in QARS1 deficiency

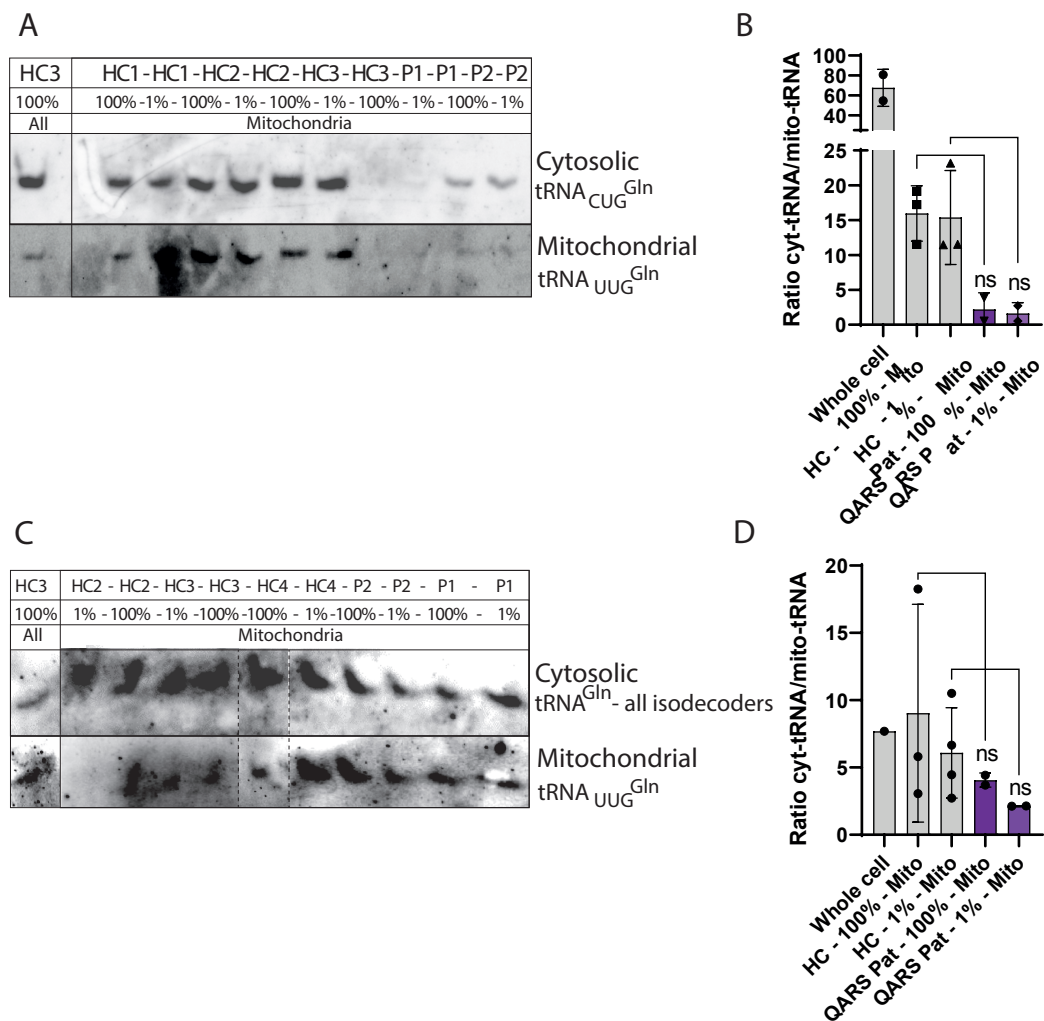


**Figure 2: Northern blot showing the mitochondrial import of cytosolic tRNA<sub>CUG</sub><sup>Gln</sup> species in healthy controls and patients.**

(A) Showing northern blot results of mitochondrial RNA in healthy controls and patient-derived fibroblasts. Fibroblasts were treated with media containing either normal or 1% glutamine concentrations for 2 days before cells were harvested and mitochondria were isolated.

(B) Quantification of the northern blot results. For normalization, the band intensity of the mitochondrially imported cytosolic tRNA<sup>Gln</sup> was normalized against the band intensity of the

mitochondrial tRNA<sub>UUG</sub><sup>Gln</sup> species.

(C) Showing the second attempt of the northern blot using the same protocol as Fig 2A/B. However, here, shorter tRNA<sub>CUG</sub><sup>Gln</sup> probes were used that bound to all isodecoders of tRNA<sub>CUG</sub><sup>Gln</sup>.

(D) Quantification of the northern blot results. For normalization, the band intensity of the mitochondrially imported cytosolic tRNA<sup>Gln</sup> was normalized against the band intensity of the mitochondrial tRNA<sub>UUG</sub><sup>Gln</sup> species.

P1<sup>QARS1</sup> presented with severe developmental delay, seizures, and daily vomiting, potentially of epileptic origin. Glutamine treatment was initiated at seven years of age, and titrated to a dose of 100 mg/kg/day. Initial titration to 100mg/kg/day led to temporary fatigue, however, these complaints resolved spontaneously. During glutamine treatment, vomiting frequency decreased to once a week, and the patient experienced his first, five-week seizure-free interval. Subsequently, seizures recurred but at a reduced frequency (from 40 to  $\pm 5$  episodes per day). Despite ongoing seizures, P1<sup>QARS1</sup> showed improved alertness, better interaction with parents, and seemed happier. Prior to glutamine treatment, infections frequently resulted in apathy, pneumonia and hospital admissions. With glutamine treatment, the severity of infections markedly diminished, since the patient did not experience pneumonia's or hospital admissions. Additionally, his constipation resolved, and he stopped using laxatives. Growth parameters remained unaffected by treatment (**Figure S2**).

P2<sup>QARS1</sup> presented at the age of seven months with focal febrile status epilepticus triggered by viral infections, delayed development, short stature, microcephaly and failure to thrive.<sup>20</sup> With carbamazepine she became seizure-free for four years. At four years and seven months of age, glutamine supplementation was initiated, which was increased every six weeks to 110mg/kg/day without side effects. Since initiation of glutamine, unaided walking improved from 5 to 1000 meters, her axial hypotonia improved, and she started to engage more with her environment, all within 6 months. At six years of age, she is not able to form words or sentences, but she has learned to express her emotions non-verbally and through vocalization. Six months

## Mitochondrial dysfunction in QARS1 deficiency

after glutamine supplementation, short focal seizures re-appeared, with a frequency of once a month, gradually increasing to once every couple of days. EEG showed occasional sharp waves but no subclinical seizures. Initiation of a ketogenic diet reduced seizure frequency again to once every two months. Since glutamine supplementation initiation, head circumference significantly improved, but height and weight remained similar (**Figure S2**).

Patient	P1 <sup>QARS1</sup>	P2 <sup>QARS1</sup>	P3 <sup>QARS1</sup>
Genetic variant	c.2084+2_2084+3del; c.793C>T p.? p.Arg265Cys	c.1132C>T; c.1574G>A p.Arg378Cys; p.Arg525Gln	c.143T>C; c.1825G>A p.Ile48Thr; p.Ala609Thr
Current age	10 years	6.5 years	6 years
Age of onset	2.5 months	7 months	3 years
Symptoms	Progressive microcephaly, refractory epilepsy developmental delay, occipital visual impairment, feeding difficulties, constipation	Microcephaly, seizures, developmental delay, feeding difficulties, failure to thrive.	Seizures, developmental delay
Treatment onset (Age)	7 years	4 years 7 months	3.5 years, stopped at 5 years 5 months of age
Dosage	100mg/kg/day	110 mg/kg/day	60mg/kg/day
Additional medication	Fenobarbital 2x50mg, Topiramaat 2x 50mg, Clonazepam, 2x 5mg,	Trileptal 56mg/kg/day	Lamotrigine 0.3mg/kg/day, Ethosuximide, Topiramate, Sodium valproate, Clobazam

**Table 1:** Overview of QARS1-deficient patients included in this study.

P3<sup>QARS1</sup> developed normally until 3 years of age, when he started to show seizures and his development plateaued. He showed generalised tonic, tonic-clonic, atypical absence and myoclonic seizures with limited response to treatment. At three years and six months of age, glutamine treatment was initiated. With 100mg/kg/day he developed bruising and itchiness, however, 60 mg/kg/day was well tolerated without any side effects. After initiation of glutamine, he became seizure free for six weeks, however, seizures reoccurred while taking glutamine, although with reduced frequency as before



treatment. Since three months, he has stopped using glutamine, without any changes in seizure frequency or overall functioning. Recently, glutamine was re-introduced again.

## Discussion

While QARS1 has been considered a purely cytosolic glutamine-coupling enzyme, we here show that QARS1 deficiency results in significant mitochondrial dysfunction during glutamine deprivation. Northern blot studies revealed that this might be due to decreased mitochondrial import of cytosolic tRNA<sup>Gln</sup> in QARS1-deficient patients, although these experiments should be repeated before definitive conclusions can be drawn. To prevent mitochondrial dysfunction and subsequent clinical deterioration, we treated QARS1-deficient patients with glutamine. Amino acid supplementation was well-tolerated and safe. Overall, glutamine supplementation resulted in some clinical improvements, especially concerning frequency of seizures and patients feeling more comfortable.

We hypothesized that QARS1 deficiency contributes to mitochondrial dysfunction due to diminished mitochondrial import of tRNA<sup>Gln</sup>. In order for this hypothesis to be true, QARS1 should play an essential role in mitochondrial import of cytosolic tRNA<sup>Gln</sup>. Presumably, mitochondria can only import charged tRNAs, and malfunctioning QARS1 leads to reduced tRNA charging and import. This concurs with results seen in yeast studies, where mitochondrial import of cytosolic tRNA<sub>CUU</sub><sup>Lys</sup> can only take place after it is charged by cytosolic KARS.<sup>21</sup> Whether human mitochondria can import charged or uncharged tRNA species has not been investigated thus far. Nevertheless, the absence of a mitochondrial protein capable of effectively charging tRNA<sub>CUG</sub><sup>Gln</sup> within mitochondria suggests the potential involvement of QARS1. Unfortunately, our experimental protocol did not allow discrimination between charged and uncharged tRNA species, and investigating the levels of charged tRNA<sub>CUG</sub><sup>Gln</sup> in mitochondria presents an intriguing avenue for future research. Alternatively, rather than charging cytosolic tRNA<sup>Gln</sup>, QARS1 could release cytosolic tRNA<sup>Gln</sup> from the ribosomal machinery,

allowing them to be imported in mitochondria. Free tRNA species are kept at low levels in mammalian cells<sup>22</sup>, and only when tRNA's are actively released from the ribosomal machinery, import into mitochondria can occur.<sup>23</sup> In yeast, pre-KARS2 has been shown to fulfill this role, allowing mitochondrial import of tRNA<sup>Lys</sup>.<sup>23</sup> In humans, QARS1 may fulfill this role, although this remains to be studied.

After the evaluation of amino acid supplementation in QARS1-deficient patients, concerns were raised regarding the safety of glutamine treatment for QARS1 deficiencies.<sup>13</sup> Glutamine is an excitatory neurotransmitter that potentially exacerbates intractable seizures. Overall, we found that seizure frequency decreased rather than increased for QARS1-deficient patients upon glutamine supplementation. There were no concerns regarding safety over the course of this study. However, given the side-effects observed, our recommendation emphasizes the gradual increment of glutamine dosages, coupled with frequent weight assessments to ensure proper adjustment of glutamine dosage. While QARS1-deficient patients showed some improvements during glutamine treatment, aggregated N-of-1 studies or randomized controlled trials are still needed to assess the efficacy of glutamine supplementation in these patients.

While the northern blot results were suggestive of decreased tRNA<sup>Gln</sup> import in patients with QARS1 deficiency, the quality of the blots was suboptimal, thereby impeding reliable interpretation of the results. The decrease in both mitochondrial and cytosolic tRNAs in fibroblasts derived from QARS1-deficient patients observed in the first northern blot shown in **Figure 2A** could have affected normalization.<sup>24</sup> The second northern blot yielded lower quality results, but nevertheless confirmed the decreased presence of cytosolic tRNA species in QARS1-deficient patients. To unambiguously demonstrate decreased cytosolic tRNA import into mitochondria in QARS1-deficient patients, and assess whether this import depends on glutamine, additional experiments are required. At the moment, our laboratory is optimizing qPCR of mitochondrial tRNA's using stem-loop primers, providing a more straightforward approach to measure levels of tRNA species. During these

experiments, treatment with micrococcal nuclease can be used to disintegrate any cytosolic tRNA species after mitochondrial isolation. Additionally, a cytosolic U6 probe should be used to formally exclude the possibility of cytosolic tRNA contamination during mitochondrial isolation.

While decreased import of cytosolically charged tRNA<sup>Gln</sup> seemed like the most straightforward explanation for the mitochondrial dysfunction seen in patients, we considered alternative causes underlying the mitochondrial dysfunction of QARS1-deficient patients. First of all, defective cytosolic translation of nuclear-encoded mitochondrial subunits due to QARS1 deficiency could have impaired mitochondrial function. However, the absence of mitochondrial dysfunction in IARS1- and LARS1-deficient patients argued against this. All mitochondrial oxidative phosphorylation complexes are built using approximately equal levels of different amino acids, and therefore it would not make sense that QARS1 deficiency specifically could result in defective nuclear translation opposed to other ARS1 deficiencies. Another explanation could be related to the essential role of glutamine in cellular metabolism. Glutamine can be converted into  $\alpha$ -ketoglutarate, which directly fuels the TCA cycle, and additionally, it is used to maintain a healthy cellular redox balance. Glutamine is one of the major nitrogen donors that facilitates the production of amino acids and nucleotides.<sup>25</sup> However, there is limited evidence available as to why QARS1-deficient patients would react more strongly to these specific glutamine-dependent injuries opposed to healthy controls or other ARS1 deficiencies. There may be a role for QARS1 in interacting with AKT1 to suppress apoptosis during low glutamine concentrations.<sup>26</sup> Pathogenic *QARS1* variants may affect the interaction with AKT1 and lead to increased apoptosis during glutamine depletion. However, we found similar levels of apoptotic cells in healthy controls and P1/P2<sup>QARS1</sup> making this hypothesis less likely. However, since novel non-canonical functions of ARSes are still being discovered, we do not exclude the possibility of other non-canonical functions of QARS1 playing a role within mitochondrial pathology. Nonetheless, the charging mechanism of tRNA<sup>Gln</sup> with glutamine in mitochondria is unique, and together with the specific mitochondrial dysfunction observed in QARS1-deficient patients, this suggest

a potential functional correlation between these two phenomena.

In conclusion, our studies show glutamine dependent QARS1 deficiency-induced mitochondrial dysfunction and illuminate some of the intricate mechanisms underlying mitochondrial dysfunction. Experimental follow-up studies could provide a more detailed understanding of how QARS1 participates in mitochondrial translation and unravel the intriguing interaction between cytosolic and mitochondrial translation, leading to a more optimized treatment strategy for QARS1-deficient patients. Based on our preliminary treatment experience, we would advise to explore the therapeutic potential of glutamine in larger patient cohorts, since it provides a safe, well tolerated and easily available therapy.

### **Acknowledgements**

The authors would like to thank Oncode for the Seahorse Equipment, and MetaKids for their Funding (grant on behalf of S.A. Fuchs).

### **Conflict of interest**

The authors declare no conflict of interest exists.

### **References**

1. Friederich MW, Timal S, Powell CA, et al. Pathogenic variants in glutamyl-tRNA<sup>Gln</sup> amidotransferase subunits cause a lethal mitochondrial cardiomyopathy disorder. *Nat Commun.* 2018;9(1). doi:10.1038/s41467-018-06250-w
2. Nagao A, Suzuki T, Katoh T, Sakaguchi Y, Suzuki T. Biogenesis of glutamyl-*mt* tRNA<sup>Gln</sup> in human mitochondria. *Proc Natl Acad Sci U S A.* 2009;106(38):16209-16214. doi:10.1073/pnas.0907602106
3. Friederich MW, Timal S, Powell CA, et al. Pathogenic variants in glutamyl-tRNA<sup>Gln</sup> amidotransferase subunits cause a lethal mitochondrial cardiomyopathy disorder. *Nat Commun.* 2018;9(1). doi:10.1038/s41467-018-06250-w
4. Heckman JE, Sarnoff J, Alzner-DeWeerd B, Yin S, RajBhandary UL. Novel features in the genetic code and codon reading patterns in *Neurospora*

- crassa mitochondria based on sequences of six mitochondrial tRNAs. *Proc Natl Acad Sci U S A*. 1980;77(6 I):3159-3163. doi:10.1073/pnas.77.6.3159
5. Agris PF, Vendeix FAP, Graham WD. tRNA's Wobble Decoding of the Genome: 40 Years of Modification. *J Mol Biol*. 2007;366(1):1-13. doi:10.1016/j.jmb.2006.11.046
  6. Zeharia A, Shaag A, Pappo O, et al. Acute Infantile Liver Failure Due to Mutations in the TRMU Gene. *Am J Hum Genet*. 2009;85(3):401-407. doi:10.1016/j.ajhg.2009.08.004
  7. Hagervall TG, Edmonds CG, McCloskey JA, Björk GR. Transfer RNA(5-methylaminomethyl-2-thiouridine)-methyltransferase from *Escherichia coli* K-12 has two enzymatic activities. *Journal of Biological Chemistry*. 1987;262(18):8488-8495. doi:10.1016/s0021-9258(18)47440-6
  8. Guan MX, Yan Q, Li X, et al. Mutation in TRMU related to transfer RNA modification modulates the phenotypic expression of the deafness-associated mitochondrial 12S ribosomal RNA mutations. *Am J Hum Genet*. 2006;79(2):291-302. doi:10.1086/506389
  9. Vogel GF, Mozer-Glassberg Y, Landau YE, et al. Genotypic and phenotypic spectrum of infantile liver failure due to pathogenic TRMU variants. *Genetics in Medicine*. 2023;25(6):100828. doi:10.1016/j.gim.2023.100828
  10. Rubio MAT, Rinehart JJ, Krett B, et al. Mammalian mitochondria have the innate ability to import tRNAs by a mechanism distinct from protein import. *Proc Natl Acad Sci U S A*. 2008;105(27):9186-9191. doi:10.1073/pnas.0804283105
  11. Nagao A, Suzuki T, Katoh T, Sakaguchi Y, Suzuki T. Biogenesis of glutaminyl-mt tRNA<sup>Gln</sup> in human mitochondria. *Proc Natl Acad Sci U S A*. 2009;106(38):16209-16214. doi:10.1073/pnas.0907602106
  12. Kok G, Tseng L, Schene IF, et al. Treatment of ARS deficiencies with specific amino acids. *Genetics in Medicine*. Published online 2021. doi:10.1038/s41436-021-01249-z
  13. Shen YW. Correspondence on "Treatment of ARS deficiencies with specific amino acids" by Kok et al. *Genetics in Medicine*. 2022;24(2):503-505. doi:10.1016/j.gim.2021.10.001
  14. Muffels IJJ, Wiame E, Fuchs SA, et al. NAA80 bi-allelic missense variants result in high-frequency hearing loss, muscle weakness and de-

- velopmental delay. *Brain Commun.* 2021;3(4). doi:10.1093/braincomms/fcab256
15. Kok G, Tseng L, Schene IF, et al. Treatment of ARS deficiencies with specific amino acids. *Genetics in Medicine*. Published online 2021. doi:10.1038/s41436-021-01249-z
  16. Milanese C, Bombardieri CR, Sepe S, et al. DNA damage and transcription stress cause ATP-mediated redesign of metabolism and potentiation of anti-oxidant buffering. *Nat Commun.* 2019;10(1). doi:10.1038/s41467-019-12640-5
  17. Preble JM, Kondo H, Mc Cully JD, Pacak CA, Mackay AA, Cowan DB. Rapid isolation and purification of mitochondria for transplantation by tissue dissociation and differential filtration. *Journal of Visualized Experiments.* 2014;(91). doi:10.3791/51682
  18. Huang J, Wang G. Improved Mammalian Mitochondrial RNA Isolation. *Bio Protocol*. Published online 2019.
  19. Oswald S, Steinbruecker K, Achleitner M, et al. Treatment of Mitochondrial Phenylalanyl-Trna-Synthetase Deficiency (Fars2) With Oral Phenylalanine. *Neuropediatrics*. Published online 2023. doi:10.1055/a-2008-4230
  20. Chan DL, Rudinger-Thirion J, Frugier M, et al. A case of QARS1 associated epileptic encephalopathy and review of epilepsy in aminoacyl-tRNA synthetase disorders. *Brain Dev.* 2022;44(2):142-147. doi:10.1016/j.braindev.2021.10.009
  21. Tarassov I, Entelis N, Martin RP. Mitochondrial import of a cytoplasmic lysine-tRNA in yeast is mediated by cooperation of cytoplasmic and mitochondrial lysyl-tRNA synthetases. *EMBO J.* 1995;14(14):3461-3471. doi:10.1002/j.1460-2075.1995.tb07352.x
  22. Negrutskii BS, Deutscher MP. Channeling of aminoacyl-tRNA for protein synthesis in vivo. *Proc Natl Acad Sci U S A.* 1991;88(11):4991-4995. doi:10.1073/pnas.88.11.4991
  23. Gowher A, Smirnov A, Tarassov I, Entelis N. Induced tRNA Import into Human Mitochondria: Implication of a Host Aminoacyl-tRNA-Synthetase. *PLoS One.* 2013;8(6). doi:10.1371/journal.pone.0066228
  24. Honda S, Shigematsu M, Morichika K, Telonis AG, Kirino Y.

Four-leaf clover qRT-PCR: A convenient method for selective quantification of mature tRNA. *RNA Biol.* 2015;12(5):501-508. doi:10.1080/15476286.2015.1031951

25. Yoo HC, Yu YC, Sung Y, Han JM. Glutamine reliance in cell metabolism. *Exp Mol Med.* 2020;52(9):1496-1516. doi:10.1038/s12276-020-00504-8

26. Ko YG, Kim EK, Kim T, et al. Glutamine-dependent Antiapoptotic Interaction of Human GlutaminyI-tRNA Synthetase with Apoptosis Signal-regulating Kinase 1. *Journal of Biological Chemistry.* 2001;276(8):6030-6036. doi:10.1074/jbc.M006189200

## Supplementary Files and Figures

**Supplementary Table 1:**

<b>Probe</b>	<b>DNA Sequence</b>
Cytosolic-tRNA-Gln-CTG All Isodecoders	Biotin-CCAGAGTGCTAACCATTACACCATGGG
Cytosolic-tRNA-Gln-CTG	Biotin-TTCCTGACCGGGAATCGAACCCGGGCCGCGGCGG TGAGAGCGCCGAATCCTaACCACTAGACCACCAGGGA
Mitochondrial-tRNA-Gln-TTG All Isodecoders	Biotin-GGATTCAGAGTCCAGAGTGCT
Mitochondrial-tRNA-Gln-TTG	Biotin-AGGTCCCACCGAGATTCGAACTCGGATTGCTGGA TTCAAAGTCCAGAGTGCTaACCATTACACCATGGGACC

**Table 1:** Probes used to perform northern blot in Figure 2.



**Supplementary Figure S1: Laboratory Values before and after amino acid treatment.**

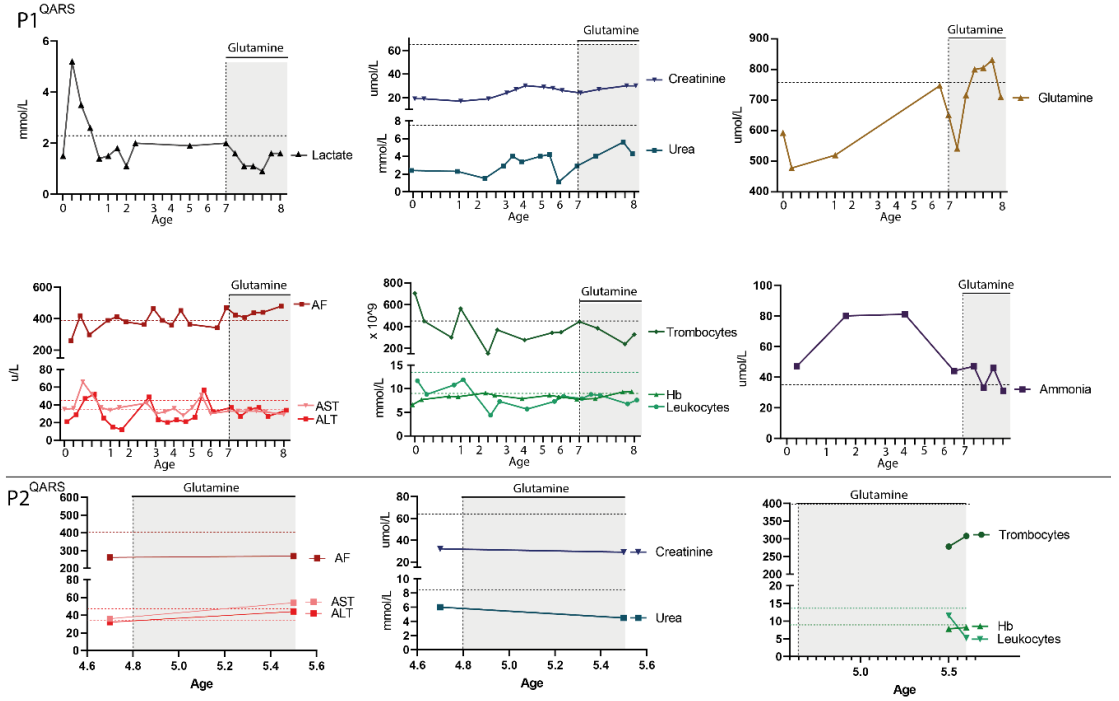


**Figure S1:** Laboratory values of P1<sup>QARS1</sup> and P2<sup>QARS1</sup> before and after glutamine supplementation. Grey areas indicate the period where amino acid treatment was given. The dotted horizontal lines indicate normal values in the reference population. The vertical dotted lines indicate the age of treatment initiation.

**Supplementary Figure S2: Growth Values before and after amino acid treatment.**

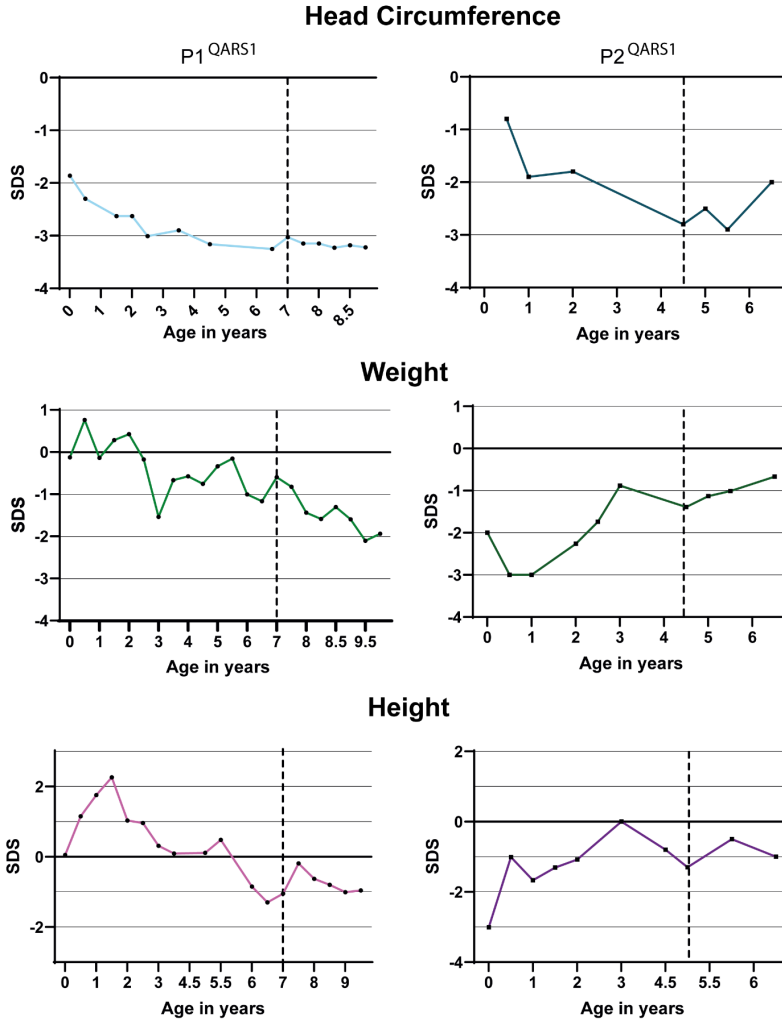
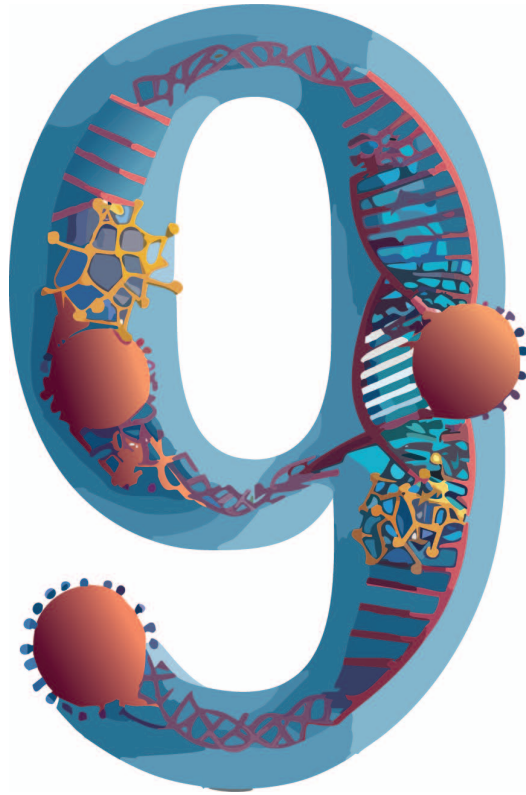


**Figure S2:** Growth parameters of QARS1-deficient patients (P1<sup>QARS1</sup>, P2<sup>QARS1</sup>) before and after glutamine treatment. The vertical dotted lines indicate the age of treatment initiation. Growth values are shown as SDS compared to the healthy Dutch reference population (TNO) for P1<sup>QARS1</sup> or the Australian reference population (P2<sup>QARS1</sup>).



# Chapter



# General Discussion

## General Discussion

### *Context in a field with many unknowns*

‘How do you plan to solve a puzzle where so many of the pieces are missing?’ asked one of the metabolic fellows, when I explained the work I aimed to do during my PhD. My strategy of solving VUS cases by looking at cellular mechanisms in patient-derived cells, turned out to be a much more complex endeavor than I ever imagined. By using context, I aimed to collect relevant information in a scientific field with many unknowns. This discussion is structured in three parts, that follow the subdivision of this thesis. The first paragraphs are focused on solving individual VUS cases, the second part focuses on the usefulness of functional screening for individuals with VUS, and the final part focuses on this functional screening to elucidate disease mechanisms in patients with genetic diseases.

### **How should VUS cases be solved?**

Many novel diseases have been discovered over the recent years: while the number of studies describing novel disease genes was only 175 per year in 2003, it expanded to almost 1200 studies in 2013.<sup>1</sup> Characteristic of VUS cases is their high reporting variability. While some reports focus solely on clinical presentation within patient cohorts, others undertake extensive functional characterizations of patient-derived cells or model organisms. The broad spectrum of approaches reflects the diverse methodologies employed to unravel the mysteries of VUS.

### *The appreciation of rare and shared phenotypic features*

The prevailing approach of solving VUS cases typically involves examining large patient cohorts with similar phenotypes. While larger numbers indeed diminish the chance of attributing significance to accidental genetic findings, there are some inherent limitations to this view. Notably, looking for similar phenotypes disregards the fact that genetic variants may exert various (pleiotropic) effects on protein function. Different protein domains

can exert different functions, which is actually quite common, as one in five genes is considered pleiotropic.<sup>2</sup> Therefore, pathogenic variants affecting different domains can result in different phenotypes, even though these variants are located within the same gene. If we had applied the traditional view of “One gene, one Phenotype” to individuals with *LIMK1* variants, we might have disregarded the possibility that both variants were pathogenic. Only through a nuanced understanding of LIMK1’s pathway dynamics and domain interactions could we recognize the full spectrum of potential phenotypic manifestations associated with *LIMK1* variants. Thus, when appreciating the clinical and functional phenotypes of specific genetic variants, the researcher should always take the location within its respective protein domain into account to establish significance.

As stated earlier, most researchers seek for shared phenotypes when solving VUS cases. During this process, phenotypic prevalence is usually not taken into account. The prevalence of phenotypic features in genetic diseases differs largely, illustrated by developmental delay which is associated with 2407 different genetic diseases, while pancreatic dysfunction is eight times as rare.<sup>3</sup> Statistically, it would make sense that rare features shared by all members in the cohort are attributed more value than common features. Additionally, the likelihood of a shared pathophysiological basis increases proportionally with each phenotypic feature that overlaps within a given cohort. Therefore, researchers should always strive to describe the phenotype of novel diseases as exhaustively as possible, to allow extraction of these rare features. Additionally, researchers can prioritize the phenotypes that need to be studied by leveraging both the rareness and prevalence within the patient cohort using occurrence ratios.<sup>4</sup> Rare and shared features not only enhance the statistical significance of novel diseases, they also better reflect the pathophysiology at stake.<sup>4</sup> While common phenotypic features can be due to many pathophysiological mechanisms, extremely rare or pathognomonic features usually characterize very specific and unique parts of pathophysiology. In this thesis, the power of rare features was exemplified by the patients with *NAE1* variants. Initially overlooking delayed endochondral bone development and periodic lymphopenia as key phenotypes, phenotypic

prioritization revealed its rarity and its universal presence within the cohort. These rare features proved instrumental in framing the interpretation of our RNA sequencing results, highlighting the relevance of incorporating such nuances in phenotypic characterization. Additionally, leveraging these rare, but prevalent features, helped us to delineate the main pathophysiological mechanisms of NAE1-deficient patients.

### *The value of mechanistic insights when solving VUS cases*

In the exploration of novel diseases, the emphasis on clinical case descriptions often takes precedence. Research groups addressing VUS cases, typically rooted in clinical settings, frequently lack the infrastructure to perform extensive mechanistic investigations. Consequently, many novel monogenetic diseases remain mechanistically under-explored, representing a missed opportunity for the field, as ‘Human Allelic Knockouts’ are considered unique models to attribute significance to genes whose function has remained largely elusive. Since most genes involved in monogenetic disorders also contribute to the pathophysiology of polygenetic diseases, these insights can be crucial to discover disease mechanisms for other, more common, disorders. One example involves the identification of pathogenic *PARK2* variants, attributed to early-onset Parkinson’s disease.<sup>5</sup> Patients and patient-derived cells with *PARK2* variants have been intensively studied to comprehend the general mechanisms behind Parkinson’s disease, a lethal and yet incurable disease. These insights could be used to develop cellular- or animal models, that contribute to the development of novel treatment targets. Thus, we advocate that studies describing novel disease genes can be optimized by simultaneously assessing underlying pathophysiological mechanisms in patient-derived cells or cellular models. In this thesis, we tried to provide a pathophysiological context for all VUS cases presented. Our approach shows that even without extensive mechanistic studies, certain insights into underlying pathophysiological mechanisms can still be generated. Comparing phenotypes to well-known diseases, prioritizing phenotypes based on rareness, and studying pathway dynamics to explain divergent phenotypes, were crucial in this regard.

*Characterization of primary and secondary disease mechanisms facilitates diagnosis and treatment for individuals with VUS*

Patient-derived cells of patients with monogenetic diseases usually show functional consequences beyond their primary disease pathophysiology. Some of these responses involve compensatory mechanisms, that allow patients to cope with their primary injury. For example, cellular models with pathogenic variants in *CFTR* have revealed a compensatory upregulation of alternative ion channels to maintain ion balance and fluid secretion.<sup>6</sup> The IFC-based screening performed in chapter 4 revealed that almost all well-known genetic diseases and individuals with VUS exhibit multiple functional changes in their cells, some of which reflect compensatory mechanisms in response to primary injury. For example, mitochondrial disease patients exhibited increased autophagy, facilitating increased mitophagy, allowing for the degradation of defective mitochondria. Additionally, autophagy facilitates recycling of amino acids, which can be utilized to produce new respiratory chain proteins that are subject to rapid turnover caused by pathogenic variants.<sup>7</sup>

For many genetic diseases, compensatory mechanisms are thought to be pivotal for disease progression and pathophysiology. In fact, for some diseases, compensatory mechanisms are thought to be even more detrimental than the primary genetic injury itself. Thus, it is essential to characterize both primary and secondary mechanisms in genetic disease to allow effective characterization of disease pathophysiology and to identify relevant treatment targets. Not only can these compensatory mechanisms serve as means to diagnose or recognize diseases in patient-derived cells, they also help to better recognize and cluster genetic diseases, based on our results in chapter 4 and 5. We advocate that extensive mechanistic characterization, including the characterization of compensatory mechanisms, is essential for solving VUS cases and understanding genetic diseases. The use of broad cellular screening tools, such as IFC-based screening, microscopy, or untargeted OMICS approaches, can be useful in this regard.



### *Functional interpretation at the basis of solving VUS cases*

In the current era, where genome sequencing combined with large-scale OMICS approaches allows fast recognition of straightforward VUS cases, most unsolved VUS cases are characterized by inherent complexity. These examples include VUSes situated within genes not associated with disease or in genes with unknown functions, or instances where patients harbor multiple VUSes. While functional studies are crucial to solve these cases, it seems almost impossible to design a cellular read-out without any prior knowledge about the function of a gene. Having a valid starting point – knowing where to look – might thus be the most challenging step in disease elucidation. While untargeted OMICS techniques have been brought forward as hypothesis-generating approaches, that can provide such a starting point, they also come with their own well-known limitations. The interpretation of these large datasets without prior knowledge about underlying pathophysiology is notoriously complex. Moreover, OMICS are expensive and time-consuming. Finally, the results generated with OMICS still require functional validation, and again, without sufficient knowledge, designing these functional studies, validating OMICS results, is incredibly difficult. Alternative to - or complementary to - OMICS, we felt that a rapid, straightforward functional assessment of overall cellular health could help. Chapter 4 is the result of this line of thought, where we used Imaging Flow Cytometry (IFC) to rapidly assess cellular function in a large number of cells, in a straightforward manner.

### *IFC-based screening – lessons learned*

In the end, the IFC-project established in Chapter 4 allowed us to screen many patients with known- and unknown genetic diseases. While we found IFC-based functional screening was indeed useful to provide so-called “Starting points” (that will be discussed in the next paragraphs), the project taught us two additional – somewhat surprising - lessons.

Unexpectedly, the combination of functional aberrancies rather than single assays was essential to delineate clear-cut, disease-specific profiles. Several pathways contributed to this clear separation, for example, increased versus decreased NF- $\kappa$ B translocation helped to discriminate patients with pathogenic *DRP1* variants from patients with pathogenic *TAZ* variants. Since both of

these variants are primarily associated with mitochondrial dysfunction, thus showing similar mitochondrial aberrancies, NF- $\kappa$ B was significantly different between the groups and helped to recognize these diseases as separate entities.

The second lesson learned was that some well-known genetic diseases were recognized through aberrancies that were not considered known parts of pathophysiology at first instance. For example, we did not expect that mitochondrial disorders associated with pathogenic *ACAD9* variants showed very mild mitochondrial aberrancies, but were recognized through a unique combination of increased ER stress and severe Golgi fragmentation. Thus, these insights underscore the importance of a broad functional assessment, focused on both primary and secondary aberrancies, to allow faster recognition of specific phenotypes that suggest disease pathologies in individuals with VUS.

*The potential of IFC-based screening for individuals with VUS in well-known disease genes*

For individuals with VUS that were compared to patients with pathogenic variants, the overlap in cellular phenotypes identified with IFC-based screening helped to accurately predict pathogenicity. Subsequent application of well-established functional assays validated the high accuracy of IFC-based screening for all individuals. Only one out of seven individuals harboring *EPG5* VUSes was clustered with healthy controls, due to its mild cellular phenotype. This correlated with functional assay results, showing very mild induction of autophagy on western blot. Similarly, a mild and somewhat aspecific clinical phenotype was observed in this individual. Together, these results raise the suspicion that either the *EPG5* VUS leads to a very mild disruption of *EPG5* function, or is of benign nature. This mildness was reflected in IFC-based assays.

One could argue why IFC-based screening is needed for individuals with VUSes in well-known disease genes when functional assays were available. We propose two key rationales for broad screening for individuals with

VUS in well-known genes, even when functional assays are available. First of all, IFC-based assays circumvent the need for expert-craft, expensive and time-consuming functional assays. To perform functional assays for all of the seven individuals with VUS in well-known disease genes included in Chapter 4, we had to reach out to three different academic centers and consult several different experts. In contrast, IFC-based screening comprises of one single assay, and does not require any expert knowledge about the pathway of interest.

Second, IFC-based screening is augmented by the incorporation of novel phenotypic profiles derived from well-established genetic diseases. In contrast, performing only highly-targeted and specific functional assays, does not help recognition of novel genetic diseases that lack these functional assays. In other words, the inclusion of a broader array of well-known genetic diseases allows for the comparative analysis of unknown diseases, enabling their recognition through shared pathophysiological characteristics. Precise and specific assays for isolated disease entities may eventually come at the expense of recognizing and understanding novel, unknown diseases through broad functional assays.

*The potential of IFC-based screening for individuals with VUS in GUS*

To highlight the potential of IFC-based screening for individuals with VUS in Genes Of Uncertain Significance and the importance of adding positive control patients, we here highlight two of the clusters identified in Chapter 4.

The first cluster included the two individuals with *LIMK1* VUS described in Chapter 3. Surprisingly, the opposite effect that these VUSes imposed on LIMK1 activity was not recapitulated in IFC assays. Instead, we identified similar levels of lysosomal accumulation and ER stress for both individuals. The most striking shared phenotype for these individuals was revealed when looking at all 1800 features, where we found a significantly increased number of cells in S/M phase compared to all other patients (N=20) and healthy controls (N=8). Earlier work has shown that both decreased LIMK1 activity

as well as increased LIMK1 activity can cause a delay in anaphase onset and misorientation of the mitotic spindle.<sup>8</sup> Therefore, the results identified with IFC-based screening correlate with either increased or decreased LIMK1 activity. Mechanistic exploration of mitotic defects in individuals with *LIMK1* VUS could have been an alternative strategy to elucidate disease pathophysiology, that eventually might have led to the same discovery of altered cytoskeletal dynamics associated with LIMK1 dysfunction as shown in Chapter 3.

The second cluster identified involved two individuals with VUS in *GUS*, alongside a patient harboring pathogenic variants in *ERCC1*. Within this cluster, one individual exhibited heterozygosity for a pathogenic *BLM* variant, accompanied by VUSes in *TNKS* and *DLGAP2*. The other individual harbored a VUS in *RAD54L2*. *ERCC1* participates in Nucleotide Excision Repair (NER) and the rectification of harmful double-strand DNA breaks.<sup>9-10</sup> *RAD54L2* has not been associated with any genetic disease, but is acknowledged for promoting genome stability and contributing to effective DNA damage repair.<sup>11</sup> *BLM* variants lead to defective repair of double-strand DNA breaks in an homozygous state, but heterozygous carriers already exhibit mildly deficient DNA damage repair.<sup>12</sup> Alternatively, the *TNKS* or *DLGAP2* VUSes identified in this individual could have driven the clustering of this individual with other DNA-damage-like patients. The DNA-damage-like cluster was functionally characterized by mild mitochondrial dysfunction and altered Golgi morphology. Both of these manifestations have been previously associated with *ERCC1* dysfunction.<sup>13,14</sup>

Using additional functional studies, we found individual 211 included in the DNA-damage-like cluster was found to have slower recovery of RNA synthesis after DNA damaging agents, and slightly decreased overall transcription levels, indicative of dysfunction of the Nucleotide Excision Repair pathway (NER), the pathway primary affected in patients with pathogenic *ERCC1* variants. Additionally, we found decreased survival in fibroblasts with *RAD54L2* VUS after chemotherapeutic treatment and slightly decreased transcription levels overall. Collectively, these findings suggest that the

clustering of the patient with a pathogenic *ERCC1* variant and individuals with VUS is most likely linked to defective DNA damage repair, resulting in transcriptional stress and subsequent metabolic rewiring, giving rise to the mild metabolic dysfunction. Thus, IFC-based screening holds the potential to identify the phenotypic fingerprint associated with DNA damage repair defects, allowing for faster discovery of underlying pathophysiology in individuals with VUS in GUS.

Overall, IFC-based cellular screening helped to identify aberrancies in one or more pathways for all individuals with VUS in GUS. While we hypothesized that these aberrancies could be used as a stepping stone to structure follow-up experiments, we were not able to verify this hypothesis for 8 individuals with VUS in GUS in our study. The fact that these individuals had VUSes in genes with unknown functionality, together with the lack of relevant overlap with positive control patients, impaired effective structuring of relevant follow-up assays within the limited timeframe we still had. For these individuals, in-depth exploration of the specific aberrancies with additional methods, for example performing Seahorse assays and SDS-PAGE in patients where mitochondrial function was observed, their pathophysiological mechanisms might have been elucidated. Although we feel that starting such an experimental trajectory would be more efficient when using the IFC-screening results opposed to starting from scratch, it would still be a time-consuming process. We foresee that the addition of novel positive controls is crucial to allow more rapid interpretation of pathophysiology in the future. The IFC-based screening should therefore be seen as an iterative process, that will generate more relevant data with each novel patient included. For now, it will remain uncertain whether the IFC aberrancies identified for these eight individuals with VUS in GUS were truly reflective of relevant disease pathophysiology.

Despite its limitations, we can conclude that IFC-based screening for individuals with VUS is a valuable addition to currently available methods. Especially when individuals with VUS were directly compared to patients with well-known pathogenic variants, IFC-based assays demonstrated the capaci-

ty to discern pertinent phenotypic commonalities indicative of pathogenicity. Unfortunately, the diagnostic accuracy of our approach for individuals with VUS in GUS could only be determined for a subset of individuals where functional follow-up studies were performed. However, most VUS cases have also been included in the ZOEMBA trial, that assesses the use of metabolomics, transcriptomics, proteomics and whole genome sequencing to establish diagnosis in individuals with VUS. This dual inclusion represents a unique opportunity to directly compare IFC assay results with OMICS data, allowing the exploration of complementarity for these two approaches in the future. Additionally, it could aid the interpretation of the diagnostic accuracy of the IFC-based screening for individuals with VUS in GUS.

*Functional cellular screening at the basis of understanding known genetic diseases*

In the previous section, we emphasized the importance of a multifaceted functional screening approach to solve VUS cases. However, the results obtained in Chapter 4 led us to believe that IFC-based functional assays could be useful for all types of genetic diseases, including well-known diseases. In Chapter 5, we explored the potential of IFC-based assays for patients with mitochondrial diseases, given the gaps in knowledge surrounding the relationship between clinical phenotype, cellular phenotype, and genetic background in these patients.

To this aim, we screened 31 patients with nine different subtypes of mitochondrial disease using IFC. Rather than employing the same six assays as chapter 4, we focused on the mitochondrial assay alone and expanded this double assay to five assays that collectively characterized the most important aspects of mitochondrial functionalities. While genetic diseases are typically functionally categorized based on disease subtype or affected genes, IFC-based screening failed to reveal distinct patterns correlating with mitochondrial disease subtypes or genes. This aligns with prior research demonstrating divergent cellular phenotypes, even among patients sharing the same mitochondrial disease subtype or genetic variant.<sup>15,16</sup> Instead, IFC identified two clusters that transcended disease subtypes, showing similar

responses to primary mitochondrial injury. Roughly, these two clusters suggested that patient-derived cells could either show a hypo- or hypermetabolic response to mitochondrial pathology. The first cluster was characterized by low-to-normal membrane potential and enhanced ROS production, while the second cluster showed increased membrane potential, mitochondrial mass and mitochondrial swelling. Literature review suggested that IFC-based clustering could be attributed to shared underlying deficits, associated with either an independently operating N module or defective proton pumping activity.

To unequivocally evaluate the efficacy of our mitochondrial IFC-approach, it is imperative to conduct additional experiments. Primarily, assessing the accumulation of complex I assembly intermediates, especially the individually operating N module, could help distinguish whether the clustering of mitochondrial disease patients was indeed based on this functional characteristic. Additionally, measuring mitochondrial oxygen consumption using seahorse respirometry in patients could indicate whether the increased membrane potential, mitochondrial mass and swelling indeed reflect an overall hypermetabolic state. Completion of these experiments will provide another line of evidence supporting the notion that mitochondrial diseases may be more accurately categorized according to functional deficits rather than relying solely on subtype- or gene-specific characterization.

Mitochondrial diseases have long been challenged by the absence of effective therapies and diagnostic tools. In our opinion, diagnostic tools and therapeutics might only be applicable to a specific functional subgroup of mitochondrial disease. For example, therapeutics increasing oxidative phosphorylation or membrane potential are probably not feasible for patients that already experience a hypermetabolic state. Therefore, we believe that the proposed novel approach of functional-based categorization for mitochondrial diseases carries substantial implications for diagnosis, therapy allocation, and disease stratification for patients with mitochondrial disease, if developed further.

The penultimate chapter of this booklet was focused on therapy development rather than diagnosis of genetic diseases. Nevertheless, functional characterization of patient-derived cells played an important role. While this chapter was initially focused on translating a therapy developed for cytosolic ARS1 deficiencies to mitochondrial ARS2 deficiencies, the limited insights into disease mechanisms of ARS2 deficiencies made it challenging to predict what we could expect from treatment. Additionally, we were not sure whether supplemented amino acids would go to the mitochondria to aid mitochondrial translation. However, our functional studies in patient-derived cells made it clear that amino acid depletion resulted in striking mitochondrial dysfunction in ARS2 deficiencies. Since mitochondrial dysfunction in neurons is thought to be at the basis of severe neurological pathologies, such as Alzheimer's disease<sup>17:19</sup>, and Parkinson's disease<sup>20</sup>, we hypothesized that mitochondrial damage caused by local depletion of amino acids could similarly be at the basis of irreversible neurological damage. Based on these findings, we expected that the irreversible neurological damage should be prevented and might not be completely reverted by treatment. Indeed, we found certain neurological signs, such as spasticity, could only be stabilized and not reversed. In support, discontinuation of treatment in one patient with pathogenic *EARS2* variants resulted in severe neurological regression. Armed with this knowledge, we optimized our treatment strategy, aiming to treat patients at an early stage.

Similar to many mitochondrial diseases, ARS2 deficiencies encompass a highly heterogeneous group of disorders, impacting organs such as the heart, brain, muscle, or retina. The heterogeneous clinical phenotype made it challenging to unambiguously discern amino acid treatment effects. Overall, treatment effects were most pronounced for cardiac function and development, while the effects of treatment on retinal function and spasticity/dystonia were limited. This could be related to the reversibility of damage – as proposed in the previous paragraph. However, the age where treatment was initiated or organ-specific differences in the availability of amino acids for mitochondrial translation could have played a role. Recent work has shown that differences in clinical phenotype in AARS2-, RARS2- and EARS2- de-



ficient patients may be attributed to different compensatory mechanisms that are activated through the integrated stress response.<sup>21</sup> To elucidate how and why distinct clinical phenotypes respond differentially to treatment, a comprehensive assessment of the effects of amino acid depletion and supplementation in various cell types, including neurons, cardiac cells, and retinal cells, might be warranted.

Amino acid treatment in ARS2 deficiencies represents a readily available, cheap and effective strategy to treat a severe form of mitochondrial disease. Additionally, the mitochondrial dysfunction upon cognate amino acid depletion was highly specific, and has the potential to be converted into a diagnostic assay for a group of diseases currently lacking any kind of diagnostic assays.

However, to formally assess treatment effects in ARS2-deficient patients, N-of-1 studies and preset outcome measures are still needed. The potential effectiveness of N-of-1 studies was recapitulated in the EARS2- and VARS2-deficient patients in our cohort, that showed significant neurological-, developmental- or cardiac regression after discontinuation of amino acid supplementation. However, when setting up these N-of-1 studies, we should consider whether abrogating treatment in severely ill patients is ethical. Alternatively, comparing treated patients to carefully described historic case reports or older siblings that did not receive treatment might provide an alternative.

When screening patient-derived fibroblasts of ARS1-, ARS2- and dual ARS-deficiencies for Chapter 6, we found that QARS1-deficient patient fibroblasts – in contrast to other cytosolic ARS1 deficiencies – showed mitochondrial dysfunction upon glutamine depletion. In Chapter 7, we studied this surprising finding, and aimed to explore why QARS1 deficiency is the only cytosolic ARS1-deficiency presenting with mitochondrial dysfunction

We hypothesized that the unique properties of mitochondrial charging of tRNA<sup>Gln</sup> could have explained the mitochondrial dysfunction seen in QARS1 deficiencies. As thiolation of mitochondrial tRNA<sup>Gln</sup> would compromise its

interaction with glutamine, import of cytosolic tRNA<sup>Gln</sup> species would be the only way of rescuing mitochondrial translation. The absence of a mitochondrial counterpart of QARS1 and the fact that cytosolic tRNA<sup>Gln</sup> is a poor substrate for GATC would necessitate cytosolic charging of tRNA<sup>Gln</sup> by QARS1 prior to its import. Thus, QARS1 could hypothetically be involved in mitochondrial function through charging cytosolic tRNA's with glutamine, which are then imported into mitochondria.

The northern blots conducted in Chapter 7, while preliminary and warranting repetition for definitive conclusions, revealed a clearly discernible import of cytosolic tRNA species into mitochondria in healthy controls across two independent experiments, aligning with previous findings from literature.<sup>22</sup> QARS1-deficient patients exhibited a potential decrease in mitochondrial import of cytosolic tRNA species, although the sensitivity of the northern blots limited the detection of significant differences. Nevertheless, these results substantiate the capability of cytosolic tRNA species to be imported into mitochondria, marking it the first report demonstrating the physiological relevance of tRNA import and its potential implication for QARS1 deficiency.

The preliminary findings from Chapter 7 emphasize the need for additional research on this matter. Part of this research is currently performed in the UMCU, where we aim to verify the presence of cytosolic tRNA<sup>Gln</sup> species in mitochondria using stem-loop primers and qPCR experiments. However, numerous sequencing studies have identified the existence of other tRNA species, such as tRNA<sub>UAA</sub><sup>Leu</sup> within mitochondria<sup>23</sup>; but their significance in mitochondrial translation and overall mitochondrial health remains uncertain. Shedding light on whether additional tRNA species are similarly imported into mitochondria provides an interesting avenue for further research. If a broad array of cytosolic tRNA species can be imported into mitochondria, this could have significant therapeutic implications for different ARS2 and other tRNA-related mitochondrial diseases, as they could be rescued by their cytosolic counterpart.

### **Concluding and future remarks**

As we are moving into a scientific era of not knowing enough to an era where we are flooded with knowledge, our challenges lie not in gathering data but in its correct interpretation. This thesis underscores the transformative power of context in unraveling the intricacies of genetic diseases. The metaphorical puzzle of VUS cases, laden with missing pieces, necessitates novel approaches for comprehensive solutions. Several contextual frameworks were used in this thesis, making use of theoretical insights derived from enzyme kinetics, information theory and phenotype-first approaches.

Our functional cellular screening of patients with VUS proved relevant for discerning pathogenicity and pathophysiology for VUSes in well-known disease genes and VUS in GUS. Additionally, we found that the potential of IFC-based screening extends to known genetic diseases, particularly mitochondrial disorders, where the traditional characterization based on complex-specific subtypes or affected genes was challenged. IFC-based assays revealed disease subtype-overarching patterns, offering a functional framework that correlates with responses to mitochondrial injury. This thesis concludes with a focus on therapy development for QARS1- and ARS2 deficiencies, based on functional insights in patient derived cells, highlighting the importance of understanding disease mechanisms in informing treatment strategies.

As we enter an era marked by advancements in genetic therapies for the correction of genetic diseases, the significance of functional studies may undergo a shift, assuming a diminished role. At first glance, the development of genetic therapies requires minimal insights into disease mechanisms. However, it is plausible that genetic therapies will be accessible primarily for severe cases and only upon definitive diagnoses. To stratify and diagnose patients, insights into underlying disease mechanisms are still needed. Furthermore, given the existing challenges in the delivery of genetic therapies, there may be limitations when it comes to targeting all organs effectively. Thus, traditional therapy based on functional aberrancies might remain the most effective therapeutic option for a subset of organs.

Moreover, the efficacy of genetic therapies is primarily evaluated in patient-derived cells, requiring useful disease-specific read-outs that can only be developed through knowledge of underlying systems. In all likelihood, we anticipate a continued interdependence between functional insights into genetic diseases and the ongoing development of therapeutic strategies, both in the present and the foreseeable future.

## References

1. Ehrhart F, Willighagen EL, Kutmon M, van Hoften M, Curfs LMG, Evelo CT. A resource to explore the discovery of rare diseases and their causative genes. *Scientific Data*. 2021;8(1).
2. Sivakumaran S, Agakov F, Theodoratou E, Prendergast JG, Zgaga L, Manolio T, et al. Abundant pleiotropy in human complex diseases and traits. *Am J Hum Genet*. 2011;89(5):607–18.
3. Köhler S, Gargano M, Matentzoglou N, Carmody LC, Lewis-Smith D, Vasilevsky NA, et al. The human phenotype ontology in 2021. *Nucleic Acids Res*. 2021;49(D1):D1207–17.
4. Haijes HA, Jaeken J, van Hasselt PM. Hypothesis: determining phenotypic specificity facilitates understanding of pathophysiology in rare genetic disorders. *J Inherit Metab Dis*. 2019;
5. Zagorovskaia TB, Illarioshkin SN, Slominskiĭ PA, Ivanova-Smolenskaia IA, Markova ED, Limborskaia SA, et al. Clinical and genetic analysis of juvenile parkinsonism in Russia. *Zhurnal Nevrologii i Psihatrii imeni SS Korsakova*. 2004;104(8).
6. Lallemand JY, Stoven V, Annereau JP, Boucher J, Blanquet S, Barthe J, et al. Induction by antitumoral drugs of proteins that functionally complement CFTR: A novel therapy for cystic fibrosis? [2]. *Lancet*. 1997;350(9079):711–2.
7. Morán M, Delmiro A, Blázquez A, Ugalde C, Arenas J, Martín MA. Bulk autophagy, but not mitophagy, is increased in cellular model of mitochondrial disease. *Biochim Biophys Acta Mol Basis Dis*. 2014;1842(7):1059–70.
8. Kaji N, Muramoto A, Mizuno K. LIM kinase-mediated cofilin phosphorylation during mitosis is required for precise spindle positioning.

Journal of Biological Chemistry. 2008;283(8):4983–92.

9. Weeda G, Donker I, De Wit J, Morreau H, Janssens R, Vissers CJ, et al. Disruption of mouse ERCC1 results in a novel repair syndrome with growth failure, nuclear abnormalities and senescence. *Current Biology*. 1997;7(6):427–39.
10. Dollé MET, Kuiper R V., Roodbergen M, Robinson J, de Vlugt S, Wijnhoven SWP, et al. Broad segmental progeroid changes in short-lived Ercc1  $^{-/\Delta 7}$  mice . *Pathobiology of Aging & Age-related Diseases*. 2011;1(1):7219.
11. D’Alessandro G, Morales-Juarez DA, Richards SL, Nitiss KC, Serano-Benitez A, Wang J, et al. RAD54L2 counters TOP2-DNA adducts to promote genome stability. *Sci Adv* [Internet]. 2023;9(49):eadl2108. Available from: <http://www.ncbi.nlm.nih.gov/pubmed/38055822>
12. De Voer RM, Hahn MM, Mensenkamp AR, Hoischen A, Gilissen C, Henkes A, et al. Deleterious Germline BLM mutations and the risk for early-onset colorectal cancer. *Sci Rep*. 2015;5.
13. Kirschner K, Singh R, Prost S, Melton DW. Characterisation of Ercc1 deficiency in the liver and in conditional Ercc1-deficient primary hepatocytes in vitro. *DNA Repair (Amst)*. 2007;6(3):304–16.
14. Milanese C, Bombardieri CR, Sepe S, Barnhoorn S, Payán-Gómez C, Caruso D, et al. DNA damage and transcription stress cause ATP-mediated redesign of metabolism and potentiation of anti-oxidant buffering. *Nat Commun*. 2019;10(1).
15. Distelmaier F, Koopman WJH, Van Den Heuvel LP, Rodenburg RJ, Mayatepek E, Willems PHGM, et al. Mitochondrial complex i deficiency: From organelle dysfunction to clinical disease. *Brain*. 2009;132(4):833–42.
16. Ganetzky RD, Stendel C, McCormick EM, Zolkipli-Cunningham Z, Goldstein AC, Klopstock T, et al. MT-ATP6 mitochondrial disease variants: Phenotypic and biochemical features analysis in 218 published cases and cohort of 14 new cases. *Hum Mutat*. 2019;40(5):499–515.
17. Du H, Guo L, Yan SS. Synaptic mitochondrial pathology in Alzheimer’s disease. *Antioxid Redox Signal*. 2012;16(12):1467–75.
18. Liang WS, Reiman EM, Valla J, Dunckley T, Beach TG, Grover A, et al. Alzheimer’s disease is associated with reduced expression of energy

metabolism genes in posterior cingulate neurons. *Proc Natl Acad Sci U S A*. 2008;105(11):4441–6.

19. Calkins MJ, Manczak M, Mao P, Shirendeb U, Reddy PH. Impaired mitochondrial biogenesis, defective axonal transport of mitochondria, abnormal mitochondrial dynamics and synaptic degeneration in a mouse model of Alzheimer's disease. *Hum Mol Genet*. 2011;20(23):4515–29.

20. Bido S, Soria FN, Fan RZ, Bezard E, Tieu K. Mitochondrial division inhibitor-1 is neuroprotective in the A53T- $\alpha$ -synuclein rat model of Parkinson's disease. *Sci Rep*. 2017;7(1).

21. Podmanicky O, Gao F, Munro B, Jennings MJ, Boczonadi V, Hathaizi D, et al. Mitochondrial aminoacyl-tRNA synthetases trigger unique compensatory mechanisms in neurons. *Hum Mol Genet*. 2023;

22. Rubio MAT, Rinehart JJ, Krett B, Duvezin-Caubet S, Reichert AS, Söll D, et al. Mammalian mitochondria have the innate ability to import tRNAs by a mechanism distinct from protein import. *Proc Natl Acad Sci U S A*. 2008;105(27):9186–91.

23. Mercer TR, Dinger SNME, Crawford J, Smith MA, Shearwood AMJ, Haugen E, et al. The human mitochondrial transcriptome. *Cell*. 2011;100(2):130–4.

---

## Nederlandse Samenvatting

Sinds de ontdekking van de complete sequentie van het genoom in 2003 is onze kennis over genetische ziekten enorm toegenomen. Tegelijkertijd weten we nu ook hoe complex het menselijke genoom is, en dat veel genetische ziekten van veel meer factoren afhankelijk zijn dan de DNA-code verankerd in ons genoom. Daarnaast zijn er de laatste jaren veel technieken op de markt gekomen, die het mogelijke maken op grote schaal data te verzamelen over het genoom, en over de consequenties van genetische afwijkingen op celniveau. Hoewel deze grote hoeveelheid data onze kennis enorm verbreed heeft, gaat de grootte van de datasets soms het menselijke begrip te boven.

Een van de grootste uitdagingen van het huidige genetische tijdperk zijn zogenaamde “Varianten van Onbekende Betekenis”, ook wel VUS genoemd in het Engels. Dit zijn genetische varianten waarvan de klinische betekenis onduidelijk is, die worden ontdekt als het genoom gecontroleerd wordt op erfelijke ziekten. Als een VUS wordt gevonden, is het onduidelijk of deze variant ziekteverwekkend is of juist alleen maar geassocieerd is met goedaardige variaties. Een VUS brengt grote onzekerheid met zich mee, omdat een patiënt met een VUS geen diagnose heeft, en niet weet hoe zijn of haar symptomen zich over de tijd zullen ontwikkelen. Daarnaast kunnen artsen moeilijk een behandeling instellen bij een patiënt die geen eenduidige diagnose heeft.

Er zijn beperkte richtlijnen en hulpmiddelen beschikbaar om VUS-casussen te helpen oplossen. In veel gevallen is het belangrijk om functionele studies te verrichten in cellen van de patiënt. Omdat er heel veel verschillende genetische ziekten zijn, zijn er over de jaren veel van dit soort functionele studies ontwikkeld. Het is soms lastig om deze functionele studies uit te voeren, omdat ze soms niet geprotocolleerd zijn en in veel verschillende ziekenhuizen worden uitgevoerd. Voor sommige VUSen is er geen functionele studie beschikbaar, omdat de VUS in een gen zit waar de functie niet van bekend is. In dit geval moet er een nieuwe functionele studie worden opgezet, maar dit is erg complex als de functie van het gen onbekend is.

Om de groeiende hoeveelheid data en complexiteit van genetische ziekten te begrijpen is de juiste context nodig. Hetzelfde geldt voor het oplossen van een VUS-casus, en voor het structureren van functionele experimenten. De juiste context kan zorgen voor een effectief raamwerk dat een onderzoeker of arts helpt bij het extraheren van relevante informatie om erachter te komen wat er speelt op genetisch niveau.

In dit proefschrift tonen wij verschillende methoden hoe context of een raamwerk kan helpen bij het oplossen van genetische ziekten en VUS-casussen. In de eerste drie hoofdstukken gebruiken wij verschillende raamwerken, bijvoorbeeld het gebruik van klinische kenmerken van bestaande genetische ziekten, enzymkinetiek en fenotypische prioritering om specifieke genetische varianten te duiden. In het vijfde hoofdstuk beschrijven wij een functionele cellulaire screening om VUSen te duiden. In het zesde, zevende en achtste hoofdstuk beschrijven we hoe een functioneel raamwerk kan helpen bij het duiden van bestaande genetische ziekten.

In Hoofdstuk 2 beschrijven wij twee broers met zeldzame genetische varianten in het *NAA80* gen. Deze broers waren doof, hadden een ontwikkelingsachterstand en verslechterden klinisch tijdens infecties. Genetische ziekten geassocieerd met het **NAA80** gen zijn nog nooit beschreven, echter is de functie van NAA80 wel bekend. NAA80 kan het actine cytoskelet acetyleren, waardoor de dynamiek verandert. In fibroblasten en T cellen van patiënten hebben we allereerst de functie van NAA80 bestudeerd, welke sterk verminderd bleek te zijn. Daarnaast toonde het actine cytoskelet zichtbare afwijkingen, hadden fibroblasten meer filopodia en was er toegenomen actine polymerisatie. Ondanks het feit dat we de VUS-casus hadden opgelost waren nog niet alle vragen voor ons beantwoord. Ondanks een uitgebreide zoektocht wereldwijd, waarbij we zelfs een presentatie hebben gegeven aan een Portugees ziekenhuis, vonden we maar twee patiënten in de hele wereld met pathogene *NAA80* varianten, terwijl het gen redelijk gevoelig was voor mutaties. Om inzicht te krijgen hoe dit mogelijk was, hebben we de patiënten



---

met pathogene *NAA80* varianten vergeleken met andere patiënten met actine-gerelateerde ziekten. Door deze vergelijking kwamen we erachter dat er weinig ziekten bekend zijn waar er meer dan 50% van de cytoplasmatische actines zijn aangedaan. Onze kinetische data liet zien dat ondanks een ernstig verlies van *NAA80* eiwitactiviteit van 95%, er maar net iets minder dan 50% van de actine moleculen waren aangedaan in onze patiënten. De kans dat *NAA80* activiteit ernstig genoeg is aangedaan – maar niet té ernstig – is extreem klein. Het vergelijken van het klinisch fenotype van verschillende genetische ziekten en het gebruiken van enzymkinetiek gaf ons het juiste raamwerk om erachter te komen waarom pathogene *NAA80* varianten zo extreem zeldzaam zijn.

In Hoofdstuk 3 beschrijven wij vier patiënten met VUSen in het *NAE1* gen. Er waren tot nu toe nog geen genetische ziekten geassocieerd met dit gen. De patiënten hadden een ernstig fenotype, omdat ze verlies van hersenweefsel en ontwikkelingsvaardigheden lieten zien na ernstige infecties en ziekenhuisopnames. Ook hadden zij ernstige vorm van epilepsie welke verergerde tijdens ziekte. We vonden een sterk verlaagde *NAE1* aanwezigheid in patiënt fibroblasten. De directe activiteit van *NAE1* leek niet veranderd (de hoeveelheid geneddyleerde cullins was vergelijkbaar, echter leek de hoeveelheid ongeddyleerde cullins wel verhoogd. Om meer inzicht te krijgen in de correlatie tussen deze bevindingen en het klinisch fenotype van patiënten, wilden we aanvullende experimenten doen. Er was veel bekend over *NAE1* en zijn vermeende functies, echter was er echter zoveel informatie over het gen dat het bijna onmogelijk was om te kiezen welke functies we moesten testen. We wilden relevante cellulaire studies opzetten, die ons zouden leren hoe het klinisch fenotype veroorzaakt werd. Om de juiste experimenten te kiezen, hebben wij ons eerst gefocust op het klinisch fenotype. We hebben alle fenotypische kenmerken gesorteerd op basis van hun zeldzaamheid. Onze theorie, gebaseerd op eerdere studies, voorspelde dat de meest zeldzame fenotypes het meest inzicht gevend zouden zijn in onderliggende pathofysiologie. Op basis van deze ‘Fenotypische Prioritering’ hebben wij de juiste functionele studies weten uit te voeren die ons inzicht gaven in het fenotype. Hierdoor kwamen we erachter dat *NAE1* betrokken is

bij de overleving van cellen tijdens cellulaire stress, en belangrijk is om het immuunsysteem te beschermen tijdens infecties.

In hoofdstuk 4 beschrijven we onze laatste VUS-casus, geassocieerd met genetische varianten in het *LIMK1* gen. Dit was een unieke casus, omdat de twee patiënten een totaal ander fenotype hadden. De ene patiënt toonde ernstige ontwikkelingsachterstand en epilepsie, terwijl de andere patiënt een immuunstoornis, glucose deregulatie en hartritme stoornissen toonde. We vroegen ons af hoe dit mogelijk was, en of de patiënten wel dezelfde ziekte zouden hebben.

We bestudeerden de functie en structuur van het *LIMK1* gen aandachtig en kwamen erachter dat de genetische varianten op twee verschillende plekken in het eiwit zaten met elk een andere functie. De variant van de eerste patiënt zat op één van de meest essentiële plekken van het eiwit, en we voorspelden dat de patiënt hierdoor een sterk verminderde eiwitfunctie zou hebben. De variant van de tweede patiënt echter zat gelokaliseerd aan het begin van het eiwit, in een domein wat zorgt voor remming (auto-inhibitie) van het eiwit. Hierdoor voorspelden we dat het eiwit actiever zou zijn. Onze functionele studies in patiënt fibroblasten bevestigden dat het eiwit minder actief was in de eerste patiënt, terwijl het eiwit actiever was in de tweede patiënt. Om erachter te komen hoe deze afwijkende LIMK1 activiteit kon leiden tot het fenotype van de patiënten, bestudeerden we insuline secretie in alvleesklier-achtige cellen die de twee varianten tot expressie brachten. We vonden een tegenovergesteld effect van beide varianten op de insuline secretie, welke overeenkwamen met de glucose regulatie die we klinisch in de patiënten waarnamen. Dit bevestigde ons vermoeden dat de genetische varianten in de patiënten tegenovergestelde effecten hadden, én leidde het tot nieuwe inzichten in de secretie van insuline en de rol van LIMK1 daarin.

De eerste drie hoofdstukken in dit proefschrift hebben laten zien hoe complex het is om een VUS-casus op te lossen, en dat terwijl er van alles bekend was over de genen waar de VUSen in gelokaliseerd waren. Helaas zijn er nog steeds veel genen waarbij dit niet bekend is. Voor dit soort genen is het immens complex om functionele studies te ontwerpen. Theoretisch zou elk

---

cellulair systeem aangetast kunnen zijn. Het zou helpen om een startpunt te hebben, vanuit waar gericht gezocht kan worden naar een goed functioneel vervolg.

In Hoofdstuk 5 beschrijven we onze functionele cellulaire screening, die bedoeld is om complexe VUS casussen op te lossen. Voor deze studie hebben we zes cellulaire assays ontworpen en gevalideerd, die een overzicht geven van het algemeen cellulair functioneren op verschillende domeinen. Na validatie hebben we deze assays toegepast op patiënten met VUSen. Zowel voor patiënten met VUS in bekende ziektegenen als voor patiënten met VUS in onbekende genen bleek de screening helpend. Voor de bekende ziektegenen konden VUSsen snel worden vergeleken worden ‘echte’ patiënten, waardoor er duidelijkheid kwam over de diagnose zonder dat er uitgebreide functionele studies hoefden te worden gedaan. Voor patiënten met VUSen in onbekende ziektegenen werden er afwijkingen gevonden die richting gaven voor vervolgstudies. Zo zijn er bij drie patiënten afwijkingen gevonden die aanwijzingen gaven dat er mogelijke DNA-schade reparatie problemen waren, die vervolgens heel gericht onderzocht konden worden. Onze functionele cellulaire screening kan dus duidelijk richting geven bij patiënten met VUSen.

Nadat we onze functionele cellulaire screening hadden ontwikkeld en getest op patiënten met VUSen, waren we benieuwd of deze screening ook van nut kon zijn voor patiënten met bekende genetische ziekten. Ons gevoel was dat het gemak, de snelheid en de veelzijdigheid van de screening van toegevoegde waarde kon zijn voor vraagstukken bij bekende genetische ziekten.

In hoofdstuk 6 gebruiken we een specifiek onderdeel (mitochondriële functietesten) van onze functionele cellulaire screening ontwikkeld in hoofdstuk 5 om patiënten met mitochondriële ziekten te onderzoeken. Mitochondriële ziekten worden gekenmerkt door heterogene klinische en cellulaire fenotypes, waardoor het diagnosticeren en behandelen van mitochondriële ziekten extreem moeilijk zijn. Mitochondriën hebben veel functies, die allemaal van elkaar afhankelijk zijn. Echter worden mitochondriële ziekten nu vaak

alleen bekeken vanuit hun specifieke functionele groep, bijvoorbeeld vanuit hun specifieke complex afwijking. In hoofdstuk 6 hebben wij een breed scala aan patiënten met verscheidene onderliggende mitochondriële ziektes gescreend met onze functionele experimenten. We includeerden bewust twee of drie patiënten van ieder subtype, omdat we verwachtten dat elk subtype een uniek profiel of afwijkingen zou laten zien. Die afwijkingen konden we dan vertalen naar de onderliggende functie van het eiwit of het onderdeel waar het probleem gelokaliseerd zat. Echter kwamen we er tijdens het scree-nen al achter dat patiënten met hetzelfde type mitochondriële ziekte totaal tegenovergestelde afwijkingen konden vertonen. Uiteindelijk zagen we dat er grofweg twee soorten afwijkingen waren bij patiënten: een verlaging van de membraanpotentiala en verhoogde productie van schadelijke zuur-stofradicalen, or een verhoging van de membraanpotentiala, toegenomen mitochondriële massa en mitochondriële zwelling. Door middel van litera-tuuronderzoek kwamen we erachter dat de eerste soort afwijkingen waar-schijnlijk te maken hebben met een loskoppeling van een onderdeel van mi-tochondrieel complex 1, terwijl het tweede type reactie te maken heeft met afwijkend transport van protonen over het mitochondriële membraan. Ook in andere onderzoeken komen deze twee typen reacties vaak naar voren. Op basis van deze data, vermoedden we dat mitochondriële ziekten patiënten beter ingedeeld kunnen op basis van hun functionele respons dan op hun pri-maire ziekte. Mogelijk kan deze nieuwe informatie helpen de diagnostiek en behandeling van mitochondriële ziekten verbeteren, door deze te richten op een specifieke functionele respons in plaats van op de primaire afwijking.

Hoofdstuk 7 is het eerste en het enige hoofdstuk in dit proefschrift wat zich voornamelijk richt op behandeling van genetische ziekten in plaats van diagnostiek. Desalniettemin gebruiken wij ook hier een functionele benadering en experimenten om onze behandeling te testen in patiënt cellen voordat wij hem toepassen. Amino-acyl tRNA synthetase deficiënties zijn een groep ernstige genetische ziekten die vaak ontstaan op de zuigelingen- of kindereleeftijd. Er zijn verschillende types (ARS1-, ARS2- en gecombineerde ARS defecten). Recent heeft onze onderzoeksgroep de effectiviteit van specifieke aminozuren getest voor de behandeling van één van deze types (ARS1) met

---

goede resultaten in klinische studies. Wij waren echter benieuwd of deze aminozuren ook voor de andere twee types (ARS2, gecombineerde ARS defecten) nuttig konden zijn. Echter zijn ARS2- en gecombineerde ARS defecten van wezenlijk andere aard, omdat ze in de mitochondriën tot uiting komen. We wisten niet zeker of de aminozuren wel in de mitochondriën terecht zouden komen als we deze aan patiënten zouden geven. Om zeker te zijn van onze behandeling, hebben we daarom eerst mitochondriële functie getest in cellen van patiënten, tijdens extreem lage en hoog-normale aminozuurconcentraties. We kwamen erachter dat mitochondriële functie in deze patiënten sterk afhankelijk was van de hoeveelheid specifieke aminozuren, en dat lage aminozuurconcentraties schadelijk waren. Met dit inzicht zijn we overgegaan tot aminozuurbehandeling in negen patiënten, met goede resultaten. Afhankelijk van de patiënt, verbeterde de hartfunctie, de ontwikkeling, de epilepsie en/of de misselijkheid. Als vervolg willen we graag grotere studies opzetten om deze effecten nog robuuster te testen, maar het feit dat aminozuurbehandeling mitochondriële functie kon beïnvloeden, veilig was én de patiënten kon helpen, maakt dit een veelbelovend onderzoek.

Tijdens onze zoektocht naar een behandeling voor ARS2-defecten, stuitten we op een onverwachte bevinding. Normaal gezien laten ARS1-defecten - welke niet in de mitochondriën tot uiting komen- geen mitochondriële dysfunctie zien. Echter was er één uitzondering op deze regel: QARS1-defecten. QARS1 zorgt ervoor dat glutamine gebruikt kan worden om eiwitten te bouwen. Na een uitgebreid literatuuronderzoek kwamen we erachter dat het mechanisme rondom glutamine inbouw in mitochondriën heel uniek was, en tegelijkertijd heel fragiel, waardoor dit systeem kan haperen met desastreuze gevolgen. Om de machinerie weer op gang te brengen, moet er hulp komen vanuit het cytoplasma – en dus van QARS1. Om dit fenomeen te onderzoeken, isoleerden we mitochondriën uit gezonde- en patiënt-huidcellen, en analyseerden we de hoeveelheid tRNA met glutamine welke gebruikt kan worden voor het glutamine inbouwen in eiwitten. We keken specifiek waar die tRNA's vandaan komen – uit het cytoplasma of uit mitochondriën. Als de tRNA's uit het cytoplasma zouden komen was onze theorie deels bewezen, want dan zou QARS1 inderdaad een mogelijke rol

spelen bij het inbouwen van glutamine in mitochondriële eiwitten. Tijdens onze experimenten zagen we dat er inderdaad tRNA's uit het cytoplasma de mitochondriën in werden getransporteerd, en dat dit sterk afgenomen was bij patiënten bij QARS1-defecten. Dit toonde een mogelijk nieuw verband tussen QARS1 functie en mitochondriële functie. Echter was de kwaliteit van de experimenten niet optimaal, en moeten deze herhaald worden om definitieve conclusies te trekken. Als we dit mechanisme kunnen bevestigen, zou dit een van de eerste studies zijn die aantoont dat er cytosolaire tRNA's de mitochondriën in kunnen worden getransporteerd én dat deze tRNA's een fysiologische functie hebben.

### **Conclusie**

Naarmate we een wetenschappelijk tijdperk ingaan waar er een overvloed aan data is, liggen onze uitdagingen niet zozeer in het verzamelen van gegevens, maar in de juiste interpretatie ervan. Dit proefschrift benadrukt de transformerende kracht van context bij het ontrafelen van genetische ziekten. De puzzel die gelegd moeten worden om VUS-gevallen op te lossen, met veel ontbrekende stukjes, vereist innovatieve contextuele benaderingen. Verschillende contextuele kaders werden gebruikt in dit proefschrift, waarbij theoretische inzichten werden toegepast uit enzymkinetica, informatietheorie en fenotypische prioritering.

Onze functionele cellulaire screening van patiënten met VUS bleek relevant voor het onderscheiden van de onderliggende pathofysiologie. Bovendien ontdekten we dat het potentieel van onze screening zich uitstreckte tot bekende genetische ziekten, met name mitochondriële aandoeningen, waarbij de traditionele karakterisering op basis van specifieke subtypes werd uitgedaagd. Onze mitochondriële screening onthulde ziekte-subtype-overkoepelende patronen, waarbij een functioneel kader werd ontdekt dat correleert met twee verschillende type reacties op mitochondriële schade. Dit proefschrift eindigt met een focus op therapieontwikkeling voor QARS1- en ARS2-deficiënties, gebaseerd op functionele inzichten in cellen afkomstig van patiënten, waarbij het belang van het begrijpen van ziektemechanismen voor het ontwikkelen behandelingsstrategieën wordt benadrukt.

---

Er komen steeds meer genetische therapieën beschikbaar voor de behandeling van genetische ziekten, waardoor functionele studies minder belangrijk worden. Op het eerste gezicht vereist de ontwikkeling van genetische therapieën namelijk maar minimale inzichten in ziektemechanismen. Het is echter mogelijk dat genetische therapieën alleen toegankelijk zullen zijn voor ernstige gevallen en pas na definitieve diagnoses. Om patiënten te stratificeren en te diagnosticeren, zijn inzichten in onderliggende ziektemechanismen nog steeds nodig. Bovendien, gezien de bestaande uitdagingen bij de toediening van genetische therapieën aan sommige organen, kunnen er beperkingen blijven voor sommige ziektes. Traditionele therapie, waarvoor er kennis nodig is van functionele afwijkingen, blijft dus mogelijk nog een lange tijd belangrijk. Bovendien wordt de doeltreffendheid van genetische therapieën voornamelijk geëvalueerd in cellen afkomstig van patiënten, waarbij de effectiviteit wordt getest door het meten van functionele verbetering. Die functionele verbetering kan alleen gemeten worden met kennis van onderliggende systemen. Waarschijnlijk kunnen we blijven rekenen op een voortdurende onderlinge afhankelijkheid tussen functionele inzichten en de ontwikkeling van therapeutische strategieën, zowel in het heden als in de nabije toekomst.

---

## List of Publications

### In this thesis:

**1. Muffels, I.J.J.**†, Wiame, E.†, Fuchs, S.A., Massink, P.G., Rehmann, H., Musch, J.L.I., Haaften, G., Vertommen, D., Schaftingen, E., Hasselt, P.M. *NAA80* Bi-allelic missense variants result in high-frequency hearing loss, muscle weakness and developmental delay.

*Brain Communications*. 2021;3(4). doi:10.1093/braincomms/fcab256

**2. Muffels I.J.J.**, Schene IF, Rehmann H, Massink, M.P.G., Wal, M.M., Bauder, C., Labeur, M., Armando, N.G., Lequin, M.H., Houben, M.L.L., Giltay, J.C., Haitjema, S., Huisman, A., Vansenne, F., Bluvstein, J., Pappas, J., Shailee, L.V., Zarate, Y.A., Morcky, M., Haaften, G.W., Nieuwenhuis, E.E.S., Refojo, D., Wijk, F., Fuchs, S.A., Hasselt, P.M.

Bi-allelic variants in *NAE1* cause intellectual disability, ischiopubic hypoplasia, stress-mediated lymphopenia and neurodegeneration.

*American Journal of Human Genetics*. 2023;110(1):146-160. doi:10.1016/j.ajhg.2022.12.003

**3. Muffels, I.J.J.**, Carter, T., Rehmann, H., Vastert, S.J., Verrijn Stuart, A.A., Blank, A.C., Garde, A., Zwaag, B., De Lange, I.M., Giltay, J.C., van Gassen, K.L.I., Koop, K., Asensio, C.S., van Hasselt, P.M., *LIMK1* variants are associated with divergent endocrinological phenoty-pes aligning with divergently altered exocytosis dynamics.

*iScience*. 2024; *Conditionally Accepted*.

**4. Muffels, I.J.J.**, Waterham, H., D'Allessandro, G., Zagnoli-Vieira, G., Sacher, M., Lefeber, D.J., Vinne, C., Roifman, C., Van Haaften-Visser, D.Y., Nieuwenhuis, E.E.S., Jackson, S., Fuchs, S.A.,† Wijk, F.,† Hasselt, P.M.

Imaging Flow Cytometry-based cellular screening elucidates pathophysiology in individuals with Variants of Uncertain Significance.

*Genome Medicine*. 2024; *In Review*



---

**5. Muffels, I.J.J.,** Rodenburg, R., Willemsen, H.L.D.M., Van Haften-Visser, D.Y., Waterham, H., Eijkelkamp, N., Fuchs, S.A., Hasselt, P.M. Imaging Flow Cytometry identifies divergent responses to mitochondrial pathology in patients with mitochondrial disease.

*iScience*. 2024; *Conditionally Accepted*.

**6. Muffels, I.J.J.,** Kok, G., Tang, Z., Medeiros, L.S., Poswar, F.O., Vermeij, W.P., Rodenburg, R. Smit, K., Sukumaran, S.K., Kwok, A.M.K., Nieuwenhuis, E.E.S., Hasselt, P.M., Schwartz, I.V.D., Lubout, C.M.A., Bosch, A.M., Koop, K., Hoytema van Konijnenburg, E.M.M., Fuchs, S.A.

Tailored amino acid treatment for mitochondrial Aminoacyl-tRNA synthetase deficiencies.

### **Not in this thesis:**

**7. Muffels, I.J.J.,** Sadek, M., Kozicz, T., Morava, E., Assessing age of onset and clinical symptoms over time in patients with heterozygous pathogenic *DHDDS* variants.

*Journal of Inherited Metabolic Diseases*. 2024; 10.1002/jimd.12769

**8. Koppens, M., Joore, I., Shehata, S., Muffels, I.J.J.,** Castro Alpizar, J., Jimenez-Curiel, E., Tang, Z., Smit, K., Rodenburg, R., Fuchs, S.A.

Mitochondrial base editing for pathogenic mutations in mitochondrial DNA.

*Plos Biology*. 2023; *Conditionally accepted*

**9. Budhraj, R., Radenkovic, S., Jain, A., Muffels, I.J.J.,** Hicham Alaoui Ismaili, M., Kozicz, T., Pandey, A., Morava E.

Liposome-encapsulated mannose-1-phosphate therapy improves global N-glycosylation in different congenital disorders of glycosylation.

*Molecular Genetics and Metabolism*. 2024;142(2):108487. doi: 10.1016/j.ymgme.2024.108487

**10. Samra, N.N., Morani, I., Bayan, H., Bakry, H., Shaalan, M., Saadi, H., Sh-rem, S.B., Sawaed, A., Kok, G., Muffels, I.J.J.,** Fuchs, S.A., Shapira-Rootman,

M., Morshaked, G., Mandel, H.

Next-Generation sequencing performed in patients raising the suspicion of an inborn error of metabolism uncovered a homozygous variant in *YARS1* allowing a novel therapeutic trial.

*Harefuah*. Published online 2023.

11. Parenti I, Lehalle D, Nava C, Torti, E., Leitão, E., Person, R., Mizuguchi, . Matsumoto, N., Kato, M., Nakamura, K., Man, S.A., Cope, H., Shashi, V., Undiagnosed Disease Network, Friedman, J. Joset, P., Steindl, K., Rauch, A., **Muffels, I.J.J.**, Hasselt, P.M., Petit, F., Smol, T., Le Guyader, G. Bilan, F., Sorlin, A., Vitobello, A., Philippe, C., Laar, I.M.B.H., Slegtenhorst, M.A., Campeau, P.M., Au , B.P.Y., Nakshima, M., Saitsu, H., Yamamoto, Y., Nomura, T., Nomura, Y., Louie, R., Lyons, M.J., Dobson, A., Plomp, A.S., Motazacker, M.M., Kaiser, F.J., Timberlake, A.T., Fuchs, S.A., Depienne, C., Mignot, C.

Missense and truncating variants in *CHD5* in a dominant neurodevelopmental disorder with intellectual disability, behavioral disturbances, and epilepsy.

*Human Genetics*. 2021;140(7):1109–1120. doi:10.1007/s00439-021-02283-2

12. **Muffels IJJ**, Schoots E, Bax J.

Cafeïne en prestatievermogen: een update.

*Sportgericht*. 2017;6(71):43-45

13. Kieboom J van den†, **Muffels IJJ**†, Friederich PW, Jharap B. Leveraces door *Fusobacterium*: Denk aan een tandheelkundige ingreep als infectiebron. *Nederlands Tijdschrift voor Geneeskunde*. 2018;162:D2869.

† These authors contributed equally

---

## Curriculum Vitae

Irena Muffels moved to Utrecht in 2012 to study medicine at Utrecht University. In her second year, a Neuroscience elective sparked her interest in research. She completed two voluntary internships at the Rudolf Magnus Brain Institute, focusing on psychiatric diseases in children and adults. In her fourth year, after attending a lecture by Dr. Van Hasselt on metabolic diseases, she decided to pursue two curricular internships at the Department of Metabolic Diseases under the supervision of Peter van Hasselt, Sabine Fuchs, and Edward Nieuwenhuis. She was immediately fascinated by the complex puzzles in metabolic diseases and the urgent need for better diagnosis and treatment. Between these internships, she spent three months on a brief internship at a hospital in Nicaragua. Upon completing medical school, she pursued a PhD at the Department of Metabolic Diseases, driven by the desire to solve more puzzles. She worked at the Hubrecht Institute's metabolic diseases department for four years, diagnosing eight patients with VUS and discovering three new diseases. She became an expert in the Imaging Flow Cytometry technique, allowing her to optimize complex diagnostic processes for individuals with VUS. After her PhD, she spent two months at the Mayo Clinic in Minnesota, then moved to New York with her new Principal Investigators (Eva Morava and Tamas Kozicz) to work as a postdoctoral researcher. Currently, she studies brain organoids derived from patients with metabolic diseases to identify new treatment targets. After her postdoc, she aspires to become a Clinical Geneticist and hopes to remain involved in translational science. In her free time, she enjoys staying busy, and likes running, cycling, climbing, craft beers, nights with friends, and playing the piano.

## Dankwoord

Dit proefschrift had ik niet kunnen maken zonder de inzet en hulp van jullie, mijn lieve familie, vrienden en collega's. Ik zou graag de gelegenheid nemen om jullie hiervoor te bedanken. Jullie waren en zijn mijn grootste steun waardoor dit alles mogelijk was.

**Peter**, je plukte me uit de les tijdens mijn studie geneeskunde omdat je dacht dat ik metabole ziekten leuk zou vinden. En wat had je gelijk! Ik ben ontzettend geïnspireerd geraakt door je vermogen om uit elk onderzoeksproject het beste te willen halen, en de creatieve 'bril' waarmee jij naar nieuwe bevindingen kijkt. Ik kon elke vraag die ik had aan je stellen - je dacht altijd mee - en nog vaker bedacht je gewoon een hele slimme oplossing. Tot nu toe is elk hoofdstuk in mijn boekje een bijzonder verhaal geworden, en dat heb ik grotendeels aan jou te danken. Daarnaast ben je ontzettend slim, geestig, en heb je me door weer en wind bijgestaan. Ik had dit absoluut niet zonder je gekund, en ik heb genoten van onze wekelijkse meetings. Hopelijk blijven we elkaar in de toekomst vinden voor mooie inspirerende projecten!

**Sabine**, ik weet niet hoe je het doet, maar je weet precies de juiste mensen te vinden waardoor het Fuchs lab altijd een hele fijne en inspirerende plek is geweest en nog steeds is. Je hebt een natuurlijke gave om iedereen te motiveren. Daarnaast vind ik het heel bijzonder om te zien hoe je altijd weet te zorgen voor een fijne sfeer, en ik voel me altijd thuis als ik bij je over de vloer kom, mogelijk daarom ook dat mijn idee voor de Fuchs meeting/ borrelmeeting bij jou in goede aarde viel! Ik vind het fijn dat je me steunde op een persoonlijke manier, en ik heb veel aan je advies gehad. Ik ben blij dat ik heb mogen meemaken dat we zulke goede stappen zetten om therapie voor metabole ziekten een stap dichterbij te brengen. Ik hoop dat onze groep mag blijven groeien en dat ik deel mag blijven uitmaken van je mooie plannen!

---

**Edward**, toen ik een PhD wilde doen hebben we vaak met elkaar gesproken of deze plek de juiste was. Dankzij jou kon ik met meerdere labs praten, en kan ik nu zeggen dat ik blij ben met deze ontzettende juiste keuze. Het duurde even eer alle puzzelstukjes op hun plaats vielen, maar achteraf terug kijkend heb ik ontzettend veel geleerd onder jullie vleugels. Na mijn PhD hielp je mij om in de VS aan de slag te kunnen, en nu hier de puzzelstukjes ook op zijn plaats beginnen te vallen, besef ik me dat je toch verdacht vaak aan het begin staat van hele juiste keuzes. Hopelijk mag ik je blijven lastigvallen met mijn levensvragen, carrièreplannen en overpeinzingen!

**Klaas en Eva**, dankjewel dat jullie me onderdeel lieten uitmaken van de ‘metabole familie’. Jullie liefde voor het metabole veld is bijzonder om te zien en ik genoot van de inspirerende en fijne sfeer op de afdeling. Ik hoop dat we elkaar nog vaak tegen komen in de toekomst!

**Lief Lab**, dear Lab members, nu ik weg ben besef ik me pas hoe uniek de fijne sfeer was in ons lab. **Indi en Imre**, dank voor jullie advies over de jaren, jullie namen altijd de tijd om met me mee te denken en ik heb veel van jullie geleerd. **Ibrahim**, ik ken niemand die grappigere presentaties gaf dan jij. **José en Eveline**, het was altijd gezellig met jullie! **Sawsan**, onze (en mijn) rots in de branding. Wat ben jij een topper! **Emi**, wat fijn dat je bent gebleven en bij Sabine in de groep bent gekomen! **Martijn**, ik bewonder je doorzettingsvermogen en ik heb altijd fijn met je samengewerkt. Ik hoop nog veel mitochondriële projecten van jouw hand te zien langskomen! **Remi**, jij was een korte maar waardevolle toevoeging aan ons lab. Gelukkig zie ik je nog steeds af en toe! **Ewart**, bedankt voor de persoonlijke en fijne manier waarop je me hebt bijgestaan mijn laatste maanden. Ik kon altijd bij je terecht! **Marit**, wij liepen vaak gelijk op qua timing van onze promotie. Ik vond het altijd heel gezellig en fijn om met je te werken, en ik heb genoten van onze trip naar EMG Innsbruck en SSIEM Freiburg! Daarnaast; voor iedereen die ik niet heb genoemd (inclusief studenten). Ik heb altijd heel erg van jullie genoten. Dankjulliewel dat jullie mijn dagen altijd een beetje dragelijker en me hielpen het lab en onderzoek iets minder serieus te nemen!

**Femke**, veel dank voor je mentorschap. Ik bewonder de manier waarop jij een fijne groep en werksfeer hebt weten te creëren, die daarnaast ook heel mooi en kwalitatief werk oplevert. **Van wijk lab members**, veel dank voor jullie bereidheid me op te nemen in jullie groep en jullie hulp de afgelopen jaren!

**Holger**, I truly valued your comments and advice, most of them turned out to be crucial for my work. **Niels en Hanneke**, ik heb veel te danken aan jullie hulp met mijn eerste stappen in de mitochondriële biologie. Ik heb altijd heel fijn met jullie samen gewerkt en ik heb genoten van de goede sfeer die er in jullie groep hing. **Rowena en Michel**, jullie maakten mijn eindeloze Imagestream dagen een heel stuk dragelijker. Dank jullie wel voor de fijne gesprekken en de lekkere koffie! **Paul en Jorg**, dankjewel voor jullie steun. Ik meen het als ik zeg dat ik dit niet zonder jullie had gekund. **Ziqin, Wilbert en Kimberley**, thank you for all your help with the seahorse experiments and all other thoughts we exchanged over the years. **Cedric and Theo**, thank you for your valuable help with the LIMK1 paper. **Dr. Waterham**, bedankt voor je vertrouwen in ons Imagestream project. **Eva en Tamas**, dankjewel dat jullie me onder jullie vleugels hebben genomen voor mijn volgende avontuur! **Sylvia, Rameen and Graeme**, thank you for introducing me to your lab for helping me with the big move. Hopefully there is much more fun science to come!

Lieve **Borrelclub**. Altijd een luisterend oor. Altijd gezellig. Jullie hebben me er doorheen gesleept. Dankjewel voor alle leuke avonden die we hebben gehad, zoals de Parade, Trek, talloze avondjes bij Tilt, weekendjes op de camping, Hubrecht borrels en promotieborrels. Ik hoop nog lang met jullie bevriend te blijven! **Suze**, dankjewel voor al je goede advies over de jaren en jouw bezoek aan NY toen ik het meest een vriend nodig had. **Maaïke**, ik kon altijd bij je terecht en je was altijd bereid tot een (oordeelloos) ongedwongen praatje. **Marliek**, wij hebben niet veel samengewerkt maar gelukkig des te meer samen geborreld. Bedankt voor al je lieve steun! **Gautam**, jij was elke woensdag mijn luisterend oor, borrelpartner in crime en stamgast bij Willem Slok. Dankjewel voor de talloze leuke avonden, festivals, fietstochten, en dat je me meer dan eens liet inzien dat je dingen beter luchtig kan bekijken.

---

Ik bewonder hoe relaxt jij in het leven staat en ik hoop dat we nog veel leuke dingen samen blijven doen.

Lieve **Robin**. Op een of andere manier volgen wij al bijna vijftientig jaar hetzelfde levenspad, waarbij steeds de één of de ander net voorloopt. Ik kan altijd heel fijn met je sparren en je Italië avonturen zijn fantastisch om te volgen!

Lieve **Bonie's**, lieve **Suus**, **Pomme** en **Soppie**. Wij leerden elkaar op de eerste dag van geneeskunde kennen en vonden elkaar in Nandoe's, kittige katjes en vooral heel veel gezelligheid. Ik ben dankbaar om na 12 jaar nog steeds jullie vriendin te zijn. Bonie's zijn we allang niet meer, gelukkig zijn jullie ter compensatie wel in opleiding (hopelijk kan spuit 11 nog volgen). Ik bewonder jullie om jullie passie voor het doktersvak en je durf om je eigen weg te vinden, en natuurlijk een vriendschap die zo vertrouwd voelt dat jullie als familie zijn. Lieve **Sop**, ik ben heel dankbaar dat ik altijd bij jou terecht kan voor goed advies, of het nou over New York, kakkerlakken of de diepere zaken des levens gaat. Biertjes en bitterballen bij Broers zijn allang geen vijf euro meer, maar ik hoop nog heel vaak met jou te kunnen proosten!

Lieve **Bonnie**. Jouw nuchtere kijk op de wereld doet soms wonderen. Dank voor de talloze avondjes op het terras waarbij je me steunde en hielp om iets van de andere kant te bekijken. Ik hoop nog heel vaak met jou en **Maureen** te kunnen proosten!

Lieve **Lot**, **Jos** en **Juul**. Ik vind het heel bijzonder dat wij altijd vriendinnen zijn gebleven. Ik kan altijd bij jullie terecht en veel dank voor alle lieve steun en waardevolle vriendschap.

**Bien**, **Cat** en **Jos**. Wat hebben wij veel meegemaakt. Van 1.5 uur op de fiets naar Awakenings naar hutjes op de hei en wandeltochten. Wij zijn echt samen opgegroeid en ik kom altijd terug van een avondje met jullie samen met een frisse blik op de wereld.

Lieve **Gustanen**, ik leerde jullie kennen toen ik liever andere dingen deed dan studeren en aan de wetenschap denken. Ik had geen enkel moment van onze elf jaar lange vriendschap willen missen. Ik heb met niemand meer (hele goede) inside jokes dan met jullie. Jullie sleepten me er altijd weer doorheen en ik ben dankbaar voor alle avondjes dat ik bij jullie terecht kon. Dit dankwoord is te kort om jullie één voor één te bedanken, maar weet dat ik dit niet zonder jullie had gekund!

Lieve paranimfen **Nathalie** en **Rose**. Wat begon als een afvalrace waarbij alleen wij overbleven (iets met paarden), bleek een hele waardevolle vriendschap te zijn. Ik voelde me altijd echt gehoord door jullie als ik het had over de dingen die ik moeilijk vond tijdens mijn PhD. Daarnaast heb ik echt genoten van onze Corona borrelfestijnen en logeerpartijen (Maasstraat laat je horen!), Rome avonturen en ons Frankrijk avontuur in ons koekblik (waar we nu gelukkig om kunnen lachen). Dankjewel voor jullie waardevolle steun!

Lieve familie **Teunissen** en **Muffels**, dankjewel voor jullie steun en wat leuk dat jullie in grote getalen naar de verdediging willen komen. Lieve **schoonfamilie Tjalma**, dankjewel voor jullie gezelligheid en het fijne samenkomen de afgelopen jaren. Ik geniet van de ongedwongen sfeer die er bij jullie hangt en wat fijn dat we altijd weer mogen komen aanzetten met een nieuwe oppas-hond!

Lieve **Powermufgirls**, lieve **Alissa** en **Nadine**. Jullie kennen me als geen ander. Onze avondjes samen zijn altijd bijzonder, of het nou voor de draaitafel van **Alissa** is, of op stap in Den Haag.

Lieve **Papa**. Goed voorbeeld doet goed volgen. Het zien van jouw bevlogenheid voor de wetenschap als kind heeft me geleerd dat dit ook voor mij ook mogelijk was. De prachtige dag die we mochten meemaken toen je afscheid nam als professor heeft dat alleen maar onderstreept. Zo hard werken als jij kon, kon ik niet, maar ik heb zeker wat trekjes van je overgenomen.



---

Het zal niet de eerste keer zijn dat Age me in mijn jas achter mijn laptop ziet werken omdat ik eigenlijk tien minuten geleden boodschappen wilde doen. Ik bewonder jouw carrière, passie en doorzettingsvermogen, voor zowel de wetenschap als voor je zolder. Ik hoop nog vele avonden met een glas goede wijn bij jou aan tafel over de wetenschap te mogen praten.

Lieve **Mam**. Over voorbeelden gesproken. Ik ken niemand die sterker is als jij, en dat heeft het afgelopen jaar alleen maar onderstreept. Ik geniet nog steeds na van onze vroege ochtend-koffietjes in mijn keuken in New York. Ik hoop dat ik wat van jouw kracht heb overgenomen en mag blijven overnemen. Ik had het absoluut niet zonder jou gekund.

Lieve **Age**, ik weet niet eens waar ik moet beginnen. Ik ken niemand (inclusief mezelf) die zo enthousiast wordt van mijn werk als jij. Dank voor de talloze keren dat je op een creatieve en intelligente wijze met mij meedacht. Nog grotere dank voor de keren dat je me hielp om even niet aan werk te denken. Zonder jouw onvoorwaardelijke steun had ik het niet gekund. Ik kan niet wachten op jouw promotie, als ik trots aan de andere kant mag staan. Ik heb nog meer zin in ons leven samen in New York, als ons Team weer compleet is, en in ons hele leven samen daarna.



